



Terms and Conditions of Use of Digitised Theses from Trinity College Library Dublin

Copyright statement

All material supplied by Trinity College Library is protected by copyright (under the Copyright and Related Rights Act, 2000 as amended) and other relevant Intellectual Property Rights. By accessing and using a Digitised Thesis from Trinity College Library you acknowledge that all Intellectual Property Rights in any Works supplied are the sole and exclusive property of the copyright and/or other IPR holder. Specific copyright holders may not be explicitly identified. Use of materials from other sources within a thesis should not be construed as a claim over them.

A non-exclusive, non-transferable licence is hereby granted to those using or reproducing, in whole or in part, the material for valid purposes, providing the copyright owners are acknowledged using the normal conventions. Where specific permission to use material is required, this is identified and such permission must be sought from the copyright holder or agency cited.

Liability statement

By using a Digitised Thesis, I accept that Trinity College Dublin bears no legal responsibility for the accuracy, legality or comprehensiveness of materials contained within the thesis, and that Trinity College Dublin accepts no liability for indirect, consequential, or incidental, damages or losses arising from use of the thesis for whatever reason. Information located in a thesis may be subject to specific use constraints, details of which may not be explicitly described. It is the responsibility of potential and actual users to be aware of such constraints and to abide by them. By making use of material from a digitised thesis, you accept these copyright and disclaimer provisions. Where it is brought to the attention of Trinity College Library that there may be a breach of copyright or other restraint, it is the policy to withdraw or take down access to a thesis while the issue is being resolved.

Access Agreement

By using a Digitised Thesis from Trinity College Library you are bound by the following Terms & Conditions. Please read them carefully.

I have read and I understand the following statement: All material supplied via a Digitised Thesis from Trinity College Library is protected by copyright and other intellectual property rights, and duplication or sale of all or part of any of a thesis is not permitted, except that material may be duplicated by you for your research use or for educational purposes in electronic or print form providing the copyright owners are acknowledged using the normal conventions. You must obtain permission for any other use. Electronic or print copies may not be offered, whether for sale or otherwise to anyone. This copy has been supplied on the understanding that it is copyright material and that no quotation from the thesis may be published without proper acknowledgement.



Towards stable molecular nanostructures on a semiconductor surface

A thesis submitted to
The University of Dublin
for the degree of
Doctor of Philosophy in Physics

Nina Christina Berner
School of Physics
University of Dublin, Trinity College
Dublin 2, Ireland

December 12, 2012

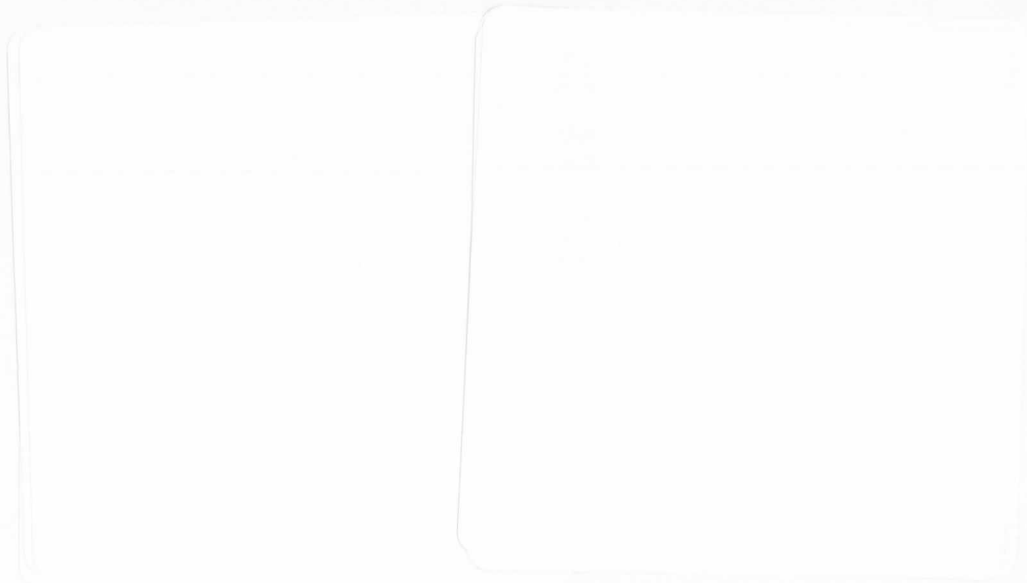


Thesis 9905

Declaration

I declare that this thesis has not been submitted as an exercise for a degree at this or any other university and it is entirely my own work.

I agree to deposit this thesis in the University's open access institutional repository or allow the library to do so on my behalf, subject to Irish Copyright Legislation and Trinity College Library conditions of use and acknowledgement.

Two large, empty rectangular boxes with rounded corners, positioned side-by-side. These boxes are intended for the student's signature and the date of the declaration.

Abstract

The miniaturisation trend in the construction of electronic devices has recently sparked an interest in the *bottom-up* construction of 2-dimensional nanostructures from single organic molecular building blocks on surfaces. Covalently bonded networks are the most desirable due to their high thermal, mechanical and chemical stability. Several different reaction mechanisms have been successfully demonstrated on coinage metal substrates over the past decade. This work explores the possibility of reproducing some of these results on a more technologically relevant semiconductor surface, in particular germanium(001), using both scanning tunnelling microscopy (STM) and photoemission spectroscopy (PES) in an ultra-high vacuum environment.

An initial investigation of the adsorption mechanism of 5,10,15,20-tetrakis(4-bromophenyl)porphyrin, a molecular precursor previously shown to form networks via a dehalogenation reaction on noble metal surfaces, revealed strong interactions between both the bromine-substituents and the conjugated π -system of the molecular macrocycle and the clean Ge(001) surface. These interactions prevent the organic molecules from diffusing on the surface, which is essential for the formation of covalent organic frameworks (COFs).

A solution is to passivate the surface with atomic hydrogen. However, when initiating thermally activated dehalogenation of the bromine-substituted porphyrin precursors on this surface, the hydrogen-passivation desorbed prematurely due to a pairing mechanism with the created bromine radicals. Therefore, a more stable passivation method is required. The adsorption and desorption characteristics of several halogens on Ge(001) are investigated in order to find a more suitable passivation agent for the desired COF formation.

Finally, a study of several reaction mechanisms and precursors for COF formation yielded best results using porphyrin molecules reacting via dehalogenation on the chlorine-passivated Ge(001) surface, which shows that the dehalogenation reaction does not require a catalysing metal surface as suggested in the literature. However, the intrinsic defects of the surface passivation and/or insufficient non-covalent molecule-substrate interactions leading to premature desorption of small precursor molecules have been found to significantly limit all of the investigated reaction mechanisms.

“The dashboard melted but we still have the radio.”

Isaac Brock (Modest Mouse), 2007

Acknowledgements

First of all I would like to thank my supervisor Prof. Iggy McGovern for his guidance, support, advice and friendship throughout the past four years. I would also like to thank Dr. Tony Cafolla for his constant availability for discussions, the generous access to his lab and his enthusiasm. I thank Dr. Cormac McGuinness for his advice and the work he has done for this thesis, Dr. Graham Cross for allowing me to use his STM system in CRANN, and Dr. Zheshen Li for his invaluable technical support during my stays at ISA.

Furthermore, I am very grateful for the support and friendship of the all people I worked with or alongside during my doctoral studies. In particular, I would like to thank Dr. Brendan Holland, Zhiming Wang, Dr. Simon O'Brien and Dr. Andrew Norris for their advice in the very beginning of my experiments, Dr. Nadjib Baadji, Dr. Sankar Kesanakurthi and Anna Lawless for their DFT calculations, and most of all Dr. Toby Hallam for his generous availability for discussions and help in the lab during the last few years. Additionally, I would like to thank my fellow PhD students for making my time at Trinity College very pleasant and memorable, especially Andrea, Ruggero, Roseanne, Evelyn, Aaron, Sandip, Mauro, Rohit, Olaf, James and Cormac.

I also want to thank my collaborators in DCU, UNSW and IM2NP, especially Catherine Doyle, Dr. Hooi Ling Lee and Dr. John Cunniffe for their help and support, Prof. Marian Radny for sharing his calculations and thoughts, and Prof. Mathieu Abel, Mathieu Koudia and Dr. Sylvain Clair for the warm welcome at IM2NP and the support during my stay there and afterwards.

I greatly acknowledge the funding I received from Trinity College Dublin, SFI, EU-ELISA and IRCSET (Ulysses). I would also like to thank the workshop and the administration in the School of Physics and in CRANN for all they have done for me.

Lastly, I want to express gratitude to my close friends and family. I specifically acknowledge Carmen, Antje and Kubi at home in Germany, as well as Kathrine, Aisling, Mary, Victoria, Ole, Gerard and Maggie for being great friends. Most importantly, I thank Adam for supporting me in more ways than anyone else. Very special thanks go to my parents for their financial and non-financial help, and in particular to my mother Heike for her selfless support throughout my entire education.

Publications and Conferences

N. C. Berner, Y. N. Sergeeva, N. N. Sergeeva, M. O. Senge, A. A. Cafolla, I. T. McGovern, *Adsorption of 5,10,15,20-tetrakis (4-bromophenyl)porphyrin on germanium(001)*, *physica status solidi c* **9** (2012) 1404

ISA User Meeting 2010 N. C. Berner, Zh. Wang, Y. N. Sergeeva, N. N. Sergeeva, M. O. Senge, A. A. Cafolla, I. T. McGovern, *Adsorption of H₂TBr₄PP on Ge(001)*, poster presentation, January 2010

ECOSS 27 N. C. Berner, Zh. Wang, Y. N. Sergeeva, N. N. Sergeeva, M. O. Senge, A. A. Cafolla, I. T. McGovern, *Adsorption of H₂TBr₄PP on Ge(001)*, poster presentation, September 2010

ICFSI-13 N. C. Berner, Zh. Wang, Y. N. Sergeeva, N. N. Sergeeva, M. O. Senge, A. A. Cafolla, I. T. McGovern, *Adsorption of H₂TBr₄PP on Ge(001)*, poster presentation, July 2011

ECOSS 28 N. C. Berner, N. Baadji, Y. N. Sergeeva, N. N. Sergeeva, M. O. Senge, A. A. Cafolla, I. T. McGovern, *Adsorption of tetra(4-bromophenyl)porphyrin on Ge(001)*, poster presentation, August 2011

IOPI Rosse Medal 2012 N. C. Berner, Y. N. Sergeeva, N. N. Sergeeva, M. O. Senge, A. A. Cafolla, I. T. McGovern, *Towards stable molecular nanostructures on a germanium surface*, poster presentation and talk, March 2012. Winner of Rosse Medal.

Contents

1	Introduction	3
2	Background	5
2.1	Crystal Structure	5
2.1.1	Miller Indices	5
2.1.2	Surface Reconstructions	6
2.2	Synchrotron Radiation	7
2.3	Photoemission Spectroscopy	8
2.3.1	Basic theory	8
2.3.2	Energy spectrum	10
2.3.3	Line intensity	13
2.3.4	Chemical shift	15
2.3.5	Core-level analysis	16
2.3.6	Experimental apparatus	17
2.4	Scanning Tunnelling Microscopy	18
2.4.1	Quantum tunnelling	18
2.4.2	Tunnelling current	19
2.4.3	Basic operational principle	21
2.4.4	Spectroscopy	22
2.5	Density Functional Theory	23
3	Materials	25
3.1	Germanium	25
3.1.1	Germanium(001)	26
3.1.2	Passivation	27
3.1.3	Germanium(111)	29
3.1.4	Germanium(110)	29
3.2	Gold	30
3.3	Organic Molecules	31
3.3.1	5,10,15,20-Tetrakis(4-bromophenyl)porphyrin	31
3.3.2	2,3,6,7,10,11-Hexabromotriphenylene	32
3.3.3	1,3,5-Tris(4-bromophenyl)benzene	33

3.3.4	4,4''-Diiodo-p-terphenyl	33
3.3.5	1,4-Benzene-diboronic acid	34
3.3.6	1,2,4,5-Tetracyanobenzene	34
3.3.7	Tetrathiafulvalene	34
4	Experimental Details	37
4.1	Ultra High Vacuum	37
4.1.1	The Omicron Multiprobe System	38
4.1.2	Vacuum pumping	40
4.2	Halogen Sources	40
4.3	Mass Spectrometry	41
4.4	Photoemission Spectroscopy	41
4.4.1	Beamlines	42
4.4.2	Omicron systems	42
4.4.3	Fitting software	43
4.4.4	DFT Calculations	43
4.5	Scanning Tunnelling Microscopy	44
4.5.1	Experimental apparatus	44
4.5.2	Tip preparation	45
4.5.3	Image processing software	46
5	Adsorption of selected organic molecules on germanium(001)	47
5.1	Literature Review	47
5.2	Molecule-substrate interactions	53
5.2.1	Substrate and macrocycle core-levels	53
5.2.2	Bromine substituents	56
5.2.3	Valence band	58
5.2.4	Ge(111) and Ge(110)	60
5.2.5	Conclusions	61
5.3	Adsorption geometry	62
5.3.1	STM of H ₂ TBr ₄ PP	63
5.3.2	STM of H ₂ TPP	68
5.3.3	Comparison	69
5.4	Adsorption of smaller organic molecules	71
5.5	Summary	73
6	Halogen adsorption and passivation on germanium(001)	75
6.1	Literature Review	75
6.2	Bromine on Ge(001)	79
6.2.1	Passivation	79

6.2.2	Lower coverages	84
6.3	Chlorine on Ge(001)	86
6.3.1	Passivation	86
6.3.2	Lower coverages	88
6.4	Iodine on Ge(001)	90
6.5	Halogen deposition from electrochemical cells	94
6.6	Summary	95
7	Dehalogenation reactions	97
7.1	Literature Review	97
7.2	Covalent organic network formation on gold substrates	101
7.2.1	H ₂ TBr ₄ PP	102
7.2.2	TBB	103
7.2.3	DITP	105
7.3	Dehalogenation reactions on passivated Ge(001)?	106
7.3.1	Dehalogenation on Ge(001):H	107
7.3.2	H ₂ TBr ₄ PP on Ge(001):Br and Ge(001):Cl	110
7.3.3	Other molecules on Ge(001):Cl	113
7.4	Summary	117
8	Other reaction mechanisms	119
8.1	Literature Review	119
8.2	Dehydration of BDBA on Ge(001):Cl	124
8.3	Formation of polymeric Mn-phthalocyanine	125
8.3.1	TCNB precursors	126
8.3.2	TCN-DBTTF precursors	128
8.4	Summary	131
9	Conclusions	133

List of abbreviations

2D	2-Dimensional	IR	Infrared
AFM	Atomic Force Microscopy	LDA	Local density approximation
BDBA	1,4-Benzene-diboronic acid	LDOS	Local density of states
BR	Branching ratio	LT	Low temperature
Br₂I₂TPP	5,15-bis(4'-bromophenyl)-10,20-bis(4'-iodophenyl)porphyrin	LUMO	Lowest unoccupied molecular orbital
CAE	Constant analyser energy	LW	Lorentzian width
CHA	Concentric hemispherical analyser	ML	Monolayer
COF	Covalent organic framework	MPc	Metal phthalocyanine
CRR	Constant retard ratio	NC-AFM	Non-contact atomic force microscopy
DB	Dangling bond	NEXAFS	Near Edge X-Ray Absorption Fine Structure
DBDPP	5,10-Dibromo-10,20-diphenylporphyrin	Pc	Phthalocyanine
DBTF	Dibromoterfluorene	PES	Photoemission spectroscopy
DCU	Dublin City University	PPP	Poly(p-phenylene)
DFT	Density functional theory	QMS	Quadropole mass spectrometer
DITP	4,4''-Diiodo-p-terphenyl	RMS	Root mean square
DOS	Density of states	RT	Room temperature
EAS	Electrophilic aromatic substitution	SOS	Spin-orbit splitting
ESCA	Electron spectroscopy for chemical analysis	STM	Scanning tunnelling microscopy
fcc	Face centred cubic	STS	Scanning tunnelling spectroscopy
FEL	Fast entry lock	SXPS	Soft X-ray photoemission spectroscopy
FWHM	Full width at half maximum	TCNB	1,2,4,5-Tetracyanobenzene
GGA	Generalised gradient approximation	TBB	1,3,5-Tris(4-bromophenyl)benzene
GNR	Graphene nanoribbon	TPD	Temperature programmed desorption
GW	Gaussian width	TPP	Tetraphenylporphyrin
HBTP	2,3,6,7,10,11-Hexabromotriphenylene	TSP	Titanium sublimation pump
hcp	Hexagonal close packed	TTF(CN)	Tetrathiafulvalene (with cyano-group substituents)
HOMO	Highest occupied molecular orbital	UHV	Ultra high vacuum
HOPG	Highly ordered pyrolytic graphite	UPS	Ultraviolet photoemission spectroscopy
H₂TBr₄PP	5,10,15,20-tetrakis(4-bromophenyl)porphyrin	VB	Valence band
IM2NP	Institute Matériaux Microélectronique Nanosciences de Provence	XPS	X-ray photoemission spectroscopy

1 Introduction

The construction of electronic devices from semiconductors has seen a remarkable miniaturisation trend over the last few years. To be able to continue this trend, the size of such devices will soon have to reach the size of molecules or a few atoms. This goal requires a new concept for the device structures [1], and one of the great hopes is that carefully chosen organic molecules can be connected into predesigned nanostructures with the desired functions such as switching or rectifying. Porous networks are of particular interest, since they can be used to capture and confine secondary molecules in a host-guest relationship [2–4].

The application of traditional lithographic or so-called *top-down* techniques for device fabrication becomes increasingly demanding with feature sizes smaller than 100 nm [5]. An alternative strategy in the construction of 2-dimensional (2D) nanostructures on surfaces is the *bottom-up* technique, which exploits non-covalent intermolecular interactions leading to self-assembly of carefully chosen functional organic molecular building blocks [6]. The geometry of the molecules and the type of interactions lead to a variety of different architectures [5, 7]. The interest in this field has increased rapidly over the past decade, and organic molecular structures held together by hydrogen bonding [2, 7–10], π - π stacking [11], dipolar [12], van der Waals [13], metal-ligand [14, 15] or substrate-mediated interactions [16] have been demonstrated.

The main disadvantage of self-assembled organic nanostructures is their low stability, which disqualifies them for use in devices and outside the ultra-high vacuum (UHV) or liquid environment in which they are created. Covalent bonds between the molecular building blocks are more desirable, giving the structures high stability and more efficient charge transport [17] or semiconducting characteristics through their 2D conjugated π -systems [18]. The first covalently bonded nanoporous network on a gold surface was demonstrated by Grill *et al.* via a dehalogenation reaction of specifically functionalised porphyrin molecules in 2007 [19]. Since then, a variety of other reaction mechanisms leading to 2D covalent organic frameworks (COFs) of different architectures has been developed [20, 21].

The progress in the field of on-surface chemistry has been fueled by the development of the scanning tunnelling microscope (STM), which provides structural and electronic information with sub-nm resolution and can operate in different environments and temperatures. Yet it does not always provide chemical information and additional techniques

are necessary to investigate whether a reaction has taken place. Photoemission spectroscopy (PES) is a powerful tool for this purpose and has been employed for the experiments in this work, in addition to STM in a UHV environment. Some theoretical calculations using density functional theory (DFT) methods to support both STM and PES data will be presented as well. Chapter 2 presents background information on all experimental techniques that have been used in this work, while Chapter 4 discusses relevant experimental details.

Almost all of the research on COFs is done on noble metal surfaces, mostly due to their low reactivity which ensures the mobility of the organic adsorbates that is necessary for the formation of both self-assembled and covalently bonded molecular networks. The work presented in this thesis extends this idea to a technologically relevant semiconductor surface. Silicon, the most common inorganic semiconductor used in devices today, may be the most obvious choice as a substrate. However, for this study, germanium has been chosen for several reasons. Firstly, it has many properties that are very similar to those of silicon but has proven to be more tolerant experimentally due to problems with water contamination of silicon. Additionally, it is of growing interest on its own merits because of its small bandgap and high carrier mobility, which make it a potential material to be used in high performance devices [22]. Chapter 3 of this thesis discusses relevant characteristics of the substrates and organic molecules used in the experiments presented in this work.

The (001) faces of both silicon and germanium are known to exhibit a unique reactivity which facilitates selective covalent attachment of organic compounds and makes them attractive substrates for organic functionalisation [23]. Chapter 5 discusses some aspects of the adsorption mechanisms of a few selected organic molecules on clean Ge(001). However, the reactivity of these surfaces also limits the mobility of organic adsorbates, which makes the desired COF formation impossible. Surface passivation is a well-established technique to suppress reactivity and create inert substrates for further functionalisation [24]. Chapter 6 presents a study of the halogen-passivation of Ge(001) as a basis for subsequent COF formation, as well as an investigation of the underlying adsorption and desorption mechanisms of the halogen atoms on this surface. The investigation of COF formation on passivated Ge(001) surfaces will then be discussed in Chapter 7 and 8, utilising the dehalogenation reaction and two other reaction mechanisms as intermolecular connection mechanisms.

2 Background

This thesis deals almost exclusively with effects on the surfaces of solids, in particular the interactions of organic molecules with semiconductor and noble metal surfaces and with each other. To investigate these interactions, the “traditional” surface science techniques of photoemission spectroscopy (PES) and scanning tunneling microscopy (STM) have been employed for chemical and structural information about the surfaces, respectively. This chapter gives the relevant background on the theory behind these techniques as well as on surface reconstructions of crystalline solids and synchrotron radiation, which has been used for most of the PES experiments.

2.1 Crystal Structure

A crystal is a solid material whose atoms or groups of atoms are arranged in a periodic three dimensional pattern. A single atom or atom group forms the basis of a crystal lattice. Every point of the lattice can then be described as a linear combination of the unit vectors \vec{a}_i :

$$\vec{T} = u_1\vec{a}_1 + u_2\vec{a}_2 + u_3\vec{a}_3 \text{ with } u_i \in Z \quad (2.1)$$

The unit vectors form the simplest structural unit of the crystal lattice, referred to as the *unit cell*. The length of the unit cell edges and the angles between them are the *lattice parameters* of the structure.

The defining property of crystal lattices is that after operations like lattice translation, rotation around an axis, point inversion or plane mirroring, the lattice can remain unchanged. There are 14 possible symmetries of different crystal lattice systems in three dimensions, referred to as the *Bravais lattices*. They can be divided into seven lattice systems (from least to most symmetric): triclinic, monoclinic, orthorhombic, rhombohedral, tetragonal, hexagonal and cubic.

2.1.1 Miller Indices

A plane through the crystal that goes through several lattice points is referred to as a *lattice plane*. A family of parallel lattice planes, i.e. a direction in the crystal, is described by three integers commonly denoted as (h, k, l) . These *Miller indices* are determined by

the inverses of the interceptions of the lattice plane in the basis of the lattice vectors, as shown in Fig. 2.1. They are usually written in the smallest terms, i.e. the smallest set of integers with the same ratio. When a lattice plane does not intercept a crystal axis, the Miller index is zero. Negative integers are conventionally written with a bar ($\bar{2}$ for -2). The notation of the Miller indices in curved instead of round brackets refers to all equivalent planes in the crystal lattice.

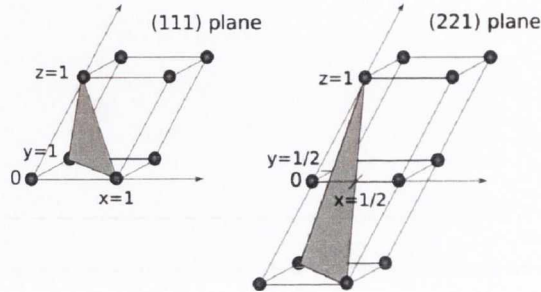


Figure 2.1 Examples of determining indices for a plane using intercepts with axes; left (111), right (221).

2.1.2 Surface Reconstructions

In the most simple case the atoms on the surface form a well-defined lattice plane in positions that correspond to the periodicity of the bulk crystal. In reality, the bulk-terminated surface is almost never observed. In most cases the surface atoms change positions and the phenomena of *relaxation* or *reconstruction* can be observed. For semiconductor surfaces, reconstruction is the most prevalent process, which occurs as a consequence of unsatisfied valences on the surface, so called *dangling bonds* (DB). By reconstructing the surface the number of DBs and therefore the surface energy are minimised.

The most common way to describe surface reconstructions is *Wood's notation*. It describes a reconstruction or an ordered overlayer in terms of the ratio of the lengths of the superlattice and bulk crystal lattice vectors, represented here as $\vec{b}_{1,2}$ and $\vec{a}_{1,2}$, respectively:

$$|\vec{b}_1| = p|\vec{a}_1|, \quad |\vec{b}_2| = q|\vec{a}_2|. \quad (2.2)$$

In addition, the angle ϕ through which the superlattice is rotated with respect to the substrate lattice may be indicated. The structure is then referred to as

$$X(hkl) p \times q R\phi - Y, \quad (2.3)$$

where X is the substrate material, (hkl) are the Miller indices of the surface plane in question and Y the material of an adsorbed overlayer, if present. If the superlattice is not rotated with respect to the substrate unit cell, the $R\phi$ is omitted.

In some instances it is possible to use a centred unit cell description for a structure for which the primitive unit cell cannot be described using Wood's notation. To distinguish between the two representations, the letter c or p is noted in front of $(p \times q)$.

A more general method of describing surface reconstructions, a matrix notation proposed by Park and Madden [25], will not be discussed here.

2.2 Synchrotron Radiation

When charged particles are in relativistic motion on a curved trajectory, they emit light, or *synchrotron radiation*. The total power spectrum of radiation produced in this case is proportional to γ^4 , where

$$\gamma^{-1} = \sqrt{1 - \frac{v^2}{c^2}} = \frac{m_0 c^2}{E}. \quad (2.4)$$

v is the velocity of the particle, m_0 its rest mass, c the speed of light and E its energy. To achieve high spectral power, the particle must therefore have a high energy and a low rest mass, which is why electrons are a typical choice. At relativistic velocities the radiation is directed along the tangent of the curved motion, with an angular distribution proportional to γ^{-1} . It is also strongly polarised in the plane of the particle motion. A more detailed theoretical description can be found in [26].

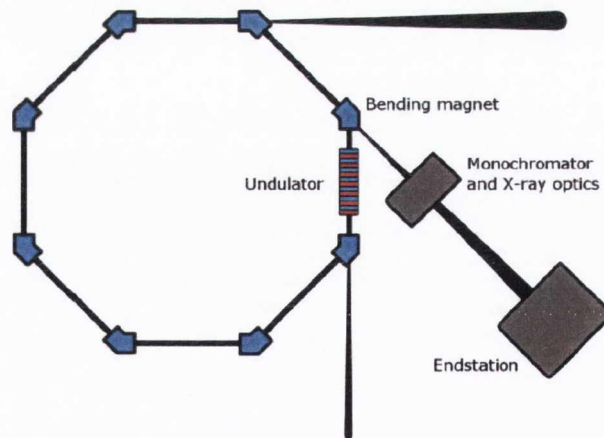


Figure 2.2 Schematic of a basic synchrotron storage ring. [27]

To generate synchrotron radiation, electrons are accelerated to relativistic speeds in a linear accelerator or ring and then injected into a storage ring under high vacuum. A typical storage ring consists of straight sections joined by curved sections equipped with bending magnets, as shown in Fig. 2.2. Various other magnet arrangements like wigglers, shifters or undulators are also used on the straight segments in order to achieve specific

photon distributions. However, none of the latter have been utilised for the experiments presented in this work.

The light beam is then focused by X-ray optics such as slits, attenuators and mirrors and monochromated with a movable diffraction grating, before arriving at the endstations with various experimental setups. Synchrotron radiation is of high intensity, well focused, polarised and with tunable energy, making it increasingly popular and important for use in many different surface science techniques.

2.3 Photoemission Spectroscopy

Photoelectron or photoemission spectroscopy (PES) is an established and widely used technique which yields chemical information about the elements present at the surface or in the near surface bulk. It is based on the Photoelectric Effect, which describes the emission of electrons from atomic orbitals after the adsorption of electromagnetic radiation. If the incident radiation is monochromatic and of a known energy, analysis of the kinetic energy of the emitted electrons reveals information about their initial binding energy in the material. PES is sometimes historically referred to as electron spectroscopy for chemical analysis (ESCA).

Depending on the spectral range of the incident radiation, PES is commonly divided into two main categories. When electrons are excited by radiation of energies in the 16 to 41 eV range [28] it is typically referred to as *ultraviolet photoemission spectroscopy* (UPS) and used to probe the loosely bound valence states. At higher excitation energies it is called *X-ray photoelectron spectroscopy* (XPS) or sometimes *soft X-ray photoelectron spectroscopy* (SXPS) when conducted with synchrotron radiation (see 2.2) at the lower end of the X-ray energy range. The high energy radiation allows for excitation of the element specific core level electrons and therefore chemical analysis of the sample material.

This section details the important aspects of the theory behind photoelectron spectroscopy as well as the analysis of the resulting spectra. The experimental apparatus as used for the experiments in this work will be described in more detail in section 4.4.

2.3.1 Basic theory

The theory behind photoemission is very complex since it requires the description of both the equilibrium and the excited state of the material and its interaction with the driving electromagnetic fields, which are modified by this interaction. Furthermore, there is almost always (except for the hydrogen atom) more than one electron involved in the excitation/emission process, making photoemission theory a complicated many-body theory. These problems must also be solved in the vicinity of the surface, which changes all system properties dramatically.

It is not the object of this thesis to describe the theory in detail. This section only contains the basic and simplified theory of electron excitation and emission which is required for an appropriate understanding of some of the results discussed in this work. For more detailed discussions of the photoemission theory see references [28–30].

The probability w of the excitation of an electron from its initial state i with wave function Ψ_i to the final state f with wave function Ψ_f by an assumed small perturbation Δ is given by Fermi's Golden Rule [30]

$$w \propto \frac{2\pi}{\hbar} |\langle \Psi_f | \Delta | \Psi_i \rangle|^2 \delta(E_f - E_i - \hbar\omega) \quad (2.5)$$

in which the delta function describes the energy conservation due to absorption of a single photon of energy $\hbar\omega$.

The most general form of Δ (for an electron in an electric field) is

$$\Delta = \frac{e}{2mc} (\vec{A} \cdot \vec{p} + \vec{p} \cdot \vec{A}) - e\phi + \frac{e^2}{2mc^2} \vec{A} \cdot \vec{A} \quad (2.6)$$

with \vec{A} as the vector potential of the incident radiation, $\vec{p} = i\hbar\nabla$ the momentum operator, ϕ the scalar potential, e the elemental charge, m the rest mass and c the speed of light. Applying the commutation relation results in $\vec{A} \cdot \vec{p} + \vec{p} \cdot \vec{A} = 2\vec{A} \cdot \vec{p} + i\hbar(\nabla \cdot \vec{A})$. Equation 2.6 can be further simplified by neglecting the term $\vec{A} \cdot \vec{A}$ which represents two photon processes, and by assuming that the potential at the site of the core hole creation is translationally invariant throughout the solid and therefore $\nabla \cdot \vec{A} = 0$. Using the gauge $\phi = 0$, the perturbation Δ is finally reduced to

$$\Delta = \frac{e}{mc} \vec{A} \cdot \vec{p}. \quad (2.7)$$

Additionally, for a wide range of experiments it can be assumed that the wavelength of the incident light is very large when compared to the electron wavefunction, so \vec{A} can be considered as a constant A_0 . This is commonly referred to as the *dipole approximation*. This changes Eqn. 2.5 to

$$w \propto |\langle \Psi_f | \vec{p} | \Psi_i \rangle|^2 \delta(E_f - E_i - \hbar\omega) \quad (2.8)$$

with \vec{p} as the operator. This finally leads to the heart of all theories about PES, the *sudden approximation*. It means that the escape of the photoelectron and the creation of the core-hole is assumed to be instantaneous and without giving the rest of the electrons in the system time to relax. Under that assumption, the transition matrix can be separated into one component for the photoexcited electron with initial and final state wave functions ψ_i and ψ_f and another one of overlap integrals of the initial and final state wave functions $\Psi_{i,R}$ and $\Psi_{f,R}$ of the remaining $N - 1$ electrons after photoionisation:

$$\langle \Psi_f | \vec{p} | \Psi_i \rangle = \langle \psi_f | \vec{p} | \psi_i \rangle \langle \Psi_{f,R} | \Psi_{i,R} \rangle. \quad (2.9)$$

These simplifications will be referred to again in the following discussions about energies and line intensities in the photoemission spectra.

2.3.2 Energy spectrum

The energy spectrum of photoelectrons observed in PES reflects the complexity of the underlying theory briefly discussed in 2.3.1. Many different processes contribute to the overall spectra, the most prominent ones of which are shown in Fig. 2.3 and will be discussed in this section.

The spectra can generally be divided into two parts, the element specific core-levels and the valence band. The latter gives information about the electrons directly involved in bonding but is difficult to interpret since the observed peaks result from combinations of valence electrons. Additionally, the low-energy background of inelastically scattered electrons is significant when compared to the line intensities in this region.

The core-level spectrum consists of the core-level photoemission lines and their satellites, Auger lines resulting from hole deexcitation via the Auger process, and a background of inelastically scattered electrons, as mentioned for the valence band region.

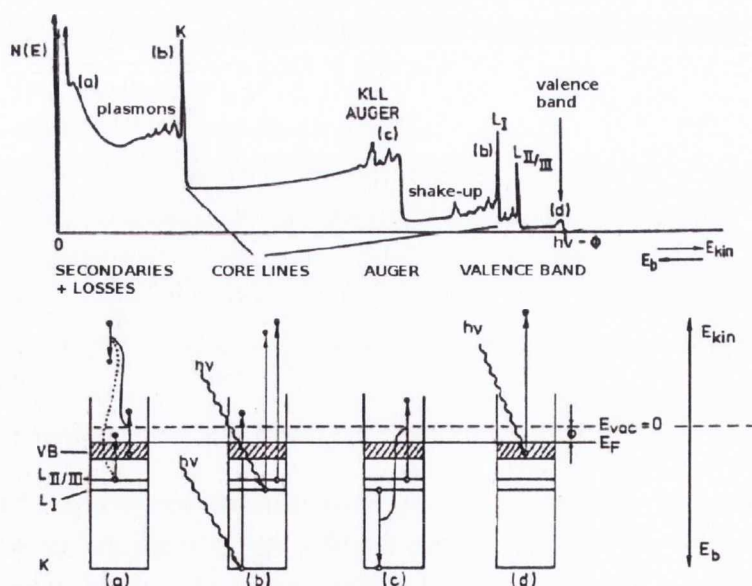


Figure 2.3 Basic processes contributing to a photoemission spectrum, including (b) core lines due to direct photoexcitation of core-level electrons or (d) valence band electrons, (c) emission of electrons due to the Auger effect, and (a) inelastic losses giving rise to secondary electrons and plasmon satellites. [28]

Photoexcitation Spectra

The most basic transition probability as it is discussed above results from assuming that $\Psi_{i,R} = \Psi_{f,R}$ in Eqn. 2.9. This leaves a single electron transition matrix element and simplifies the theory into the most commonly found equation for the kinetic energy E_{kin} of the photoelectron, sometimes referred to as Einstein's photoelectric equation:

$$E_{kin} = \hbar\omega - E_B - \phi \quad (2.10)$$

where $\hbar\omega$ is the photon energy of the incoming radiation, E_B is the binding energy of the electron in the sample (relative to the Fermi level E_F), and ϕ is the minimum energy needed for the electron to escape into the vacuum (see Fig. 2.4). Despite the multiple simplifications and approximations leading to this formula, it serves as a good description of the major photoemission lines in most cases.

However, the effects of the relaxation of the remaining electrons after photoionisation often result in a distinct difference between the initial and final state wavefunctions, whose overlap integral therefore leads to several possible excited states with a spectral output. One example is the asymmetric lineshape with an elongated tail on the low kinetic energy side commonly seen in metals [32,33], another one are the so-called *shake-up* peaks in the spectra of many organic molecules or some transition metal complexes [34].

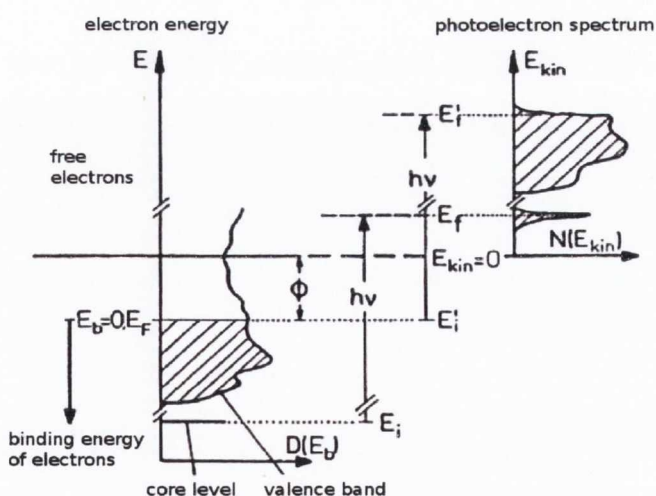


Figure 2.4 Principle of Photoelectron Spectroscopy. E_b : Binding energy of the electron in the sample, $D(E_b)$: density of states in the sample, E_F : Fermi energy, ϕ : work function, $h\nu$: photon energy of the incident light, E_i : initial energy of the electron, E_f : final energy of the electron, E_{kin} : kinetic energy of the free electron, $N(E_{kin})$: kinetic energy spectrum of the free electrons. [31]

Auger Spectra

Another prominent feature in photoemission spectra are the lines caused by *Auger electrons*, emitted due to the Auger effect. When the hole left by a photoexcited electron is filled by an electron from a higher energy level, the released energy can be transferred to another electron which is then emitted from the material (see Fig. 2.3c). It is important to note that the kinetic energy of the emitted electron is therefore only dependent on the difference between the core-levels of the specific material, and *independent* of the energy of the incident radiation. In practice, this means that the photon energy for a particular experiment has to be carefully chosen to avoid overlap of photoemission and Auger peaks.

Background

As mentioned before, the background spectrum is due to the inelastic scattering of photoexcited electrons by either other electrons or ions in the solid. The most general theoretical description of the background is given by

$$B(E) = \int_{E' > E} \lambda(E)S(E, E')P(E')dE' \quad (2.11)$$

where $\lambda(E)$ is the mean free path of the electron at energy E , $S(E, E')$ is the scattering function and $P(E')$ is the spectrum. $\lambda(E)S(E, E')$ is referred to as the energy loss function and its accurate determination is difficult, both experimentally and theoretically. However, there are two commonly used methods to approximate the electron energy loss. The first one was proposed by Shirley in 1972 [35] and is based on the assumption that the scattering is constant. This gives the formulation of Eqn. 2.11 as

$$B_S = A \int_{E_1}^{E_2} (P(E') - P_0)dE' \quad (2.12)$$

with $E_1 > E_2$, A as a constant fitted to the experimental data and P_0 as the background intensity at E_0 , a point on the high kinetic side of the peak at which the intensity of the tails of the peak is approximately zero. The Shirley background is only a rough approximation, but works sufficiently well when applied to short energy ranges like for the fitting of a single peak. It is however known to often yield inaccurate results in the case of metals [30]. For these cases Tougaard suggested a “universal” energy loss function derived from empirical results [36], generally referred to as the Tougaard background:

$$\lambda(E)S(E, E') = \frac{A(E - E')}{(B + (E - E')^2)^2} \quad (2.13)$$

with A and B being empirically determined constants. Their values are originally $A = 1643$ (eV)² and $B = 2866$ (eV)², although A is often left as a variable to be fitted to the data.

2.3.3 Line intensity

The intensity of the core-level lines in the PES spectra is measured as the area of a peak and depends on a number of factors, the most important of which will be discussed in this section. As will be shown, the calculation or measurement of most of these factors is complicated and the combination of errors in the determination of each of them results in a total error in the range of $\pm 25 - 30\%$.

Equipment related effects

The intensity of the spectra will vary greatly with the incident photon flux, the geometry of the experimental setup and the operating conditions and type of the energy analyser. However, these variations are uniform over the entire spectrum and can therefore be ignored when comparing relative intensities. While the type of analyser is a fixed parameter for any given chamber, its operating conditions can be selected to match the requirements of any particular experiment, generally with the choice between intensity and resolution. This will be discussed in more detail in section 2.3.6.

The intensity variation due to the geometry of the experimental setup is mostly determined by the angle of emission. On increasing the angle of emission, the electrons must travel $\frac{1}{\cos^2(\theta)}$ times further through the solid to escape. The intensity of emitted electrons decays exponentially with thickness (see the following section about escape depth) and therefore an increased angle of emission gives a higher proportion of signal from the surface, increasing surface sensitivity.

Escape depth

Electrons in solids have a finite mean free path λ which is the average distance an electron travels before it loses energy due to inelastic scattering through effects such as plasmon or conduction electron excitation. These depend on the energy of the electron and are generally material independent, as seen in Fig. 2.5. The broad minimum of the mean free path ($< 10 \text{ \AA}$) occurs in the energy range of 50 - 100 eV, which means that photoelectrons emitted at those energies yield the greatest surface sensitivity.

The probability of an electron escaping without undergoing inelastic scattering is proportional to $e^{-\frac{x}{\lambda}}$ with x as the distance

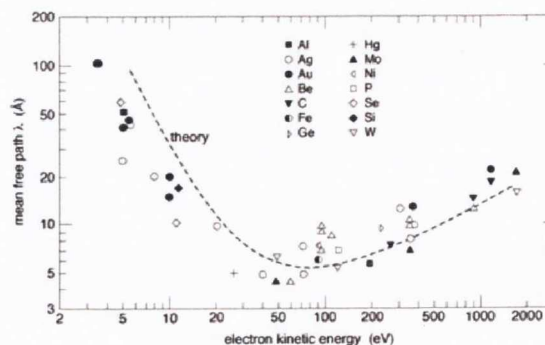


Figure 2.5 Escape depth λ of electrons in various solids. [37]

travelled through the solid. This dependence can be used to calculate the thickness of a film or overlayer by comparing the core-level intensities with and without the overlayer:

$$I = I_0 e^{-\frac{x}{\lambda}} \quad (2.14)$$

where I is the intensity of the photoelectrons emitted through the overlayer, I_0 the intensity without it (after considering all other factors influencing the intensity).

Core-level occupancy

Since XPS is a core-level spectroscopy, all probed core-levels are fully occupied, i.e. 2, 6, 10 and 14 for s , p , d and f orbitals, respectively. The intensity of the respective lines is directly proportional to the number of electrons occupying the orbital. However, for orbitals with a quantum number $l \neq 0$ spin-orbit coupling influences the spectral lines and the peaks split into doublets. The quantum number of the angular momentum is

$$j = |l \pm s| \quad (2.15)$$

where l is the quantum number of the orbital momentum and s the quantum number of the spin momentum. The total angular momentum for a given electron has the magnitude $\hbar\sqrt{j(j+1)}$ and components in any specified direction of $\hbar m_j$, where $m_j = j, j-1, \dots, -j$. This gives a total of $2j+1$ degenerate states. The ratio of occupation and therefore of the intensities of the spin orbit peaks can consequently be determined with

$$\frac{2(l+1/2)+1}{2(l+1/2)-1} \quad (2.16)$$

The core-levels are typically denoted with

$$nX_j \quad (2.17)$$

where n is the principal quantum number, X is the subshell s, p, d or f for $l = 0, 1, 2$ or 3 , respectively, and j is given by Eqn. 2.15 (s is always $1/2$ for a single electron). So for example $3d_{3/2}$ refers to an electron with the quantum numbers $n = 3, l = 2, j = 3/2$.

Cross section

The probability for an electron to be excited by a photon varies strongly with the photon energy and the specific core-level. This is referred to as the cross section. In general the cross section decays towards higher photon energies. For photon energies just above the threshold the cross section changes significantly, depending on the type of orbital.

In order to get manageable signal to noise ratios in experiments, it is critical to select photon energies with optimised cross sections. A set of calculated cross sections for all

elements has been published by Yeh and Lindau [38]. The choice of the incident photon energy is generally a compromise between the cross section resulting in the maximum intensity, the escape depth yielding the highest surface sensitivity and the attempt to avoid interference with Auger electron peaks.

2.3.4 Chemical shift

The core-level energies are characteristic of the particular element. However, small shifts in the energy levels can occur as a result of a changed chemical environment. A change of the element's bonding configuration primarily affects the arrangement of the valence electrons, which then alters the electrostatic fields in the vicinity of the core and therefore also the core energy levels. These shifts are small but observable, and much easier to interpret than the complex rearrangement of valence electron levels [28].

The effect of the valence charge of the atom on the core-level energies can be described by the potential created by that charge. It is the sum of two components, the Coulomb potential of the atom and the Madelung potential describing the influence of the surrounding lattice [30]:

$$\Delta V = \frac{\Delta Q_i}{4\pi\epsilon_0 r_v} + \sum_{j \neq i} \frac{\Delta Q_j}{4\pi\epsilon_0 R_{ij}} \quad (2.18)$$

where ΔQ_i is the change in charge in atom i , r_v is the average valence shell radius, ΔQ_j is the change in charge in the surrounding lattice atoms j and R_{ij} are the distances between the atoms j and i . The Coulomb potential is in the order of 12 eV per electron transferred and the Madelung potential is in the order of 10 eV per electron transferred. The two energies are of opposite sign, which results in a total energy shift in the order of 2 eV per electron transferred.

An example of the chemical shifts in the C 1s level of ethyl fluoroacetate is shown in Figure 2.6. The carbon atoms in this molecule are bound in four different chemical environments resulting in four different C 1s peaks. Assigning each peak to a specific bonding configuration can often be done by considering the electronegativity χ of the bonding partners (in this case $\chi_H < \chi_C < \chi_O < \chi_F$) or by consulting reference energy values available in the literature (e.g. [39]).

The chemical shifts have so far only been discussed as a result of initial state effects, but they are also partly due to final state effects arising from the charge redistribution as

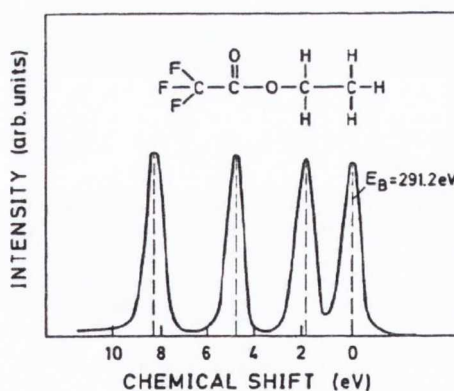


Figure 2.6 Chemical shift of the C 1s core-level in $C_2H_5CO_2CF_3$ [28].

a reaction to the creation of a local hole. The discussion of the latter is more challenging (see references [40, 41]) and is of no major significance for the results presented in this work.

2.3.5 Core-level analysis

Extracting and assigning all components of a core-level spectrum is the goal of the analysis process. This is not an easy task in practice, as the peaks are often not clearly separated and lie on a non-zero background. The relative intensity and position of the components have to have physical meaning and result in a reasonably good fit of the experimental data.

Background Subtraction

To analyse a core-level correctly, the background spectrum generated by inelastic scattering of excited electrons must first be subtracted from the data. This is usually done by fitting it numerically, following one of the two methods described in section 2.3.2. The Shirley background is commonly used for semiconductor samples, whereas the Tougaard background yields better fit results for metals. Sometimes an additional polynomial of first or second order can be necessary to account for inelastic scattering from core levels of lower binding energy in the spectrum.

In the case where the background contains features that are related to the substrate and the area of interest is an adsorbate film, a difference spectrum between post- and pre-deposition can be sufficient.

Line Shape

The line shape of every core-level peak is usually assumed to be a *Voigt profile*, which is a convolution of a component with a Lorentzian and a component with a Gaussian linewidth. The Lorentzian linewidth $f_L = 2\gamma$ is associated with the element specific lifetime broadening whereas the Gaussian linewidth $f_G = 2\sigma \ln(2)$ is a result of all experimental broadening (i.e. the monochromator and analyser resolution) and possible broadening due to sample inhomogeneity. Mathematically, the Voigt profile is defined as

$$V(E; \sigma, \gamma) = \int_{-\infty}^{\infty} G(E', \sigma) L(E - E', \gamma) dE' \quad (2.19)$$

with the Gaussian component

$$G(E; \sigma) = \frac{e^{-E/2\sigma^2}}{2\pi\sigma} \quad (2.20)$$

and the Lorentzian component

$$L(E; \gamma) = \frac{\gamma}{\pi(E^2 + \gamma^2)}. \quad (2.21)$$

For metallic core levels with an asymmetric tail due to the final state relaxation (as mentioned in section 2.3.2), the Doniach and Sunjic lineshape is commonly used:

$$DS(E; \alpha, \gamma) = \frac{\cos \left[\frac{\pi\alpha}{2} + (1 - \alpha) \tan^{-1} \left(\frac{E}{\gamma} \right) \right]}{(E^2 + \gamma^2)^{(1-\alpha)/2}}. \quad (2.22)$$

To obtain fits with physical meaning, it is usually a reasonable assumption for all components of the same core-level to have the same Lorentzian and Gaussian linewidth as well as the same spin-orbit splitting and branching ratio. However, distinctly different chemical environments of the components may result in differences in broadening and the branching ratio can vary slightly due to diffraction effects.

2.3.6 Experimental apparatus

Figure 2.7 shows the basic configuration of a typical XPS experiment.

The photon source is either synchrotron radiation (see 2.2) or an X-ray source, the latter typically equipped with both an Al and a Mg anode. The sample and the analyser are usually grounded, but in some cases a known voltage can be applied to the sample to shift its energy levels, e.g. to determine its ionisation potential.

Before the emitted photoelectrons enter the analyser, they are focused and retarded in an array of lens elements. This allows the choice between collecting as many electrons as possible from a large sample area (for example for lab experiments with low incident photon intensity) or focusing electrons from a small spot size, as in synchrotron experiments for angular resolved experiments.

The analyser shown in Fig. 2.7 is a concentric hemispherical analyser (CHA), the most commonly used type of analyser for high resolution PES. The outer hemisphere is at a negative potential with respect to the inner one, thereby only allowing electrons of a very specific energy to follow the semi-circular path between the entrance and exit slits of the analyser. This energy is referred to as the *pass energy* E_P , given by

$$E_P = \frac{eV}{\frac{R_1}{R_2} - \frac{R_2}{R_1}} \quad (2.23)$$

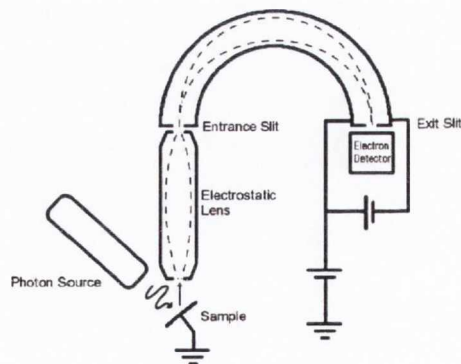


Figure 2.7 Schematic of the basic experimental setup for PES. [27]

with V being the voltage between the two hemispheres and R_1 and R_2 the radii of the outer and inner hemispheres, respectively. The exit and entrance slits as well as the acceptance angle result in a finite range of electron energies that pass the analyser. The full width at half maximum (FWHM) of that energy distribution is defined as the energy resolution ΔE of the analyser, which can be determined from

$$\Delta E = E_P \cdot \frac{S}{2R_0} + \alpha. \quad (2.24)$$

S is the slit width, R_0 the mean radius of the two hemispheres and α is a term to take angular effects into account. In most experiments, the pass energy of the analyser is held constant and the retarding field at the entrance slit is varied to provide energy selectivity, which is usually referred to as constant analyser energy (CAE) mode. Another option is the constant retard ratio (CRR) mode, in which the pass energy is varied. However, this mode will give a poor energy resolution ΔE at high energies as can be seen from equation 2.24.

There are several types of electron detectors that are employed for PES, all relying on electron multipliers which utilise the secondary emission of electrons. A series of single electron multipliers or channeltrons along the length of the exit slit is most commonly used for detection in smaller analysers, whereas some of the larger ones feature channel plates. The output from a channel plate array of multipliers is typically detected with a CCD camera on a phosphorescent screen, which can give both energy and momentum information in a single snapshot.

A more specific description of the equipment used for the experiments presented in this work is given in section 4.4.

2.4 Scanning Tunnelling Microscopy

The Scanning Tunnelling Microscope (STM) was developed by Binnig and Rohrer in the 1980s [42, 43] and since then has become one of the most widely used techniques in surface science. It facilitates the real space imaging of surface structures like reconstructions, adsorbates or defects down to the atomic scale by scanning a metal tip over a surface and thereby probing the local density of states (LDOS). This is possible due to the quantum mechanical phenomenon of the tunnelling current, which will be detailed in the following sections.

2.4.1 Quantum tunnelling

In classical mechanics, a particle with the energy E in a potential $U(z)$ can only surmount a potential barrier U_0 if $E > U_0$ or it will be reflected elastically. However, in quantum mechanics a particle is described with a wavefunction $\psi(z)$ which satisfies Schrödinger's

equation:

$$\left(-\frac{\hbar^2}{2m} \frac{d^2}{dz^2} + U(z)\right) \psi(z) = E\psi(z). \quad (2.25)$$

Solving the equation for $E > U$, meaning in the classically allowed region, gives wavefunctions of the form

$$\psi(z) = \psi_0 e^{\pm ikz}, \quad (2.26)$$

with the wave vector

$$k = \frac{\sqrt{2m(E - U)}}{\hbar}. \quad (2.27)$$

Inside the potential barrier, 2.25 has the solution

$$\psi(z) = \psi_0 e^{-\kappa z}, \quad (2.28)$$

with the decay constant

$$\kappa = \frac{\sqrt{2m(U - E)}}{\hbar}. \quad (2.29)$$

This means there is a nonzero probability for a particle to penetrate the potential barrier, which is generally referred to as the *tunnel effect*.

Starting from this simple model, some basic features of metal-vacuum-metal tunnelling can be explained. As mentioned in 2.3.2, the minimum energy to remove an electron from a solid to the vacuum level is referred to as the work function ϕ . The value of ϕ generally depends on the specific material and the crystallographic orientation of the surface. In metals, the highest occupied state is the Fermi level E_F and with the vacuum as the reference point of the energy $E_F = -\phi$ [44].

By applying a bias voltage V , a sample state ψ_μ at the energy level E_μ lying between $E_F - eV$ and E_F has the chance of tunnelling into the empty states of the tip and a net tunnelling current occurs, which is the basic principle allowing STM to probe the LDOS on a sample surface (illustrated in Fig.2.8a). A theoretical description of the tunnelling current will be given in the following section.

2.4.2 Tunnelling current

The most extensively used formalism for the theoretical treatment of the tunnelling current in STM was developed by Bardeen in 1961 [45]. His theory is based on the tunnelling process in a metal/insulator system and the assumption that the metal electrodes are a weakly interacting system, in which the tunnelling process is facilitated by the overlap of the wavefunctions inside the insulating layer, as shown in Fig. 2.8b and c. Using

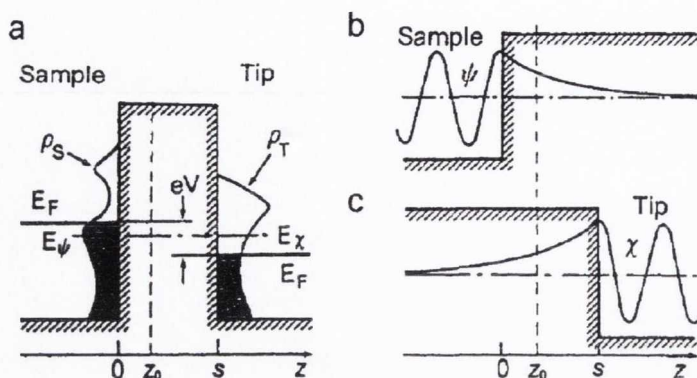


Figure 2.8 (a) Metal-vacuum-metal tunnelling junction. (b) and (c) Illustration of the Bardeen approach to tunnelling theory. [44]

time-dependent perturbation theory and Fermi's golden rule (see Eqn. 2.5) he found an expression for the tunnelling current in that system. Tersoff and Hamann [46] later extended that approach to a metal-vacuum-metal tunnelling junction, as present in the STM. For the case of absolute zero $T = 0$ K and for small biases V they found the following expression for the tunnelling current:

$$I = \frac{2\pi}{\hbar} e^2 V \sum_{\mu, \nu} |M_{\mu\nu}|^2 \delta(E_\mu - E_F) \delta(E_\nu - E_F). \quad (2.30)$$

E_μ and E_ν are the energies for the states ψ_μ and χ_ν , relative to the Fermi level of the respective electrodes. $M_{\mu\nu}$ is the matrix element between the two states, which Bardeen showed to be a surface integral on the separation surface between the two electrodes, $z = z_0$:

$$M_{\mu\nu} = \frac{\hbar}{2m} \int_{z=z_0} \left(\chi_\nu^* \frac{\partial \psi_\mu}{\partial z} - \psi_\mu \frac{\partial \chi_\nu^*}{\partial z} \right) dS. \quad (2.31)$$

To solve equation 2.30, the exact energy values, wave functions and the atomic structures of both tip and sample surface are needed. However, the tip geometry is usually unknown, which prompted Tersoff and Hamann to introduce a simplified model. By assuming an ideal sensor tip with a point charge at \vec{r}_{tip} with the radius R , only s -wavefunctions have to be considered for the electrons in the tip (s -wave-tip model [47]). This means the angle dependence of the charge distribution can be neglected and the tunnelling matrix element is proportional to the sample state ψ_μ . The tunnelling current therefore becomes

$$I(\vec{r}_{\text{tip}}, V) \propto \sum_{\mu} |\psi_\mu(\vec{r}_{\text{tip}})|^2 \delta(E_\mu - E_F) \equiv \rho_S(\vec{r}_{\text{tip}}, E_F). \quad (2.32)$$

Equation 2.32 shows that the tunnelling current depends on the LDOS $\rho_S(\vec{r}_{\text{tip}}, E_F)$ of

the sample surface at the Fermi level E_F and the centre of the curvature of the tip \vec{r}_{tip} . Furthermore, the wavefunction ψ_μ decays exponentially along the surface normal z :

$$\psi_\mu \propto e^{-\kappa z}. \quad (2.33)$$

At \vec{r}_{tip} , $z = R + s$ with s as the distance between tip and sample. Equation 2.32 therefore yields the following fundamental dependency for the tunnelling current:

$$I \propto e^{-2\kappa s}. \quad (2.34)$$

In conclusion, the tunnelling current in STM strongly depends on the distance between tip and sample and additionally on the LDOS of the sample surface.

2.4.3 Basic operational principle

Figure 2.9 shows the basic operational principle of an STM. A metallic tip scans a conducting surface at a distance of a few Ångströms. As explained in the previous section 2.4.2, applying a bias V between the tip and the sample results in a measurable tunnelling current between the two. The tip is attached to three piezo-drives in the x , y and z directions, which allows the nanometer-precise movements of the tip. A more detailed description of the instrumentation used for the experiments contributing to this work can be found in section 4.5.

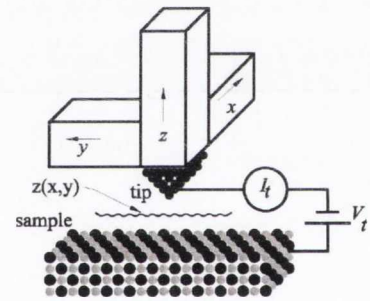


Figure 2.9 Basic operational principle of the STM.

Modes of operation

There are two scanning modes that can be employed with the STM. Either the tunnelling current or the height of the tip above the surface can be held constant and the respective other parameter is then measured, yielding topological data. The advantage of the *constant height mode* is that scanning is much faster than in constant current mode since the z -piezo does not have to be constantly adjusted to maintain the set current. The fast scanning speed additionally makes it less susceptible to low frequency noise. However, in most experiments the *constant current mode* is used because the height differences in the surface are usually quite significant and are likely to cause the tip to crash into the surface.

In addition, there are two modes of current measurement, depending on the polarity of the applied bias V . Fig. 2.8a shows electrons being able to tunnel from the filled states of the sample (below E_F) into the empty states of the tip (above E_F) by applying a negative

bias V to the sample. This is referred to as *filled state* imaging since it probes the filled states of the sample surface. If a positive bias V is applied, the Fermi level E_F of the tip is shifted above the Fermi level of the sample, resulting in electrons tunnelling in the opposite direction and thereby probing the empty states of the sample (*empty state* imaging).

Resolution

The resolution of an STM generally depends on the geometry of the tip and the sample and on their respective electronic structure. When imaging large (μm) objects, the geometry of the tip on the μm length scale plays an important role on how the image is modified by the tip shape. However, on those length scales it is usually possible to determine the tip shape and to partially correct the resulting image.

On an atomic scale, there are no general resolution criteria in STM like the diffraction limit in optical microscopy, but various resolution criteria have been published in the literature [47–51]. The semiclassical model by Simmons [50] and a more complex calculation for metals by Tersoff [47] yield the same functional behaviour for the effective diameter L_{eff} of the tip as a measure for the resolution on an atomic scale. Tersoff's calculation results in a Gaussian distribution with a root mean square (RMS) width of

$$L_{\text{eff}} = \left(\frac{z_0}{2\kappa_0} \right)^{1/2}, \quad (2.35)$$

where $z_0 = d + R$ is the distance between the sample and the centre of the curvature of the tip and κ_0 is the decay constant of the wavefunction of electrons tunnelling normal to the surface. This shows that the resolution of the STM depends critically on the radius R of the curvature at the apex of the tip, suggesting that ideally, very narrow tips with single atom apexes should be used. However, these tips are not stable while scanning and the forces between tip and sample tear them apart. Hence a high resolution tip has to be a compromise between stability and high curvature. It has been found that tip radii of a few nm to a few 10 nm give best results.

Finally, Tersoff notes that for semiconductors or semimetals like graphite the resolution of an STM is higher than for metals imaged with the same tip [47].

2.4.4 Spectroscopy

The tunnelling current measured by STM at a finite bias in imaging mode consists of contributions of all states within eV of the Fermi level E_F . This integrated current reflects the topology of the surface. But another great strength of the STM is that it can also be used to get spatially resolved spectroscopic data. At its simplest, this data is obtained by placing the tip at a fixed height over a specific site on the surface and by then varying the applied voltage over a specified range and measuring the current. Assuming a free electron metal tip, equation 2.32 implies that

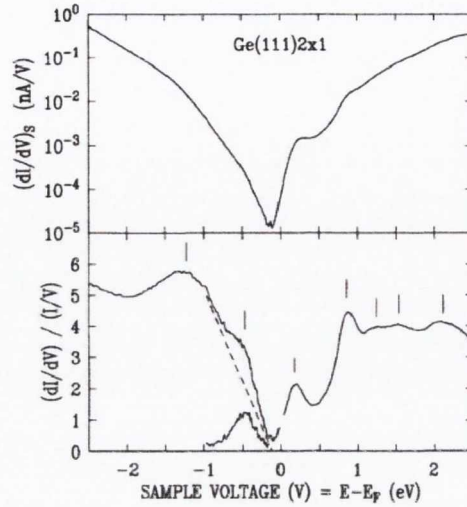


Figure 2.10 STS of the Ge(111)-2 \times 1 surface. The thin dashed line shows an example of the linear background used for determining peak positions (indicated by vertical lines). [52]

$$\frac{dI}{dV} \propto \rho_S(E_F - eV), \quad (2.36)$$

meaning that the derivative of the measured I - V data is proportional to the DOS of the sample. Figure 2.10 shows an example tunnelling spectrum of the Ge(111) surface. Reproducible tunnelling spectra like in this example require a relatively blunt metal tip [53], since the DOS of the tip is more likely to deviate from the ideal unstructured free electron metal DOS the sharper it is. This compromises atomic resolution, but STS still provides more localised valence and conduction band spectra than any other spectroscopic method.

2.5 Density Functional Theory

Density functional theory (DFT) is a powerful and well established quantum mechanical modelling method to computationally determine the electronic properties of materials. It is widely used in physics and chemistry and has proven to be a useful tool to provide a better understanding of experimental results.

The theory is based on two principles stated in the Hohenberg-Kohn theorems [54]. Firstly, they state that all ground state properties of any material are determined by its electron density $\rho(\vec{r})$. Secondly, the ground state is always the lowest energy configuration. Minimising the energy functional $E[\rho(\vec{r})]$ is therefore the main goal of DFT.

Kohn and Sham proposed the most commonly used approach to minimise the energy functional [55], in which the latter is broken down into four separate parts:

$$E[\rho(\vec{r})] = T_S[\rho] + J[\rho] + E_{Ne}[\rho] + E_{xc}[\rho], \quad (2.37)$$

where T_S is the kinetic energy of a *non-interacting* system of electrons, J is the classical Coulomb energy, E_{Ne} is the potential energy due to nuclei-electron interactions and E_{xc} is the exchange-correlation energy. All of these components have an exact form, except for E_{xc} . In the majority of practical calculations it is assumed that the exchange-correlation energy is a universal function of the charge density at any given point in space \vec{r} , using what is known as the local density approximation (LDA). While this approximation produces reasonable results for simple problems like molecular geometries, more complicated calculations such as for the electronic properties of molecules require a more refined approach. The generalised gradient approximation (GGA) which includes a component of the density gradient is commonly used for molecular systems and results in more accurate results.

Although there have been many improvements to the theory over the past decades, there are still difficulties when applying DFT to properly describe intermolecular interactions like van der Waals forces, charge transfer excitations, transition states, strongly correlated systems and in calculations of the band gap in semiconductors. Developing new DFT methods to overcome these problems, either by altering the functional or by including additional terms, is a current research topic.

3 Materials

The work presented in this thesis investigates the possibility of creating 2-dimensional nanostructures from single molecular building blocks on a germanium surface. It mainly concentrates on the (001) surface of germanium and its passivation, with some additional results on Ge(111) and Ge(011) as well as some noble metal surfaces for comparison. The relevant properties of these surfaces are described in this chapter, as well as the various organic molecules that have been studied as candidates for on-surface network creation.

3.1 Germanium

Germanium is a chemical element in the carbon group (IV) of the periodic table, chemically similar to its group neighbour silicon. It is a semiconductor with an indirect bandgap of 0.66 eV at room temperature. Germanium was the main component in the first available transistors and various other electronic devices, until it was mostly replaced by silicon due to its higher cost and poor native oxide. Today its main applications are in infrared optics, thermistor devices and once again in electronics when alloyed with silicon [56].

Germanium has the diamond bulk crystal structure as shown in Fig. 3.1, consisting of two interpenetrating face centred cubic (fcc) Bravais lattices, displaced along the body diagonal of the cubic cell by one quarter of the length of the diagonal. Its lattice constant is $a_0 = 5.65 \text{ \AA}$ [57] and the bulk bond length 2.45 \AA [58]. The electron mobility in germanium is approximately $3.6 \times 10^3 \text{ cm}^2/(\text{Vs})$ and the hole mobility $1.7 \times 10^3 \text{ cm}^2/(\text{Vs})$, roughly three and six times the respective mobilities in silicon [59]. The germanium wafers used for the experiments in this work are *n*-doped with antimony, meaning some Ge atoms have been replaced with Sb, introducing excess electrons.

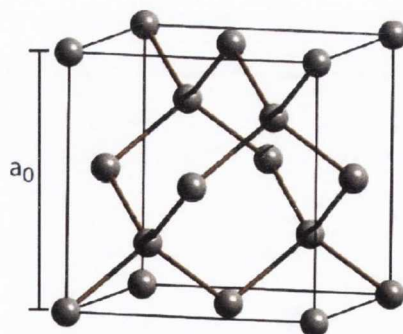


Figure 3.1 Diagram of the bulk crystal structure of germanium.

The choice of germanium as a substrate for this work is based on three reasons. First of all it is a semiconductor with a small band gap and high carrier mobility, which makes it ideal for application in high performance devices [60]. Secondly, germanium is very

similar to the industrial standard semiconductor material silicon. Finally, germanium is easier to work with in experiments than silicon. It does not easily react with the ambient water which is unavoidable in vacuum chambers, and can be repeatedly cleaned, requiring much lower annealing temperatures. Especially when time is essential, as with synchrotron measurements, or in case the exact quality of the vacuum conditions is uncertain, these practical considerations become important.

3.1.1 Germanium(001)

The germanium surface mainly investigated in this report is of the (001) crystal orientation, which is the most widely used germanium face in technological applications. Like the (001) face of silicon, Ge(001) reconstructs with adjacent surface atoms that pair into buckled dimers [61,62]. Each Ge atom has four valence electrons, two of which are used to bond to the second layer and another one to form the dimer, leaving one valence electron in a DB on each surface atom. The dimers are tilted by 10° to 20° with respect to the surface plane, which results in a charge transfer from the “down” dimer atom to the “up” dimer atom [23]. Consequently, the down dimer atom is electrophilic whereas the up dimer atom is nucleophilic [63].

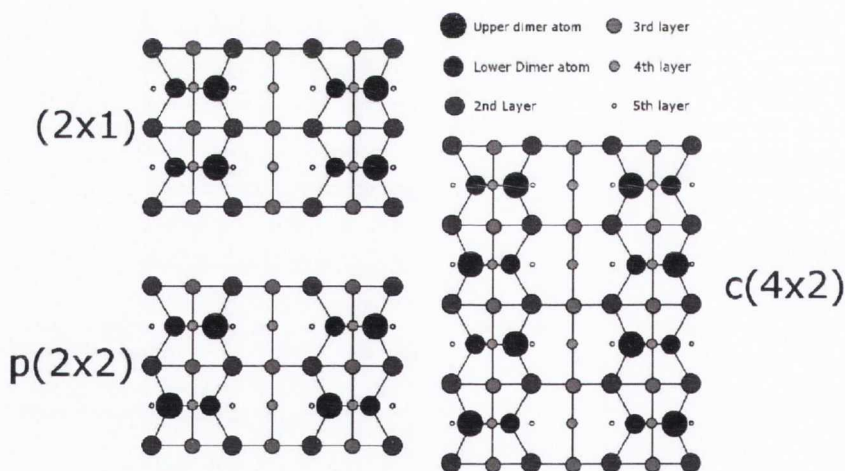
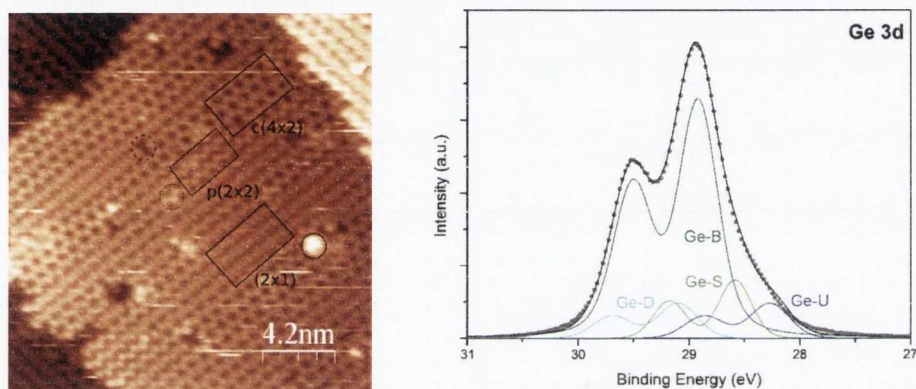


Figure 3.2 Schematic of the different reconstructions of the Ge(001) surface at room temperature. Reproduced from [27].

At RT some of the dimers flip rapidly, thereby effectively losing their tilt and yielding the (2×1) reconstruction. However, near defects and step edges the dimers tend to get locked in one configuration [64] and form the almost degenerate $c(4 \times 2)$ and the $p(2 \times 2)$ reconstructions, only differing in the up/down configuration of the dimers [65,66] as shown schematically in Fig. 3.2. At low temperatures only the $c(4 \times 2)$ and $p(2 \times 2)$ reconstructions are observable, with the $c(4 \times 2)$ regarded as the ground state [65,67].

The filled state STM image in Fig. 3.3a shows the three different surface reconstructions

as imaged with the STM. In buckled dimers, only the up dimer atom is visible in the filled state STM, reflecting the uneven charge distribution among the dimers. Additionally, there are two different domain orientations on the typical Ge(001) surface, separated by one-atomic step edges and rotated 90° with respect to each other. Other commonly observed features of clean Ge(001) surfaces are missing dimer defects (marked with the dashed circle in Fig. 3.3a), single hydrogen atoms adsorbed on one dimer atom [68] (dotted circle) and other contaminants (full circle), most likely carbon.



(a) STM image of the clean and reconstructed Ge(001) surface at room temperature (taken on the UHV system in CRANN at imaging conditions -1.4 V and 0.11 nA).

(b) Ge 3d core level for the clean Ge(001)-2x1 surface (spectrum taken at ASTRID with an incident photon energy of 60 eV).

Figure 3.3 STM and PES of clean Ge(001). See text for explanation of markings.

The 3d core level photoemission spectrum of a clean germanium surface is shown in Figure 3.3b. The fit consists of four spin-orbit split doublets, in agreement with the literature [69, 70]. One of these is from the bulk material (B) and the other three are surface components: the up dimer atoms (U), the down dimer atoms (D) and the second layer (S). Typical fitting parameter values are listed in Table 5.1.

The Ge(001) surface is cleaned in UHV by bombardment with 500 eV argon ions and a resulting sample current of 2-10 μA . The duration of the bombardment varies with the degree of surface contamination and the sample current. To obtain a high quality, flat surface with the reconstructions discussed above, the sample is subsequently annealed for 40 min at 550-600 $^\circ\text{C}$ and then cooled down slowly at a rate of approximately 10 $^\circ\text{C}/\text{sec}$ until 400 $^\circ\text{C}$, at which point the sample can be cooled down rapidly. If necessary, this cleaning cycle can be repeated.

3.1.2 Passivation

Although the number of dangling bonds on the Ge(001) surface is reduced through the reconstruction, it is still highly reactive to selected adsorbates and the sticking coefficients

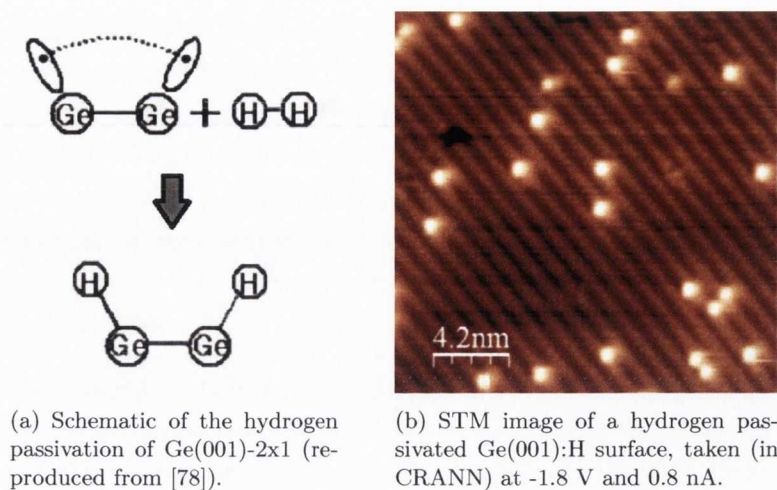


Figure 3.4 Hydrogen passivation of Ge(001).

of many organic molecules are near unity at room temperature (RT) [71]. To minimise molecule-substrate interactions and thereby enable adsorbed molecules to be mobile on the surface, as it is required for on-surface reactions between molecules, the dangling bonds can be saturated with either hydrogen or halogens. Both hydrogens and halogens are missing one electron to fill their outer shell, so by bonding to the valence electrons in the Ge(001) dangling bonds (see Fig. 3.4a) the surface becomes chemically inert. This is referred to as surface *passivation*. Numerous other passivation agents like sulphur [24,72], hydrogen peroxide [73] or several organic compounds [24,74] (and references therein) have also been explored.

The saturated monohydride Ge(001)-2x1:H surface is prepared by dosing with 500 to 1000 L of molecular hydrogen, cracked by a tungsten filament held at around 1500°C, at a distance of 5 to 10 cm from the sample. Subsequent annealing to 150 °C results in a more uniform monohydride phase. Exposing the surface to significantly more atomic hydrogen leads to the dihydride phase in which the dimer bonds are broken, resulting in a 1x1 reconstruction and a roughening of the surface [75,76].

Figure 3.4b shows an STM image of a passivated Ge(001):H surface, where the bright spots originate from unsaturated dangling bonds, as described in reference [77]. These intrinsic defects in the passivation are inevitable. The desorption of the hydrogen passivation is expected to start at temperatures of around 220°C [78]. The intentional introduction of defects with voltage pulses from an STM tip has also attracted recent attention as a lithographic technique [79].

The preparation and characteristics of several halogen-passivated Ge(001) surfaces are described in Chapter 6.

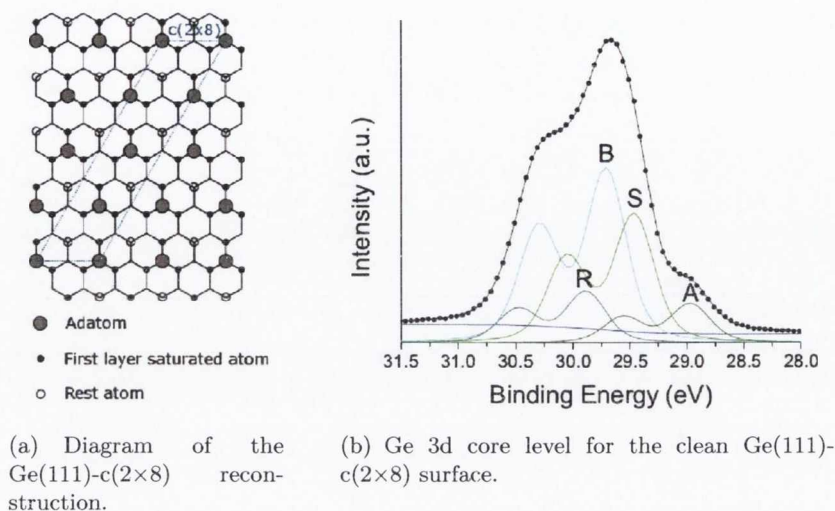


Figure 3.5 Schematic and PES of clean Germanium(111), reproduced from [27].

3.1.3 Germanium(111)

Although germanium is similar to silicon in many ways, the (111) surfaces of the two materials reconstruct very differently. While Si(111) has the famous 7×7 reconstruction [80], Ge(111) reconstructs in a $c(2\times 8)$ pattern as shown in Fig. 3.5a [81,82].

As for Ge(001), high resolution PES of the Ge 3d core level for the Ge(111) surface reflects the surface reconstruction and can be fitted with four components [83,84] as shown in Fig. 3.5b. The components can be assigned to bulk atoms (B), adatoms (A), rest atoms (R) and second layer atoms (S), with an intensity ratio A:R:S of 1:1:3 as expected due to the number of each species present.

The cleaning procedure for Ge(111) is the same as described for Ge(001) in 3.1.1, although a shorter anneal without a slow cool down is sufficient to get a well-ordered surface.

3.1.4 Germanium(110)

The (110) face of germanium has been the subject of very little research and there are still no generally accepted structural models which consistently explain the energetics, the geometry and the electronic structure observed in STM images. However, the most commonly assumed reconstruction at RT is a 16×2 structure. Fig. 3.6 shows a model proposed by Ichikawa [85], a slightly different one has been published by Stekolnikov *et al.* [86]. Both models feature an up-and-down sequence of terraces and pentagon structures of adatoms, the most prominent building elements of this surface as observed in the STM.

According to Ichikawa [85], the 16×2 surface undergoes an order-disorder phase transition at 430°C , with an unstable interstitial $c(8\times 10)$ structure above 380°C .

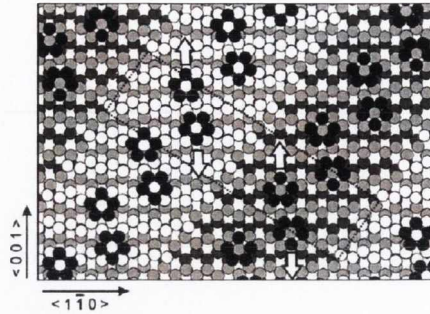
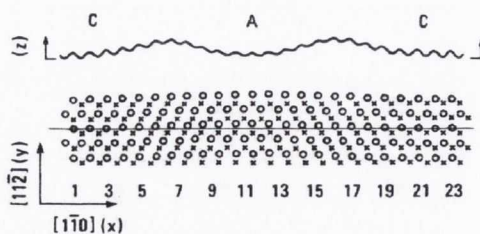


Figure 3.6 Top view of 16×2 model. Closed, open, light gray and dark gray circles represent adatoms, topmost-layer atoms, second-layer atoms and third-layer atoms, respectively. Arrows show movement of pairs of pentagons by relaxation. Reproduced from [85].

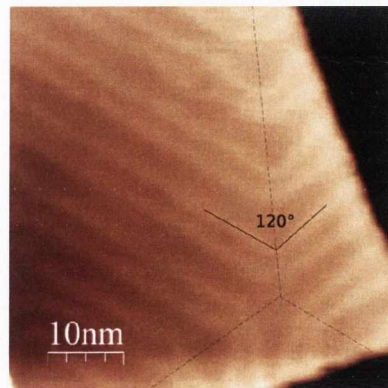
Like Ge(111), the Ge(110) surface can be cleaned in UHV by sputtering and annealing as described for Ge(001) in 3.1.1.

3.2 Gold

Gold is a transition metal in group XI of the periodic table. It is one of the least reactive chemical elements and is therefore typically referred to as a *noble metal*. Its bulk structure is of the fcc type and it has been found to be the only fcc metal whose (111) surface reconstructs [87]. The Au(111) surface exhibits large (>100 nm) atomically flat terraces, which, combined with being generally chemically inert, makes it a good substrate for STM



(a) Model of the reconstructed Au(111) surface. Crosses denote positions of second layer atoms, open circles atoms in the reconstructed top layer. C and A mark the regions of fcc and hcp stacking, respectively. Reproduced from [87].



(b) Filled state STM image of a clean Au(111) surface (with step edge), taken (in CRANN) at -0.9 V and 0.12 nA. Dashed lines mark domain boundaries.

Figure 3.7 The $(22 \times \sqrt{3})$ reconstruction of Au(111).

investigations.

Au(111) reconstructs in a $(22 \times \sqrt{3})$ structure characterised by alternating domains of fcc and hcp (hexagonal close packed) stacking of Au atoms [88], with two parallel corrugation lines per unit cell in the $[11\bar{2}]$ direction as shown in Fig. 3.7a [87]. Additionally, three different rotational domains have been observed [88]. In most cases the transition from one domain into another one occurs by a correlated bending of the corrugation lines by 120° , resulting in zig-zag features that are easily recognisable in STM images as shown in Fig. 3.7b. Defects in the surface reconstruction can lead to additional features like U-shaped connections between neighbouring corrugation lines [89].

The Au(111) surface can be cleaned in UHV with (repeated) cycles of Ar^+ ion sputtering and subsequent annealing at $400\text{-}600^\circ\text{C}$. Once cleaned, the surface typically does not contaminate in good vacuum conditions for weeks.

3.3 Organic Molecules

A variety of organic molecules has been used for the work presented in this thesis, mostly out of interest for their capabilities in covalently interconnecting into 2D networks on a surface. Some general properties of the molecules employed are detailed in this section, whereas the different reaction pathways, both actual and potential, are described in the respective results Chapters 7 and 8.

3.3.1 5,10,15,20-Tetrakis(4-bromophenyl)porphyrin

Porphyrins are a group of organic compounds frequently found in nature. There are many different types of porphyrins, all of which share the characteristic heterocyclic macrocycle. It is composed of four pyrrole subunits which are interconnected at their α -carbons via methine ($=\text{CH}-$) bridges. The porphyrin macrocycle is aromatic and therefore a highly conjugated system with 26 delocalised π -electrons. This results in intense absorption bands in the visible region, typically making them appear deeply coloured.

The *free base* 5,10,15,20 - tetrakis(4-bromophenyl)porphyrin ($\text{H}_2\text{TBr}_4\text{PP}$) molecule is utilised in most of the experiments in this thesis. It consists of the porphyrin core and four *meso*-phenyl¹ groups with bromine atoms as substituents (Fig. 3.8a). That is 44 carbon atoms, 26 hydrogen atoms (24 attached to carbon, two to nitrogen), four nitrogen atoms and four bromine atoms. The two hydrogen atoms in the centre of the core can be replaced by a metal ion, i.e. nickel (NiTBr_4PP) or the magnetic cobalt (CoTBr_4PP). This is usually done during the initial synthesis, but the *in situ* metallation of porphyrin films adsorbed on a surface by evaporation deposition of metal atoms has also been demonstrated [90].

¹Phenyls (C_6H_5) are closely related to benzene (C_6H_6), but with one hydrogen atom replaced by a connection to a substituent

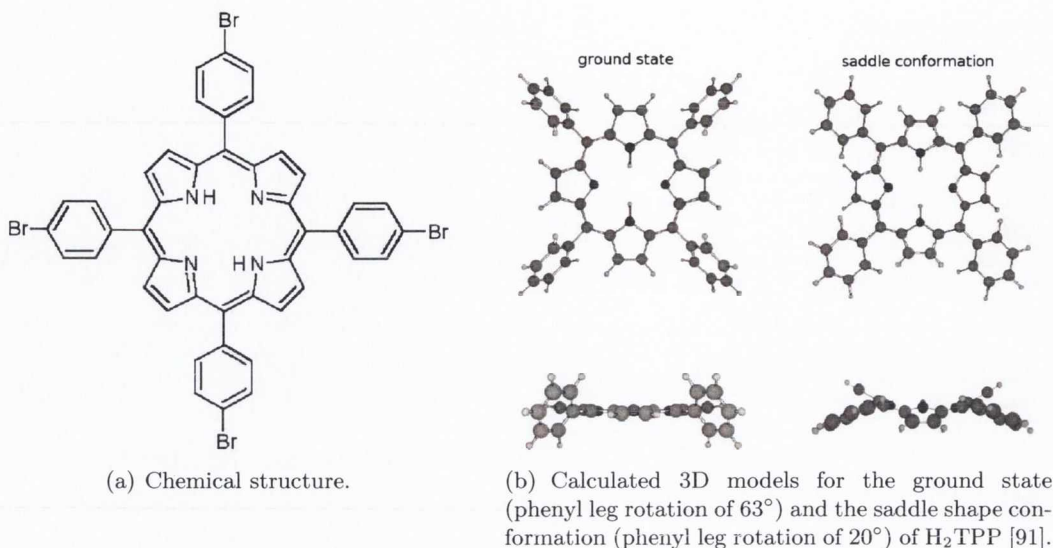


Figure 3.8 The H_2TBr_4PP molecule.

DFT calculations show that the macrocycle of the free tetraphenylporphyrin (TPP) is planar. However, the phenyl legs have a rotational degree of freedom around the axis of their σ -bonds and are rotated by about 60° with respect to the core (Fig. 3.8b) [91,92]. If the phenyl legs are forced to be rotated at angles below 60° and are bent down towards an underlying surface, steric interactions with the macrocycle lead to a non-planar saddle shaped conformation of the core, as it is shown in Fig. 3.8b [91]. Such conformational changes determine the physical, chemical and magnetic properties of porphyrins [92,93] and can be induced by interactions with a substrate upon adsorption, which will be discussed in Chapter 5.

The dimensions of the molecules are 18 \AA between two opposite bromine substituents and 13 \AA between two adjacent ones. The C-C bond length is generally around 1.4 \AA , which can be used as a measure of the dimensions of all molecules discussed in the following sections.

The H_2TBr_4PP molecules used for the experiments described in this thesis have been synthesised by Y. N. Sergeeva, N. N. Sergeeva and M. O. Senge of the SFI Tetrapyrrole Laboratory in Trinity College Dublin.

3.3.2 2,3,6,7,10,11-Hexabromotriphenylene

Triphenylene is an organic compound of four fused benzene rings. The aromatic polycycle has 18 delocalised π -electrons which keep the molecular structure planar. Triphenylene derivatives have been of interest for possible applications in discotic liquid crystals, utilizing the semiconducting behaviour of the charge transfer through π -conjugated systems in close proximity along the stacking direction [94].

2,3,6,7,10,11-Hexabromotriphenylene is a six-fold bromine-substituted triphenylene as shown in Fig. 3.9a. The three-fold rotational symmetry of the triphenylene molecule is thereby preserved.

The HBTP molecules used for this work were purchased from Tokyo Chemicals Industry Europe (TCI) and have a specified purity of >98%.

3.3.3 1,3,5-Tris(4-bromophenyl)benzene

Benzene is an aromatic six-membered hydrocarbon ring and a basic constituent or building block of many organic compounds. 1,3,5-tris(4-bromophenyl)benzene has three bromophenyl substituents like those in H_2TBr_4PP (3.3.1) and the same three-fold symmetry as HBTP (3.3.2). The rotation angle of the phenyl legs with respect to the benzene core has been determined to be $20\text{--}30^\circ$ in solution [95]. The molecular structure of TBB is shown in Fig. 3.9b.

The TBB molecules were purchased from Tokyo Chemicals Industry Europe (TCI), with a specified purity of >98%.

3.3.4 4,4''-Diiodo-p-terphenyl

Terphenyls are a group of closely related aromatic hydrocarbons. They consist of a central benzene ring substituted with two phenyl groups and are therefore sometimes referred to

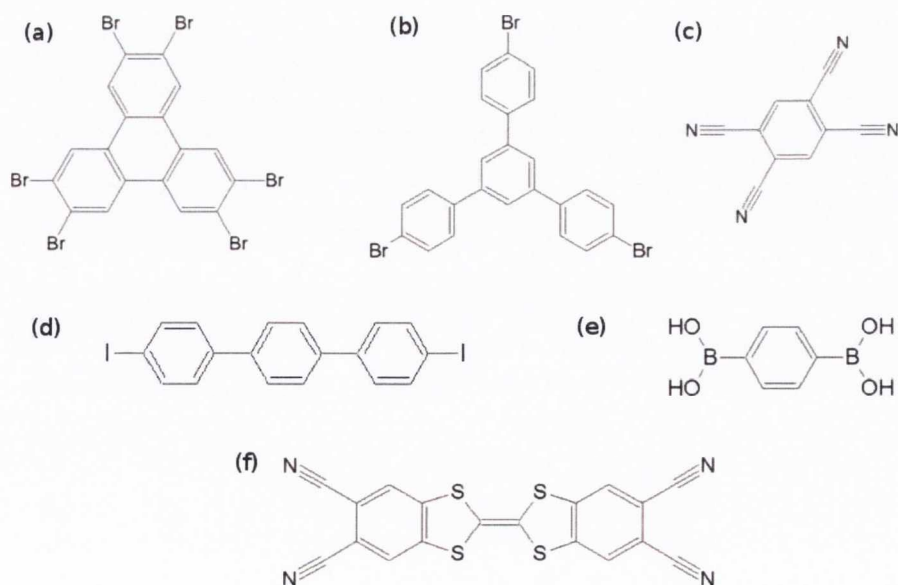


Figure 3.9 Molecular structures of (a) HBTP, (b) TBB, (c) TCNB, (d) DITP, (e) BDBA, (f) TCN-DBTTF.

as diphenylbenzenes. Isolated *para*-terphenyl molecules achieve their lowest energy conformations when adopting intramolecular torsion angles of approximately 50° [96] around the σ -bonds. 4,4''-Diiodo-*p*-terphenyl (DITP) has two iodine substituents on each end of the molecule, as shown in Fig. 3.9d.

Repeating units of *p*-phenylene are known as poly(*p*-phenylene) (PPP), a precursor to a conducting polymer. Oxidation or the use of dopants is used to convert the non-conductive form to a semiconductor [97].

DITP was purchased from Tokyo Chemicals Industry Europe (TCI) and has a purity of $>98\%$.

3.3.5 1,4-Benzene-diboronic acid

Like TBB (3.3.3), 1,4-benzene-diboronic acid (BDBA) is an organic compound with a benzene ring as its central building block. It is substituted with two opposite boric acid groups as shown in Fig. 3.9e. An aryl (or alkyl) substituted with boric acid in this way is referred to as boronic acid.

Boronic acids act as Lewis acids, meaning they can accept a lone electron pair to complete their stable form. A unique feature of boronic acid is its ability to form reversible covalent complexes with sugars, amino acids, hydroxamic acids, etc. and they are used extensively as building blocks and intermediates in organic chemistry.

The BDBA molecules were purchased from Sigma-Aldrich and have a purity of $>99\%$.

3.3.6 1,2,4,5-Tetracyanobenzene

1,2,4,5-Tetracyanobenzene (TCNB) consists of a benzene core substituted with four cyano groups. A cyano group is a carbon atom triple bonded to a nitrogen atom. Its molecular structure is shown in Fig. 3.9c. TCNB is commonly used in organic chemistry for the synthesis of derivatives of the phthalocyanine molecule (shown in Fig. 3.10). Phthalocyanines consist of a macrocycle similar to the porphyrin's, with four additional *meso* nitrogen atoms.

The TCNB molecules were purchased from Sigma-Aldrich and have a purity of $>99\%$.

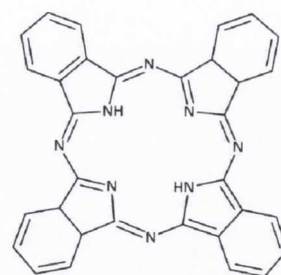


Figure 3.10 Molecular structure of phthalocyanine.

3.3.7 Tetrathiafulvalene

Tetrathiafulvalene (TTF) is an organosulfur compound, closely related to pentafulvalene by replacement of four CH groups with sulfur atoms. Pentafulvalene consists of two five-membered carbon rings, cross-conjugated by an exocyclic double bond. TTF became of high scientific interest when the discovery of its salt $[\text{TTF}^+]\text{Cl}^-$ being a semiconductor [98]

contributed to the development of the field of molecular electronics. Since then, many derivatives of TTF have been investigated [99].

The TTF derivative used in this work is 1,3-benzodithiole-5,6-dicarbonitrile, 2-(5,6-dicyano-1,3-benzodithiol-2-ylidene)-tetracyanodibenzotetrathiafulvalene, in the following abbreviated with TCN-DBTTF. As shown in Fig. 3.9f, it has two benzene rings fused to a TTF core, which are then substituted with four cyano groups, giving it the same “outer” functionality as TCNB.

The TCN-DBTTF molecules were synthesised by L. Chen in the group of X. Feng at the Max Planck Institute for Polymers in Mainz, Germany.

4 Experimental Details

In this chapter, the experimental setups and the equipment used for the experiments presented in this thesis will be detailed.

4.1 Ultra High Vacuum

Ultra-high vacuum is characterised by pressures lower than 10^{-9} mbar. The mean free path of gas molecules at this pressure is of the order of a km, which means that they are much more likely to hit the wall of a vacuum chamber than each other. The rate F of impinging molecules on a surface is defined by the Hertz-Knudsen formula

$$F = \frac{P}{\sqrt{2\pi mkT}} \quad (4.1)$$

where P is the pressure, m the molecular mass, k the Boltzmann constant¹ and T the temperature. This shows that at a very low pressure only very few molecules will contaminate surfaces, which is why the majority of surface science experiments requiring atomically clean surfaces are conducted under ultra-high vacuum conditions.

A common way to numerically quantify the amount of gas a surface is exposed to is the unit Langmuir (L). It is defined by the product of the pressure of the gas above the surface and the time of exposure: $1 \text{ L} = 10^{-6} \text{ torr s}$. If a gas has a *sticking coefficient* of unity, a dosage of 1 L leads to a coverage of roughly one monolayer of gas molecules or atoms on the surface. The sticking coefficient depends on the reactivity of both the surface and the gas.

Several different UHV systems have been used for the experiments in this thesis. Apart from the UHV chambers at the SXPS endstations SGM1 and SX700 at the Aarhus Storage Ring in Denmark (ASTRID), almost all other experiments have been carried out on commercial UHV systems manufactured by Omicron Nanotechnology GmbH (Germany). This section outlines the characteristics of the Omicron Multiprobe System and several vacuum pumping techniques which form the basis for the STM system in the Centre for Research on Adaptive Nanostructures and Nanodevices (CRANN), Trinity College Dublin as well as for the STM/XPS systems in Dublin City University (DCU) and at the Institute Matériaux Microélectronique Nanosciences de Provence (IM2MP) in Marseille. Fig. 4.1

¹ $k = 1.38 \times 10^{-23} \text{ JK}^{-1}$

shows a picture of the CRANN system with labels of different components which will be described in this chapter.

4.1.1 The Omicron Multiprobe System

Standard UHV chambers are made out of stainless steel and equipped with multiple flanges which provide flexibility in where different components can be mounted. Materials used within a high vacuum must have low vapour pressure. To achieve ultra-high vacuum pressure within a chamber, the pumps have to be suitable (see section 4.1.2) and the whole system has to be “baked” i.e. heated up to temperatures above 100°C in order to accelerate the removal of adsorbed water and other contaminants off the system walls. All filaments of equipment within the chamber are subsequently “outgassed”, i.e. run at slightly higher temperatures than usual in order to avoid massive desorption of the adsorbed gas later.

A common practice is to divide a UHV system into a preparation chamber and an analysis chamber with a gate valve to protect highly sensitive measurement equipment from contamination that might occur during sample preparation. To introduce samples or STM tips into the chamber without breaking the vacuum, a fast entry lock (FEL) is generally used. The FEL is separated from the chamber by a gate valve and can be quickly (~1h) pumped down to a sufficiently low pressure to permit sample or tip transfer.

The Omicron Multiprobe System can be set up in different configurations. While both the system at DCU and at IM2MP have separate analysis and preparation chambers, the system in CRANN has only a single chamber. Since the evaporation of organic molecules can be highly contaminating, especially if the evaporation parameters are unknown in the beginning, this element of the sample preparation process had to be moved into the FEL.

For the argon ion sputtering of samples, the main chamber is equipped with an PSP ISIS 3000 ion gun with a leak valve connected to an argon gas line. This particular type of gun can operate with ion energies below 1 keV and down to 0.5 keV, which is important for the cleaning of germanium (see section 3.1.1). The samples can be heated by a filament on the sample manipulator. The standard heating stage in the Omicron Multiprobe System also offers the possibility of heating by running a direct current through the sample. This requires a specific sample holder and can achieve high temperatures in the order of 1000°C very quickly, which is important for the cleaning process of silicon. However, germanium requires lower temperatures and slow gradients, making resistive heating more suitable. Both the systems at DCU and at IM2MP had similar ion guns and heating stages, while IM2MP had the additional option of cooling the sample by pumping liquid nitrogen through tubing in the manipulator. The temperature of the sample was either determined with a chromel-alumel (K-type) thermocouple attached to the manipulator or measured with a UV pyrometer through a ZnSe viewport.

Molecules were evaporated from a homebuilt thermal evaporator, consisting of a tanta-

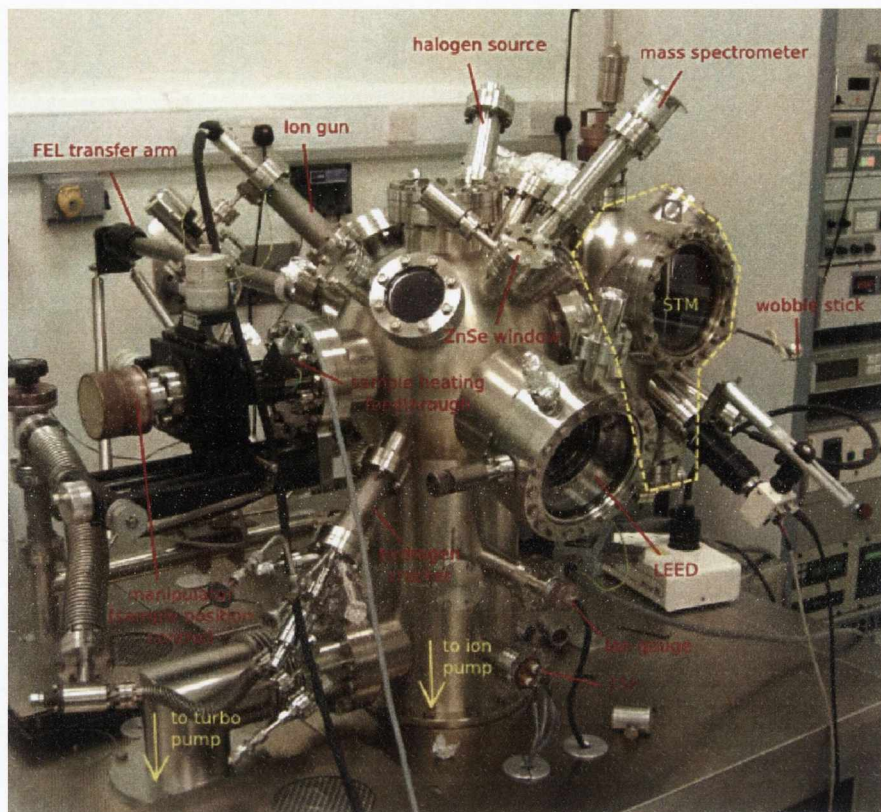


Figure 4.1 Omicron Multiprobe System in CRANN, Trinity College Dublin.

lum crucible and a filament for heating. Evaporation temperatures varied widely with the different molecules and are specified in the respective results chapters. At IM2MP, metals were evaporated from an e-beam evaporator consisting of a high purity metal rod heated by a filament and with water-cooling to stabilise the temperature.

Passivation of the germanium samples with hydrogen was either done by leaking hydrogen gas into the chamber through the ion gun gas line and then cracking the H_2 molecules on a hot ($> 1000^\circ C$) filament at a distance of 5-10 cm from the sample, or by using a specific hydrogen cracker which works on the same principle. The halogen sources are detailed in section 4.2, the measurement techniques in sections 4.3 to 4.5. Fig. 4.1 additionally shows a low energy electron diffraction (LEED) unit, which has not been used for the experiments in this work.

In all cases Bayard-Alpert ion gauges with a range of $10^{-4} - 10^{-11}$ mbar were used for pressure measurement in the UHV chambers, and a cold cathode or Penning gauge with a range of $10^{-2} - 10^{-9}$ mbar for the load lock preparation chamber in CRANN.

4.1.2 Vacuum pumping

The base pressure during the experiments conducted in CRANN and DCU was $2(\pm 1) \times 10^{-10}$ mbar, and $2(\pm 1) \times 10^{-9}$ in IM2MP. The latter was sufficient for inert metal surfaces, whereas Ge(001) had to be passivated immediately after cleaning to prevent fast contamination.

In all three systems the base pressure was maintained by a combination of an ion getter pump and a titanium sublimation pump in each chamber. A turbomolecular pump backed by a rotary pump is used for initial pumping to high vacuum (10^{-6} – 10^{-9} mbar) in order to start ion pump operation, and during Ar^+ ion sputtering, which requires a gas pressure in the order of 10^{-5} mbar. The turbo pump is also used for pumping the FEL or preparation chamber in CRANN.

4.2 Halogen Sources

The reproducible generation and dosing of halogens in UHV systems is challenging due to their high reactivity and the concomitant danger of corrosion damage to vacuum hardware. This discourages the possibility of dosing halogen gases through leak valves, as is done for less reactive gases. Spencer *et al.* [101] therefore designed an electrochemical cell which allows the controlled dosage of halogens in UHV. This method also facilitates the depositions of very small coverages, which makes it possible to study the adsorption of single halogen atoms on surfaces as discussed in Chapter 6. Spencer's cell design is only applicable to chlorine, bromine and iodine; the extremely reactive nature of fluorine requires a different source [102].

Fig. 4.2 shows a schematic of the cell design. All halogen sources used for the experiments presented in this work were homebuilt following this design.

The operational basis of the source is an electrochemical cell comprised of an AgX ($X = \text{Cl}, \text{Br}, \text{I}$) pellet with a silver electrode at the bottom and a platinum gauze electrode at the top. The inset photograph in Fig. 4.2 shows a AgBr pellet, which has been pressed from AgBr powder (99%, Sigma-Aldrich) in a pellet press with a diameter of $1/2$ inch and an applied pressure of ~ 1 metric ton. The pellet is then placed inside a Pyrex tube which is surrounded by a tantalum filament for resistive thermal heating. At

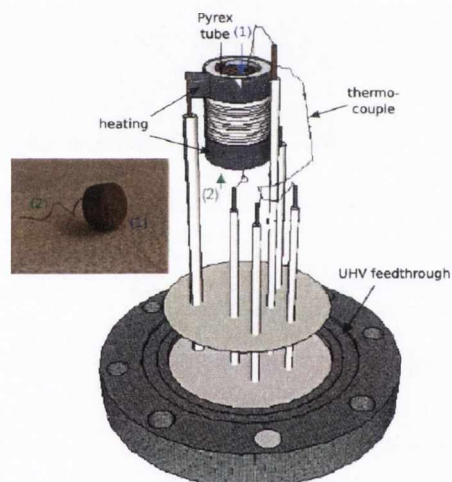


Figure 4.2 Schematic of halogen source design [100], with inset photograph of AgBr electrochemical pellet. (1) shows the platinum gauze electrode, (2) the silver contact.

operational temperatures of $\sim 170^\circ\text{C}$, the Ag^+ and Br^- ion mobility within the pellet has increased enough to release bromine through the positively biased top electrode. Chlorine and iodine cells work on the same functional principle². Typical parameters are 1.2 A for the heating current and between 50 and 10 V for the bias between Ag and Pt electrode, resulting in halogen pressures in the order of 10^{-10} or 10^{-9} mbar as desired. The temperature of the pellet was measured with a K-type thermocouple sandwiched between the pellet and Pyrex tube.

4.3 Mass Spectrometry

A mass spectrometer is commonly used to analyse the residual gases in the UHV chambers. It distinguishes charged molecules and atoms by their mass to charge (m/z) ratio. The specific model which has been used for the experiments in this thesis is a Thermo Vacuum SMART IQ+. It was utilised frequently to analyse the background gas composition, check for leaks, cleanliness of argon for sputtering, and to determine the presence and quality of the halogens deposited from the cells discussed in the previous section 4.2.

In a quadrupole mass spectrometer (QMS), an electron beam ionises gas species at the intake of the mass spectrometer. The charged molecules or atoms are then accelerated towards the quadrupole. The quadrupole consists of four cylindrical metal rods with an applied bias (with opposite sign on diagonally opposed rods)

$$V_{\text{applied}} = \pm(U + V \cos(\omega t)) \quad (4.2)$$

where U and V are the constant and oscillating voltages applied to the rods and ω their oscillating frequency. The ion beam passes between the four metal rods and only species with a resonant (m/z) ratio are not deflected by the quadrupole. The unaffected particles are then detected by an electron multiplier. By modifying U and V the quadrupole can select different m/z ratios, building up a spectrum of different gas species. The mass spectrometer can only operate reliably in a vacuum where the mean free path of gas particles is longer than the ion path length within the quadrupole. Therefore, the QMS must be operated under pressures lower than 10^{-6} mbar.

4.4 Photoemission Spectroscopy

The PES experiments were mainly conducted at the SGM1 and SX700 beamlines at ASTRID, and also at DCU and IM2MP as an addition to STM imaging available on the same UHV systems.

²AgCl, 99.999%, Sigma-Aldrich; AgI, 99.999%, Sigma-Aldrich

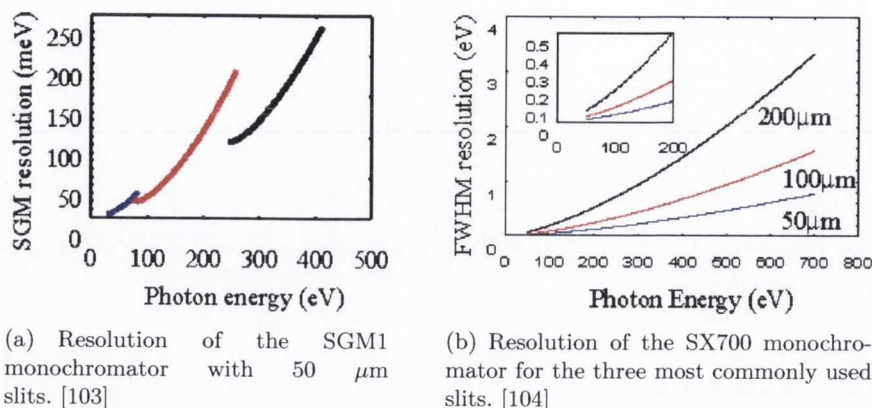


Figure 4.3 Monochromator resolutions at ASTRID.

4.4.1 Beamlines

The SGM1 beamline at ASTRID is named after its spherical grating monochromator, which has an energy range of 30 eV to 400 eV and yields a photon flux of $\geq 10^{10}\text{sec}^{-1}$ at 130 eV for the 50 μm slits and $\geq 10^9\text{sec}^{-1}$ at 350 eV for the 100 μm slits. The energy resolution for the 50 μm slits is shown in Fig. 4.3a. The beamline is furthermore equipped with a 200 mm mean radius spherical electron analyser (Scienta) with a video based multi-channel detector system. A typical working resolution for this analyser is around 40 meV [103].

The SX700 monochromator at ASTRID has an energy range of 20 eV to 700 eV. The 100 μm slits yield typical flux values of $\geq 10^{10}\text{sec}^{-1}$ at 125 eV and $\geq 10^9\text{sec}^{-1}$ at 600 eV. Its resolution for different slit widths is shown in Fig. 4.3b. The energy analyser for non-angle resolved PES is a 100 mm mean radius analyser (VG-CLAM2) [104].

4.4.2 Omicron systems

The DCU and IM2MP systems are both equipped with an Omicron EA 125 electron energy analyser (Fig. 4.4) and an Omicron DAR 400 twin anode (Al, Mg) X-ray source. The Al K_α line has an energy of $h\nu = 1486.6$ eV and has a broadening of 0.85 eV when it is not monochromated. Mg K_α lies at $h\nu = 1253.6$ eV with a broadening of 0.7 eV. At a typical pass energy E_P of 50 eV and a mean slit width of 3 mm the EA 125 analyser has a resolution of 0.6 eV, as determined by equation 2.24. Together with the line broadening of the non-monochromated Al [Mg] anode, this results in a total resolution of

$$\Delta E = \sqrt{(0.6\text{eV})^2 + (0.85\text{eV}[0.7\text{eV}])^2} = 1.04\text{eV}[0.92\text{eV}].$$

Entry and exit slits of the EA125 could be varied in shape (circular, rectangular) and size (1-6 mm). Unless otherwise specified, the entry aperture was set to a spot of 2 mm diameter and the exit slit was wide open for maximum intensity.

4.4.3 Fitting software

The analysis of all spectra presented in this work, including normalisation of the recorded data, background subtraction and line shape fitting, has been done with the software Unifit 2004 [106]. Details of the analysis process varied widely with each experiment and are discussed in the respective results chapters.

4.4.4 DFT Calculations

The electronic structure of $\text{H}_2\text{TBr}_4\text{PP}$ (see section 3.3.1) was calculated by ab-initio DFT methods within the Stockholm-Berlin (StoBe) implementation of the demon package [107]. The approach is based on self-consistent solutions of the Kohn-Sham Density Functional Theory equations (see section 2.5) using a Linear Combinations of Gaussian Type Orbitals (LCGTO) approach. All StoBe calculations are by nature spin-polarized calculations, but with even electron occupations of $\text{H}_2\text{TBr}_4\text{PP}$ no complications arise due to this. The $\text{H}_2\text{TBr}_4\text{PP}$ calculations are single (free) molecule calculations which are made subject to point group symmetry constraints with the geometry optimised to minimize the energy. In each case the geometry has been optimized using a triple- ζ valence plus polarisation (TZVP) basis set for all C, and N (7111/411/1) and a double- ζ valence plus polarisation (DZVP) basis (63321/5321/41) for Br and H (41/1). Auxiliary basis sets were applied to fit the electron density and the exchange-correlation potential. All the computations included the generalized gradient approximation correction of Perdew and Wang [108] and the exchange correlational of Becke [109] throughout the spin-polarized calculations.

The calculated DOS of the valence band may be broken down into the partial density of states (PDOS) of each elemental and angular momentum component on a site-specific basis. A comparison with photoemission data obtained at a specific photon energy may then be made by weighting each site-specific PDOS with the value of the subshell photoionisation cross section that is found for that element and orbital [38]. This mainly serves to increase the prominence of the N 2p states that participate in the valence band DOS which are located as part of the HOMO or HOMO-1 levels.

A proper calculation of the core-level binding energies is through a ΔKS approach, where the total energy of the molecule with a specific core-hole is subtracted from that of a molecule with fully occupied core-orbitals, which allows the final state effect and the

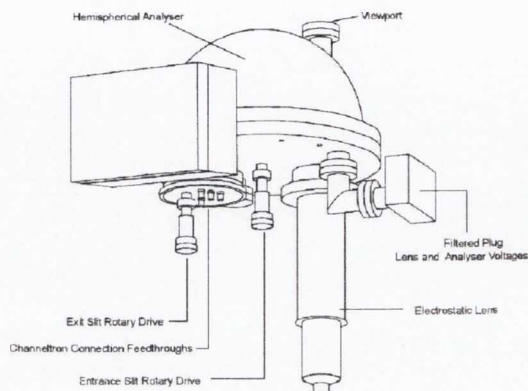


Figure 4.4 Schematic of the Omicron EA125 analyser. [105]

relaxation of the molecule in the presence of a core-hole to be taken into account. These calculated C 1s core-level binding energies can then be used to generate a profile of the XPS spectrum which can be matched to the experimental data.

4.5 Scanning Tunnelling Microscopy

The STM experiments for this work were carried out in CRANN, DCU and IM2MP. All three UHV systems have an Omicron Variable Temperature (VT)-STM, a popular commercial STM [110] which is detailed in this section.

4.5.1 Experimental apparatus

The Omicron VT-STM has a reported ideal x, y and z resolution of 0.01 nm, a current sensitivity of 1 pA, coarse motion range of 10 mm in each direction and a scan range of 12 μm in the x and y , and 1.5 μm in the z direction. Additionally, it has the ability to operate with sample temperatures from 25 K to 1500 K. For some of the experiments performed at IM2NP the sample was cooled down to temperatures of 80-100 K via contact with a copper “cold finger” in the cryostat stage of the STM (as shown in Fig. 4.5), which itself is thermally connected to an external liquid nitrogen reservoir.

Scanner tube

The motion of the STM tip is controlled by two different piezoelectric mechanisms. One controls the coarse position of the tip on initial approach and a second, more accurate set of piezo actuators is used for imaging motion.

The coarse positioning piezo motor brings the tip to a distance of around 1 μm from the surface. It uses a stick-slip motion mechanism where slow extension of a piezo “leg” moves the entire STM stage and a quick retraction slips the leg back to begin another step.

The fine motion scanner tube is mounted on the coarse motion drive. It is a tube of piezoelectric material with four outer quadrants defined by metallic contacts. These contacts control motion in x and y , and an internal contact is used to control the z extension. The control electronics scan the x and y axis of freedom while using feedback from the tunnel current signal to modify z . The STM tip is mounted on the scanner tube magnetically. Three metal feet on the STM tip fit into three slots made from permanent magnets which hold the tip in place.

Vibrational isolation

To achieve atomic resolution with the extremely vibration sensitive STM, the vibrational noise level must be significantly less than the atomic corrugation of the surface. In the

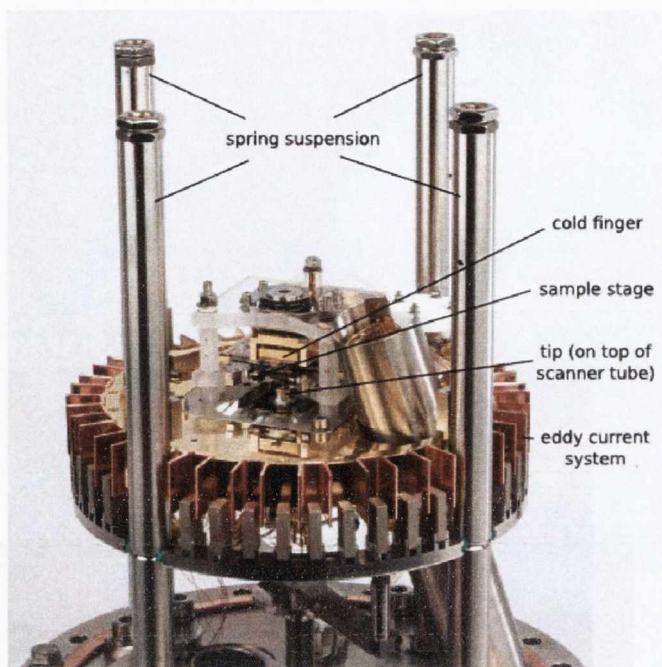


Figure 4.5 The Omicron VT-STM. [110]

VT-STM, vibrational isolation is achieved by suspending the entire scanning and coarse approach mechanism on four soft springs which are protected by surrounding columns, as shown in Fig. 4.5. The resonance frequency of the spring suspension is about 2 Hz. Vibrations are reduced by a magnetic dampening system which consists of a ring of copper fins on the STM stage suspended within a ring of permanent magnets (eddy current system).

4.5.2 Tip preparation

The tip is an important element of the STM and must be prepared carefully so that it is atomically sharp and clean. This prevents tip induced imaging effects like multiple tips or reverse imaging which can be confusing when interpreting the images [111]. Additionally, a cleaner tip does not contaminate the surface.

The most common tip materials are crystalline W or a Pt/Ir alloy. A large variety of tip preparation methods like electrochemical etching [111, 112], ion milling or electron beam deposition [113] have been proposed in the literature.

There is no generally accepted method for tip preparation and it is a challenge for every STM user to find their own way of preparing tips.



Figure 4.6 Si(100)/Au,Pt sample used for STM tip conditioning.

For the STM experiments in CRANN, tips were prepared by electrochemical etching, similar to the method described in detail by Yu *et al.* [112]. Tungsten wire of 0.15 mm diameter was immersed approximately 1 mm deep in 2 M KOH solution, serving as the anode. The cathode was a ring of platinum wire around the tungsten anode, fixed close to the surface of the solution. The Omicron tip etching kit provided a controller to set the voltage and cutoff current parameters. The best parameters were found to be 9 V and 2 mA, respectively. The tungsten tip was subsequently attached to a three-legged Omicron tip holder and rinsed with deionised water. No further *ex situ* treatment of the tips were necessary to achieve atomic resolution. However, to remove contaminants picked up by the tip during scanning operation or to recover a crashed tip *in situ*, a specifically prepared tip conditioning sample was used, consisting of thin films of gold and platinum deposited on a Si(100) substrate³. Fig. 4.6 shows one such sample on a standard Omicron stainless steel sample plate. The films were cleaned by cycles of ion sputtering and annealing and then utilised for STM tip cleaning. The tip was crashed into either the gold or the platinum film and then pulled out slowly while applying a high bias. This results in the deposition of film material on the tungsten tip and ideally in the formation of a monoatomic tip.

4.5.3 Image processing software

The STM imaging (and spectroscopy) data was further processed with the free software WSxM, developed by Horcas *et al.* [114].

Some of the main features of WSxM's image processing function that were used in this thesis are the definition of subtraction planes to compensate for slight angles of the sample with respect to the scanning plane of the tip, the "Gaussian smooth" to even out high frequency noise levels and color and contrast adjustment to emphasise certain image features. WSxM also offers functions to determine coverages and calculate surface roughness, as well as Fourier transformation of the images to identify noise frequencies or other periodicities in the original image.

³Samples were grown by Peter Gleeson, Intel Researcher-in-Residence in CRANN, TCD.

5 Adsorption of selected organic molecules on germanium(001)

As indicated in the Introduction, it is important to understand the adsorption mechanisms of organic molecules on surfaces since their chemical bonding determines the mobility of the molecular building blocks and therefore directly influences their controlled self-assembly. Additionally, the interactions of the molecule with the substrate can induce changes in the molecule's conformation, chemical composition or electronic structure, making them a crucial factor when trying to create devices from either single or interconnected molecules.

The combination of organic molecules with semiconductor surfaces like the highly technologically relevant silicon(001) or the very similar germanium(001) promises new functional possibilities. Organic molecules have many tunable properties like size, shape, chemical composition, conductivity, flexibility and adsorption spectrum. This makes them suitable for light emission or detection devices as well as chemical sensors, applications which silicon or germanium alone are not very well suited for.

This chapter concentrates on a comparative study of 5,10,15,20-tetrakis(4-bromophenyl)porphyrin (H_2TBr_4PP) and 5,10,15,20-tetraphenylporphyrin (H_2TPP) molecules adsorbed on the clean Ge(001) surface, using STM and PES. The influence of the bromine substituents on the adsorption mechanism and the nature of the molecule-substrate interactions, as well as substrate-induced conformational changes in the molecules are investigated. Additionally, studies of the interactions of H_2TBr_4PP with the Ge(111) and (110) surfaces as well as the adsorption sites of 1,3,5-tris(4-bromophenyl)benzene (TBB), a smaller organic molecule without a macrocycle, on Ge(001) are presented.

5.1 Literature Review

There are no adsorption studies of porphyrins on the Ge(001) or the Si(001) surface reported in the literature. However, a few groups have investigated the reaction pathways of small organic molecules on these surfaces, providing valuable basic knowledge of the bonding mechanisms which could prove relevant in the adsorption of larger molecules since these can be structurally divided into smaller functional groups.

Interestingly, the surface chemistry of the (001) faces of silicon and germanium has been shown to be very similar to carbon bonds, which are the basis of all organic chemistry [23, 71, 115]. This similarity is based on the full σ - and the partial π -bond between the

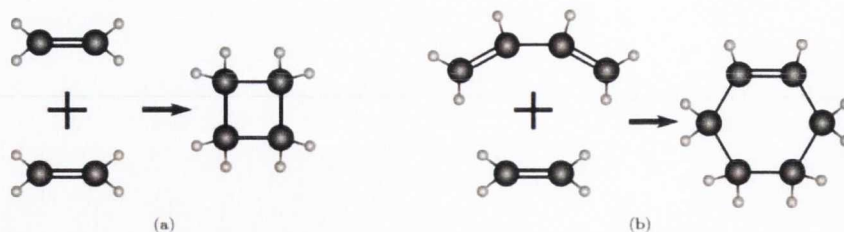


Figure 5.1 Schematic of the (a) [2+2] reaction between two ethylene molecules and (b) the [4+2] or Diels-Alder reaction between ethylene and butadiene. Reproduced from [27].

surface dimer atoms of the 2×1 reconstruction exhibited by Ge(001) as well as Si(001) [116] and C(001) (diamond), which can be viewed as analogous to the carbon-carbon double bond frequently found within organic molecules. This makes group IV semiconductor surfaces distinctively different from metals, where bonding is not strongly site-specific [71].

Basic reaction mechanisms

There are a number of reaction mechanisms known which form bonds with an alkene group, which resembles the Ge/Si/C(100)- 2×1 surface dimers. Firstly, there are *cycloaddition* reactions which are very common in organic synthesis [117, 118]. Cycloaddition refers to two π (double)-bonded molecules coming together to form a new cyclic molecule by making two σ (single)-bonds. They are distinguished by the number of π -electrons involved. The simplest [2+2] and [4+2] reactions are shown in Fig. 5.1. The [4+2] cycloaddition reaction is often referred to as *Diels-Alder* reaction [119]. Both of these reaction pathways are subject to the Woodward-Hoffman selection rules, which follow from their frontier orbital theory [120] and predict how readily an organic reaction will occur.

According to these symmetry considerations, the [2+2] reaction is “forbidden”, and not expected to happen without significant energy activation. However, the sticking coefficient of alkenes on Si(001)- 2×1 has been shown to be near unity at room temperature [115]. This has been proposed to be due to the asymmetry of the surface dimer, allowing the alkene to approach and bond to the surface through an alternative pathway on the down-dimer atom side, with a considerably lower activation energy [121–123]. The sticking probability of molecules bonding through the [2+2] reaction on Ge(001) is ~ 0.1 and in the order of 10^{-3} on C(001) since the diamond dimers do not tilt [121, 124].

The Diels-Alder reaction for more complex alkenes is symmetrically allowed and has also been theoretically predicted and observed to happen on Si(001)- 2×1 [125, 126]. However, 20% of the complex alkenes expected to undergo a Diels-Alder reactions still reacted via the [2+2] pathway [121], demonstrating the limits of the analogies between traditional organic chemistry and the Si(001) surface. While Ge(001) shows Diels-Alder reactions with conjugated dienes, the presence of [2+2] side products has not been evaluated [124, 127].

Some of the differences between Si(001) and Ge(001) in reactions with organic molecules become clear when looking at the adsorption of benzene. Models of different possible adsorption sites for benzene on these surfaces are shown in Fig. 5.2. On Si(001), benzene has been shown to bond only through the Diels-Alder reaction, resulting in the three different geometries in Fig. 5.2c, d and e, as extensively reviewed by Wolkow [115]. However, the configuration in Fig. 5.2e only appears on surface sites with two parallel buckled dimers, known as type C defects. The lack of [2+2] products

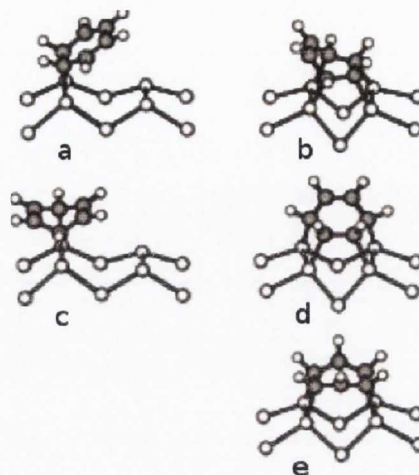


Figure 5.2 Schematic diagrams of benzene adsorbed on Si(001) or Ge(001)- 2×1 . Adapted from [115].

in contrast to other systems like 1,3-butadiene [128] or 1,3-cyclohexadiene [129,130] can be explained with the aromaticity of benzene, making it necessary to break the delocalised nature of the π -electrons upon bonding. This results in the loss of resonance stabilisation energy which is enough to destabilise the more weakly bound [2+2] products [23]. While the adsorption of benzene on Ge(001) has been shown to happen exclusively via the [4+2] reaction as on Si(001), the only confirmed adsorption site is the “butterfly” configuration in Fig. 5.2c [131]. Most importantly, benzene desorbs from Ge(001) at room temperature while remaining stable on Si(001) until over 500 K [131]. This is in agreement with the relative bond strengths for group IV elements, with a trend of C-C > C-Si > C-Ge.

Another common reaction mechanism are *electrophilic/nucleophilic* reactions, which can occur as a result of the uneven charge distribution among the Si/Ge(001)- 2×1 dimer atoms as described in section 3.1.1 [23]. For organic functional groups containing non-carbon atoms like the pyrroles in the porphyrin core, three different electrophilic/nucleophilic reactions are possible. Firstly, the lone pair of the pyrrolic nitrogen could form a so-called *dative* bond by donating both of its electrons to the electrophilic down dimer atom. Secondly, one of the hydrogens attached to the aromatic carbon system could be substituted by a bond to the down-dimer atom, with the resulting hydrogen radical bonding to the nucleophilic up-dimer atom. This is referred to as an electrophilic aromatic substitution (EAS). Lastly, the hydrogen bonded to the pyrrolic nitrogen could be substituted in a similar manner to the EAS in a N-H dissociation reaction. All possible reaction pathways for a pyrrole group are shown in Fig. 5.3. Infrared (IR) spectroscopy data and theoretical calculations by Wang *et al.* [132] indicate that pyrrole adsorbs and bonds to Ge(001) (and Si(001)) mostly by N-H dissociation via an alternative pathway involving dative bonding through one of the carbon atoms rather than the nitrogen, which is only possible due to

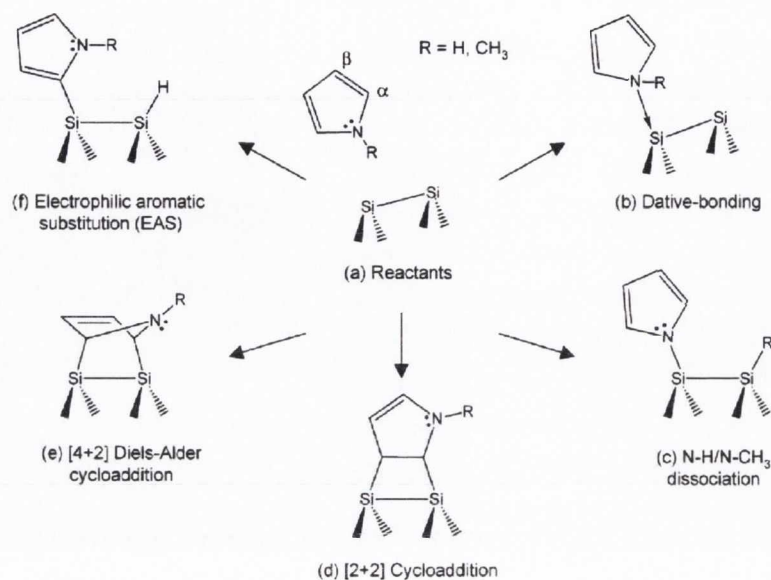


Figure 5.3 Possible reaction pathways between pyrrole and the Si(001) or Ge(001)-2×1 surface. Reproduced from [132].

the delocalised electrons in the pyrrole ring. A minor side product has been found to result from EAS reactions. Both N-H cleavage and EAS products retain their aromaticity.

Large organic molecules

There is no literature on the specific bonding sites of larger, macrocyclic organic molecules like porphyrins or the very similar phthalocyanines (Pc) on either Ge(001) or Si(001). However, STM images of metal phthalocyanines (MPc) on Ge(001) suggest three different adsorption sites as shown in Fig. 5.4a [27, 133]. The majority of MPc molecules adsorb with their metal centre between two dimer rows as displayed in the model in Fig. 5.4b, while low bias STM images suggest interactions between molecule and surface dimers beyond the dimensions of the molecule. The interpretation of the other two adsorption sites is less obvious and has to remain speculative without supporting DFT calculations. Possible geometries are upstanding Pc molecules and an adsorption site with the metal centre of the molecule on top of a dimer row.

CoPc and CuPc on Si(001)-2×1 have been shown to adsorb on three different sites, two in between two dimer rows and the other one centred on a row [134, 135].

Porphyrin conformations

Although there is no literature of porphyrins adsorbed on group IV semiconductor surfaces, much work has been done on porphyrins on metal surfaces or HOPG (highly ordered

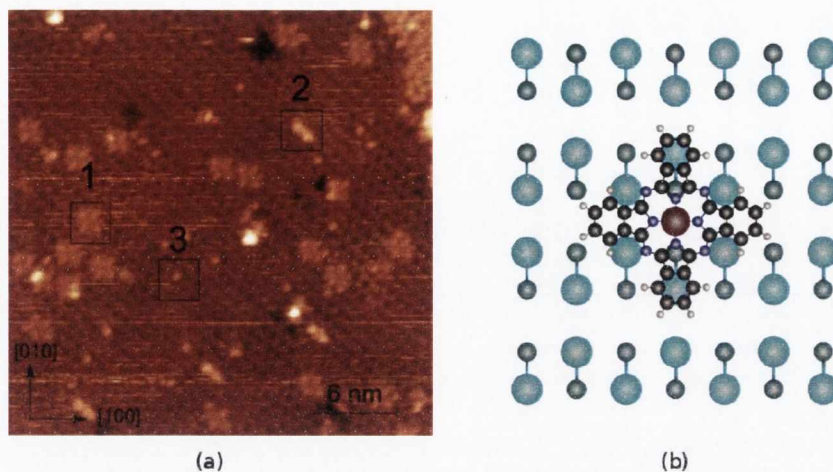


Figure 5.4 (a) STM image of a sub-monolayer coverage of MgPc on Ge(001) with three adsorption sites, taken at -1.5 V and 0.16 nA. (b) Model of the adsorption geometry of species 1 of MPc on Ge(001). Reproduced from [27].

pyrolytic graphite). On very weakly interacting surfaces like HOPG, molecule-molecule interactions govern the adsorption behaviour whereas the influence of the molecule-substrate interactions becomes more apparent on more reactive metal surfaces [136]. The reactivity or level of interactions of the frequently studied (111) faces of the “coinage” metal substrates generally follows the trend $\text{Cu} > \text{Ag} > \text{Au}$ [137]. However, different surface planes and different reconstructions can change the reactivity of a surface.

Interactions with a surface, confinement within a crystal structure or other external influences are known to induce conformational changes in almost all porphyrin derivatives. The molecular conformation was furthermore found to often have a significant influence on the physicochemical properties of the porphyrin [92,93].

The nature of the conformational flexibility of the tetraphenylporphyrin derivatives used for this work is quite well known, as briefly discussed in section 3.3.1. The most significant conformational degree of freedom is the rotation angle θ around the σ -bond to the phenyl substituents. Jung *et al.* investigated a TPP derivative with two bulky *tert*-butyl substituents per phenyl leg, which appear as bright protusions in the STM. This enabled them to identify different rotational angles of the phenyl legs, depending on the type of substrate and the annealing temperature. They concluded that the degree of conformational change reflects the interaction strength of the molecule with the substrate [138].

The “saddle-shape” of TPP as shown in Fig. 3.8b has been theoretically predicted by Yokoyama *et al.* [91] and Weber-Bargioni *et al.* [140] as a consequence of a rotational or dihedral angle $\theta < 60^\circ$. An average distortion of the macrocycle, measured by the out-of-plane tilt of the pyrrole units ρ , for $\theta \leq 10^\circ$ and a tilt angle of the phenyl substituents

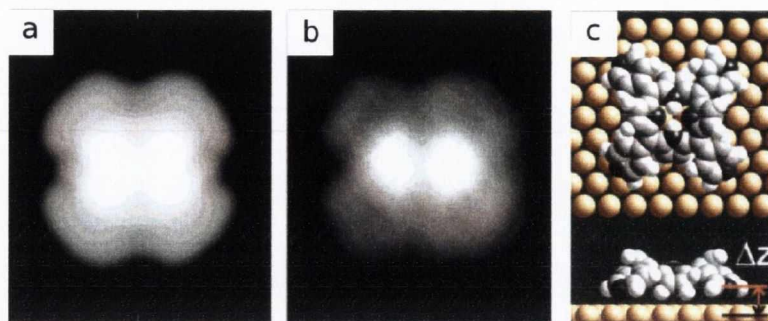


Figure 5.5 (a) DFT simulated STM image of TPyP with $\theta = 0^\circ$, $\phi = 30^\circ$, $\rho = 35^\circ, 45^\circ$. (b) STM image ($V = -0.5$ V, $I = 0.15$ nA, width 10 Å) of TPyP on Cu(111). (c) Top and side view of adsorption geometry model for TPyP on Cu(111), $\Delta z = 2.5$ Å. Adapted from [139].

$\phi \simeq 20^\circ$ is 35° [139]. Auwärter *et al.* used similar angles to calculate a charge density image for tetrapyrroldiporphyrin (TPyP)¹, which matches the experimentally determined STM image of TPyP adsorbed on Cu(111) very well as shown in Fig. 5.5. The two upward bent pyrrole units produce bright features in the STM images, breaking the planar molecule's four-fold symmetry and thereby indicating the non-planar distortion of the macrocycle. This study is one of the very few examples where the full adsorption geometry, i.e. conformation and adsorption site, of a large functional organic molecule could be determined [139].

The same group also found a saddle-shaped conformation for Co-TPP on Cu(111) by comparing NEXAFS and STM/STS results. The STM images show the molecules in a two-fold symmetric appearance with a cigar-shaped lobe along the main axis similar to the appearance of TPyP as shown in Fig. 5.5b. The dihedral angle was determined to be $\theta = 30^\circ$ with a resultant macrocycle distortion $\rho = \pm 20^\circ$, which is much less than for TPyP on Cu(111). Additionally, Co-TPP showed higher surface mobility than TPyP, despite the additional interaction of the Co centre with the copper surface. These differences clearly show the influence of the substituent on the adsorption geometry, in this case the nitrogen lone pair of the pyridil groups [140].

Similar results regarding the conformational changes and the influence of the substituents on the adsorption geometry have been reported for TPP derivatives on noble metal surfaces [91, 141]. Additionally, there are several examples of controlled switching between porphyrin conformations using an STM tip and thereby changing properties like the tunnelling current [142, 143] or the Kondo temperature [144].

¹only differing from TPP by a nitrogen atom instead of a carbon atom in the 4-position of the phenyl ring

5.2 Molecule-substrate interactions

Unlike noble metal surfaces, all faces of germanium are expected to interact strongly with many adsorbates, especially large organic molecules. This is due to their localised dangling bonds, as discussed in section 3.1. PES is a powerful tool to investigate the nature of these interactions by probing the shifts in the core-level binding energies of both substrate and adsorbate. This section discusses core-level and valence band spectra of $\text{H}_2\text{TBr}_4\text{PP}$ adsorbed on Ge(001) and to a lesser extent Ge(111) and Ge(110), which have been recorded at the SGM1 beamline at ASTRID unless otherwise specified.

The Ge(001) surface was cleaned as described in section 3.1 and cleanliness was confirmed by analysing the Ge 3d core-level spectrum as described in section 3.1.1. Additionally, the absence of the main contaminants carbon and oxygen was confirmed by recording the background of the C 1s and O 1s core-level, respectively. $\text{H}_2\text{TBr}_4\text{PP}$ was then deposited on the clean surface out of a Knudsen cell at a temperature of 350°C with a flux rate of ~ 1 ML/min. The film thickness was estimated using the beam-current normalised Ge 3d core-level intensities and equation 2.14.

5.2.1 Substrate and macrocycle core-levels

The Ge 3d core-level after the deposition of ~ 2 ML of $\text{H}_2\text{TBr}_4\text{PP}$ is shown in Fig. 5.6a. All Ge 3d core-levels were taken in normal emission and with a photon energy of 60 eV, close to the maximum cross section for this orbital and the resulting kinetic energy yields a small escape depth for high surface sensitivity. Additionally, the photon energy yields the best monochromator resolution (see Fig. 4.3).

After deposition of molecules, the intensity of the up dimer component as seen in the fit for the clean surface Ge 3d core-level (Fig. 3.3b) reduces and a new component on the high binding energy side of the spectrum appears (red component in Fig. 5.6a). The intensity values, energy positions and other peak fitting parameters of the different components

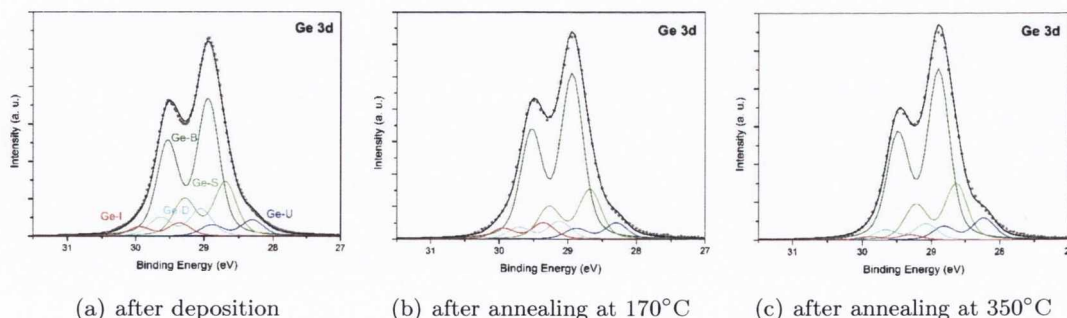


Figure 5.6 Core-level spectra of the Ge 3d orbital after deposition of 2 ML of $\text{H}_2\text{TBr}_4\text{PP}$ on the clean Ge(001)- 2×1 surface. B: bulk, S: second layer, U: up dimer, D: down dimer, I: interface component.

	I_B	I_S	I_U	I_D	I_I	E_B	E_S	E_U	E_D	E_I	BR
clean	0.56	0.23	0.11	0.10	0	28.94	-0.26	-0.6	0.16	-	0.65
as dep.	0.55	0.22	0.06	0.11	0.06	28.94	-0.25	-0.64	0.12	0.41	0.67

Table 5.1 Fitting parameters of the Ge 3d core-levels for the clean Ge(001)-2 \times 1 surface and after the deposition of 2 ML of H₂TBr₄PP. I : Intensities relative to the total peak, E : Binding energy values in eV (relative to E_B), BR: Spin-orbit branching ratio. All components have been fitted with a spin-orbit splitting of 0.59 eV, a Gaussian width of 0.30 eV and a Lorentzian width of 0.15 eV.

I_1	I_2	I_3	I_4	I_5	I_6	E_1	E_2	E_3	E_4	E_5	E_6	GW	LW
0.45	0.18	0.09	0.09	0.09	0.09	286.92	-0.68	0.37	-0.22	-0.95	0.98	0.64	0.11

Table 5.2 Fitting parameters of the C 1s core-level of 4 ML of H₂TBr₄PP on Ge(001):H as shown in Fig. 5.7, numbering of components from 1 (red) to 6 (magenta). I : Intensities relative to the total peak, E : Binding energy values in eV (relative to E_1), GW: Gaussian width in eV, LW: Lorentzian width in eV.

before² and after deposition of molecules are listed in Table 5.1. This shows that while approximately half of the up dimers of the clean surface are still in their original state after the adsorption of molecules, the other half is interacting with the adsorbate. The down dimer intensity does not seem to be affected by the adsorbed molecules, although this component is the most difficult to fit accurately because of its central position.

The exact nature of these interactions is difficult to deduce from the PES data alone since the shift of the additional component is small and the adsorbate molecule quite complex. A similar component with the same energy shift and relative intensity has been observed for the adsorption of MPc on clean Ge(001)-2 \times 1 and has been interpreted as a general interface component [27, 133]. Since both MPc and porphyrin molecules give rise to this component, it cannot be assigned to an interaction of the surface atoms with the bromine substituents of H₂TBr₄PP because they are not present in the MPc. Additionally, there are only four bromine atoms in the molecule, as opposed to 44 carbon atoms in macrocycle and phenyl legs. It is therefore unlikely for a bromine-germanium interaction to be distinguishable in the Ge 3d core-level spectrum. The same applies to the four nitrogen atoms of the macrocycle.

The N 1s core-level has not been recorded in this experiment due to its low intensity and time restrictions. The literature reports that it splits into two components for *free base* porphyrins [145]. They are 2 eV apart, with one originating from hydrogenated nitrogen atoms and the other one from the unsaturated pyrrolic nitrogens. For low coverages of free base phthalocyanines in experiments by Holland [27], the N 1s spectrum suggests an interaction between the pyrrolic nitrogens and the germanium surface. A similar interaction is therefore to be considered for the porphyrin macrocycle. It is important to note that

²spectrum not shown, compare Fig. 3.3b

the nitrogen atoms in the macrocycle are part of a conjugated electron system, making it difficult to distinguish between the contributions of nitrogen and carbon atoms to the overall interactions.

The C 1s core-level signal is comparatively weak due to intensity losses in the SGM1 monochromator at the incident photon energy of 350 eV, which makes it difficult to interpret. However, some conclusions can be drawn when comparing its general shape to a C 1s core-level spectrum of a higher coverage of H₂TBr₄PP deposited on the *non-interacting* hydrogen-passivated Ge(001) surface as shown in Fig. 5.7. This core-level has been fitted by applying relative binding energy values calculated by Cormac McGuinness and Anna Lawless [146] using the StoBe code as described in detail in section 4.4.4. The six different components are contributions from carbon atoms in

different bonding configurations in the H₂TBr₄PP molecule, with the relative intensities reflecting their multiplicity. There are 28 carbon atoms in the phenyl legs, all of which have very similar binding energies (red component in Fig. 5.7), except the four carbons bonded to the bromine substituents (magenta). Eight of the carbon atoms in the macrocycle are bonded to the central nitrogen atoms, and another eight form the rest of the pyrrole units. Unlike in a similar fit of the C 1s core-level of ZnTPP performed by Cudia *et al.* [147], the calculations show that the binding energies of these pyrrolic carbons differ depending on whether they are part of a pyrrole unit with or without a central hydrogen (see legend in Fig. 5.7). The relative shifts in binding energy and other fitting parameters are displayed in Table 5.2. This fit is obviously not unique and may appear relatively poor, but it successfully accounts for all possible components in a non-interacting H₂TBr₄PP molecule and explains the overall line shape in agreement with the calculations and within the 1 σ error range. Differences between the fit and the data most likely originate from interactions between the different layers of molecules, e.g. π - π stacking, causing small shifts or broadening of the different components.

The C 1s core-level for 2 ML of H₂TBr₄PP on the clean, unpassivated Ge(001) surface has not been fitted due to insufficient statistics at this comparatively low coverage and the lack of supporting DFT calculations as available for the non-interacting molecule. However, it clearly shows an energy shift of \sim 1 eV to lower binding energy and a broadening of the overall line-shape when compared to the non-interacting molecules, as shown in the open circles in Fig. 5.7. This indicates significant interactions between the carbon atoms

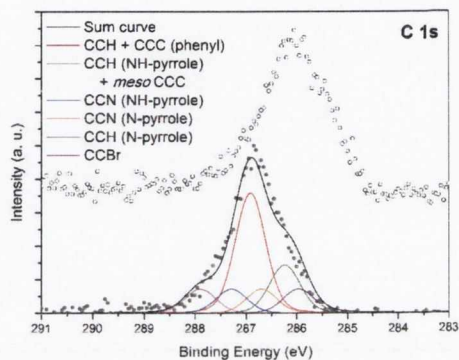


Figure 5.7 C 1s core-level spectrum of 4 ML of H₂TBr₄PP on Ge(001):H (solid circles) and 2 ML of H₂TBr₄PP on clean Ge(001) (open circles).

and the clean germanium surface and therefore suggests that the substrate-adsorbate interaction observed in the Ge 3d core-level can be attributed to the macrocycle of the molecule.

Since the motivation of this work is the formation of covalent networks via the reaction between molecular building blocks on a supporting surface at an increased temperature, the 2 ML coverage of H₂TBr₄PP was subsequently annealed at 170°C for 40 min³. The bromine substituents have been reported to dissociate from the molecules at this temperature [19], leaving the reactive ends of the molecule. The Ge 3d core-level after this first annealing step shows no major change, as shown in Fig. 5.6b. The intensity ratio of all five components is the same as directly after deposition, with the only exception of a slight increase in the intensity of the down dimer signal. However, this is considered to be within the error range since the signal-to noise ratio in 5.6b is worse than in 5.6a and the stepwidth is larger.

When annealing the sample to 350°C, the interface component clearly reduces and the up and down dimer intensities are restored to almost their initial values (see Fig. 5.6c). Overall, the core-level resembles its clean surface shape as shown in Fig. 3.3b. This indicates either a change in the interface chemistry of the molecules and the surface or the partial desorption of the molecules at this temperature which is supported by a slight decrease in the C 1s core-level intensity after the last anneal (not shown).

5.2.2 Bromine substituents

As mentioned above, the interactions between the bromine substituents and the germanium surface are not visible in the Ge 3d core-level. However, the Br 3d core-level of the previously discussed coverage of 2 ML of H₂TBr₄PP on Ge(001)-2×1 was recorded with an incident photon energy of 110 eV, maximising the cross section and resulting in spectra with reasonable intensity.

Directly after deposition, the Br 3d core-level spectrum in Fig. 5.8a shows at least two clearly distinguishable doublet peaks. The fitting parameters are listed in Table 5.3. Considering electronegativity, the component labelled Br I at higher binding energy can be assigned to bromine atoms still attached to the molecules. The binding energy is very close to values found after the deposition of the same molecule on non-interacting surfaces like Au(111) or Ge(001):H (see Chapter 7). However, its binding energy lies 0.2 eV lower on Au(111) and 0.3 eV higher on Ge(001):H, which might be an indication for the degree of interaction or of dielectric screening for the hydrogen-passivated Ge surface.

The Br II doublet most likely originates from bromine interacting with the germanium surface, which can be confirmed by comparing it to the Br 3d core-level spectrum for bromine-passivated Ge(001) as discussed in Chapter 6. It is ~2 eV lower in binding energy

³standard annealing duration for all experiments in this chapter

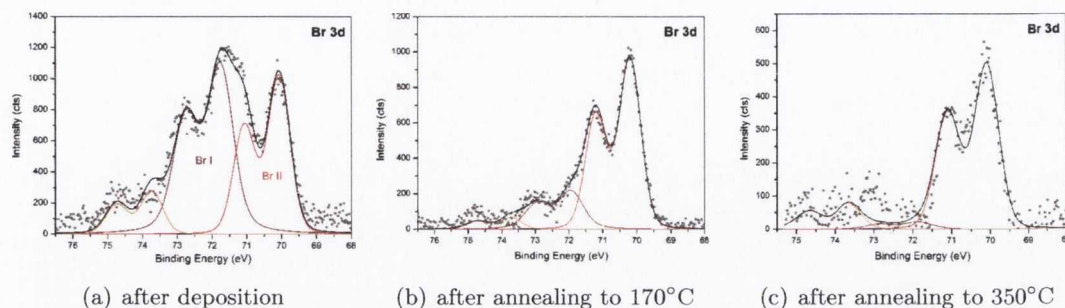


Figure 5.8 Core-level spectra of the Br 3d orbitals after deposition of 2 ML of $\text{H}_2\text{TBr}_4\text{PP}$ on the clean $\text{Ge}(001)\text{-}2\times 1$ surface.

than Br I, equivalent to the transfer of one electron from the surface to the bromine atom and therefore indicating the formation of a strong bond. This energy shift is also observed after annealing a coverage of the same molecules on $\text{Au}(111)$ [148], indicating a similar reaction. It is reasonable to assume that the bromine atoms are dissociated from the molecules in the process.

A third component at a binding energy of approximately 73.7 eV can most likely be identified as excess bromine (Br_2) which is either sitting on the surface or is trapped under the molecules.

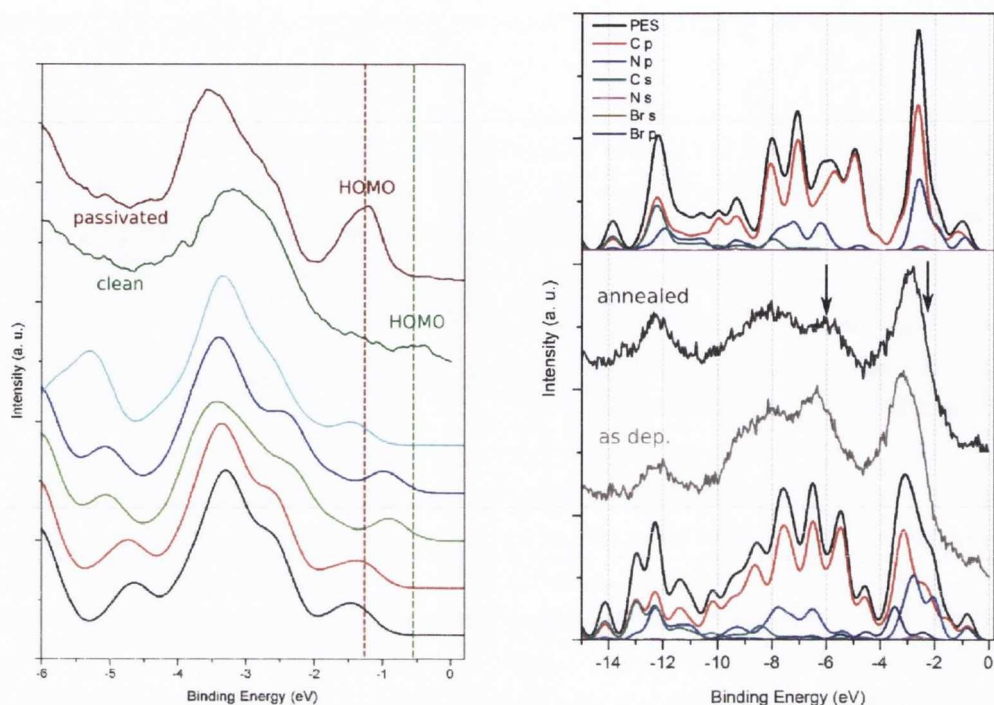
After annealing the surface at 170°C , Br I reduces significantly as shown in Fig. 5.8b. This confirms the assignment of this species to bromine atoms attached to the molecules, since they are expected to dissociate at this temperature. Br II does not gain or lose significantly in intensity, which shows that the bromine dissociating from the molecules does not subsequently bond to the surface at this temperature, but instead seems to leave into the vacuum.

There is no change in the intensity of the C 1s core-level after annealing to 170°C (spectrum not shown), which suggests that it is only the bromine atoms that are removed from the molecules and leave the surface while the main part of the molecules remains adsorbed.

Further annealing to 350°C results in the complete removal of Br I and the reduction of

	I_I	I_{II}	E_I	E_{II}	SOS	BR	GW	LW
as dep.	0.53	0.47	71.8	-1.7	1.0	0.66	0.65	0.30
170°C	0.17	0.83	72	-1.8	1.0	0.66	0.65	0.30

Table 5.3 Fitting parameters of the Br 3d core-level after the deposition of 2 ML of $\text{H}_2\text{TBr}_4\text{PP}$ on clean $\text{Ge}(001)\text{-}2\times 1$ and annealing at 170°C . I : Intensities relative to the total peak (without third component), E : Binding energy values in eV (relative to E_I), SOS: Spin-orbit splitting in eV, BR: Spin-orbit branching ratio, GW: Gaussian width in eV, LW: Lorentzian width in eV.



(a) Dark red: $\text{H}_2\text{TBr}_4\text{PP}$ on H-passivated Ge(001) (experimental), dark green: $\text{H}_2\text{TBr}_4\text{PP}$ on clean Ge(001) (experimental), cyan: planar conformation (DFT), blue: N-N axis saddle shape (DFT), green: NH-HN axis saddle shape (DFT), red: planar core and 65° phenyl leg rotation (DFT), black: planar core and 90° phenyl leg rotation (DFT).

(b) Bottom: calculated VB spectrum for $\text{H}_2\text{TBr}_4\text{PP}$ in NH-HN axis saddle conformation with contributions from different elemental orbitals (see legend), grey: experimental VB spectrum of $\text{H}_2\text{TBr}_4\text{PP}$ on clean Ge(001), dark grey: $\text{H}_2\text{TBr}_4\text{PP}$ on clean Ge(001) after annealing at 170°C , top: calculated VB spectrum (with elemental orbital contributions) for the minimum energy configuration of $\text{H}_2\text{TBr}_4\text{PP}$ with 69° phenyl leg rotation.

Figure 5.9 Experimental valence band spectra of $\text{H}_2\text{TBr}_4\text{PP}$ adsorbed on Ge(001) compared to DFT-calculated VB spectra of $\text{H}_2\text{TBr}_4\text{PP}$ without specific molecule-substrate interactions.

Br II to half of its initial intensity as shown in Fig. 5.8c. The C 1s spectrum shows only a slight decrease in intensity, indicating that most of the molecules do not desorb at 350°C and remain on the surface with nearly all their bromine atoms dissociated. The decrease of the Br II signal signifies the dissociation of Br-Ge bonds at this temperature, which is in agreement with the results of the desorption study of bromine on Ge(001) discussed in Chapter 6.

5.2.3 Valence band

The top of the valence band spectrum of 2 ML of $\text{H}_2\text{TBr}_4\text{PP}$ on clean Ge(001) is shown in dark green in Fig. 5.9a. It was taken with an incident photon energy of 55 eV. The beam-current normalised reference spectrum of the clean surface without the adsorbate

has been subtracted, making small features like the HOMO level at ~ 0.5 eV discernible. The spectrum is plotted in comparison to the valence band of 4 ML of $\text{H}_2\text{TBr}_4\text{PP}$ on hydrogen-passivated Ge(001) (dark red) and to DFT-calculated PES spectra for different conformations of the non-interacting molecule: a planar core with the phenyl legs rotated at an angle of 90° (black), a planar core with the phenyl legs rotated at an angle of 65° which has been determined to be the minimum energy configuration (red), two saddle shaped conformations as shown in Fig. 3.8b with the coplanar phenyl legs being bent down by 20° from the N-N (blue) or the NH-HN axis (green) across the porphyrin core, and a completely planar molecule (cyan). As for the C 1s core-level, the calculations have been performed by Cormac McGuinness and Anna Lawless [146]⁴. The calculated energy values with respect to the planar core/perpendicular phenyl legs conformation are listed in Table 5.4. The comparison shows that the conformation of the molecule has a significant impact on the features in this area of the valence band. The HOMO is shifted from 1.2 eV in the minimum energy configuration to 0.8 eV for the NH-HN saddle conformation. A similar shift of the HOMO is also observed in the experimental data for $\text{H}_2\text{TBr}_4\text{PP}$ on clean Ge(001) as indicated by the dashed lines in Fig. 5.9a, which suggests that the molecules adsorb in a saddle-shape conformation. The direction of the axis (NH-HN or N-N) is difficult to determine since the calculated valence band spectra as well as their total energy values are very similar and resolution of the experimental data is insufficient. In contrast, the VB spectrum of $\text{H}_2\text{TBr}_4\text{PP}$ on passivated Ge(001) agrees best with the minimum energy configuration of the molecule, which shows very clearly that strong interactions with the surface induce a conformational change in the adsorbed molecules.

Fig. 5.9b shows the comparison between the experimental VB spectrum of $\text{H}_2\text{TBr}_4\text{PP}$ on clean Ge(001) and the calculated VB spectrum for the NH-HN saddle conformation again (bottom half), but including higher binding energies and the partial contributions of the different elemental orbitals to the overall spectrum. The top half of Fig. 5.9b shows the experimental VB spectrum after annealing the $\text{H}_2\text{TBr}_4\text{PP}$ molecules at 170°C (dark grey) and the calculated spectrum for the minimum energy configuration of the same molecule without the bromine substituent, H_2TPP . The spectra match very well, with the major changes being the reduc-

conformation	ΔE (eV)
planar/ 90°	0
planar/ 65°	-0.104
saddle/NH-HN axis	+0.98
saddle/N-N axis	+0.92
planar	+7.32

Table 5.4 Calculated energy values for different conformations of $\text{H}_2\text{TBr}_4\text{PP}$, with respect to the planar/ 90° conformation [146].

⁴The energy axis has been stretched by a factor of 1.085 for the best match with the experimental data, a method which is commonly employed for comparing experimental and calculated VB spectra (e.g. in [149]).

tion of the shoulder at ~ 2.5 eV and of the peak feature at ~ 6 eV as indicated by the arrows. The apparent loss of the bromine substituents after annealing at 170°C results in a charge redistribution throughout the entire molecule, which is reflected in the valence band spectrum.

While the major features of the valence band have been shown to indicate both the conformation of the adsorbed molecules and the loss of the substituents, further interpretation of the VB spectra, e.g. regarding interactions with the surface leading to a band offset or interface dipole, is difficult due to the insufficient resolution and statistics of the experimental VB spectra.

5.2.4 Ge(111) and Ge(110)

To determine whether either Ge(111) or Ge(110) or both are more suitable candidates for on-surface reactions between molecules than Ge(001) without previous passivation, coverages of NiTBr₄PP have been probed for molecule-substrate interactions on both of these surfaces. PES experiments have been carried out at the SX700 beamline at ASTRID, yielding a lower energy resolution than the previously discussed experiments from the SGM1 beamline (see section 4.4). Since the bromine-germanium interaction with a large shift of ~ 2 eV in the Br 3d core-level is the most distinct indicator for molecule-substrate interactions, the respective spectra have been recorded with an incident photon energy of

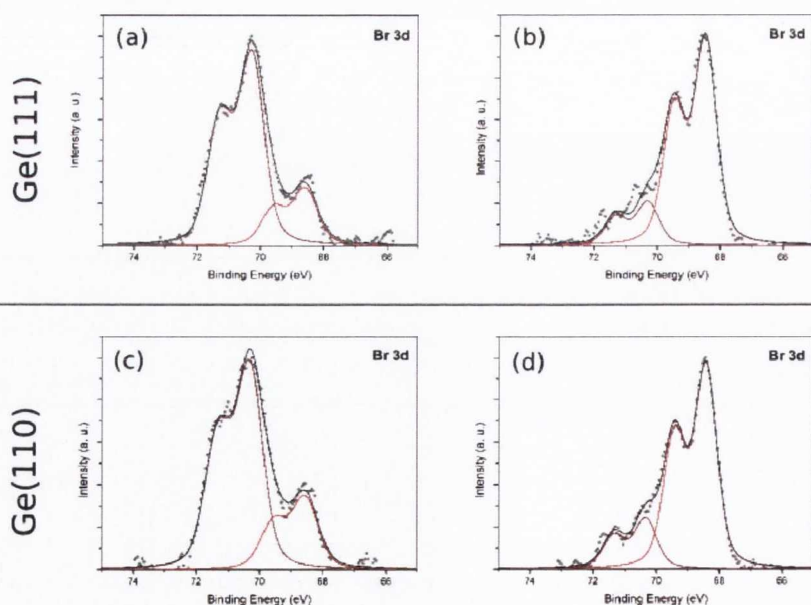


Figure 5.10 Br 3d core-levels of 2 ML of NiTBr₄PP on Ge(111) (a and b) and Ge(110) (c and d). a and c are directly after deposition of the molecules, b and d after an anneal at 170°C .

	I_I	I_{II}	E_I	E_{II}	BR	GW	LW
(111) as dep.	0.77	0.23	70.3	-1.7	0.66	0.75	0.30
(111) 170°C	0.17	0.83	70.3	-1.8	0.66	0.65	0.30
(110) as dep.	0.74	0.26	70.3	-1.8	0.66	0.80	0.30
(110) 170°C	0.20	0.80	70.3	-1.9	0.66	0.65	0.30

Table 5.5 Fitting parameters of the Br 3d core-level after the deposition of 2 ML of NiTBr₄PP on clean Ge(111) and Ge(110), and subsequent annealing at 170°C. I : Intensities relative to the total peak (without third component), E : Binding energy values in eV (relative to E_I), BR: Spin orbit branching ratio, GW: Gaussian width in eV, LW: Lorentzian width in eV.

170 eV for both Ge(111) and Ge(110) surfaces and are displayed in Fig. 5.10. The nickel centre in this molecule is not expected to make any difference in this part of the overall molecule-substrate interactions.

The spectra clearly show that the bromine bonds to both germanium surfaces directly after deposition, exactly like on Ge(001). The fitting parameters for all Br 3d peaks in Fig. 5.10 are displayed in Table 5.5 and show that for Ge(111) and Ge(110) the bromine species at lower binding energy, previously assigned to the Br-Ge bonds, is shifted by 1.7 eV and 1.8 eV, respectively. This matches the values found for Ge(001).

After annealing at 170°C, the bromine species assigned to bromine attached to the molecules goes down as expected in both cases, but unlike in the previously discussed experiments on Ge(001) all bromine detaching from the molecules is found attached to the surface after the anneal on both Ge(111) and Ge(110), which can be deduced from the absolute intensities. Furthermore, the Gaussian width of both core lines after annealing is significantly smaller than before, which suggests the presence of more than just two bromine species directly after deposition.

The Ge 3d core-levels have been recorded for both surfaces for coverage determination, but due to the low resolution show no major shifts or changes in shape that could be interpreted.

5.2.5 Conclusions

PES results show that the adsorption of H₂TBr₄PP on clean Ge(001) is governed by two different interaction mechanisms.

The first one is through the macrocycle of the molecule and can be identified in an additional interface component in the Ge 3d core-level spectrum as it has also been observed for MPc, and in a shift of the C 1s core-level when compared to a non-interacting substrate. This interaction is strong, but not strong enough to indicate a full chemical bond, for example through cycloaddition reactions like described in section 5.1. This is most likely due to the aromaticity of the macrocycle, which stabilises the molecules sig-

nificantly. It is possible that the metallic nature of the Ge(001) surface dimers facilitates a charge transfer into the LUMO level, which has been reported for the adsorption of 3,4,9,10-perylene-tetracarboxylic-dianhydride (PTCDA) on Ag(111) [150]. This mechanism is similar to the *Blyholder* model [151], in which carbon-derived frontier orbitals exchange charge with a metal and as a consequence certain intramolecular bonds are weakened, often resulting in conformational changes. Other measurement techniques like X-ray adsorption spectroscopy (XAS) or inverse photoemission spectroscopy (IPES) could probe the unoccupied states, but no such measurements have been carried out since the adsorption mechanism of this molecule is not the main focus of this work. However, the comparison of the valence band spectra of the adsorbed molecules to calculated spectra for different conformations of the molecule show that the interactions with the Ge(001) surface induce a conformational change towards the saddle shape.

The second interaction has been observed between the bromine substituents and the germanium surface. A 2 eV shift between components of the Br 3d core-level spectrum indicate that a large fraction of the bromine atoms are chemisorbed on the dimers by dissociation from the molecules upon adsorption. The same shift has been observed on both Ge(111) and Ge(110). Experiments with sub- or near-monolayer coverages on a home XPS system unfortunately did not yield enough intensity to clarify if the different components originate from different layers of molecules.

Both of these mechanisms are expected to significantly limit the mobility of H₂TBr₄PP on all three surfaces. This aspect and the conformational change indicated by the valence band of the molecule will be further discussed for Ge(001) in section 5.3.1.

5.3 Adsorption geometry

While PES has been used to obtain information about the chemical processes involved in the adsorption of H₂TBr₄PP on germanium surfaces, the structural information like conformational changes in the adsorbed molecules or changes in the surface reconstruction of the substrate can only be indicated but not accurately attained from the spectroscopy data alone. STM data contains information about both the electronic and topographic structure of surfaces as discussed in section 2.4, and is therefore a very suitable method to determine the specific adsorption geometry of organic molecules on surfaces.

This section presents results on the adsorption geometries of H₂TBr₄PP and H₂TPP on Ge(001). No STM experiments have been carried out on the Ge(111) and Ge(110) surfaces. Comparative DFT calculations of the local density of states (LDOS), which are often essential to interpret the physical meaning of STM topographs, have been attempted but remained inconclusive due to the comparably large size of the molecule and the necessity of a large Ge(001)/germanium bulk cluster requiring very high computing power for accurate results.

5.3.1 STM of H₂TBr₄PP

The STM experiments on the adsorption geometry of H₂TBr₄PP on Ge(001) have been carried out in Dublin City University and CRANN, Trinity College Dublin. On both systems, the molecules have been evaporated on the clean Ge(001) surface at cell temperatures of 280°C to 320°C, with low flux rates of around 1.25 ML/h for good coverage control. The temperature had to be increased slightly with every new evaporation, most likely due to polymerisation of the molecules in the crucible. Due to an unstable tip in the empty state regime, all STM images in this particular experiment are of the filled states.

Fig. 5.11a shows a typical STM image of a low coverage (~ 0.1 ML) of H₂TBr₄PP on clean Ge(001). The underlying surface is clearly recognisable with all three surface reconstructions present. It shows more defects than without the adsorbate molecules, most of which are missing surface dimer atoms in several small etch pits. These are very likely due to bromine-etching, which will be discussed in Chapter 6. Additionally, a few features, marked in green in Fig. 5.11b, resemble individually adsorbed bromine atoms (also discussed in Chapter 6) which confirms the dissociation of bromine atoms from the molecules as observed with PES and discussed in the previous section.

The most striking characteristic of the adsorbed molecules are the two distinct adsorption geometries, which are in approximately equal proportion throughout all the STM images. They are marked S and A in Fig. 5.11a for “symmetric” and “asymmetric”, respectively. A close-up STM image of both types is shown in Fig. 5.11b. Despite some streaks in Fig. 5.11a indicating loose material on the surface being dragged along by the tip, none of the molecules has ever been observed moving position from one image frame to the next. Additionally, the comparably good resolution down to submolecular features indicates very strong interactions between molecules and germanium surface, holding the adsorbates in place at the room temperature imaging conditions.

Symmetric adsorption

The symmetric feature appears to be rectangular with the long side across the dimer rows, which indicates that it is distorted from its relaxed, square conformation upon adsorption due to interaction with the germanium surface. A line profile analysis, partly shown in Fig. 5.11c, suggests molecule dimensions of 1.1×1.7 nm², which is in good agreement with the repeatedly reported rectangular saddle shape for very similar porphyrins on other substrates (see section 5.1). Additionally, its shape is different from STM images of the planar molecule on Ag(111) [152] and on Ag/Si(111) [153], where it consists of two lobes in seemingly random orientations (rotated by 90°) and, less bright, the four phenyl legs. The difference from the molecule’s appearance on metal surfaces is a further indication of the presence of the strong molecule-substrate interactions on Ge(001). The bright lobe in the centre of the symmetric feature, always pointing along the dimer rows, is either due

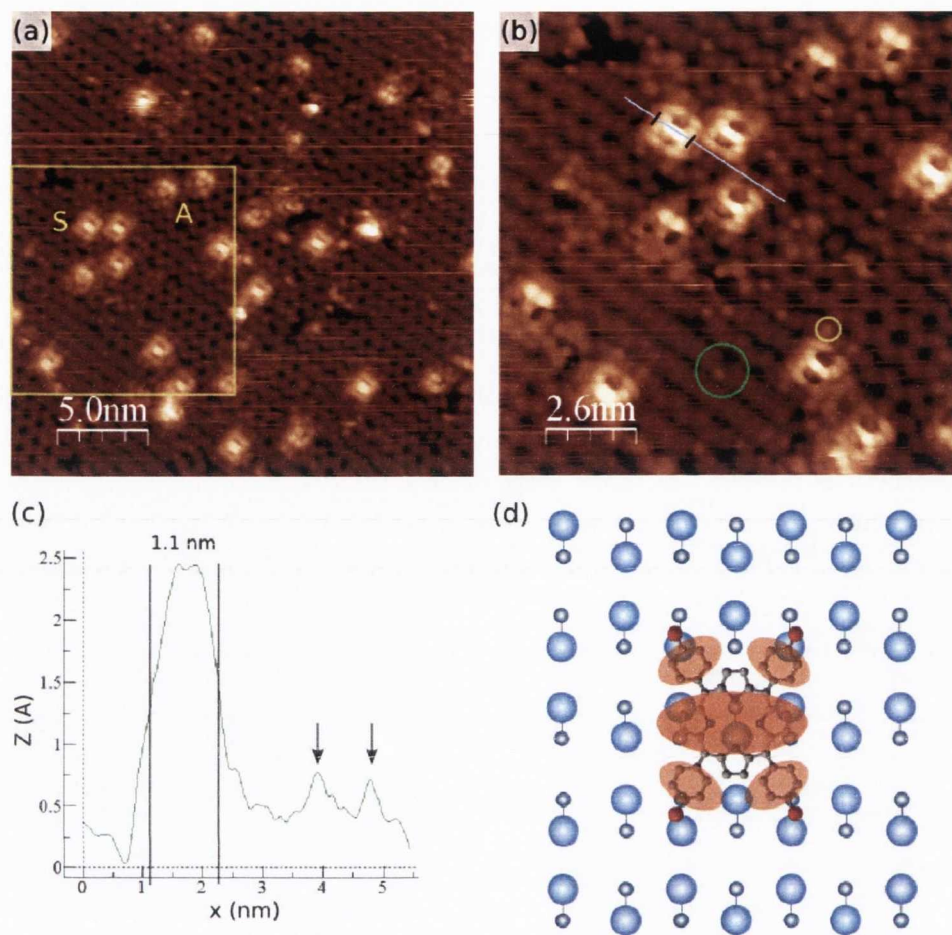


Figure 5.11 Adsorption of $\text{H}_2\text{TBr}_4\text{PP}$ on $\text{Ge}(001)$. (a) Filled state STM image of a coverage of ~ 0.1 ML, taken at -1.6 V, 0.28 nA; (b) filled state STM image of marked area in (a) (labels explained in the text), taken at -1.2 V, 0.35 nA; (c) line profile along the blue line marked in (b), arrows marking features equivalent to the one circled yellow in (b); (d) simplified model of the symmetric adsorption type (hydrogens have been omitted for clarity).

to a non-planar distortion of the core caused by the altered position and/or rotation of the phenyl legs or due to the asymmetry of the central hydrogen atoms. The orientation of the central hydrogen atoms is difficult to extract from the images alone, but the DFT calculations performed for the interpretation of the valence band spectra in section 5.2 also show that the unhydrogenated pyrrolic nitrogens contribute much more to the HOMO than the hydrogenated ones, independent of the specific conformation. However, no LDOS calculations simulating STM images have been performed, which makes it impossible to clarify whether the bright contrast in the STM originates from the electronic structure, i.e. the position of the central hydrogen atoms, or closer proximity of the upward-bent pyrrole groups to the tip. The DFT/LDOS calculations and STM experiments on TPyP

by Auwärter *et al.* [139] as discussed in section 5.1 show a very similar cigar-shaped lobe as it is observed in this experiment, which they interpreted to be caused by the non-planar distortion of the core without discussing the position of the central hydrogen atoms. Assuming that their LDOS calculations are correct, the core distortion is also the most feasible explanation for the lobe feature observed for $\text{H}_2\text{TBr}_4\text{PP}$ on Ge(001).

A simplified model for the symmetric adsorption type of $\text{H}_2\text{TBr}_4\text{PP}$ on Ge(001) in its ground state $c(4\times 2)$ reconstruction is shown in Fig. 5.11d. Alterations of the surface reconstructions induced by the adsorbed molecules have not been taken into account for the model since the underlying reconstruction varies widely over all adsorbed molecules imaged with the STM. Nonetheless, the model agrees with the dimensions of the molecule measured in the STM images by explaining the distortion from the relaxed, square dimensions with a stretch of the phenyl legs towards a rectangular shape. This stretch is most likely caused by an attractive force or some kind of bonding mechanism between the bromine atoms and the germanium dimer atoms. A similar effect has been observed for $\text{H}_2\text{TBr}_4\text{PP}$ on Cu(111) by Doyle *et al.* and has also been assigned to strong interactions between the molecule and surface atoms [154]. The PES and the aforementioned etch pits and single adsorbed bromine atoms observed in the STM images suggest a surface-induced dissociation of the bromine substituents. This would leave the ends of the phenyl legs reactive and prone to react with the surface. A further indication for this can be found in the STM images in the form of four brighter features along the neighbouring dimer rows on each side of the molecules, as marked in yellow on one of the adsorbed S-type molecules in Fig. 5.11b and indicated with arrows in the line profile in Fig. 5.11c. These brighter dimer atoms match with the surface dimers closest to the phenyl leg ends in the model in Fig. 5.11d.

The rotation angle of the phenyl legs cannot be extracted from the STM pictures without markers like the *tert*-butyl groups used by Jung *et al.* [138] and, like the position of the central hydrogens, could only be clarified by matching LDOS calculations. However, the central bright lobe caused by the non-planar saddle shape distortion of the macrocycle indicates that the phenyl groups are rotated at a smaller angle than in their relaxed conformation and possibly bent down towards the surface, as indicated by the valence band spectra (see section 5.2). Assuming a bond or at least a very strong attractive interaction between the bromine-end of the phenyl leg and the surface, the rotation is most likely caused by steric interactions of the conjugated π -system of the phenyl and the surface. These interactions could be part of the interface component of the Ge 3d core-level spectra observed with PES, which in the discussion has so far been associated with the macrocycle.

In some cases and especially at biases lower than -1.3 V, differences in brightness within single molecules of the symmetric adsorption type can be observed as shown in Fig. 5.11b. These are either due to slight differences in the molecule's height above the germanium

surface or due to changes in the electronic structure of the molecular orbitals, possibly induced by bond formations or defects in the underlying surface.

Asymmetric adsorption

The shape of the second, asymmetric type consists of two bright round lobes and one or two smaller lobes, which are surrounded by a pattern of moderately bright features. This was found repeatedly in all images (sometimes rotated by 180°). Unlike for the symmetric type, no comparable STM images for the adsorption of similar molecules could be found in the literature, suggesting that the origin of this shape is very specific to interactions with the (001) face of germanium (and possibly silicon). Its overall dimensions agree with the size of the molecule, which rules out the possibility of an upstanding adsorption of the molecule, which can sometimes be observed with phthalocyanines [27]. However, within the error range and the limited resolution of these STM images, a slight tilt of the molecule cannot be ruled out and even seems like a very likely explanation of the the asymmetry of the feature.

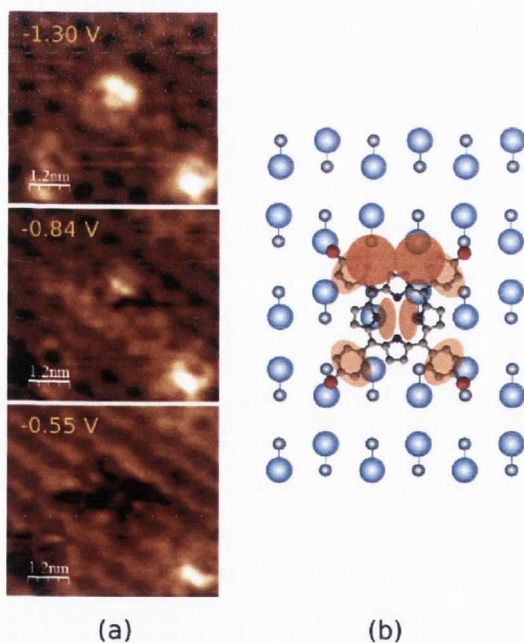


Figure 5.12 Asymmetric adsorption type of $\text{H}_2\text{TBr}_4\text{PP}$ on $\text{Ge}(001)$. (a) Filled state STM images at different biases; (b) proposed, simplified model of the asymmetric adsorption type (hydrogens have been omitted for clarity).

The centre of the molecule cannot be identified as clearly as for the symmetric shape. However, in STM images taken at higher biases four lobes of medium brightness which are reasonable to assign to the four phenyl legs become more apparent. That puts the centre of the molecule on one side of the dimer row instead of directly on top like the symmetric adsorption type. Fig. 5.12b shows a simplified model of the asymmetric adsorption based on this assumption. It suggests that the two small bright lobes in the centre of the molecule could originate from the central nitrogens interacting with the dimers as it has been shown to happen with phthalocyanines [27]. However, this does not agree with the previously proposed slight tilt explaining the two big bright circular features. It is also difficult to speculate on whether and where the molecule is attached to the surface through chemical bonds between the phenyl legs and the surface dimers after detachment of bromine,

similar to what has been proposed for the symmetric adsorption type. The surrounding moderately bright features on the darker side of the molecule could originate from germanium dimer atoms, whose charge density has been altered from its usual state by interactions or bond formations with the molecule.

When imaging the adsorbed molecules at different biases of the STM tip as shown in Fig. 5.12a, it becomes apparent that the electronic structure of the asymmetric adsorption type is different from the symmetric one's. The latter roughly retains its shape when imaging at lower biases, whereas the asymmetric type changes appearance significantly below -1.3 V until it is only visible as a depression in the surrounding surface at -0.55 V. This indicates that the asymmetric type of the adsorbed molecule has very few filled states between E_F and -0.84 eV, where it is just barely visible, and therefore almost "disappears" in the STM images when imaged with a lower bias. It is possible that this can be related to the observed broadening or shift of the HOMO level in the VB spectra as described in section 5.2.

The underlying structure of the germanium atoms is hard to distinguish from possible remains of the molecular orbitals and could only be analysed with supporting LDOS calculations of the adsorbed molecule including the underlying germanium surface. The same applies to a possible analysis of the origin of the observed difference in electronic structure between the two adsorption types.

Higher coverage

Fig. 5.13 shows a filled state STM image of a near-monolayer coverage of $\text{H}_2\text{TBr}_4\text{PP}$ on clean Ge(001). A quantitative analysis of the two different adsorption types reveals that, as for very low coverages, their ratio is roughly equal. Additionally, no long range order like the formation of islands or rows can be found in any of the STM images. This shows that the interactions between the molecules and the substrate dominate over molecule-molecule interactions, unlike on noble metals where the latter lead to the formation of self-assembled islands (e.g. [19,152]).

It seems obvious to try to connect the two different types of adsorbed molecules with the two major bromine species observed in PES directly after deposition as described in the previous section, given that their ratios are roughly

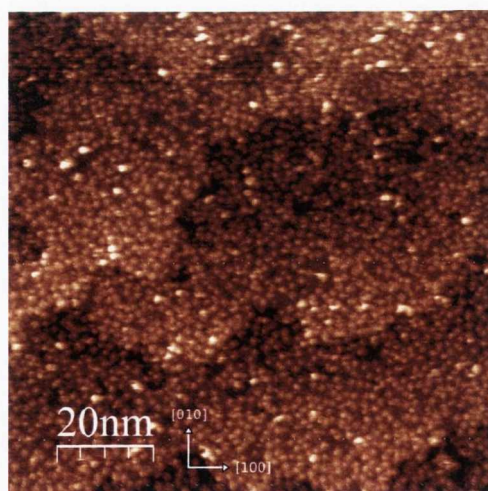


Figure 5.13 Filled state STM image of a near-monolayer coverage of $\text{H}_2\text{TBr}_4\text{PP}$ on Ge(001), taken at -1.6 V, 0.36 nA.

equal in both PES and STM experiments. One of the types could represent an intact molecule with all bromines attached (Br I) with the other type being molecules with some or all of their bromine atoms lost (Br II), either to a chemical reaction with the surface or during evaporation. However, the PES data was taken on a coverage of more than one layer of molecules and it cannot be ruled out that the two different bromine species originate from different layers of molecules. Unfortunately, XPS experiments on sub- or near-monolayer coverages did not yield enough intensity to analyse the Br 3d core-level and clarify this issue. Furthermore, the strong attachment of both adsorption types to the surface suggests chemisorption as opposed to physisorption in both cases.

5.3.2 STM of H₂TPP

Free base tetraphenylporphyrin (H₂TPP) is a very commonly available porphyrin derivative and is identical to H₂TBr₄PP apart from the missing bromine substituents. This opens up the possibility of investigating the influence of the bromine substituent in the adsorption of H₂TBr₄PP on clean Ge(001) by comparing it to the adsorption characteristics of H₂TPP on the same surface.

Filled and empty state STM images of a low coverage of around 2% of a ML show the

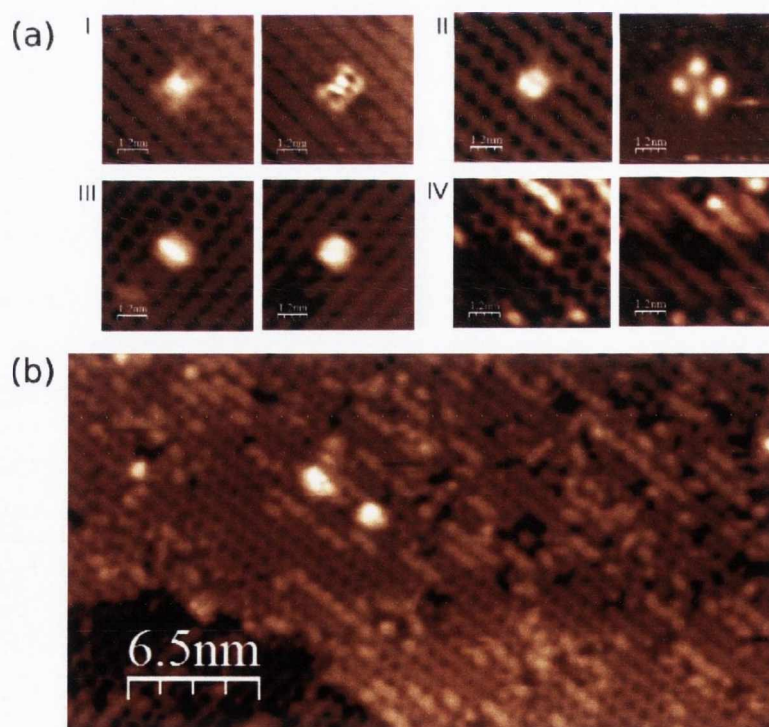


Figure 5.14 (a) Filled state (left) and empty state (right) STM images of different adsorption species of H₂TPP on Ge(001), (6×6) nm, taken at +/-1.3 V, 0.43 nA; (b) filled state STM image of 0.25 ML of H₂TPP on Ge(001), taken at -1.4 V, 0.06 nA.

H₂TPP molecules adsorbed on Ge(001) in at least four different configurations as shown in Fig. 5.14a. Some other features found in some of the images might represent even more different adsorption species, but they were not found frequently or repeatedly enough in the comparatively small STM image dataset with sufficient resolution to be certain.

As with H₂TBr₄PP, it is impossible to assign the different adsorption configurations observed with the STM to specific conformations and adsorption geometries without supporting DFT calculations. The species I and II are rectangular, with dimensions of 1.8×1.1 nm² and 1.3×1.7 nm², respectively. Species III is square (1.5×1.5 nm²), whereas IV appears to be upstanding along a dimer row (~1.5×0.65 nm²), with the core roughly perpendicular to the substrate surface.

The ratio of these different configurations is strongly coverage dependent. A quantitative analysis of the different adsorption types shows a large error range of around 20-25% because of the comparably small STM dataset. Yet even within that error range, species III has been determined to be the most common at a very low coverage while all other types appear in roughly equal amounts. This impression changes significantly at a coverage of only 25%, as can be seen in Fig. 5.14b where almost all molecules seem to be upstanding, i.e. of type IV.

Since only very little PES data has been recorded for H₂TPP on Ge(001) and the STM dataset is much smaller and less resolved than for H₂TBr₄PP, the basis for a more detailed discussion about possible bonding sites and adsorption geometries is too small. However, some differences to the adsorption mechanism of H₂TBr₄PP and therefore the influence of the bromine substituent can be deduced from the performed experiments and will be discussed in the following section.

5.3.3 Comparison

The STM experiments on both H₂TBr₄PP and H₂TPP described in sections 5.3.1 and 5.3.2 reveal that their respective adsorption mechanisms are very different, which suggests a significant influence of the bromine substituents. H₂TPP's adsorption type I is similar to the symmetric adsorption configuration of H₂TBr₄PP in both appearance and dimensions, except that the four bright germanium dimer atoms surrounding the latter are not found in H₂TPP type I images. This suggests that these features are related to the bromine substituents. Either the bromine atoms are still attached to the molecule and appear bright due to their elevated height above the surface or they are detached from the molecule and bonding occurs between the ends of the phenyl legs and the germanium surface. The latter could be supported by the fact that a more pronounced contrast of single dimer atoms in STM images of Ge(001) or Si(001) often indicates a charge transfer from one dimer atom to the other one, which makes the latter appear brighter. Other experiments on the UHV system in DCU, evaporating intact H₂TBr₄PP molecules on noble metal surfaces, show that the dissociation of bromine from the molecule in that case does not happen during

evaporation but seems to be facilitated by the germanium surface. Furthermore, H_2TPP 's type II is similar to $\text{H}_2\text{TBr}_4\text{PP}$'s asymmetric adsorption type, but it does not disappear at lower filled state biases in STM, indicating that this behaviour may also be due to a bromine-germanium interaction.

After annealing both systems at 170°C , the H_2TPP molecules appear unchanged whereas $\text{H}_2\text{TBr}_4\text{PP}$ displays at least three different configurations, as shown in Fig. 5.15. This transformation can reasonably be connected to the known detachment of the bromine substituents at this temperature. Two of the three post-anneal adsorption configurations of $\text{H}_2\text{TBr}_4\text{PP}$ (top and bottom right) match the species III and IV of H_2TPP at room temperature (see insets labelled " $\text{H}_2\text{TPP RT}$ "). The third configuration (bottom left) can be compared with the predominant configuration of H_2TPP after further annealing of the latter at 350°C (see inset labelled " $\text{H}_2\text{TPP 650 K}$ "). As with the symmetric species of $\text{H}_2\text{TBr}_4\text{PP}$, four brighter dimer atoms can now be observed around the molecule in both cases. This is another indication

of carbon-germanium bonds being formed between the phenyl legs and the germanium surface atoms, promoted by the debromination of $\text{H}_2\text{TBr}_4\text{PP}$ at 170°C and selective dehydrogenation i.e. C-H dissociation of H_2TPP at 350°C at the ends of the phenyl legs. However, apart from the four bright features the overall appearance of $\text{H}_2\text{TBr}_4\text{PP}$ changes after annealing. The central lobe changes into two bright lobes around the central axis and the well resolved STM images show another two bright germanium dimer atoms on each side of the molecule along the central dimer row. This indicates that the molecule's conformation has changed, most likely due to a change in the interaction of the macrocycle with the central germanium dimer row or even a fracture of the molecular core.

The absence of the asymmetric adsorption configuration of $\text{H}_2\text{TBr}_4\text{PP}$ after annealing to 170°C suggests that it has transformed into H_2TPP species III or IV after the anneal since there is no evidence for the desorption of a significant amount of molecules. It also means that the asymmetric adsorption configuration is only present when at least some bromine substituents are still attached to the molecule.

No anneal of $\text{H}_2\text{TBr}_4\text{PP}$ on Ge(001) at 350°C has been investigated with the STM, leaving the question of what causes the decrease in the interface component observed in PES at that temperature unresolved.

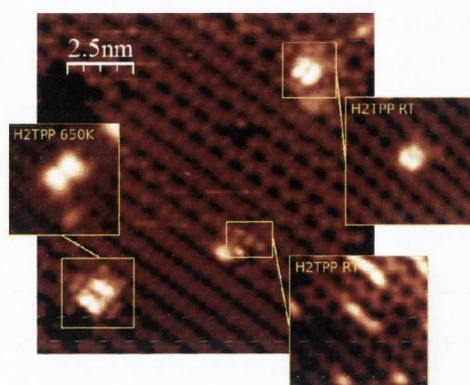


Figure 5.15 Filled state STM image of three different species of $\text{H}_2\text{TBr}_4\text{PP}$ on Ge(001), annealed at 170°C , taken at -1.3 V , 0.36 nA . Insets: corresponding filled state images of comparable adsorption species of H_2TPP on Ge(001).

5.4 Adsorption of smaller organic molecules

As an example of a small or medium sized organic molecule without a macrocycle like H_2TBr_4PP and H_2TPP , 1,3,5-tris(4-bromophenyl)benzene (TBB) has been deposited on clean Ge(001) and studied by STM on the UHV system in CRANN. The cell evaporation temperature for TBB was $170^\circ C$ with a flux rate of approximately 0.8 ML/h.

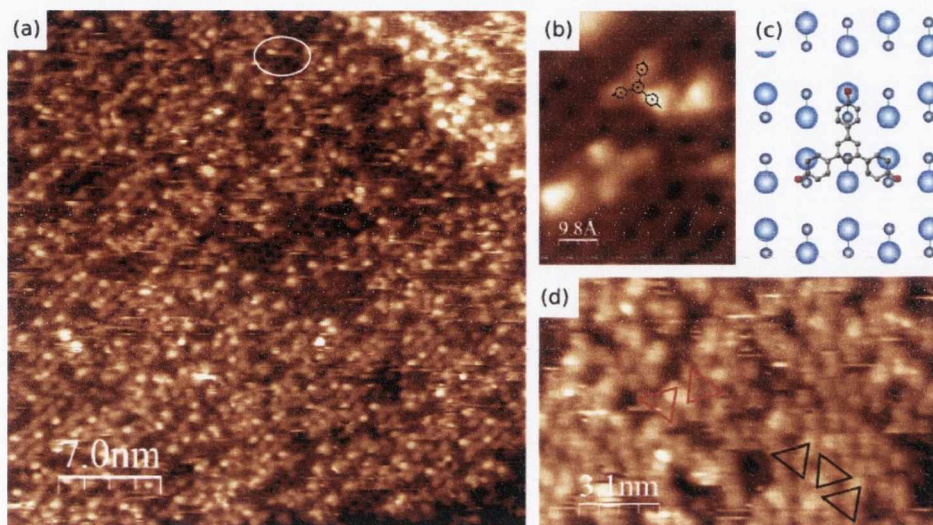


Figure 5.16 Adsorption of TBB on Ge(001). (a) Filled state STM image of a coverage of 0.8 ML, taken at -1.5 V, 0.09 nA; (b) close-up of two adsorbed TBB molecules (and contaminants), with overlay of chemical structure, taken at -1.3 V, 0.08 nA; (c) model of the adsorption of TBB on Ge(001) (hydrogens omitted for clarity); (d) empty state STM image of close-packed molecules with common packing patterns marked in black and red, taken at 1.5 V, 0.09 nA.

Fig. 5.16a shows a filled state STM image of 0.8 ML of TBB. The molecule shows only one adsorption configuration independent of coverage and therefore seems to be determined by interactions with the germanium surface rather than with neighbouring molecules. A close-up with chemical structure overlay is shown in Fig. 5.16b. TBB appears as three lobes, which almost certainly correspond to the three bromophenyl legs. The molecule adsorbs across two dimer rows, with two phenyls on one row and the third on the neighbouring one. The latter phenyl leg appears much brighter than the other two, in both filled and empty state images. The reason for this contrast difference is difficult to determine from the STM images alone. As mentioned in section 3.3.3, the phenyl legs have a rotational degree of freedom around the σ -bond to the benzene core, similar to the previously discussed porphyrin derivatives. Therefore different rotation angles are one possible explanation for the contrast difference, as is a slight tilt of the molecule as suggested for the asymmetric adsorption type of H_2TBr_4PP . Another explanation could be the formation of chemical bonds with the surface on either side of the molecule. However, no PES is avail-

able for this system, making it impossible to know even whether the bromine substituents are still attached to the molecules or if TBB displays a similar interface component in the Ge 3d core-level as porphyrins and phthalocyanines. However, when annealing the surface to the bromine dissociation temperature of 170°C, around half of the original coverage of TBB molecules desorb from the surface whereas the remaining molecules do not change their appearance. The partial desorption of molecules suggests that no strong chemical bond between surface and adsorbed molecules is formed upon deposition. It seems that the molecules leave the surface before the bromine can dissociate. Unlike the case of H₂TBr₄PP, no single adsorbed bromine atoms and almost no etch pits can be found in the low coverage STM images, additionally supporting this hypothesis.

A model of the adsorption site is shown in Fig. 5.16c and shows how the dimensions of the TBB molecule match with the underlying dimers of the Ge(001) surface. This enables the molecules to pack quite closely at higher coverages, as shown in areas of Fig. 5.16a and in Fig. 5.16d. The latter is an empty state image, showing the same contrast difference between the phenyls as the filled state images, and it also displays the most commonly found close packing patterns of TBB. The black triangles show close packing along two dimer rows, and the red ones a head-on configuration with the bright phenyls right next to each other and thereby spanning three dimer rows. These patterns appear randomly and usually only include a few molecules before the periodicity is broken. The absence of long range order and self-assembly of the molecules is further indication that molecule-substrate interactions dominate over molecule-molecule interactions. It is therefore unlikely to obtain a perfect close-packed layer of TBB on Ge(001). However, while still very low, the mobility of TBB on Ge(001) seems to be higher than that of H₂TBr₄PP, which can be seen in the frequent streaky features in STM images as in Fig. 5.16a as well as in the occasionally observed “appearing” half-molecules as marked by the white circle in Fig. 5.16a. These features are due to molecules being dragged over the surface and then dropped by the scanning STM tip and have not been observed for the porphyrins.

Since the low coverage STM images of TBB on Ge(001) are not very well resolved (and therefore not shown), it is difficult to determine the underlying structure of the germanium dimers and whether and in what way the reconstruction is influenced by the adsorbates. However, almost no 2×1 reconstruction can be observed in between adsorbed molecules in any of the images, suggesting that the adsorbed TBB pins the surface dimers into either the c(4×2) or p(2×2) reconstruction (see section 3.1.1). The model of the adsorption geometry in Fig. 5.16c suggests a possible configuration of the underlying up-down dimers, which could also explain the contrast difference between the phenyl legs by the brighter leg adsorbing on top of a charge-rich up-dimer atom.

As for H₂TBr₄PP and H₂TPP, the full adsorption geometry of TBB can only be determined by utilising additional measurement techniques and supporting DFT calculations.

5.5 Summary

Although PES and STM measurements on the adsorption of $\text{H}_2\text{TBr}_4\text{PP}$ on Ge(001) provide both chemical and structural information, the full adsorption geometry could still not be determined without additional measurement techniques or DFT calculations. Yet the comparison between the rough adsorption geometries of $\text{H}_2\text{TBr}_4\text{PP}$ and H_2TPP shows the importance of a relatively small substituent on the adsorption mechanism of a large organic molecule, as previously indicated in studies by Auwärter *et al.* on TPyP and Co-TPP [139, 140] as described in section 5.1. For $\text{H}_2\text{TBr}_4\text{PP}$, some of the bromine substituents dissociate from the molecules upon adsorption and some remain attached. It has been proposed by comparison with the behaviour of H_2TPP and after annealing, that one of the two observed adsorption types of $\text{H}_2\text{TBr}_4\text{PP}$ results from bonds between the de-brominated ends of the phenyl legs and the germanium surface dimers, whereas the other appears to have some intact substituents, possibly slightly tilted away from the substrate plane. Although the STM and the Br 3d core-level spectrum indicate the dissociation of bromine from some of the molecules upon adsorption, the valence band spectra before and after annealing at the bromine-dissociation temperature show some significant changes. While these changes match up nicely with the calculated VB spectrum for H_2TPP , they could also originate from the conformational changes observed in the STM after annealing. Additionally, the PES data has been taken on a coverage of more than a monolayer and some of the molecules contributing to the spectrum do not interact with the surface. These considerations show the complexity of the data analysis and that PES data, even with supporting DFT calculations, can be misleading. However, a more systematic synchrotron study of a single monolayer and better statistics could possibly clarify some of the issues.

A second type of interaction has been shown to occur between the conjugated π -system of the macrocycle and possibly also the rotated phenyl legs. The exact nature of this interaction remains unknown, although the conformational change observed in both the valence band spectrum of $\text{H}_2\text{TBr}_4\text{PP}$ on clean Ge(001) and the STM images is most likely related to it. The experimental VB spectrum agrees best with the calculated spectrum for the saddle shape conformation of the molecule, which matches the appearance of the symmetric adsorption type observed with the STM. However, this does not account for the asymmetric adsorption type, whose configuration, bonding state and contribution to the valence band spectrum remain unclear.

Another unresolved question is the orientation of the central hydrogens of the porphyrin core and their influence on the adsorption mechanism. As mentioned in section 5.3.1, DFT calculations show that the unhydrogenated nitrogens and their pyrrole groups make up most of the HOMO and could therefore be expected to be distinguishable in the STM images. This means that the bright central lobe observed for the symmetric adsorption

type could originate from the N-N axis rather than upward-bent pyrrole rings and the two possible orientations of the central hydrogens could thus be the origin of the two different, equally proportioned adsorption types observed in the STM. However, the relative influence of the local density of states and the proximity to the tip is impossible to gauge without supporting LDOS calculations.

Finally, the expected strong interactions between the clean Ge(001) surface and porphyrin derivatives as well as smaller organic molecules like TBB have been confirmed. In particular, the macrocyclic porphyrin molecules show almost no surface mobility. The bromine-substituted $\text{H}_2\text{TBr}_4\text{PP}$ and TBB additionally show no long-range order, which signifies that molecule-substrate interactions are stronger than molecule-molecule interactions. The larger molecules appear to be more prone to bromine-dissociation, although additional PES measurements on the adsorption of TBB would be necessary to confirm this. In any case, the passivation of all three investigated germanium surfaces is necessary in order to minimise molecule-surface interactions, increase surface-mobility and thereby facilitate self-assembly of the adsorbed molecules into the desired ordered nanostructures.

6 Halogen adsorption and passivation on germanium(001)

As shown in the previous Chapter 5, the Ge(001) surface interacts strongly with organic adsorbates. Therefore, to facilitate molecular self-assembly, the surface has to be passivated to minimise interactions with the adsorbates. There are several ways to passivate Ge(001) either with wet-chemical methods or “dry” methods in UHV. The most common passivation method in UHV uses atomic hydrogen, as outlined in section 3.1.2. However, the passivation of Ge(001) with halogens has become more and more popular, mostly due to their higher etching efficiency of the native oxide when using acids like HBr and HCl, but also due to their increased stability and the possibility of using them as precursors for further organic functionalisation of the surface [24].

This chapter explores methods to halogen-passivate Ge(001) in a UHV environment, as opposed to the well-explored wet-chemical procedures, and characterises the differently functionalised surfaces with both PES and STM. Furthermore, the adsorption of single halogen atoms on the dimers of the Ge(001)-c(4×2) reconstructed surface is investigated with STM and supporting DFT calculations, in an effort to better understand the bonding and etching mechanisms.

6.1 Literature Review

One of the main disadvantages of germanium when compared to silicon is the difficulty in growing a stable insulating oxide with dielectric properties that are comparable to SiO₂. The passivation of germanium surfaces with halogens has therefore attracted attention in research as a precursor to growing dielectric materials on top [24, 156]. Acid or wet-chemical treatment of the surfaces has proven to be one of the simplest and most promising approaches in the pursuit of that goal, since it also removes germanium’s native oxide. HF treatment of both Ge(001) and Ge(111) has been found to lead to hydrogen-terminated surfaces [157], which seems surprising considering the bond strengths as listed in Table 6.1 and fluorine’s well-known highly reactive nature. The etching

	kJ/mol
Ge-F	470
Ge-Cl	349
Ge-Br	276
Ge-I	212
Ge-H	288

Table 6.1 Germanium-halogen (and -hydrogen) bond strengths [155].

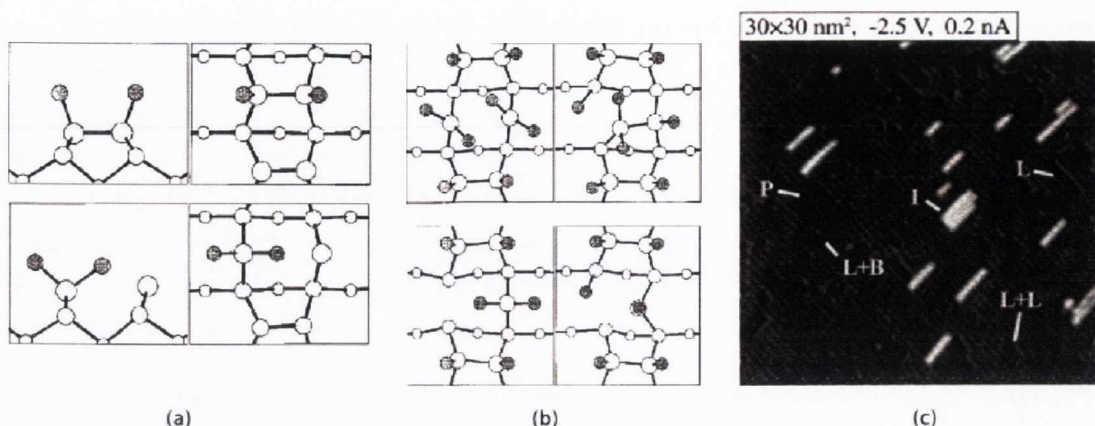


Figure 6.1 Adsorption and etching mechanism of chlorine on Si(001). (a) Monohalide-dihalide isomerisation process for low coverages, adapted from [164]. Upper panels: adsorption site of chlorine on Si(001), lower panels: formation of SiCl_2 . (b) Upper panels: possible SiCl_2 formation mechanisms at higher coverages, lower panels: after desorption of the respective SiCl_2 complexes, adapted from [164]. (c) Filled state STM image after annealing Si(001):Cl at 850 K, with one-atom-layer deep etch pits (P), Si regrowth islands (I), linear pits (L) one row wide, linear pits with one vacancy on the adjacent row (L + B), and pits that are two rows wide (L + L), taken from [165].

mechanism must therefore be kinetically rather than thermodynamically controlled [158]. In contact with the ambient atmosphere, the hydrogen-terminated Ge surfaces begin to reoxidise after only 10 min [159]. Wet-chemical cleaning and passivation using HCl and HBr has been found to be more effective, yielding oxide-free Ge substrates and with ambient stabilities against reoxidation of 10 min and 6 h, respectively [160–162]. Similar to the HF etching of germanium, reoxidation is governed by kinetics and cannot be predicted from the relative bond strengths. Additionally, Ardalan *et al.* found that the brominated germanium surfaces are less hydrophilic than the chlorinated surfaces, and therefore more prone to the adsorption of organics [74]. There is no literature on the wet-chemical iodine-passivation of germanium surfaces with HI. However, Göthelid *et al.* investigated both Ge(001):I [163] and Ge(111):I [70] after iodine deposition from an electrochemical cell after the principle described in section 4.2. No value for the ambient stability has been determined.

While the ambient stability of a passivated surface is governed by kinetics, the desorption process is both thermodynamically and kinetically controlled. The temperature at which desorption of the passivation agent begins, increases with bond strength as expected, but the overall desorption rate can vary widely due to mechanisms like pairing of the desorbing atoms, as suggested for hydrogen on Ge(001) [78]. Cohen *et al.* also proposed that pairing is the underlying process for the desorption of HCl and HBr from Ge(001), following near-first-order kinetics in the range 570–590 K [166]. In that same temperature programmed desorption study, the group found the additional desorption products GeCl_2 and GeBr_2 ,

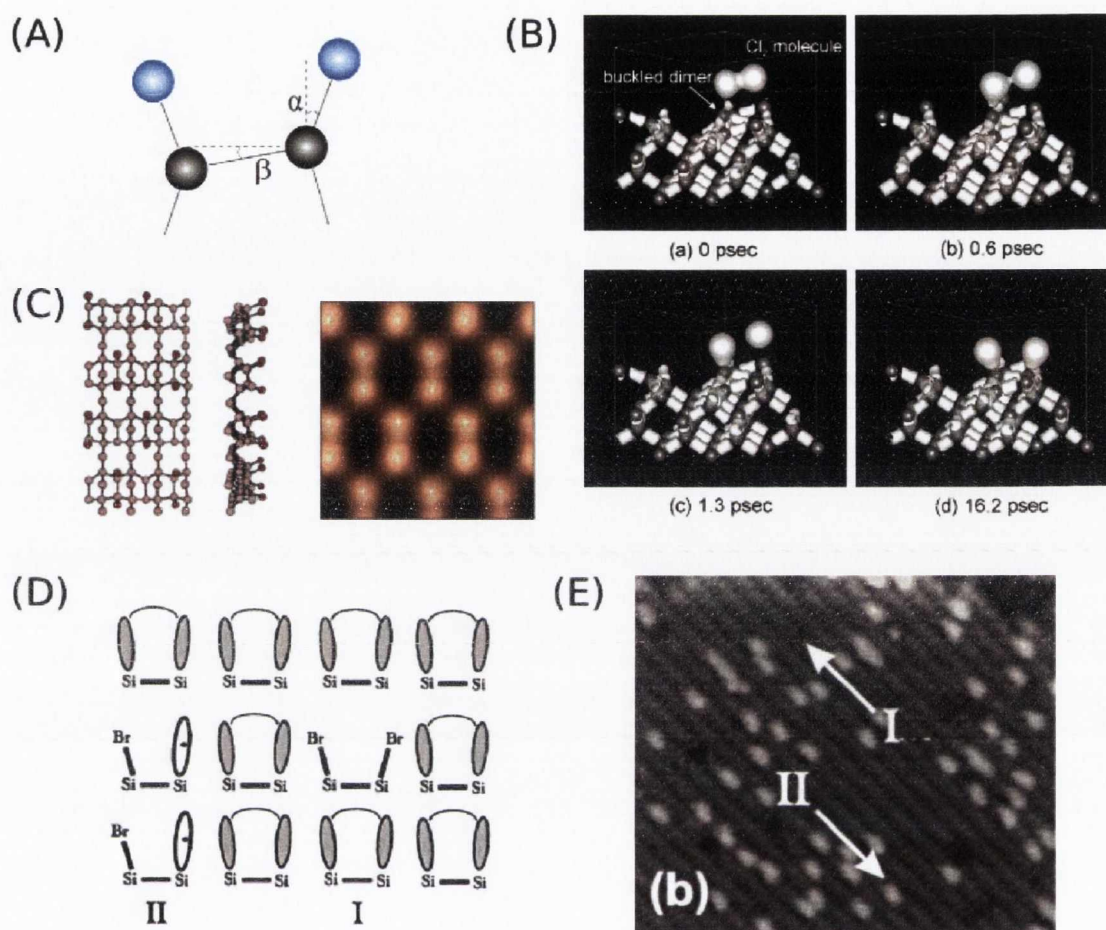


Figure 6.2 Adsorption of halogens on group IV semiconductors. (A) Model of Ge/Si dimer with off-normal, asymmetrically adsorbed halogen atoms. (B) Model of dissociative adsorption mechanism by Okada *et al.* [167]. (C) DFT calculation and simulated STM image of the $c(4 \times 2)$ structure of 0.5 ML of bromine on Ge(001) by Mikolajczyk *et al.* [168]. (D) Model of the two adsorption types of bromine on Si(001) and (E) empty state STM image (+1 V) of a sub-ML coverage by Herrmann *et al.* [169].

following second-order kinetics near 675 K and 710 K, respectively [166]. Göthelid *et al.* found the equivalent GeI_2 forming on the Ge(001) surface at temperatures of around 470 K with PES, before almost all the iodine had desorbed at 620 K [163].

The dihalide species was first suggested to be a crucial part in the etching process of group IV semiconductor surfaces by Jackman *et al.* for chlorine on Si(001) [170]. Wijs *et al.* performed a first-principles theoretical study on the etching mechanism in this system, i.e. the formation and desorption of SiCl_2 , and found two different regimes for low and higher coverages of chlorine on Si(001) [164]. Initially, the chlorine atoms saturate the surface dimer dangling bonds, analogous to hydrogen on Ge(001) as shown in Fig. 3.4. For low coverages, they found the monochlorine-dichloride isomerisation process depicted in Fig.

6.1a to be most energetically favourable. For high coverages, two possible mechanisms for the formation of SiCl_2 were identified, both involving the adsorption of additional Cl_2 as can be seen in Fig. 6.1b. The results of this study are in agreement with previous experiments on $\text{Cl}/\text{Si}(001)$ by Chander *et al.*, who used STM to identify several etching pathways like linear and branched growth along the surface dimer rows [165]. Fig. 6.1c shows one of their STM images with all common etching features marked. The thus identified etching mechanism via dihalides can be generalised to halogens on group IV semiconductors, since the same or very similar etching behaviour has also been observed for bromine [171] and iodine [172] on $\text{Si}(001)$, as well as for chlorine [173] and iodine [163] on $\text{Ge}(001)$.

Not only does the etching mechanism show very similar characteristics for halogens on group IV semiconductors, but also their adsorption sites and behaviour at sub-monolayer coverages. The most widely studied system is the already mentioned chlorine on $\text{Si}(001)$. There are a number of experimental studies confirming the main adsorption site shown in Fig. 6.1a and emphasising its off-normal character, the determined bond angles α as depicted in Fig. 6.2a ranging from 19.3° [174] to $\sim 25^\circ$ [175,176]. Okada *et al.* performed STM experiments and first principle molecular dynamics calculations on both Cl_2 and F_2 on $\text{Si}(001)$, which show that the adsorption process is dissociative as shown in Fig. 6.2b, and, remarkably, with no energy barrier [167]. The dissociative nature of the adsorption of molecular halogen results in two different types of adsorption site, schematically shown and labelled I and II in Fig. 6.2d. The empty state STM image in Fig. 6.2e shows that the different types appear as either a dark dimer for type I or as a bright oblong protrusion for type II, caused by the unpaired dangling bonds left by the adsorption of only one bromine atom on the dimer. While both types can be observed for chlorine [77] as well as bromine [169] and iodine [172] on $\text{Si}(001)$, type I with both halogen atoms adsorbed on the same dimer has been found to be energetically most favourable [167], despite higher repulsive interactions between the larger halogen atoms bromine [169] and iodine in that configuration. The presence of a steric hindrance between adsorbates becomes clearer at medium coverages, where both bromine [169] and iodine [172] adsorb in a $c(4\times 2)$ configuration as shown in Fig. 6.2c, while this behaviour is not observed for the smaller chlorine atoms.

There is only one experimental study on the adsorption of halogens on the $\text{Ge}(001)$ surface by Göthelid *et al.*, who, as previously mentioned, studied high coverages of iodine with STM and PES using synchrotron radiation [163]. The general adsorption behaviour was found to be analogous to halogens on $\text{Si}(001)$ as described in the previous paragraph. PES revealed GeI as the dominant species, with small amounts of GeI_2 . However, unlike the other halogens, iodine seems to preserve the asymmetric character of the germanium dimers, meaning the angle β in Fig. 6.2 is not zero. Göthelid *et al.* attribute this to the “size-argument” rather than charge transfer which causes the dimer tilt on the

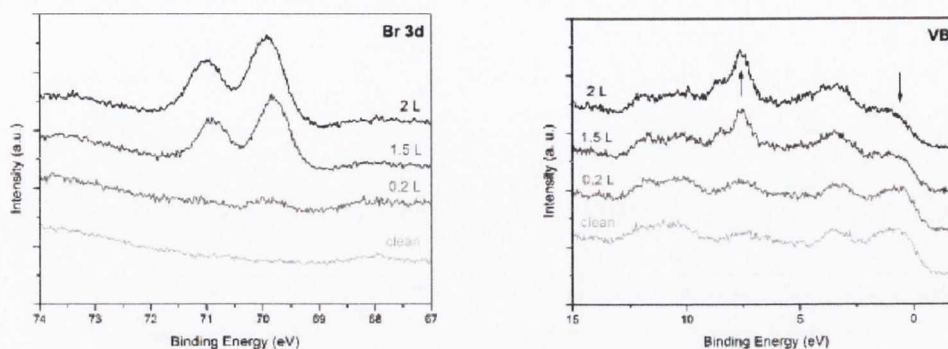


Figure 6.3 Br 3d core-level spectra (left) and valence band spectra (right) of several coverages of bromine on clean Ge(001), taken with incident photon energies of 110 eV and 60 eV, respectively.

clean Ge(001) surface, and therefore assume that the same applies to the adsorption of iodine on Si(001), although not discussed by Rioux *et al.* in [172]. The asymmetric character of the GeI-GeI dimer bond is confirmed in a later DFT study of the same system by Stankiewicz [177], although still with a much smaller dimer buckling angle than for the clean surface. Mikolajczyk and Stankiewicz also performed a DFT study on several coverages of bromine on Ge(001) [168], once again confirming the previously discussed general adsorption behaviour of halogens on group IV semiconductors.

6.2 Bromine on Ge(001)

The adsorption of bromine on Ge(001) has been investigated using both the STM in CRANN and PES at the SGM1 beamline at ASTRID. On both systems, the bromine was deposited on clean Ge(001) in UHV from a homebuilt electrochemical cell as described in section 4.2 and further discussed in 6.5. This method facilitated the deposition of very low coverages as well as a full passivating layer. However, the low coverages do not yield enough photoelectron intensity to investigate with PES and have only been investigated with the STM.

6.2.1 Passivation

Firstly, clean Ge(001) was exposed to a sequence of dosages of bromine and analysed with PES to find the saturation coverage for full passivation. The most commonly used parameter to gauge exposures from an electrochemical cell is the ion current between the electrodes. However, these currents can vary widely depending on the geometry of the cell and the exposure of the surface additionally depends on the geometry of the chamber. In this study, exposures are given in units of Langmuir, defined in section 4.1. In lieu of

the technically correct partial bromine pressure, the chamber pressure has been used to determine the exposure; the bromine pressure during deposition was in the order of 10^{-9} mbar whereas the chamber base pressure was 10^{-10} mbar and therefore negligible.

Fig. 6.3a shows the Br 3d core-level region before and after several subsequent bromine dosages, all recorded with a photon energy of 110 eV. At a low exposure of only 0.2 L, almost no bromine can be detected. At 1.5 L the Br 3d core-level is clearly distinguishable, yet it gains another 10% in intensity after exposure to another 0.5 L. Additional exposure does not change the core-level any further, which suggests that the surface is fully passivated after being exposed to a total of 2 L of bromine. This also means that the sticking coefficient of bromine on clean Ge(001) lies in the order of 0.5. The Br 3d core-level has a binding energy of 69.8 eV. Ardalan *et al.* report a binding energy of 68.8 eV for the Br 3d core-level of bromine-passivated Ge(001), using HBr [74]. The discrepancy of ~ 1 eV with respect to the value found in this experiment could be explained with either the different preparation methods resulting in different surface reconstructions of the adsorbate or with instrumental effects like calibration inaccuracies.

The valence band spectra for the same subsequent bromine dosages are shown in Fig. 6.3b, taken with an incident photon energy of 60 eV. The germanium surface state close to the valence band maximum reduces with increasing coverage of the passivation agent, as also reported for the hydrogen-passivated Ge(001) surface by Holland [27]. Additionally, a doublet peak at 7.5 eV arises at higher bromine coverages, and can be assigned Br 3d core-level electrons excited by second order light from the monochromator with a photon energy of 120 eV.

The Ge 3d core-level spectrum of the bromine-passivated surface was taken at a photon energy of 60 eV and is shown in Fig 6.4. The main components of the fit are the bulk at 29.15 eV and a shoulder shifted by 0.47 eV to higher binding energy. This component has been previously reported for bromine-passivated germanium by Schnell *et al.* [178] and Ardalan *et al.* [74] and has been attributed to a monobromide species (GeBr). Two additional smaller components arose on both the high and low binding energy side of the peak. The first one is shifted by +0.73 eV with respect to the

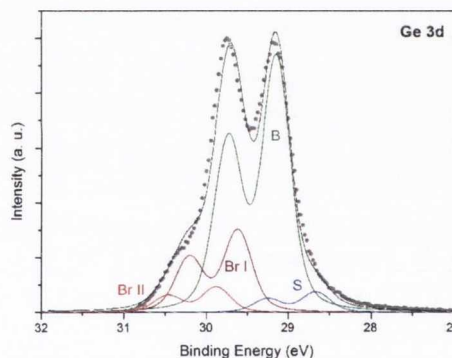


Figure 6.4 Ge 3d core-level spectrum after deposition of 2 L of bromine. B: bulk component (29.15 eV), Br I: monobromide component (+0.47 eV, 0.32 of bulk intensity), Br II: dibromide component (+0.73 eV, 0.10 of bulk intensity), S: surface component (-0.49 eV, 0.08 of bulk intensity). All components fitted with a GW of 0.32 eV, LW of 0.15 eV, spin-orbit splitting of 0.59 eV and a branching ratio of 0.67.

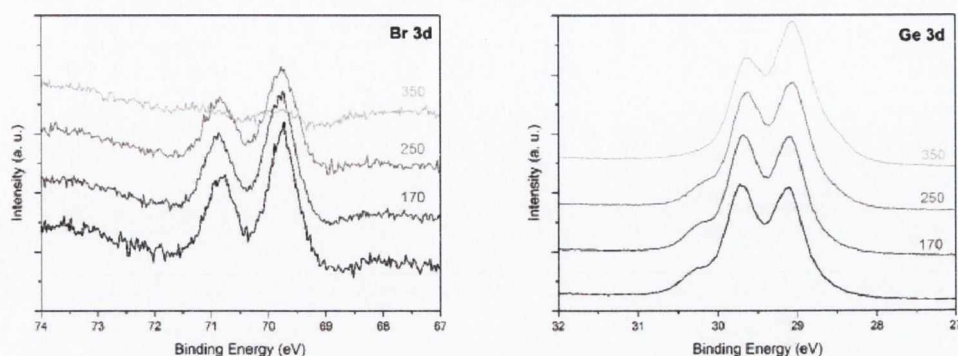


Figure 6.5 Br 3d (left) and Ge 3d core-level spectra (right) of several annealing stages (values in °C) of bromine on clean Ge(001).

bulk peak and is comparable to similar additional high binding energy components found by Ardalan *et al.* [74] for bromine and by Göthelid *et al.* [163] for iodine on Ge(001). They have been interpreted to originate from a dihalide species, in this case GeBr_2 . The relative intensities of the monobromide and dibromide components are 0.32 and 0.10 of the bulk component, similar to the values found for monoiodide and diiodide by Göthelid *et al.* but very different from the much smaller values reported by Ardalan *et al.*. However, the latter study has been conducted using a home XPS system with with much lower resolution and surface sensitivity and additionally, as mentioned before, on a wet-chemically prepared surface. The component shifted -0.49 eV from the bulk most likely results from unsaturated dangling bonds on the surface, disputing the previously found saturation coverage of 2 L of bromine. It is possible that a certain number of defects in the passivation is unavoidable, but the relatively large contribution of the surface component to the overall spectrum is still surprising. However, the insufficient statistics for the Ge 3d core-level spectrum made a perfect fit difficult and the error range for both binding energy and relative intensity values of the smaller components is estimated to be much larger than usual. Yet the observed shift of the bulk component of 0.2 eV to higher binding energy when compared to the clean surface value (as listed in Table 5.1) is in very good agreement with the shift reported by Göthelid *et al.* for Ge(001):I and has been attributed to downward bandbending due to the adsorbate-induced change of the surface structure.

Fig. 6.5 shows both the Ge 3d and Br 3d core level spectra after several different annealing stages of the bromine-passivated Ge(001) surface, with a duration of 40 min each. After annealing at 170°C , no change can be observed in either core-level spectrum. A slight decrease of the Br 3d line after annealing at 250°C is accompanied with a decrease of the high energy shoulder of the Ge 3d spectrum, identified with the Ge-Br bonds in the previous paragraph, and with an increase of the low binding energy shoulder of the

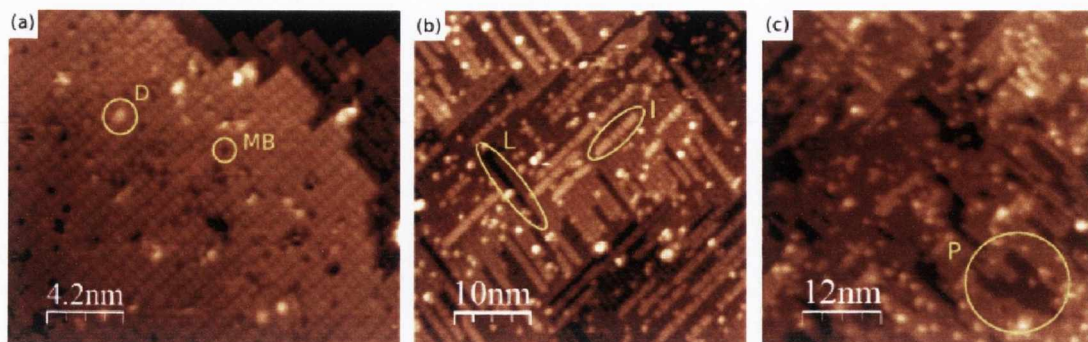


Figure 6.6 Filled state STM images of the bromine-passivated Ge(001) surface before (a) and after annealing at 270°C (b) and 350°C (c). Imaging parameters: (a) -2.1 V, 0.27 nA; (b) -1.9 V, 0.24 nA; (c) -1.6 V, 0.17 nA. Labels are explained in the text.

peak, indicative of the return of surface states of the clean surface. An increase in the dihalide species as found for iodine by Göthelid *et al.* after annealing at 200°C [163] could be neither confirmed nor disputed due to the aforementioned insufficient statistics of the Ge 3d core-level spectra taken in this experiment. After annealing at 350°C, almost no bromine is detectable on the surface, in agreement with a Ge 3d peak which has returned to its “clean” configuration.

STM

A filled state STM image of a bromine-passivated Ge(001) surface can be seen in Fig. 6.6a. It shows that the 2×1 reconstruction of the surface is preserved and both of the germanium dimer’s dangling bonds are saturated with one bromine atom and thereby lose their tilt, as predicted in the DFT calculations by Mikolajczyk and Stankiewicz [168] and observed in an STM study of bromine on Si(001) by Herrmann and Boland [169]. Micolajczyk’s DFT calculations and STM simulations predict that the bromine atoms appear brighter in the STM than the surrounding germanium surface atoms, which leads to the interpretation of the quite frequently found dark features marked “MB” in Fig. 6.6a as missing bromine atoms, i.e. unsaturated dangling bonds. This is notably different from Herrmann’s results for bromine on Si(001) and STM images of the hydrogen-passivated Ge(001) surface, where defects appear very bright as discussed and shown in section 3.1.2. Following the latter examples rather than the DFT calculations with the interpretation of bright and dark features, the dark holes would have to be assigned to missing i.e. etched germanium dimer atoms, which seems unlikely to occur as frequent as it is observed with the surface held at room temperature. The average defect density for the bromine-passivated surfaces in this experiment has been found to be $12 \pm 3\%$, which is slightly better than the best reported value for the defect density of hydrogen-passivated Ge(001) of 15% [79]. Considering their size and frequency, the less defined bright features marked “D” are possibly related to

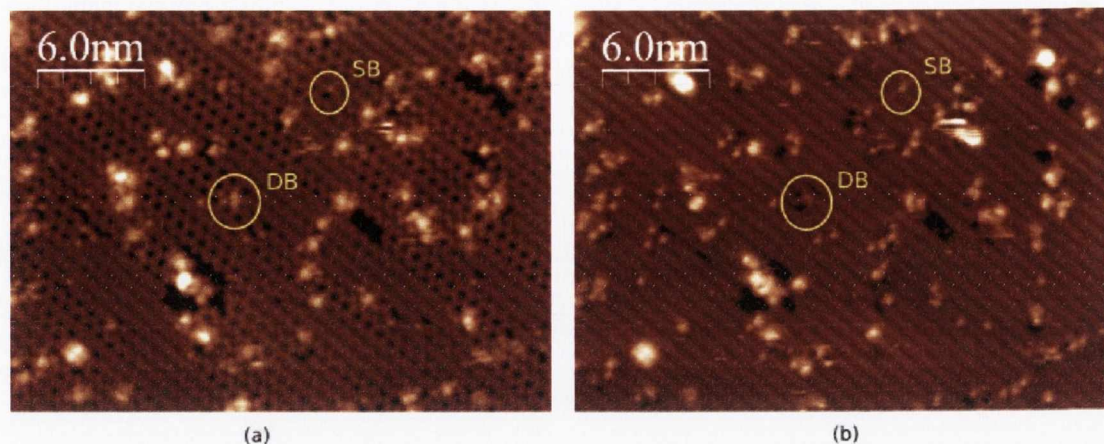


Figure 6.7 Filled (a) and empty state (b) STM images of the same area of a Ge(001) surface after deposition of a low coverage of bromine. Taken at ± 2 V, 0.12 nA, labels explained in text.

the GeBr_2 species observed in the Ge 3d core-level with PES. Empty state images of the bromine-passivation show the same features as the filled state images but are not as well resolved and therefore not shown.

After annealing the surface at 270°C for 40 min, the surface etching as described for halogens on Si(001) and Ge(001) in the literature (see section 6.1) becomes clearly visible in the STM images, as shown in Fig. 6.6b. The etching seems to occur mainly in linear rows (labelled “L”), similar to what has been observed for iodine on Ge(001) [163]. As discussed in section 6.1, the etching mechanism is believed to be based on the breaking of dimer bonds and the facilitation of GeBr_2 formation, which then desorbs from the surface. This leaves the neighbouring dimers in the row more open for GeBr_2 formation, resulting in the observed linear growth of the etch pits. Some islands of germanium regrowth, marked “I” as the silicon regrowth in Fig. 6.1c, are also observed. The literature does not offer an explanation for the growth mechanism of these islands and none of the measurements presented here offer sufficient information to speculate on their origin. After further annealing at 350°C , Fig. 6.6c shows that the etching branches out from the linear rows to form pits (labelled “P”) at higher temperatures. This suggests that branched growth of the etch pits requires more energy than linear growth for bromine on Ge(001), which is in implicit agreement with DFT calculations of the etching mechanism of chlorine on Si(001) by Wijs *et al.* [164], who state that the formation of the dihalide etch product occurs preferentially at sites where more space is available, i.e. along a dimer row once etching has started with a missing dimer. The energy difference is expected to be higher for larger halogens, meaning that branched growth and etch pits can be expected at lower temperatures for smaller halogens.

6.2.2 Lower coverages

Low coverages of bromine deposited in clean Ge(001) were investigated with the STM. Exact coverages were difficult to determine since a considerable amount of other contaminants are visible in the STM as well and the deposition times were in the order of a few seconds, resulting in very small Langmuir values with large error ranges. Fig. 6.7 shows both filled and empty state STM images of the same area of a Ge(001) surface after bromine deposition. Two features are found repeatedly throughout the entire STM dataset and are therefore likely to be associated with bromine.

The most frequent feature is a small bright spot roughly the size of the germanium dimer atoms, which always pins the two adjacent dimer atoms in the “up”-position. The bright spot also appears bright in the empty state images, whereas the adjacent dimer orientation is only discernible from the filled state images. One such feature is marked “SB” in Fig. 6.7a and b. As previously mentioned, Mikolajczyk and Stankiewicz [168] predicted the bromine adsorbates on Ge(001) to appear brighter than the surrounding germanium surface atoms, which suggests that the bright spots are single adsorbed bromine atoms. Since halogens have

previously been found to always adsorb in pairs after the dissociation of the molecule [167, 169], this raises the question whether the electrochemical cell produces molecular bromine as claimed by the original paper by Spencer *et al.* [101] and others after that, or single bromine atoms or ions or both. This issue will be further discussed in section 6.5.

The single bromine (SB) features become less discernible from the surrounding germanium atoms when imaged at lower filled state biases than in Fig. 6.7a. The contrast changes more clearly in the empty state images, where the SB features almost disappear at lower biases, as can be seen in the close-up images of one such single bromine atom adsorbed on the Ge(001)-c(4×2) surface, imaged at a bias of +1 V in Fig. 6.8b. Preliminary DFT calculations of the system, performed by Radny *et al.* [179]¹, result in the

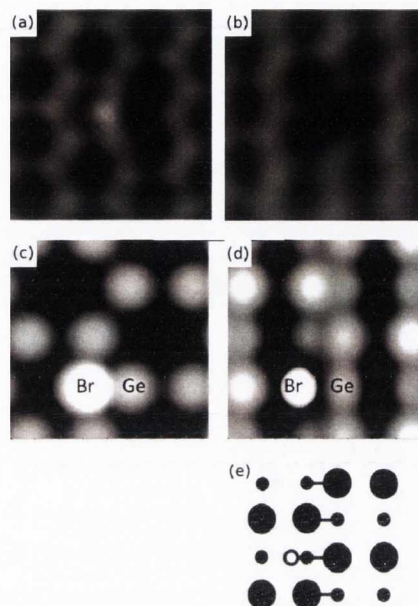


Figure 6.8 Comparison between experimental (a and b) and simulated (c and d) STM data of a single adsorbed bromine on the Ge(001)-c(4×2) surface in the configuration depicted in the model in (e). (a) and (c) are for a bias of -1 V, (b) and (d) for +1 V.

¹Spin-polarized DFT calculations have been performed using projector augmented wave (PAW) potentials and the generalized gradient approximation (GGA) for exchange and correlation with a calculated lattice constant of 5.77 Å. A single halogen atom was adsorbed on a dimer of the Ge(001)-c(4×2) surface

STM image simulations in Fig. 6.8c and d when assuming that the bromine atom bonds to a down germanium dimer atom in the $c(4\times 2)$ reconstruction as indicated by the model in Fig. 6.8e. This configuration has been found to be the most energetically favourable if a sufficiently large germanium slab is used for the calculation. When compared to the experimental data in Fig. 6.8a and b, it appears that the position of the adsorbed bromine atom between two up-dimer atoms is correct. However, the experimental images show no STM contrast for the other side of the dimer with the adsorbed bromine atom, which contradicts the calculated configuration in that respect.

The second feature which can be found consistently throughout the STM images is marked with “DB” in Fig. 6.7a and b. It is characterised by a comparably large bright spot situated between dimer rows in the filled state images and by two spots orientated diagonally across two dimer rows in the empty state images. Compared to the SB feature it appears fuzzy and not as well resolved. Additionally, the DB features are often found in close proximity to SB features, changing the overall appearance and making it more difficult to identify them. Lower bias images of two isolated DB features are shown in Fig. 6.9, resolving them a little better and revealing a more oval or even two-spot shape of the bright contrast in the filled state image. The two-spot shape of the feature and the PES results discussed in the previous section suggest GeBr_2 as a possible origin of this feature. This can also be supported by its position between dimer rows or off to the side of one of them. All previous studies on halogen adsorption on group IV semiconductors, most significantly Herrmann *et al.* on bromine on Si(001) [169], suggest that the adsorption on neighbouring dimers or one halogen atom on each dimer atom are the preferred configurations for more than one halogen atom in close proximity, and none of them report a feature which is similar to DB. As mentioned before, PES does not yield enough intensity for low coverages to clarify this issue and STS could not be performed with sufficient accuracy. In the end, it cannot be completely ruled out that the DB feature originates from

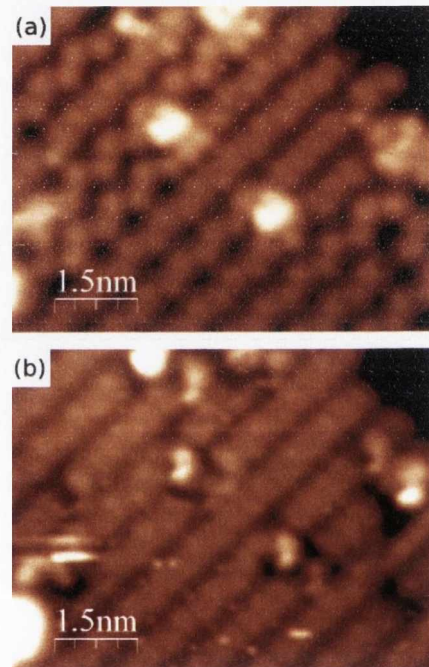


Figure 6.9 Filled (a) and empty state (b) STM images of two DB features, taken at ± 1.5 V and 0.13 nA.

represented by an asymmetric slab containing 10 Ge layers within a 4×4 surface unit cell, and terminated on the bottom surface by hydrogens. The notation $n\text{Lvm}$ is used to indicate an n layer slab in which the top m layers are allowed to move. The default energy cut-offs for the PAW potentials defined in the VASP code were used for all atoms. Simulated STM images of the surface have been obtained within the Tersoff-Hamann approximation.

an unidentified but common contaminant or by-product of the electrochemical cell.

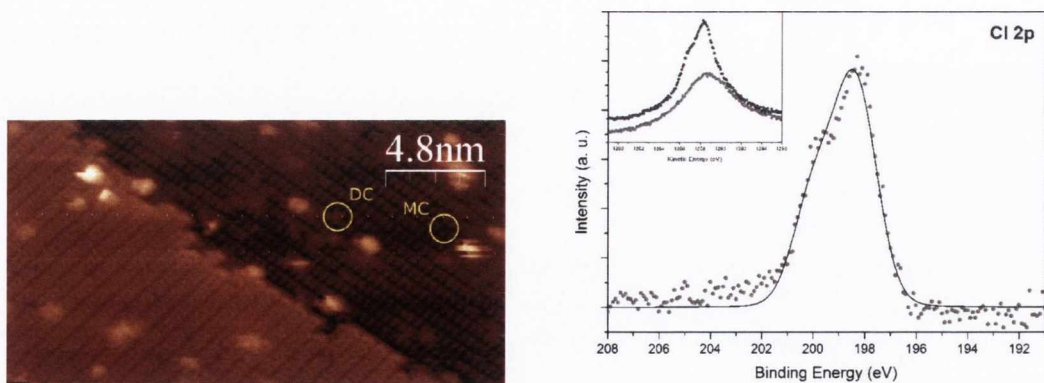
Except for a TPP molecule in the lower left corner (see section 5.3.2), all other features shown in Fig. 6.7 do not occur repeatedly and can therefore most likely be assigned to contaminants, which is supported by a slight increase in the carbon 1s line in PES after bromine deposition from the electrochemical cell.

6.3 Chlorine on Ge(001)

The chlorine-passivation of Ge(001) has been investigated with STM in CRANN, DCU and IM2NP, and with the Omicron XPS system in DCU. No systematic synchrotron PES study of adsorption and desorption of the chlorine layer as presented for bromine in section 6.2 has been performed. However, as for bromine, the adsorption behaviour of low coverages of chlorine has been studied with the STM in CRANN. On all systems, chlorine has been deposited onto the clean Ge(001) surface at room temperature from an electrochemical halogen cell.

6.3.1 Passivation

The saturation coverage of chlorine on Ge(001) is reached after the exposure to 1 L of chlorine, as has been determined with STM. This means its sticking coefficient is roughly unity and therefore higher than that of bromine (see section 6.2.1). A filled state STM image of a chlorine-passivated Ge(001) surface, taken at IM2NP, is shown in Fig. 6.10a. It is very similar to the bromine-passivation in that each dangling bond is saturated with



(a) Filled state STM image, taken at -1.4 V and 0.25 nA. Explanation of labels in text.

(b) Cl 2p core-level spectrum, taken with Al K_{α} X-rays. Fitting parameters: Binding energy 198.4 eV, spin-orbit splitting 1.6 eV [180], branching ratio 0.5 (see equation 2.16), Gaussian width 1.85 eV, Lorentzian width 0.15 eV. Inset: Raw data before (light grey) and after (dark grey) chlorine-passivation.

Figure 6.10 STM and PES of the chlorine-passivated Ge(001) surface.

a single chlorine atom, resulting in symmetric dimers. Analogous to bromine, the dark features marked “MC” are interpreted as missing chlorine atoms. However, the average defect density of the chlorine passivation has been determined to be $5\pm 2\%$, which is much better than for both bromine and hydrogen as passivation agents. Empty state STM images have been difficult to acquire in good quality since the chlorine features lose contrast with respect to the surrounding surface as will be discussed in the following paragraph and in section 6.3.2. The image in Fig. 6.10 also shows features similar to “DB” in Fig. 6.6a, marked “DC” in this case. They appear slightly brighter than the chlorine atoms, are of somewhat irregular shape and sit between two dimer rows. All other features in Fig. 6.10a can most likely be assigned to contaminants since the chamber pressure at IM2NP was comparatively high ($> 10^{-9}$ mbar). Despite the difficulties in getting an “undisturbed” image of a large surface area at this pressure, the resolution of the single chlorine atoms is still the best of all three STM systems used for the experiments presented in this thesis.

It was possible to obtain reproducible STS data on both the clean and the chlorine-passivated surface since these surfaces are uniform over a large area and the exact tip position thus does not need to be known. The dI/dV spectra in the voltage range from -2 to 2 V are shown in Fig. 6.11 (recorded with the STM in DCU). They were taken on three separate (50×50) nm frames of each surface, and averaged over a total of 165 curves for the clean surface and 98 curves for the chlorine-passivated surface. The most significant difference between the two surfaces is a significant reduction of the empty states for the chlorine-passivated surface, which is in agreement with the difficulty in obtaining empty state STM images with sufficient contrast. The surface gap of clean Ge(001) has been determined to be 0.80 ± 0.14 eV, which is in good agreement with the 0.75 eV measured by Jordan and Shvets [181]. When chlorine-passivated, the surface gap increases to 1.36 ± 0.14 eV.

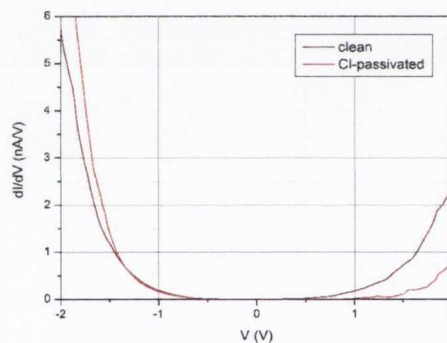


Figure 6.11 STS of clean and chlorine-passivated Ge(001).

Due to its similar appearance it is reasonable to assume that the “DC” feature has the same origin as for bromine, where it has been speculated to be a germanium-dihalide species. However, the PES for the chlorine-passivated surface has only been performed on a home XPS system and therefore lacks the resolution to identify a similar dihalide peak component in the Ge 3d core-level spectrum as for bromine. Additionally, both the Cl 2s and Cl 2p core-levels are difficult to measure with both the Al and Mg anode of the Omicron XPS system since they have the same kinetic energy as either germanium Auger

lines or plasmons, a problem which has already been identified by Ardalan *et al.* [74]. The Cl 2p doublet, sitting on a Ge 3s plasmon loss peak [39], has been recorded with Al K α X-rays (1486.6 eV) and is shown in Fig. 6.10b. The inset shows the raw spectra of the clean surface (light grey) and after chlorine passivation (dark grey), whereas the main graph displays the difference spectrum between the two. After removal of the increased scattering background on the high binding energy shoulder of the difference spectrum, the peak could be fitted reasonably well. The parameters are given in the caption of Fig. 6.10b. The binding energy of 198.4 eV is in good agreement with the 198.7 eV found by Ardalan *et al.* for a wet-chemically chlorine-passivated Ge(001) surface [74].

As mentioned before, no systematic desorption study has been conducted on the chlorine-passivation. It is however expected to be slightly more stable than bromine because of its stronger bond to germanium as listed in Table 6.1 and STM images taken after annealing the sample to 220°C show only very little etching, i.e. chlorine loss. After annealing the surface to 350°C, etching similar to the other halogens can be observed as shown in the filled state STM image in Fig. 6.12. However, the etching pathways are notably different and chlorine shows a stronger tendency towards branched growth into large etch pits than bromine. Only very few linear etching pathways and regrowth islands can be observed. This is in agreement with the previously discussed argument that smaller halogens are less spatially restricted and dihalide formation is therefore more likely to branch out across dimer rows (see section 6.2.1).

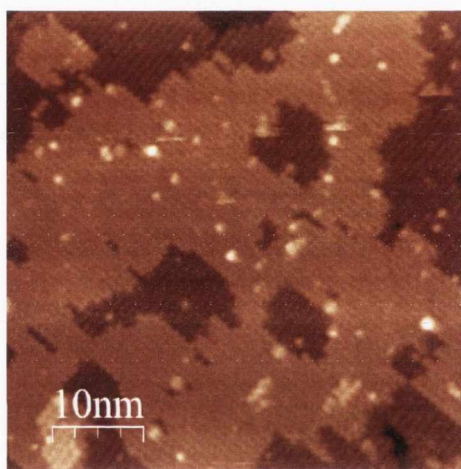


Figure 6.12 Filled state STM image of a chlorine-passivated Ge(001) surface after annealing at 350°C, taken at -1.6 V and 0.12 nA.

6.3.2 Lower coverages

Like for bromine, a low coverage of chlorine was deposited on the clean Ge(001) surface to investigate the adsorption mechanism more closely. However, a coverage as low as for bromine could not be achieved in any of the experiments, most likely due to chlorine's higher sticking coefficient (as mentioned in section 6.3.1). Fig. 6.13a and b show empty and filled state STM images of the same area of a Ge(001) surface with the lowest achieved chlorine coverage, displaying three different features that can be found repeatedly enough to assign them to chlorine. The large contaminant on the right side of the images can be used for orientation when comparing the two images.

The most frequently found feature is labelled "PC". It has also been found for chlorine

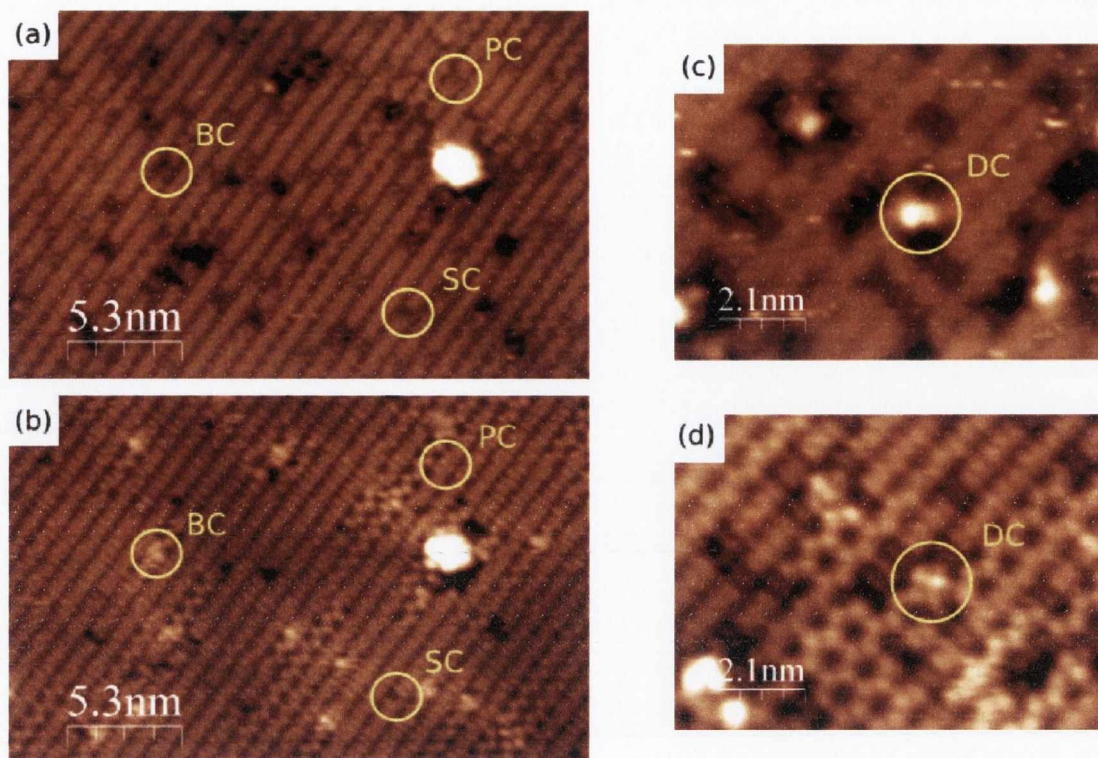


Figure 6.13 Empty (a and c) and filled state (b and d) images of a low coverage of chlorine adsorbed on the clean Ge(001) surface. Images (a) and (b) were taken at ± 1.2 V and 0.12 nA, (c) and (d) at ± 1.4 V and 0.12 nA. An explanation of the labels can be found in the text.

adsorbed on Si(001) by Boland [77] and has been assigned to two chlorine atoms each adsorbed on one of the dangling bonds of a single surface dimer. The feature is easy to identify in the empty state images, which is all Boland published, but very similar in contrast to the surrounding germanium surface dimers in the filled state images. A comparable feature could not be found for bromine in this study, which is most likely only due to the difference in coverage since bromine as well as chlorine adsorb almost exclusively in this configuration at saturation coverage.

The second most frequently found feature is labelled “SC” in Fig. 6.13a and b. It is very similar to the single adsorbed bromine feature labelled “SB” in Fig. 6.7 and is therefore interpreted as a single adsorbed chlorine atom. However, Boland does not observe this feature on Si(001). His study only reports two single adsorbed chlorine atoms on dimers next to each other, which is attributed to the dissociative nature of the adsorption for chlorine molecules. As mentioned before, the issue of molecular or atomic/ionic halogen deposition from the electrochemical halogen cells will be discussed in section 6.5. Additionally, Boland’s study shows that when a chlorine atom is adsorbed on only one dimer atom, the dangling bond of the other appears very bright in the empty state STM images

of a similar bias as shown here. As for bromine (see section 6.2.2 and [169]), this is very different from what can be observed in the images in this experiment and could therefore indicate a major difference between the Si(001) and Ge(001) surfaces.

The third feature in Fig. 6.13a and b is labelled “BC” and consists of two lobes which appear brighter than the surrounding germanium atoms in the filled state image. In the empty state images, it is characterised by a centred large spot of the same contrast as the surrounding surface but separated by dark surroundings. Although the empty state appearance is different, this feature can possibly be compared to the feature on Si(001) which Boland assigned to a bridge-bonded configuration. In this case the chlorine atom breaks the bond between the dimer atoms and adsorbs between them, leaving one dangling bond on each side. The latter could account for the bright doublet observed in the filled state images, whereas the empty state image could originate from the centrally adsorbed chlorine atom. However, Boland reports that this species is unstable and changes into one of the other two configurations due to interactions with the STM tip, whereas no fuzzy appearance of the feature or changing configurations from one image frame to the next have been observed in this study. A different interpretation of this feature is difficult to find without supporting DFT calculations or STS measurements, which as for bromine were not possible to perform with sufficient accuracy at room temperature.

Fig. 6.13c and d show an additional pair of empty and filled state STM images from a different area on the same surface, which shows another commonly found feature after the deposition of chlorine, labelled “DC”. It is very similar to the DB feature found for bromine (see Fig. 6.7 and 6.9) in that it consists of two bright spots which are oriented diagonally across a dimer row and appear especially bright in the empty state images. It is therefore most likely to be interpreted as a sign of GeCl_2 , although no definite statement can be made. An additional observation in Fig. 6.13d is that the PC feature appears much darker than in Fig. 6.13b. This difference can possibly be explained by different tip configurations, as suggested for several discrepancies in the appearance of the chlorine adsorbates in Boland’s STM study on Si(001) [77]. Since Boland only discusses empty state images, it is unknown whether this particular difference in the appearance of the PC feature is a commonly observed effect.

6.4 Iodine on Ge(001)

The adsorption mechanism of iodine on Ge(001) has been investigated on the UHV system in DCU, using both STM and XPS. Although the saturation coverage of iodine has already been investigated by Göthelid *et al.* [163], their experiment has been repeated to complete the study on halogen adsorption on Ge(001). Like both bromine and chlorine, the iodine was deposited on the clean Ge(001) surface from an electrochemical cell as described in section 4.2. In this instance, its operation has been analysed using a mass spectrometer

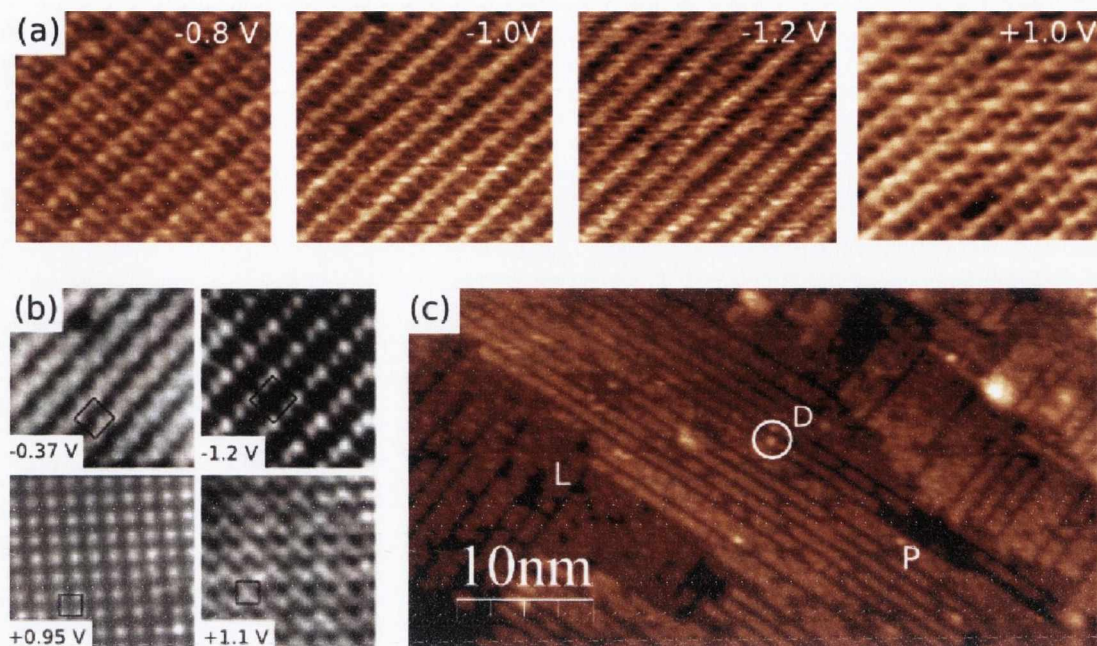


Figure 6.14 STM images of iodine-passivated Ge(001). (a) (6×6.5) nm frames of STM images taken at different biases and 0.13 nA, (b) comparable STM images by Göthelid *et al.* [163] (left column: (5.3×5.3) nm, right column: (4.3×4.3) nm), (c) filled state STM image of Ge(001):I after annealing to 320°C , taken at -1.1 V and 0.11 nA.

(section 4.3) and is further discussed in section 6.5.

Fig. 6.14a shows a set of STM images taken at different biases after exposing the clean Ge(001) surface to 1 L of iodine. The surface appears to be fully passivated after this exposure, suggesting a sticking coefficient of unity for iodine on this surface. The STM images agree very well with the previous study of iodine on Ge(001) by Göthelid *et al.* [163], whose set of images is shown in Fig. 6.14b. The most striking feature is the rows of bright contrast, especially prominent in the images in Fig. 6.14a taken at -1.0 and -1.2 V, following the direction of the germanium dimer rows. A line profile analysis shows that the distance between two rows is $\sim 8\text{\AA}$, which corresponds to the periodicity across the Ge(001) dimers [181]. As mentioned in section 6.1, both Göthelid *et al.* and a DFT study by Stankiewicz [177] suggest that while each germanium dimer atom bonds to one iodine atom like for the hydrogen-passivation described in section 3.1.2, the iodine-saturated dimers retain some of their buckled nature. While the buckling of the dimers originates in a charge transfer between up and down dimer atom on the clean surface, this mechanism is very unlikely for iodine-saturated dimers and the buckling is instead attributed to steric hindrance between the relatively large iodine atoms. Their atomic radius is 140 pm, while the Ge-Ge dimer bond length is 245 pm [66]. Another feature of the adsorbed iodine layer becomes apparent in the STM images taken at -0.8 V and $+1.0$ V in Fig. 6.14a, which show that the degree of contrast difference between the up and

down GeI dimer alternates from dimer to dimer. A similar effect can be observed in all of Göthelid's images in Fig. 6.14b. The most obvious explanation for this is that the dimer buckling angle β (as in Fig. 6.2a) alternates along the dimer rows to achieve an even more efficient iodine packing pattern. However, this hypothesis is based on the assumption that in this case the STM contrast originates from topographical and not electronic effects, which requires supporting DFT calculations to confirm or contradict.

The iodine-passivation shows only very few defects in the form of dark features in the filled state STM images, which signify missing iodine atoms according to the STM simulations by Stankiewicz [177]. The defect density could not be determined with sufficient accuracy due to the buckled nature of the dimers and the resulting difficulty in identifying the dark missing iodine features among the down dimer atoms, which are already relatively dark. No other features like the previously discussed "D"-features for bromine and chlorine could be identified in the STM images of iodine-passivated Ge(001).

This picture changes after annealing the passivated surface to 320°C, as the filled state STM image in Fig. 6.14c shows. While most of the surface still shows the 8 Å periodicity of the rows, the number of defects is significantly higher and some of the halogen-typical etching features like pits (labelled "P") and linear etching (labelled "L") can be observed. Additionally, other features like small bright protrusions very similar to the previously mentioned "D" features associated with the dihalide etching precursor for bromine and chlorine, or two to five neighbouring dimer rows without buckling can be seen. However, the STM images taken after annealing are not very well resolved, which restricts the analysis of the images. It is nonetheless reasonable to assume that the etching mechanism of iodine on Ge(001) is analogous to the other halogens.

Despite the comparatively low bond energy of the GeI bond (see Table 6.1), most of the surface still seems to be saturated with iodine after the anneal. This is possibly due to the short duration (~5 min) of the anneal, since the desorption of monoatomic passivation agents is not only temperature- but also time-dependent, as shown for iodine by Göthelid *et al.* [163] and also for hydrogen by Lee *et al.* [78]. However, iodine's large atomic radius could also prevent more efficient formation of the GeI₂ etching precursor.

A temperature programmed desorption (TPD) study using the mass spectrometer has been attempted, but did not yield any signals for both atomic (127 a.m.u.) and molecular

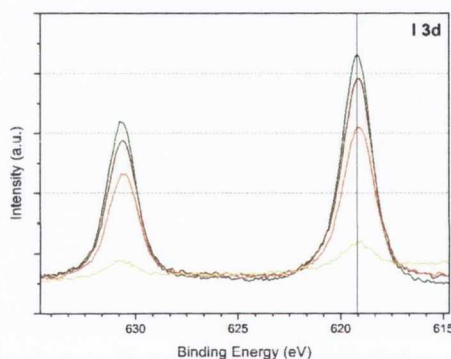


Figure 6.15 I 3d core-level spectra after different annealing stages, taken with an incident photon energy of 1486.6 eV (Al K α). Green: as deposited, brown: 200°C, orange: 320°C, yellow: 420°C.

(254 a.m.u.) iodine. This suggests that halogens desorb (and etch) as a germanium-dihalide, in this case GeI_2 , which is too high in mass to be detectable with the mass spectrometer. Instead, the desorption has been monitored in the XPS spectra of the I 3d core-level which are shown in Fig. 6.15 after annealing at different temperatures for ~ 5 min. The I $3d_{3/2}$ peak has a binding energy of 619.1 eV, with a spin-orbit splitting of 11.6 eV, which is in agreement with the literature value for most iodine compounds [39]. A slight shift of the order of 0.2 eV to lower binding energies can be observed after annealing at 320°C , but the overall resolution does not justify an interpretation of shifts, only relative intensities. The development of the latter shows that while iodine desorption is initiated at around 200°C , it accelerates significantly in the temperature range between 320°C and 420°C . Göthelid *et al.* see a significant reduction of the I 4d core level after annealing at 350°C , which narrows the window of accelerated desorption to $320\text{--}350^\circ\text{C}$.

A low coverage of approximately 5% of iodine² has also been deposited on Ge(001) and a study was attempted with the STM. However, no images of sufficient quality could be acquired due to a high noise level and frequent changes of the tip configuration. Fig. 6.16 shows a filled state STM image taken with low bias and current conditions, meaning the tip is scanning at a comparably large distance from the surface. The dimer rows of the Ge(001) surface are roughly discernible as indicated by the yellow lines, but atomic resolution is prevented by streaky features throughout the entire image. The tip had previously been cleaned and conditioned on a gold surface and imaged the same surface again without noise or contamination directly after the acquisition of Fig. 6.16. This shows that the noise and tip changes are induced by the iodine adsorbates. The iodine bonds to the germanium surface appear to be too weak to remain undisturbed by the electric field of the STM tip when imaging at room temperature and the iodine atoms are dragged along the surface by the STM tip. An analysis of the adsorption mechanism of single iodine atoms or molecules and a comparison to the respective DFT calculations by Stakiewicz [177] is therefore not possible³.

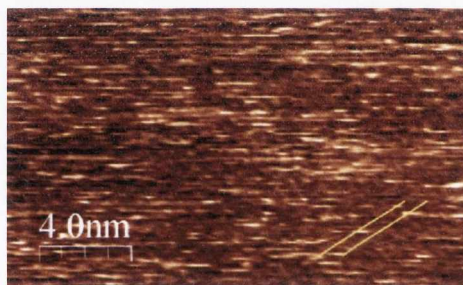


Figure 6.16 Filled state (RT-)STM image of ~ 0.05 ML of iodine on Ge(001), taken at -0.6 V, 0.06 nA.

²roughly estimated by considering the previously determined sticking coefficient of unity and thus dosing 0.05 L of iodine

³without access to a low temperature STM

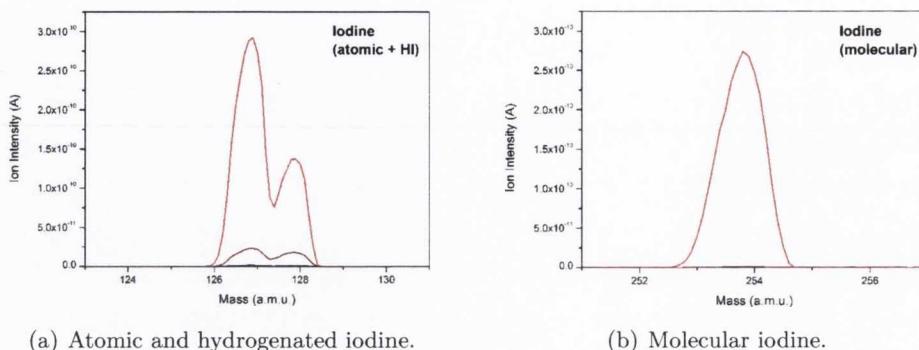


Figure 6.17 Mass spectrometry of iodine deposition in UHV from an electrochemical cell. Black: before applying bias, red: while applying a bias of 15 V, dark red: 1 min after switching off bias.

6.5 Halogen deposition from electrochemical cells

All publications on research being conducted using an electrochemical halogen source as or similar to the design described in section 4.2, including the original paper by Spencer *et al.* [101], state that the halogens emitted from the source are in their molecular form [70, 77, 100, 163, 169]. However, especially the very low coverages of bromine deposited on Ge(001) discussed in section 6.2.2 suggest that this might not be entirely correct, since isolated single bromine atoms can be observed. To investigate this issue further, the output of a halogen source has been characterised using mass spectrometry, in particular iodine because unlike chlorine and bromine, it is monoisotopic and therefore easier to interpret. Fig. 6.17 shows the recorded spectra in the atomic mass unit ranges for both atomic or ionic iodine (127 a.m.u.) and molecular iodine (I_2 , 254 a.m.u.) before (black), during (red) and after (dark red) source operation in UHV.

The signals at 127 a.m.u. and 254 a.m.u. show that when applying a bias of 15 V between the top and bottom electrodes of the electrochemical cell, both atomic and molecular iodine can be detected. An additional peak at 128 a.m.u. signifies the presence of hydrogenated iodine (HI). The operational principle of the source suggests that all halogens driven out of the ionic pellet of the respective silverhalide are negative ions, and therefore very reactive. Hydrogen is an unavoidable contaminant in UHV environments because its small atomic mass and relatively low reactivity make it difficult to pump. Since halogens are known to readily react with hydrogen, it is reasonable to assume that a fraction of the halogen ions emitted from the source combine with the ambient hydrogen. Another fraction appears to combine into the diatomic molecules characteristic for halogens, while some of the atoms remain ionic. The ratio between molecular and atomic iodine has been found to be roughly equal, whereas HI is a minority species. Additionally, the ratios between the different chemical species appear to be independent of the applied bias.

It is possible that especially the atomic/ionic or some of the hydrogenated iodine species

are artefacts of the operational principle of the mass spectrometer, which could easily cause molecular halogen bonds to break and create so-called cracking patterns. This is supported by the observation that their signals are detectable for much longer after the source is switched off (dark red in Fig. 6.17a) than the signal for molecular iodine, which disappears almost instantly (dark red in Fig. 6.17b). However, the isolated bromine and chlorine features found on the Ge(001) surface still indicate that the adsorbed halogens are not exclusively molecular.

6.6 Summary

The investigation of the adsorption of the three halogens chlorine, bromine and iodine on the clean Ge(001) surface has shown that there are many similarities and general trends among both the adsorption mechanisms of the different halogens and when comparing the results to the literature on halogens on the very similar Si(001) surface. Fluorine has not been studied due to its highly corrosive nature.

The full, passivating coverage of the surface is characterised by single halogen atoms saturating the germanium dimer dangling bonds, analogous to the hydrogen-passivation described in section 3.1.2. While the saturation of the dimers with both chlorine and bromine results in symmetric dimers, iodine's comparably large atomic radius causes the GeI-GeI dimers to retain a small degree of buckling. This observation emphasises that while the halogens are chemically equivalent, their different sizes can cause differences in their adsorption behaviour.

After annealing at elevated temperatures, STM images show that the halogen-passivated germanium surface is etched away by the adsorbates in all three cases. The etching has been proposed to originate from the formation of a germanium-dihalide species and subsequent desorption of that complex for silicon [164, 170]. High resolution SXPS of the Ge 3d core-level of the bromine-passivated surface showed evidence for the presence of GeBr₂, in agreement with similar results for iodine on Ge(001) reported by Göthelid *et al.* [163]. Some features found repeatedly in the STM images match the size and position of the proposed dihalide formation and could support this observation further. Although no highly resolved PES data is available for chlorine on Ge(001), it is reasonable to assume that it follows the same principle. While the etching mechanism is chemically equivalent for all investigated halogens, the influence of the previously mentioned "size-argument" can be noticed in the observed etching pathways. Since the formation of a dihalide species requires space, etching has been observed to mostly proceed along the dimer rows for bromine, whereas the smaller chlorine shows branched growth into comparably large etch pits at comparable temperatures, despite its stronger bond to germanium. Iodine appears to show only very little etching and desorbs at surprisingly high temperatures considering the weak Ge-I bond. This shows that the desorption process is not strictly thermodynamically

but also kinetically controlled, which makes it difficult to determine definite desorption temperatures.

Several STM studies on the adsorption of low coverages of halogens on Si(001) report dissociative adsorption of the halogen molecules and a preference for two adsorption configurations (see section 6.1), one with two halogen atoms adsorbed on each side of a single dimer and another one with two halogen atoms occupying two neighboring dimer atoms (type I and II in Fig. 6.2d). While type I has been found for both chlorine and bromine on Ge(001), neither experiment showed adsorption sites of type II. Some features with slightly brighter STM contrast than the surrounding surface have been associated with single adsorbed halogen atoms, supported by DFT calculations with reasonable agreement, which questions the generally assumed molecular nature of the halogens emitted from the electrochemical cells used for deposition in UHV. Additionally, the bright STM appearance of the halogen adsorbates is different from what has been reported for chlorine and bromine on the Si(001) surface, where the adsorbates have been interpreted to appear dark [77, 169]. However, Rioux *et al.* also interpreted the bright features found for iodine on Si(001) as the adsorbate [172], which demonstrates how difficult and complex the interpretation of seemingly obvious STM images can be. Whether the adsorbed halogen atoms appear bright or dark in comparison to the surrounding surface dimer atoms is also the subject of controversy in DFT calculations and the simulation of STM images [182], which makes this issue difficult to resolve at this time.

While the experiments presented in this chapter have made some important basic observations about the behaviour of halogens on Ge(001), it is not obvious which of the presented passivation methods is most advantageous for the subsequent deposition of organic molecules. Bromine-passivation is known to have better ambient stability and is also less hydrophilic than chlorine [74], both of which makes it the better candidate for the adsorption of organic materials. However, during the STM experiments it became apparent that bromine also readily interacts with the scanning tip, making it difficult to acquire reproducible images with good resolution. This trend continues to iodine, which has been the most difficult to image. The strong chlorine-germanium bond prevents it from being disturbed by the electric field of the STM tip, but it has been shown that a stronger bond does not necessarily equate to higher thermal stability. Additionally, the influence of organic adsorbates on the behaviour of the passivation agent is very difficult to predict and will be explored in the following chapter.

7 Dehalogenation reactions

This chapter explores the possibility of creating covalently bonded nanosized networks from organic molecular building blocks on the Ge(001) surface via a dehalogenation reaction. It has been established that the clean Ge(001) interacts strongly with organic adsorbates (Chapter 5) and therefore requires passivation (Chapter 6) to facilitate the diffusion of the adsorbed molecules, which is essential for the formation of intermolecular bonds. The suitability of several passivation methods for this purpose will be investigated as well as a few examples for dehalogenation reactions on the Au(111) surface for comparison.

The experiments have been mainly conducted on the UHV systems in CRANN and DCU, using both XPS and STM as in the previous chapters.

7.1 Literature Review

At the beginning of the 20th century, Ullmann proposed that by annealing iodobenzene in the presence of copper, two aromatic units will couple into a biphenyl by means of the elimination of copper iodide [183], as shown schematically in Fig. 7.1. The reaction of aryl halides catalysed by copper is nowadays known as the *Ullmann reaction* and is often used in organic synthesis. The reaction principle is based on the comparatively weak C-halogen bond, which can break even at room temperature, while elevated temperatures lead to the subsequent radical bonding. Since the discovery of the Ullmann reaction, other metals like Ni, Pd, Ag and Au have been found to catalyse the dehalogenation and subsequent coupling of aromatic iodides or bromides¹ [184].

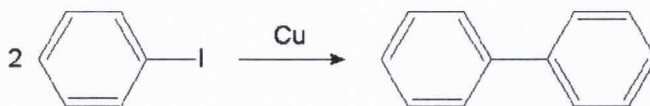


Figure 7.1 Schematic representation of the Ullmann reaction.

The Ullmann reaction was brought from solution chemistry to the copper(111) surface by McCarty and Weiss in 2004 [185]. The C-I bonds of *p*-diiodobenzene molecules were cleaved at room temperature upon adsorption on the surface and the aromatic units aligned in chain-like structures. However, no intermolecular C-C bonds were formed at room temperature and the aligned surface radicals were called “protopolymers”.

¹C-Cl and C-F bonds are stronger and cannot be cleaved as readily as C-I and C-Br.

The on-surface formation of covalent bonds between molecules via an Ullman-type reaction has first been demonstrated by Grill *et al.* in 2007 [19]. Different bromine-modified porphyrins² have been shown to form either covalently bonded dimers, chains or mesh-like structures on the Au(111) surface, depending on the functionality of the molecular “building blocks”, as shown in the STM images and respective schematics in Fig. 7.3b. Unlike on Cu(111), the C-halide bonds did not break upon contact with the Au(111) surface at room temperature and had to be thermally “activated” as shown in the concept drawing in Fig. 7.3a. The activation was achieved by either annealing of the surface after deposition of the largely intact molecules (method I) or by evaporating the molecules at elevated cell temperatures which resulted in C-Br bond cleavage inside the crucible (method II). The diffusion of the molecules on the Au(111) surface was reported to be sufficient for intermolecular bond formation at temperatures as low as 150 K. However, the growth of the covalently bonded nanostructures on the Au(111) surface has been found to be self-limiting due to the irreversible nature of the covalent bonds. Method I facilitated enhanced diffusion and therefore more efficient bond-formation, while the networks created with method II were less clustered.

In a subsequent study by the same group, two opposite bromine substituents of the previously used porphyrin molecule were replaced by more weakly bonded iodine atoms (*trans*-Br₂I₂TPP) [186]. The different activation temperatures for the iodine and bromine substituents on Au(111) (100°C and 200°C, respectively) facilitated sequenced or “hierarchial” formation of the covalent nanostructures, which resulted in larger and less defected networks. Even larger network sizes were achieved by utilising the row structure of the reconstruction of the Au(110) surface, as shown in Fig. 7.2. The polymer chains formed after activation of the iodine substituents were found to preferentially orient themselves at an angle of 55° with respect to the direction of the substrate rows. The connection points for the second activation step of bromine dissociation are therefore already in close proximity and in predefined distances, which has been suggested as the reason for the improved network quality. Furthermore, the hierarchial growth approach made it possible to grow heterogenous networks using both Br₂I₂TPP and dibromoterfluorene (DBTF).

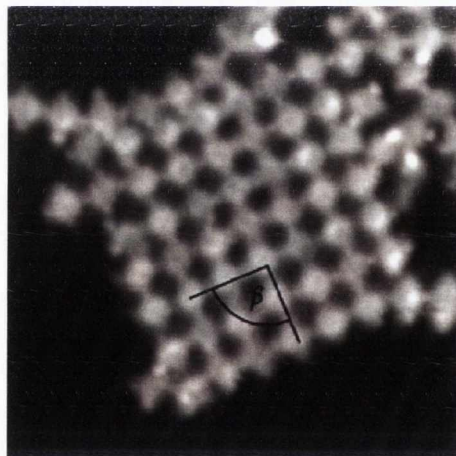


Figure 7.2 Filled state STM image ($20 \times 20 \text{ nm}^2$) of a TPP network on Au(111), formed after two subsequent activation steps as described in the text, $\beta=90^\circ$; taken from Lafferentz *et al.* [186].

²H₂TBr₄TPP as described in section 3.3.1 or similar

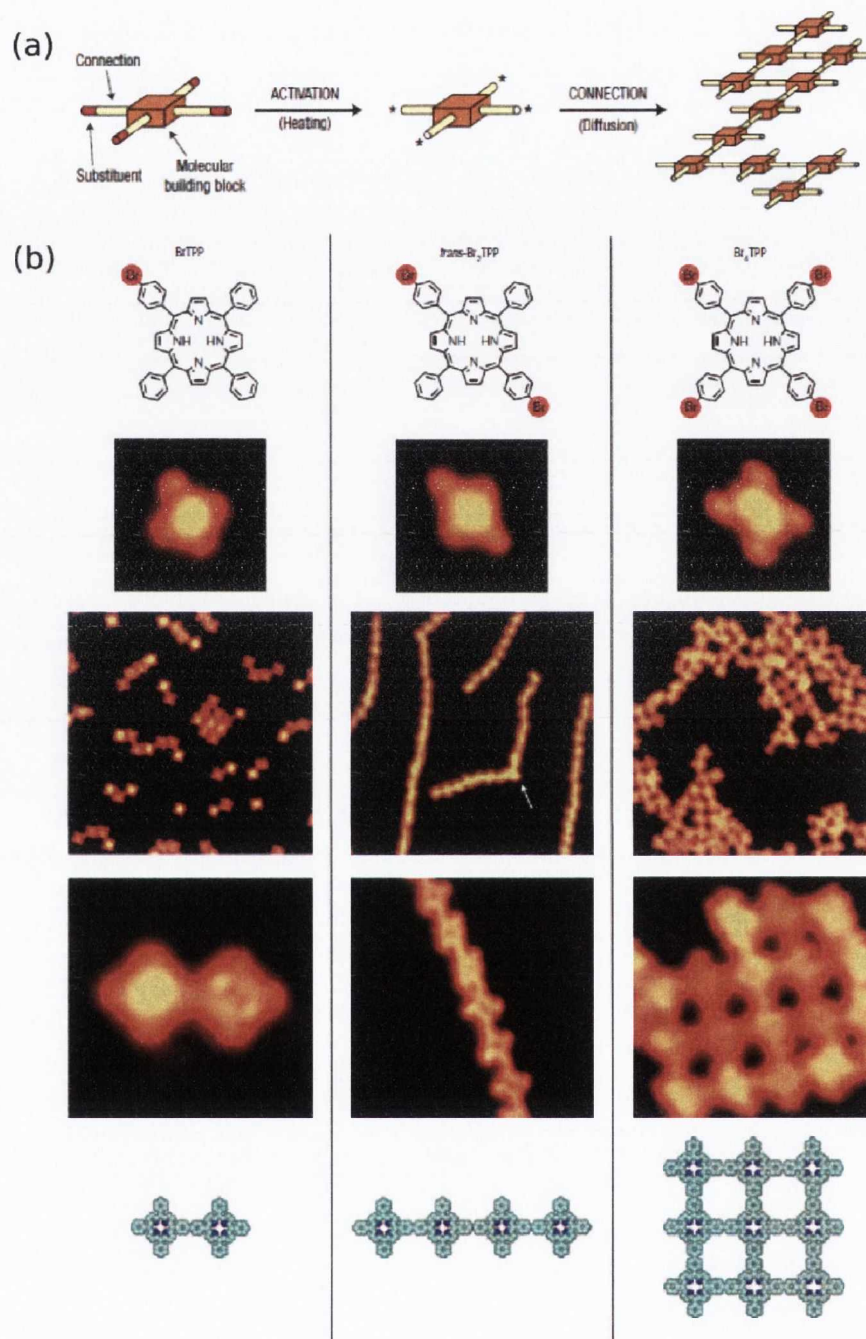


Figure 7.3 (a) Schematic of the formation of covalently bonded molecular nanostructures by activation and on-surface diffusion of molecular building blocks; (b) differently functionalised porphyrin building blocks with one (left column, prepared by method II), two (middle column, method I) and four (right column, method I) bromine substituents, with chemical structures (first row), filled state STM images of single intact molecules (second row, $3.5 \times 3.5 \text{ nm}^2$), filled state STM images after activation (third row, $30 \times 30 \text{ nm}^2$), more detailed STM images of the respective covalent structures (fourth row, $5 \times 5 \text{ nm}^2$, $10 \times 10 \text{ nm}^2$, $8.5 \times 8.5 \text{ nm}^2$) and the corresponding chemical structures. Adapted from Grill *et. al.* [19].

The Ullmann-type dehalogenation reaction has also been used for the bottom-up growth of graphene nanoribbons (GNRs) on Au(111), as reported by Cai *et al.* [187]. Fig. 7.4 shows the bromine-substituted precursor molecule (**1**) and the two activation steps. Dehalogenation and interconnection occurs after annealing the precursor to around 200°C as previously described, and then undergoes a *cyclic dehydrogenation* reaction after annealing at 400°C, which results in the straight (armchair-type) GNRs.

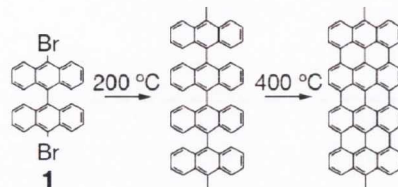


Figure 7.4 Chemical structure and reaction scheme from precursor molecule (**1**) to a straight graphene nanoribbon ($N = 7$); taken from Cai *et al.* [187].

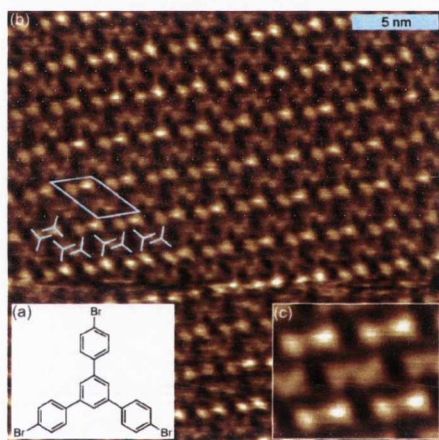


Figure 7.5 (a) Chemical structure of TBB; (b) filled state STM image of 1 ML of TBB on graphite, taken at 1.9 V and 0.08 nA, blue lines indicate unit cell ($a = 3.4$ nm, $b = 2.5$ nm, $\alpha = 44^\circ$) with four molecules (blue tripods); (c) mesh-averaged image (4.1×5.0 nm²) of (b); taken from Gutzler *et al.* [188].

Dehalogenation reactions have also been investigated on other surfaces than Au(111) and Au(110). Bieri *et al.* studied the impact of the substrate on the network formation of hexaiodo-substituted macrocycle cyclohexa-*m*-phenylene molecules for the coinage metal surfaces Cu(111), Ag(111) and Au(111) [189]. They found that both the required activation temperature and the quality of the networks follow the trend $\text{Cu} < \text{Ag} < \text{Au}$. This shows that less reactive substrates result in higher quality networks due to the increased ability of the precursor molecules to diffuse on the surface. Gutzler *et al.* performed a similar study using TBB molecules (see section 3.3.3) on Cu(111), Ag(110) and the very inert graphite(001). While the C-Br bond was cleaved upon adsorption and TBB formed protopolymers on both Cu(111) and Ag(110), the molecules were found to merely self-assemble into chains of dimers stabilized by non-covalent $\text{Br} \cdots \text{H-C}$ hydrogen bonds on graphite, as shown in Fig. 7.5. After annealing at 300°C, the protopolymers are transformed into covalently bonded networks of polygons of various sizes on both copper and silver, while the TBB molecules have almost completely desorbed from the graphite surface, which shows that no connections have been formed. Gutzler *et al.* conclude that the dehalogenation requires significantly more energy and is “strongly endothermic” without the influence of a metallic surface. However, covalent linking via a dehalogenation reaction was achieved on a bulk insula-

tor surface by Kittelmann *et al.*³ [190]. They identified the main problems of on-surface synthesis of organic molecules on weakly interacting substrates as clustering of the adsorbates and high thermal activation energies which cause the precursor molecules to desorb before intermolecular bonds can be formed. To avoid these problems, Kittelmann *et al.* used the strong interactions between the carboxylate groups of halide-substituted benzoic acids and the calcium cations of their chosen substrate calcite (CaCO_3) to enhance the molecule-substrate interactions to a degree that facilitated successful formation of intermolecular bonds after annealing. The C-Br cleavage temperature was determined to be 590 K without the presence of a metal, in agreement with the temperature Grill *et al.* used to activate $\text{H}_2\text{TBr}_4\text{PP}$ in the evaporator crucible [19].

There are different opinions in the literature on where the halogens go once the C-halogen bonds are cleaved. Lipton-Duffin *et al.* addressed this issue in their study on the formation of polyphenylene molecular wires from diiodobenzene on Cu(110) and found evidence for cleaved iodine bonded to the copper surface with both XPS and STM. Both Gutzler *et al.* and Bieri *et al.* also consider the formation of metal-halogen bonds a crucial step in the formation of covalent organic molecular networks via dehalogenation reactions [188, 189]. However, Grill *et al.* found no evidence of bromine bonding to the underlying Au(111) surface in their experiment, and neither did Krasnikov *et al.* in their demonstration of network formation from NiTBr_4PP ⁴ on the same surface, using STM and XPS as well as NEXAFS⁵ [19, 152]. This suggests that while the metal-halogen bond formation occurs on the more reactive surfaces (Cu, Ag), it is not crucial to the reaction mechanism. Krasnikov *et al.* also show that the porphyrin nanomesh networks on Au(111) are stable up to temperatures of 800 K, even after prolonged exposure to air [152].

An alternative activation method not requiring elevated temperatures has been investigated by Hla *et al.*, who successfully induced all steps of the Ullmann reaction for iodobenzene on Cu(111) with voltage pulses from an STM tip at 20 K [191].

7.2 Covalent organic network formation on gold substrates

The formation of 2D covalent organic frameworks (COF) on the Au(111) surface has first been investigated to reproduce the results by Grill *et al.* for $\text{H}_2\text{TBr}_4\text{PP}$ [19] and by Gutzler *et al.* for TBB [188], as well as to study the transferability of the results to a different precursor molecule, DITP⁶. The experiments are only discussed briefly since the main goal was to verify the methods described in the literature and to test evaporation rates and calibrate temperature measurements on the easy-to-handle gold surface before moving on

³This study was performed using non-contact atomic force microscopy (NC-AFM) in a liquid environment (not UHV).

⁴ $\text{H}_2\text{TBr}_4\text{PP}$ with a metal (nickel) ion instead of the two central hydrogens

⁵Near Edge X-Ray Absorption Fine Structure

⁶see section 3.3 for a description of the molecules

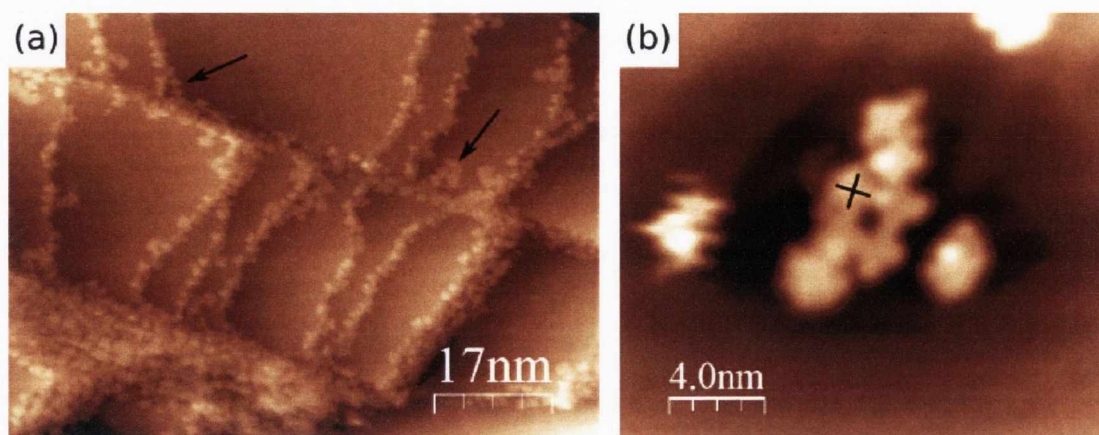


Figure 7.6 Filled state STM images of $\text{H}_2\text{TBr}_4\text{PP}$ on a thin film of Au(111) after annealing at 250°C ; (a) taken at -1.5 V , 0.11 nA ; (b) a different area, taken at -1.8 V and 0.08 nA .

to the more challenging Ge(001). $\text{H}_2\text{TBr}_4\text{PP}$ and TBB have been observed using the STM in CRANN, while DITP has been investigated using the STM and XPS system in DCU.

7.2.1 $\text{H}_2\text{TBr}_4\text{PP}$

The $\text{H}_2\text{TBr}_4\text{PP}$ molecules have been evaporated at a cell temperature of 280°C onto a thin film of Au(111) grown on silicon⁷ and subsequently annealed at 250°C , mimicking COF formation method I as described by Grill *et al.* [19]. Fig. 7.6a shows a filled state STM image of the molecules on the Au(111) surface after annealing. Most of the porphyrin molecules have adsorbed at the step edges of the surface and only very few of them can be found on the terraces. However, the molecules which are not stuck to a step edge show evidence of interconnection as indicated by the black arrows in Fig. 7.6. Covalently bonded molecules can be distinguished from non-covalently bonded, self-assembled molecules by the lack of dark contrast between them and the phenyl leg-to-leg orientation as opposed to the side-to-side arrangement as can be seen in the island in the lower left of Fig. 7.6a. The formation of fragments of COFs could furthermore be observed in a few pore-like structures as shown in Fig. 7.6b, which agree with Grill's description in STM appearance and dimensions (see right column in Fig. 7.3b), with pore sizes around 17 \AA .

Although a higher coverage and the alternative method II could have possibly led to larger networks, no further experiments have been performed on $\text{H}_2\text{TBr}_4\text{PP}$ on Au(111) since the achieved results confirmed the “recipe” for 2D COF formation using this precursor.

⁷see description of tip conditioning samples in section 4.5.2

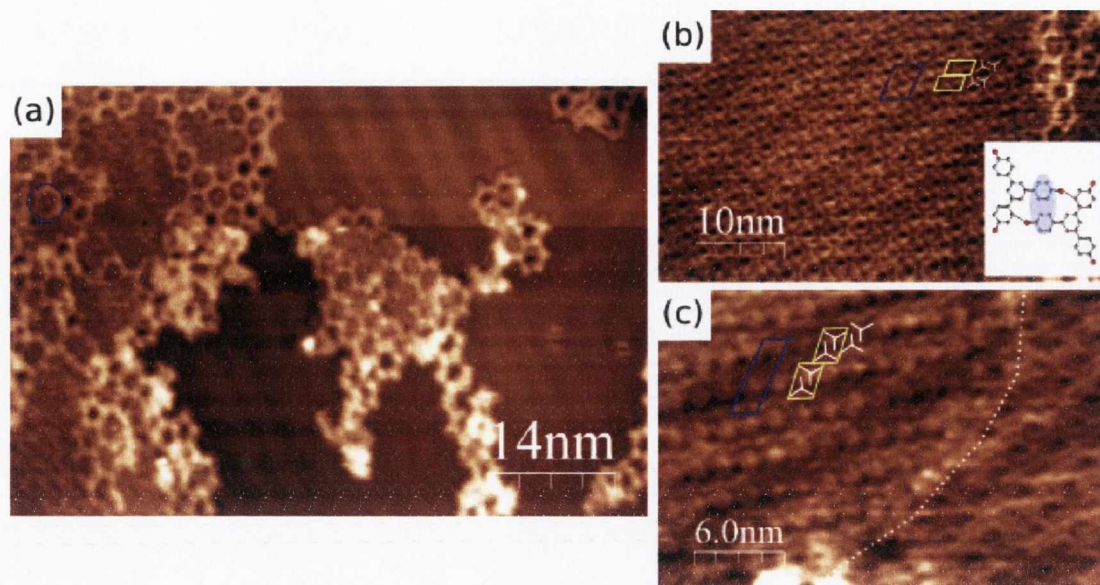


Figure 7.7 Filled state STM images of TBB on a thin film of Au(111) after annealing at 180°C; all of them taken at -1.6 V, 0.2 nA. (b) and (c) show close-ups of the different packing patterns, marked with tripods representing TBB molecules and (b) with an inset of the chemical structure of the main packing motif.

7.2.2 TBB

As with H₂TBr₄PP, TBB molecules have been evaporated on the Au(111) surface to verify COF formation. The cell temperature was 170°C as in the adsorption study described in Chapter 5, thereby leaving the molecules with their bromine substituents intact. Fig. 7.7 shows filled state STM images of approximately 0.6 ML of TBB on the surface after annealing it at 180°C. Fig. 7.7a clearly shows some polygonal COFs as reported by Gutzler *et al.* for Cu(111) and Ag(110) [188], with hexagons as the most frequent configuration. Some of the pores show a bright contrast in their centre as marked in Fig. 7.7a, which has been identified as guest TBB molecules and has not been observed or discussed by Gutzler *et al.* for TBB on Cu(111) or Ag(110).

In addition to the networks, large domains of unreacted and self-assembled TBB molecules were observed, as shown in Fig. 7.7b and c and visible between the networks on the left side of Fig. 7.7a. Gutzler *et al.* report self-assembly of TBB on graphite, but not on Cu(111) and Ag(110) due to the higher reactivity and therefore reduced mobility of the molecules on those surfaces. The degree of interactivity of Au(111) appears to lie in a region between the chemically inert graphite and the more reactive copper and silver, which allows enough mobility for the molecules to interact with each other and self-assemble, but at the same time offers sufficiently strong molecule-substrate interactions to prevent the molecules from desorbing at elevated temperatures and thereby facilitate COF formation. The preferred formation of covalent bonds at the edges of the self-assembled islands, as

can be seen in Fig. 7.7a, demonstrates the importance of surface mobility for the reaction mechanism.

Two different packing patterns have been observed, as shown in Fig. 7.7b and c. Their main structural characteristic is a unit of two TBB molecules packed with two phenyl legs next to each other, indicated with tripods in Fig. 7.7b and c and the same as for TBB on graphite as shown in Fig. 7.5. Gutzler *et al.* attribute this behaviour to $\text{Br} \cdots \text{HC}$ interactions, but do not specify the exact site. The dotted lines in the chemical structure inset in Fig. 7.7b suggest hydrogen bonding between the bromine substituents and the hydrogens in the 1-position of the phenyl legs as the most likely site considering the geometry of the molecule. While hydrogen bonding between TBB molecules is also known to stabilise the bulk structure of TBB crystals [192] and is therefore likely to occur, the parallel orientation of the two phenyl rings highlighted in blue in the inset in Fig. 7.7b could indicate additional attractive interactions between the two aromatic rings, so-called π -stacking, if the phenyl legs were rotated by 90° with respect to the benzene core. The yellow parallelograms in Fig. 7.7b and c indicate the basic packing units as discussed above, whereas blue shows the respective unit cells for each pattern. The patterns differ from each other and from the pattern observed on graphite by the relative position of the basic units. The differences are small but become very clear in the overall appearance of the pattern in the STM. The dotted line in Fig. 7.7c shows a domain boundary between the two patterns observed on Au(111).

This experiment has successfully demonstrated the COF formation with TBB precursors on the Au(111) surface, as well as this system's unique balance between molecule-molecule and molecule-substrate interactions which facilitates the controlled formation of both non-covalent and covalent organic nanostructures.

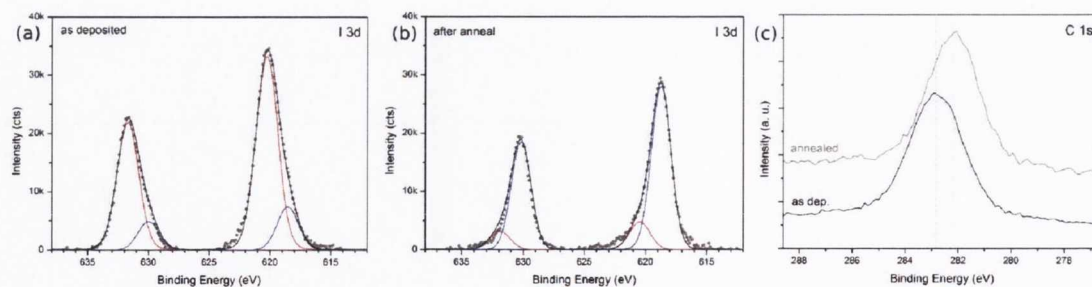


Figure 7.8 XPS of DITP on Au(111). (a) I 3d core-level after deposition of molecules and (b) after annealing at 140°C ; red: C-I, blue: Au-I. (c) C 1s core-levels after deposition (black) and annealing at 140°C (grey). All spectra have been taken with Al K_α X-rays (1486.6 eV).

	I_C	I_{Au}	E_C	E_{Au}	SOS	BR	GW	LW
as dep.	0.82	0.18	620.3	-1.7	11.45	0.66	2.0	0.15
140°C	0.15	0.85	620.4	-1.7	11.45	0.66	1.9	0.15

Table 7.1 Fitting parameters of the I 3d core-level after the deposition of 1.3 ML of DITP on Au(111) and annealing at 140°C. I : Intensities relative to the total peak, E : Binding energy values in eV (relative to E_C), SOS: Spin-orbit splitting in eV, BR: Spin-orbit branching ratio, GW: Gaussian width in eV, LW: Lorentzian width in eV.

7.2.3 DITP

A coverage of ~ 1.3 ML of DITP was evaporated onto the Au(111) surface at a cell temperature of 150°C. Fig. 7.8a shows the XPS spectrum of I 3d core-level after deposition of the molecules. It was fitted with two components at binding energies of 620.3 eV (red) and 618.6 eV (blue); the parameters are listed in Table 7.1. The binding energy of the dominant red component lies close to the value found for iodine bonded to hydrocarbons by Zhou *et al.* (620.5 eV) [193] and can therefore be attributed to intact DITP molecules. The blue component most likely originates from cleaved iodine bonding to the gold surface; its binding energy of 618.6 eV is in agreement with the trend suggested by the binding energies found for Cu-I (619.5 eV [194]) and Ag-I (619.2 eV [39]). After annealing at 140°C (see Fig. 7.8b), the red component loses most of its intensity which means that the carbon-iodine bonds are cleaved as anticipated. Some, but not all, of the cleaved iodine then bonds to the gold surface, which results in a significant intensity gain of the blue component. The C 1s core-level spectra before and after annealing at 140°C are compared in Fig. 7.8c. The loss of the iodine bonds with comparatively high binding energies [39] results in a shift of the overall peak of about -0.6 eV.

STM images were taken after the annealing step and loss of the iodine, and are shown in Fig. 7.9. The filled state image in Fig. 7.9a captures a large surface area with three different layers of DITP molecules. After the cleavage of the C-I bond, the molecules appear to have formed covalently bonded wire structures as anticipated, and three different domains distinguished by wire directions at angles of 60° with respect to each other can be observed. Furthermore, the different layers of wires appear to cross over the surface's step edges, which is often referred to as *carpet* growth. Fig. 7.9b shows a close-up STM image, clearly displaying the wire structures and a domain boundary in the top left corner. The wires show a periodicity of roughly 1 nm, which, considering the ~ 0.28 nm diameter of a phenyl ring, suggests large gaps between two neighbouring wires. However, imaging the surface with a much lower bias and higher current reveals additional rows of DITP polymers in between, as shown in the close-up image in Fig. 7.9c. The line profile in Fig. 7.9d shows a ~ 0.5 nm periodicity and wire dimensions of 0.25 to 0.3 nm, in good agreement with the dimensions of poly-*p*-phenylene wires. The different STM contrast of

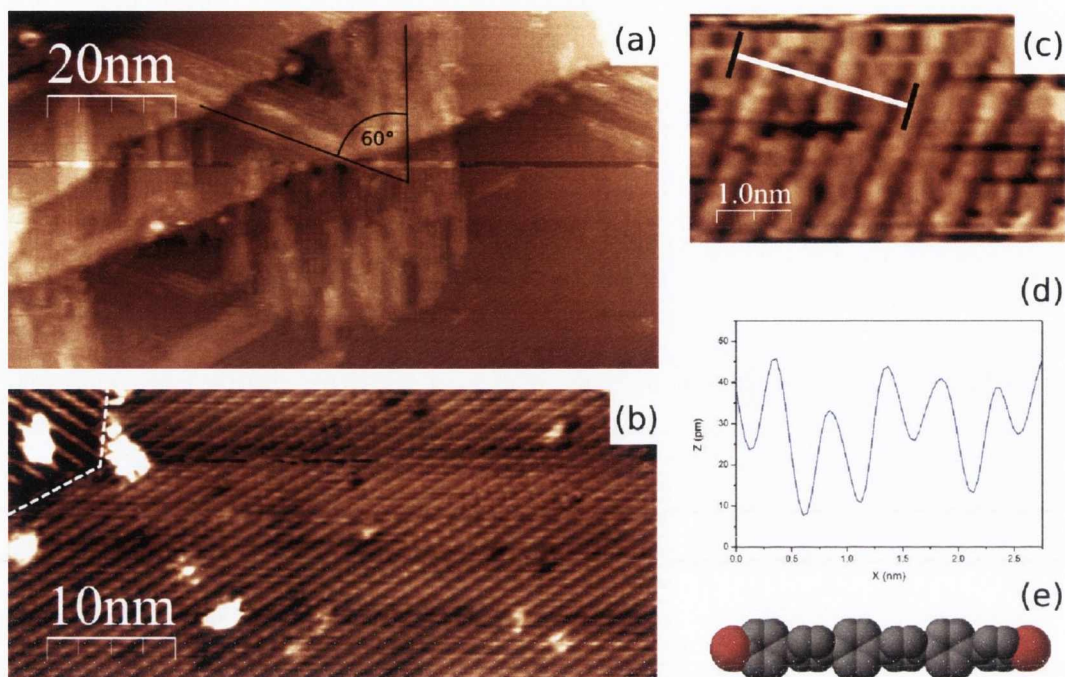


Figure 7.9 DITP on Au(111) after annealing at 140°C. (a) Filled state STM image, taken at -1 V, 0.16 nA; (b) STM image showing two domains, taken at -1 V, 0.16 nA; (c) close-up STM image, taken at -0.2 V, 2.15 nA; (d) line-profile indicated in (c); (e) 3D model of two connected DITP molecular units.

the alternating wires can only be caused by conformational differences or different heights above the surface to possibly ensure more efficient use of space, since there is no reason for alternating wires to be chemically different. Fig. 7.9e shows a 3D chemical structure of two connected DITP molecules, emphasising the possibility of different relative rotational angles of the phenyl elements of the wires.

Using the preparation methods available on the UHV systems employed for this work, all three molecules have been confirmed to form COFs on the Au(111) surface as demonstrated or predicted by the literature.

7.3 Dehalogenation reactions on passivated Ge(001)?

Although the presence of a metal surface is formally necessary for the formation of COFs via an Ullmann-type dehalogenation reaction, there is some evidence that the relatively weak carbon-halogen bonds can be cleaved without a metal catalyst: Grill *et al.* described bond-cleavage in the evaporator by increasing the temperature of the crucible to $T > 590$ K (or around 320°C) [19] and Kittelmann *et al.* observed dehalogenation reactions on a bulk insulator [190]. There is no literature on the formation of COFs on a semiconductor

surface. After successfully testing the methodology for (Ullmann-type) COF formation on the Au(111) surface, the previously characterised hydrogen-, bromine- and chlorine-passivated Ge(001) surfaces (Chapter 6) have been investigated as possible substrates for this process, using a variety of organic precursor molecules.

7.3.1 Dehalogenation on Ge(001):H

As the most commonly described and utilised passivation method for the Ge(001) surface, the hydrogen-passivation was the most obvious choice for the first experiments, as was the $\text{H}_2\text{TBr}_4\text{PP}$ molecule used by Grill *et al.*. The hydrogen-passivation has been reported to be stable for up to an hour when annealed at temperatures around 230°C [78], while the bromine-substituents have been found to dissociate from the $\text{H}_2\text{TBr}_4\text{PP}$ molecules at around 170°C on various coinage metal surfaces [195]. Assuming that carbon-halogen bond cleavage can indeed occur without the presence of a metal surface, this temperature window theoretically allows the formation of covalently bonded porphyrin-based nanomesh structures.

Fig. 7.10 shows the Br 3d core-level spectrum of a coverage of ~ 2 ML of $\text{H}_2\text{TBr}_4\text{PP}$ on Ge(001):H before and after annealing at 180°C for 40 min, taken with an incident photon energy of 110 eV at the SGM1 beamline at ASTRID. The fitting parameters are listed in the caption. The open squares show the spectrum taken directly after the deposition of the molecules. Only one component (labelled Br I) at a binding energy of 72.1 eV can be observed, assigned to bromine substituents still connected to the $\text{H}_2\text{TBr}_4\text{PP}$ molecules as discussed before in Chapter 5 (section 5.2). This observation confirms that the surface-passivation successfully prevents the molecules from interacting with or bonding to the surface as observed when they are adsorbed on the clean surface. After annealing the sample at a temperature of 180°C for 40 min, the spectrum plotted in closed squares shows a significant reduction of Br I, and the emergence of a second bromine component, equivalent to the Br II species previously assigned to bromine bonded to the germanium surface. This shows that while the carbon-bromine bonds can be cleaved with thermal activation and without the presence of a metal, some of the dissociated bromine atoms then bond to germanium atoms instead, similar to what has been observed for

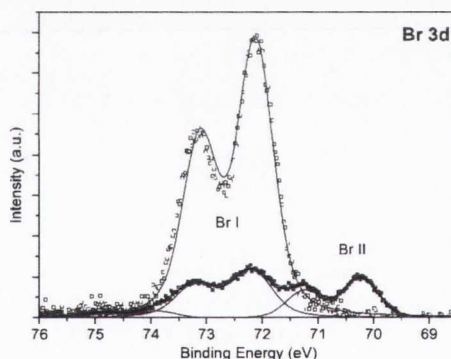


Figure 7.10 Br 3d core-level of ~ 2 ML of $\text{H}_2\text{TBr}_4\text{PP}$ on Ge(001):H before (open squares) and after (closed squares) annealing at 180°C . Fitting parameters before/after anneal: $E_I = 72.10/72.20$ eV, $E_{II} = -/70.2$ eV BR=0.64/0.69, SOS=1.10 eV, GW=0.65/0.68 eV, LW=0.30 eV.

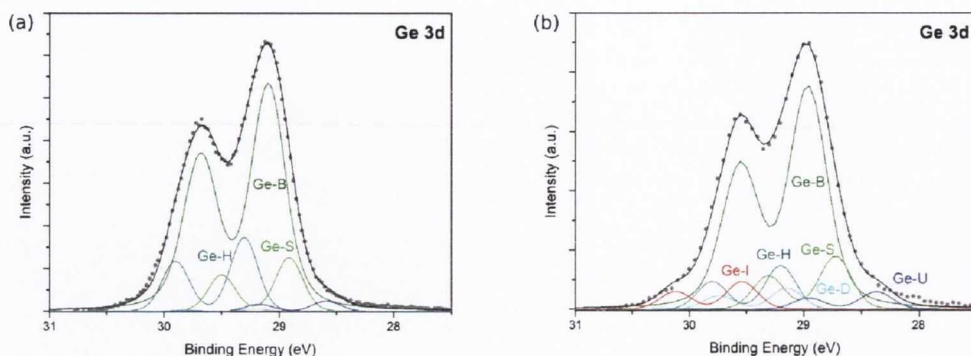


Figure 7.11 Ge 3d core-levels of ~ 2 ML of $\text{H}_2\text{TBr}_4\text{PP}$ on Ge(001):H before (a) and after (b) annealing at 180°C .

	I_B	I_S	I_D	I_U	I_H	I_I	E_B	E_S	E_D	E_U	E_H	E_I
as dep.	0.61	0.15	0.00	0.02	0.36	0.00	29.05	-0.20	0.17	-0.45	0.25	0.60
anneal	0.57	0.15	0.05	0.04	0.12	0.08	28.95	-0.23	0.17	-0.55	0.30	0.60

Table 7.2 Fitting parameters of the Ge 3d core-levels for the hydrogen-passivated Ge(001) surface after deposition of 2 ML of $\text{H}_2\text{TBr}_4\text{PP}$ and after subsequent annealing at 180°C . I : Intensities relative to the total peak, E : Binding energy values in eV (relative to E_B). All components have been fitted with a spin-orbit splitting of 0.59 eV, a branching ratio of 0.66 ± 0.02 , a Gaussian width of 0.30 eV and a Lorentzian width of 0.15 eV.

iodine on Au(111) in section 7.2.

The Ge 3d core-level spectra of the same system before and after annealing, taken with an incident photon energy of 60 eV, are shown in Fig. 7.11 and the respective fitting parameters are listed in Table 7.2. Before and after the deposition of molecules the peak could be successfully fitted with a bulk, a second layer and a Ge-H component as typical for an almost fully hydrogen-passivated Ge(001) surface [27]. A remaining small shoulder on the low binding energy side (dark blue) can be attributed to a weak signal from a few unsaturated surface dimer atoms. This picture changes after the annealing step, when shoulders on both high and low binding energy sides of the core-level emerge. The fit still requires $\sim 30\%$ of the original Ge-H component⁸ to match the data, but parts of the passivation appear to have desorbed during the 180°C anneal, resulting in a return of the interface component (Ge-I) previously observed for $\text{H}_2\text{TBr}_4\text{PP}$ on clean Ge(001) as well as stronger signals for both the up and down dimer components. The partial loss of the hydrogen-passivation layer also explains the Br-Ge component observed in the Br 3d core level.

The PES data shows that the desorption behaviour of the hydrogen-passivation appears to have been altered by the presence of the $\text{H}_2\text{TBr}_4\text{PP}$ adsorbates. This could possibly be explained by pairing of the dissociated bromine atoms with hydrogen atoms from

⁸relative intensity with respect to the total peak area

the surface, forming HBr and thus desorbing into the vacuum. No HBr signal could be measured with mass spectrometry, but the UHV system geometry did not allow close proximity of the spectrometer to the sample which could have made the relatively small amount of HBr gas difficult to detect. In any case, the loss of the passivation is expected to significantly limit the mobility of the activated molecular building blocks and prevent COF formation.

In a subsequent STM study conducted in CRANN, elevated crucible temperatures of $>360^{\circ}\text{C}$ have been used for the deposition to activate the $\text{H}_2\text{TBr}_4\text{PP}$ molecules in the evaporator and thereby avoid annealing of the Ge(001):H sample, risking the hydrogen loss observed in the PES data. Fig. 7.12 shows the hydrogen-passivated Ge(001) surface after deposition of ~ 0.3 ML of $\text{H}_2\text{TBr}_4\text{PP}$. No accompanying XPS data to confirm the activation, i.e. bromine-loss of the deposited molecules is available. The image shows the underlying dimer rows of the hydrogen-saturated Ge(001) surface well resolved, whereas the adsorbed molecules appear more fuzzy and sometimes in undefined clusters as marked with the circle in Fig. 7.12. This suggests that the adsorbed molecules are not held in place by strong interactions with the surface

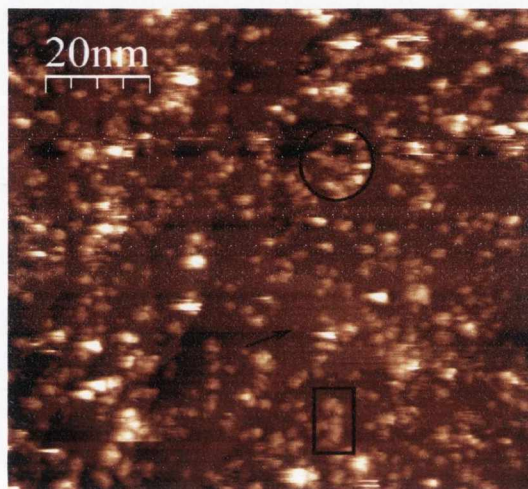


Figure 7.12 Filled state STM image of 0.3 ML of $\text{H}_2\text{TBr}_4\text{PP}$ on Ge(001):H, taken at -1.8 V and 0.32 nA. Arrow: defect in the H-passivation, rectangle: possibly interconnected molecule chain, circle: clustered molecules.

like on the unpassivated Ge(001), but are moved around by the STM tip. However, the movement is very limited and very few molecules have been observed to change position from one image frame to the next. Considering that the number of visible defects in the hydrogen-passivation decreases after the adsorption of the molecules, it is likely that the reactive ends of the activated $\text{H}_2\text{TBr}_4\text{PP}$ molecules react with the unsaturated germanium dangling bonds and are thereby kept from being more mobile. This is furthermore supported by the observation that the STM images of higher coverages are very streaky and without molecular resolution, indicating the presence of very mobile molecules on the surface after saturation of the defects. This behaviour also indicates that no COFs of significant size are formed on the surface, since interconnection would limit the mobility of the molecules significantly. Fig. 7.12 shows a few molecules assembled in chain formations as marked with the rectangle, which could indicate the formation of intermolecular

bonds. However, no images with sufficient resolution to confirm this could be obtained. Annealing of the surface at moderate temperatures around 130°C, leaving the passivation mostly intact, does not change the behaviour of the adsorbed molecules, suggesting that COF formation on Ge(001):H is either not possible or very inefficient.

7.3.2 H₂TBr₄PP on Ge(001):Br and Ge(001):Cl

As described in Chapter 6, both bromine and chlorine form mostly uniform passivation layers on the Ge(001) surface. Although it has been shown that many different factors like bond strength, pairing or the size of the adsorbate can influence the desorption process, bromine and chlorine are generally more stable than hydrogen as a passivation agent for Ge(001). Additionally, the bromine- and in particular the chlorine-passivation have a lower average defect density. After identifying both thermal stability and defects of the passivation as problems in the attempt of COF formation on Ge(001):H in the previous section, the possibility of covalent interconnection of the H₂TBr₄PP building blocks has also been investigated with the STM in CRANN on both Ge(001):Br and Ge(001):Cl.

Bromine-passivation

Firstly, a sub-monolayer coverage of H₂TBr₄PP was deposited on the bromine-passivated Ge(001) surface with a cell temperature of 360°C. Unlike the experiment on Ge(001):H, no supporting XPS data is available to confirm whether the majority of molecules has indeed been activated at this temperature as expected. The STM images after the deposition appeared very streaky in repeated experiments, indicating a high mobility of the adsorbates and most likely no COF formation. However, after annealing the sample to 200°C, the adsorbed molecules as well as the dimer rows of the underlying surface could be resolved as shown in Fig. 7.13. Various chain structures as marked by the rectangle in

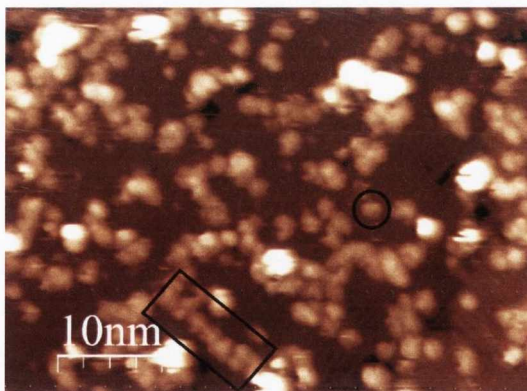


Figure 7.13 Filled state STM image of H₂TBr₄PP on Ge(001):Br after annealing at 200°C, taken at -2.0 V and 0.32 nA. Rectangle: possibly interconnected molecule chain, circle: single adsorbed molecule.

Fig. 7.13 could be observed in almost all images, suggesting covalent bonding or very strong interactions between the molecules since that would make the molecules stable enough to be imaged on the inert Ge(001):Br surface. Although bonding of the molecules to the defects of the passivated substrate as for Ge(001):H is most likely still happening

as indicated by the single adsorbed and resolved molecules (marked with a circle in Fig. 7.13a), it is unlikely to account for the observed chain-structures. No atomic resolution which could clarify the suspected covalent bonds in the chain-structures could be achieved with the STM and the molecules still appear fuzzy, indicating some remaining mobility of the structures. Imaging the structures at high biases of around 3 V would, according to Grill *et al.* [19], result in the observation of a bright contrast in between molecules in case of covalent bonds. However, increasing the bias past 2.3 to 2.5 V while imaging this surface resulted in a significant increase in the noise level, while this behaviour was not observed when imaging the tip-conditioning sample before and directly after. It is reasonable to assume that the bromine-germanium bonds of the substrate surface are cleaved at this bias, therefore causing the disturbance in the images. STS, as done by Grill *et al.*, has not been possible to perform with sufficient accuracy at room temperature.

When depositing the $\text{H}_2\text{TBr}_4\text{PP}$ molecules at lower cell temperatures and therefore presumably leaving them intact⁹, their behaviour both before and after annealing at 200°C does not change and the STM images look very similar. Assuming that the evaporation at higher cell temperatures had caused Br-C cleavage, it appears that independent of where the activation of the molecules takes place, further thermal activation is necessary to initiate interconnection.

Chlorine-passivation

Chlorine, with its low defect density and the comparatively strong Ge-Cl bonds, is expected to be the most suitable passivation agent for COF formation on Ge(001). Fig. 7.14a shows the Ge(001):Cl surface after deposition of a sub-monolayer coverage of unactivated $\text{H}_2\text{TBr}_4\text{PP}$. Unlike for the other passivation methods, the adsorbed molecules could be resolved and show non-covalent self-assembly into islands very similar to what has been observed by Grill *et al.* on Au(111) directly after deposition of the intact molecules [19]. Fig. 7.14c shows a close-up of one of those islands (white rectangle in Fig. 7.14a) with overlaid molecular structures, revealing molecular resolution down to the phenyl legs (arrow) and the *free base* core in some cases. The image is still streaky, indicating some loose molecules on the surface as could be expected, and some single adsorbed molecules on defect sites can be observed. Overall, the molecule-substrate interactions appear to be stronger than for the previously investigated passivation methods, and the molecules prefer to self-assemble rather than form clusters and show less interaction with the scanning tip throughout repeated experiments.

After annealing at 250°C for 5 min, no streaky features indicating mobile molecules can be observed and the self-assembled islands of molecules have mostly changed into chain-structures, similar to what has previously been observed on Ge(001):Br and Ge(001):H. In this case, the molecular resolution shows strong evidence for leg-to-leg orientation of

⁹The crucible had been refilled with previously unused molecules before evaporation.

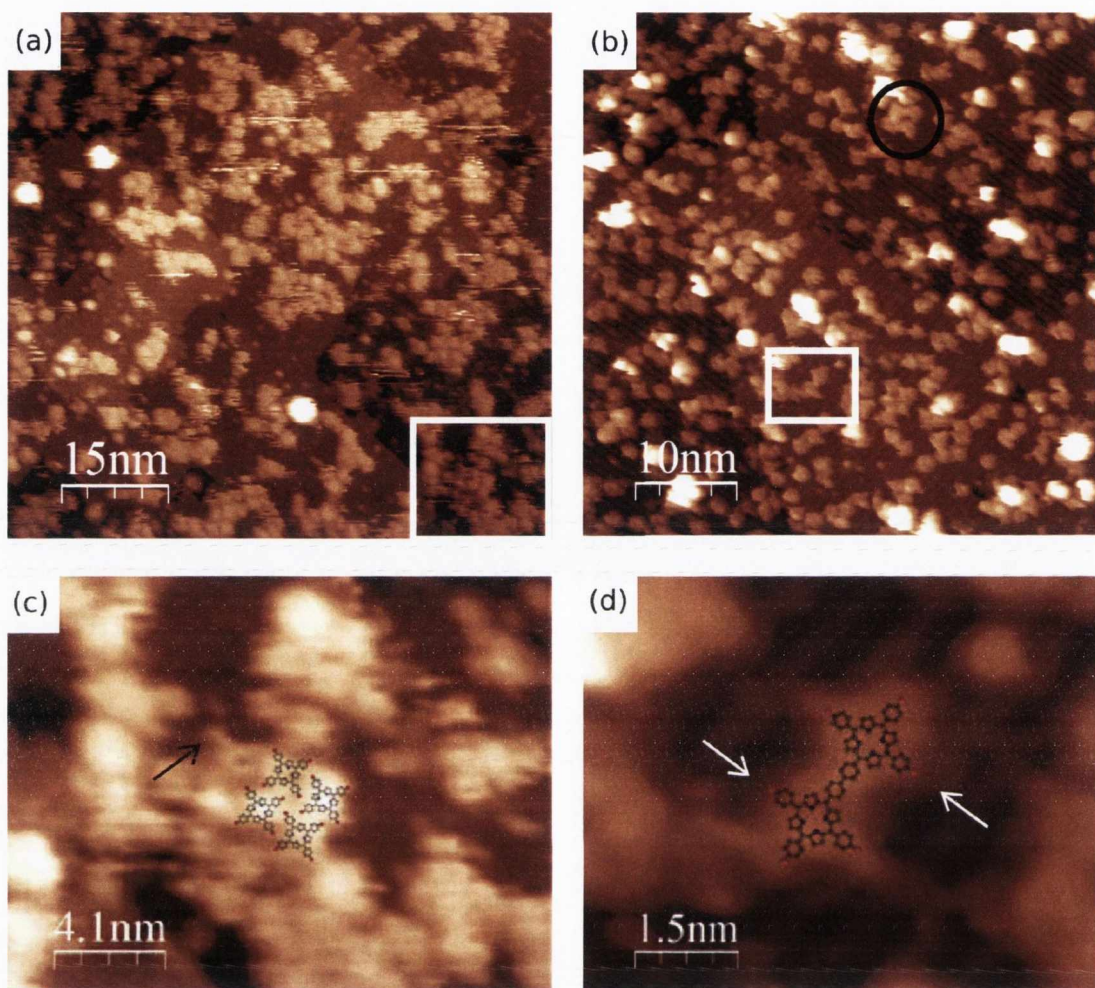


Figure 7.14 Filled state STM images of $\text{H}_2\text{TBr}_4\text{PP}$ on $\text{Ge}(001):\text{Cl}$ before (a) and after (b) annealing at 250°C . (c) and (d) shows close-ups of the white rectangles marked in (a) and (b), respectively. (a) taken at -1.7 V and 0.09 nA , (b) taken at -1.9 V and 0.11 nA . Explanations of the labels can be found in the text.

adjacent molecules without dark contrast in between, and the average distance between molecular cores in the dimers, chains and pores observed throughout the STM images has been determined as $d = (1.65 \pm 0.12)\text{ nm}$, which is in agreement with the $d = 1.71\text{ nm}$ measured and calculated by Grill *et al.* for the distance between two covalently bonded TPP molecules [19]. The close-up of a dimer in Fig. 7.14d is well enough resolved to distinguish between activated (arrows) and intact phenyl legs. As for the bromine-passivation, imaging at higher biases to further confirm the covalent nature of the bonds resulted in cleavage of the $\text{Ge}-\text{Cl}$ bonds of the passivation and strong disturbance of the STM images. In addition to the chains, some single pore structures as marked with the black circle can be found, although not sufficiently resolved to confirm covalent connections as in the pore structures found on the $\text{Au}(111)$ surface (see Fig. 7.6b).

7.3.3 Other molecules on Ge(001):Cl

While the formation of intermolecular covalent bonds appears to be in principle possible on the passivated Ge(001) surface, with chlorine as the most suitable passivation agent, the achieved COFs from H₂TBr₄PP building blocks are small and bond formation is inefficient. To investigate whether alternative precursor molecules result in more evident, larger networks after dehalogenation reactions, this section discusses some results on COF formation using the bromine substituted HBTP¹⁰ and TBB¹¹ as well as the iodine-substituted DITP¹² on the chlorine-passivated Ge(001) surface.

HBTP

Fig. 7.15a shows a filled state STM image of HBTP deposited on Ge(001):Cl at a cell temperature of 250°C. The relatively small size of the molecule makes it difficult to evaporate it at higher temperatures with a flux that is low enough to achieve controlled coverages in the monolayer range. Activation of the HBTP molecules on the surface rather than in the crucible is therefore the preferred option. The image shows the dimer rows of the substrate surface well resolved, while the adsorbed molecules appear to have formed islands without identifiable internal structure. Streaky features indicate mobile molecules. A few porphyrin molecules from a previous experiment with H₂TBr₄PP can be identified sitting on top of the HBTP islands. Other STM images after the deposition of HBTP also show some large and high clusters, which made the imaging of the surface difficult.

After annealing at 150°C, the islands and clusters of molecules have spread out and self-assembled into a comparatively uniform monolayer, as shown in the STM image in Fig. 7.15b. As indicated by the black lines, the HBTP molecules orient themselves in chains at an angle of 40° with respect to the underlying dimer rows, suggesting a certain degree of interaction with the substrate. Fig. 7.15c shows a close-up of the white rectangle marked in Fig. 7.15b. The resolution is not sufficient to identify the exact orientation of the self-assembled molecules, but two different conformations can be identified as indicated by the triangles. A possible packing pattern for self-assembled HBTP on a weakly interacting substrate is suggested in Fig. 7.15e and can sometimes be found on the Ge(001):Cl surface, but the periodicity of the self-assembled layer is often disturbed, most likely by some of the molecules bonding to defects of the chlorine-passivation.

The STM image in Fig. 7.15d shows the same surface after annealing at 250°C and presumed activation of the molecular building blocks. Since the experiment was conducted on the UHV system in CRANN, no supporting XPS data to confirm the chemical changes is available. However, the STM images reveal a clear change in the behaviour of the previously self-assembled molecules. Some pores with the dimensions and appearance of

¹⁰section 3.3.2

¹¹sections 3.3.3, 5.4 and 7.2

¹²sections 3.3.4 and 7.2

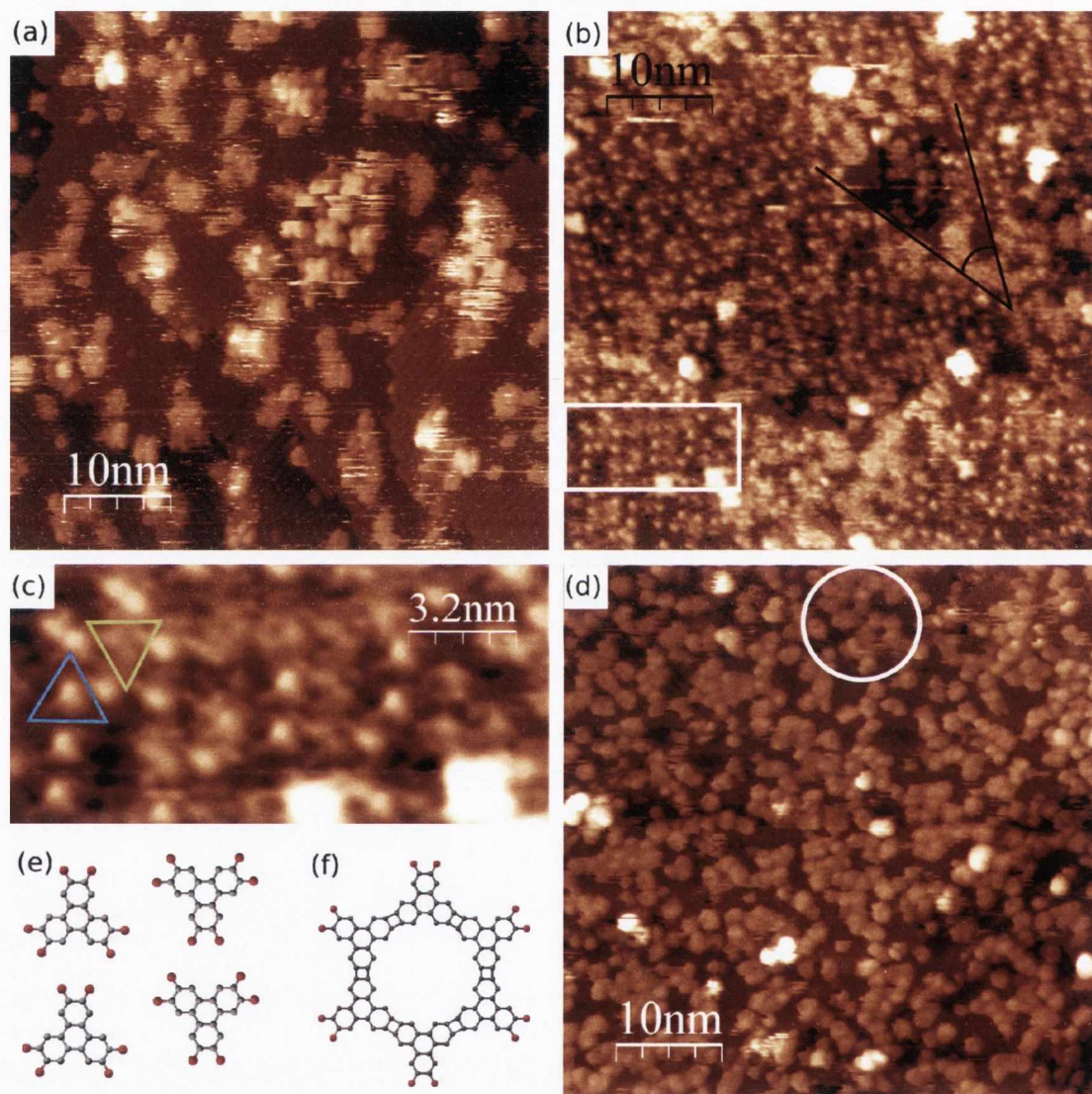


Figure 7.15 Filled state STM images of HBTP on Ge(001). (a) after deposition, taken at -1.6 V and 0.12 nA; (b) after annealing at 150°C, taken at -1.6 V and 0.10 nA; (c) close-up of white rectangle in (b), triangles indicating two different HBTP conformations; (d) after annealing at 250°C, taken at -1.8 V and 0.13 nA; (e) chemical structure of non-covalent self-assembly; (f) chemical structure of expected COF.

the expected COF as shown in Fig. 7.15f can be identified throughout the images, as the two pores marked by the white circle in Fig. 7.15d. This strongly suggests the formation of intermolecular bonds, although still comparatively inefficient as for the COF fragments observed for H₂TBr₄PP. Fragments of pores are more difficult to identify due to the lack in STM resolution and relatively high coverage.

TBB

TBB was evaporated onto the Ge(001):Cl surface at a cell temperature of 170°C. Like for HBTP, high temperatures leading to the activation of the molecules in the evaporator would result in a very high flux due to the small size of TBB. Fig. 7.16 shows a filled state STM image taken after the deposition of the equivalent amount which results in 0.6 ML on the Au(111) surface. On Ge(001):Cl, the coverage appears to be much lower. However, the STM images show many clusters like the one circled in yellow, which makes it difficult to estimate the amount of molecules adsorbed on the surface. Additionally, most of the STM images show a pattern of dumbbell structures as shown in the close-up image on the upper left of Fig. 7.16. They always appear in the same orientation, independent of the direction of the rows, which usually suggests a tip-related effect. However, STM images of the clean tip-conditioning sample taken immediately before and after measurement on the TBB/Ge(001):Cl surface do not show this effect. The shape of the features is reminiscent of the basic packing unit of the TBB self-assembly observed on both Au(111), as discussed in section 7.2, and on graphite [188]. The two tripods show the possible orientation of two molecules. The streaky nature of the features indicates movement, which possibly indicates a drag-and-drop effect of one or more basic packing units as the STM tip scans the surface.

After annealing at 170°C, most of the TBB has desorbed and only very few molecules remain on the surface, most likely adsorbed on defect sites. Apart from the slightly higher molecular weight of HBTP due to three additional bromine atoms, a significant difference between HBTP and TBB is the rotational degree of freedom around the σ -bond of the phenyl legs of TBB and the resulting lack of a large conjugated π -system parallel to the

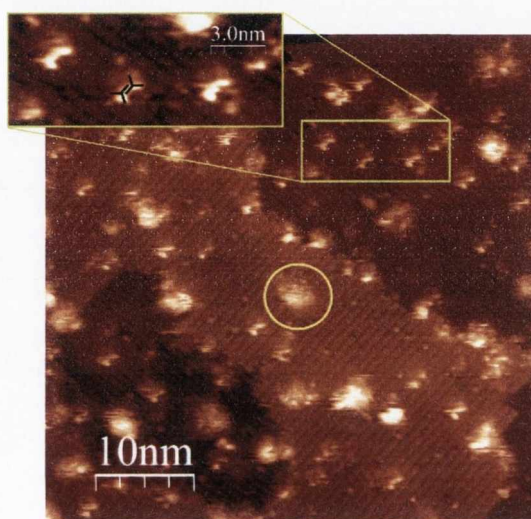


Figure 7.16 Filled state STM image of TBB on Ge(001):Cl, taken at -1.5 V and 0.08 nA. Explanations for labels can be found in the text.

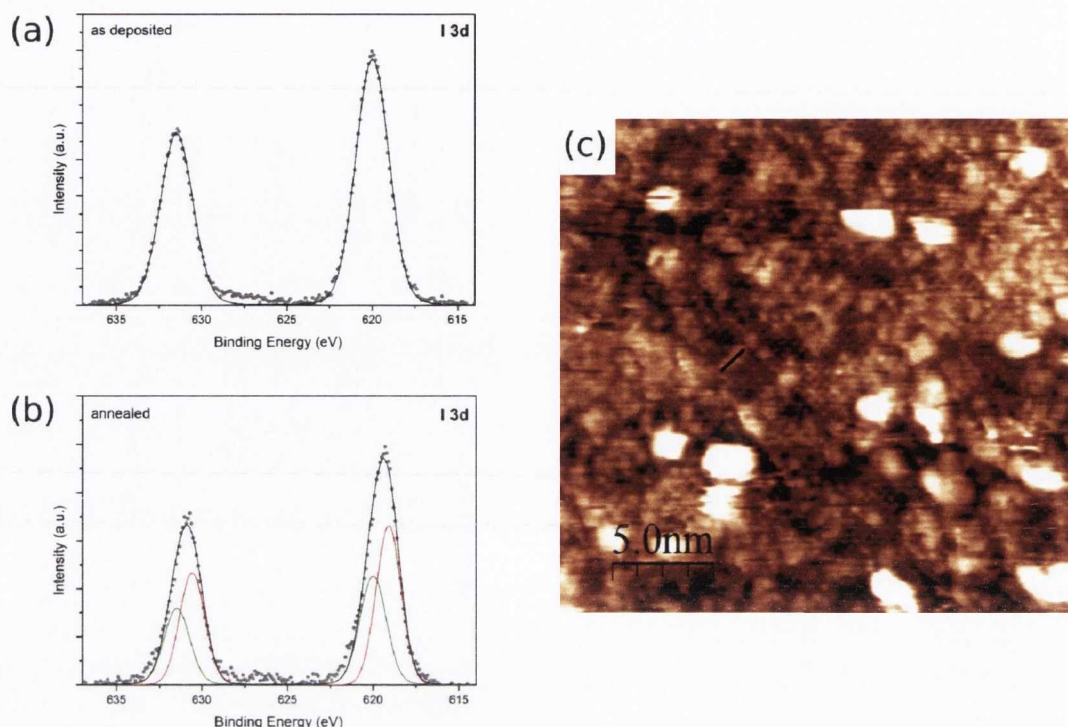


Figure 7.17 XPS and STM of DITP on Ge(001):Cl. (a) I 3d core-level after the deposition of ~ 1 ML; (b) I 3d core-level after annealing at 150°C (both (a) and (b) taken with Al K_α X-rays); (c) filled state STM image after annealing at 150°C , taken at -1.2 V and 0.10 nA.

substrate surface. The desorption of TBB but not HBTP suggests that the non-covalent interactions between organic molecules and the passivated Ge(001) surface are governed by the π -orbitals of the molecules.

DITP

A coverage of approximately 1 ML of DITP has been evaporated onto the Ge(001):Cl surface at a cell temperature of 150°C and investigated with both XPS and STM on the UHV system in DCU. No resolved STM images could be obtained directly after deposition, indicating a high mobility of the molecules on the surface; only clusters of molecules could be observed. The I 3d core-level is shown in Fig. 7.17a. It was fitted with one component at a binding energy of 620 eV, associated with the iodine-carbon bonds of the intact DITP molecules and in good agreement with the equivalent component found after the deposition of DITP on Au(111) as discussed in section 7.2. The fitting parameters are listed in Table 7.3. After annealing at 150°C , the core-level is shifted to lower binding energies and was fitted with two components as shown on Fig. 7.17b, again similar to the observations

	I_C	I_{Ge}	E_C	E_{Ge}	SOS	BR	GW	LW
as dep.	1.0	0.0	620.0	-0.9	11.45	0.69	2.2	0.15
150°C	0.4	0.6	620.0	-0.9	11.45	0.69	1.8	0.15

Table 7.3 Fitting parameters of the I 3d core-level after the deposition of 1 ML of DITP on Ge(001):Cl and annealing at 150°C. I : Intensities relative to the total peak, E : Binding energy values in eV (relative to E_C), SOS: Spin-orbit splitting in eV, BR: Spin-orbit branching ratio, GW: Gaussian width in eV, LW: Lorentzian width in eV.

on Au(111). The intensity of the component at 620 eV has been reduced in favour of a new iodine species with a binding energy of 619.1 eV, most likely originating from iodine bonding to the germanium surface. As mentioned in section 6.3.1, both the Cl 2s and 2p core-levels are difficult to interpret because they are enveloped by other features, which prevents an analysis of the state of the chlorine-passivation. Additionally, the amount of iodine bonding to the germanium surface and possibly replacing chlorine is comparatively small and only visible in the XPS due to a large cross section of the I 3d orbital in the energy range of the Al K_{α} X-ray line. Nevertheless, the successful activation of the DITP molecules on the Ge(001):Cl surface could be confirmed. Yet unlike on Au(111), the C 1s core-level did not shift after annealing of the sample.

A filled state STM image taken after annealing of the sample and shown in Fig. 7.17c still shows the DITP molecules on the surface. The underlying chlorine-passivation is very well resolved and single atoms can be distinguished, while the adsorbed molecules are mostly clustered and fuzzy and therefore difficult to identify. The black line indicates the dimensions of a DITP molecule. No evidence for covalently bonded phenylene wires as formed from DITP on Au(111) could be found, which indicates that the shift of the C 1s core-level observed on gold could be related to the wire structures.

Due to the weak iodine-carbon bond (see Table 6.1), DITP could be activated on the surface before it desorbs, which was not possible for TBB. While the activated DITP molecules do not form extended wire structures, they appear to react with either the surface or each other in different ways, which keeps them on the surface at elevated temperatures up to 250°C despite their low molecular weight and lack of a large conjugated π -system.

7.4 Summary

After the publication of the first successful covalent interconnection of organic molecular building blocks into 2D nanosized structures via a dehalogenation reaction on the Au(111) surface by Grill *et al.* [19], their approach has been imitated many times. Experiments with H_2TBr_4PP , TBB and DITP on Au(111) carried out for this work have confirmed their recipe and shown that the Au(111) surface appears to interact with organic molecules of

various sizes in a balanced way which enables both self-assembly and covalent interconnection of the molecular building blocks at elevated temperatures.

In several reviews of this research subject, the dehalogenation reaction has been referred to as a modification of the Ullmann reaction [4, 20, 21], which theoretically requires the presence of a metal for the carbon-halogen bonds to be cleaved. However, XPS experiments on both $\text{H}_2\text{TBr}_4\text{PP}$ and DITP on hydrogen- and chlorine-passivated Ge(001), respectively, have shown that halogen substituents can be thermally dissociated from their organic “parent”-molecules on a non-metallic surface. Yet this step requires a very stable passivation layer, since the comparatively weakly bonded hydrogen has been observed to partially desorb at the activation temperature of the bromine-substituted molecules (very likely due to HBr formation) and thereby restrict the mobility of the molecules, which is necessary for COF formation. The bromine- and in particular chlorine-passivation of Ge(001) have been shown to be more stable, although no well-resolved synchrotron PES data to prove their stability after activation of the precursor molecules is available as for the hydrogen-passivated surface.

STM images of several different precursor molecules on passivated Ge(001) still do not show COF formation on a scale which is comparable to the results on coinage metal surfaces. Some general problems of COF formation on a non-metallic surface previously identified by Kittelmann *et al.* [190] such as clustering and premature desorption of the precursors could be confirmed, especially for smaller molecules like TBB. While some evidence for interconnected molecules can be found for the larger precursors $\text{H}_2\text{TBr}_4\text{PP}$ and HBTP, the reaction happens very inefficiently. Several attempts to improve the size and quality of the COF fragments, e.g. different coverages, annealing temperatures or different activation methods¹³, have been unsuccessful. This problem most likely originates from the unavoidable defects found in all investigated surface passivation layers, which offer bonding sites for the adsorbed molecules and thereby disturb their mobility and ability to find reaction partners. Noble metal surfaces like Au(111) are uniform and facilitate long-range interactions between adsorbed organic molecules. It is furthermore possible that the pairing of the dissociating halogen-substituents with atoms from the passivation layer is not unique to the hydrogen-passivation and also creates additional defect sites on bromine- and chlorine-passivated Ge(001). This effect could be avoided by using a different reaction pathway than dehalogenation, which will be discussed in the following chapter.

¹³activation of the precursors in the crucible or directly on impact with the substrate held at elevated temperatures during deposition

8 Other reaction mechanisms

After establishing in the previous chapter that on-surface dehalogenation reactions between organic molecular building blocks can be observed on passivated Ge(001), i.e. without the presence of a catalytic metal, this chapter presents results on other reaction mechanisms which could potentially lead to covalently bonded organic nanostructures on a semiconductor surface. The experiments have been performed using STM and XPS¹ in IM2NP, following the resident research group's previously published approaches of interconnecting organic molecular building blocks via the dehydration of BDBA² [196] and the formation of an organometallic poly-phthalocyanine (Pc) sheet from TCNB³ and metal atoms [197].

8.1 Literature Review

The on-surface covalent coupling of organic molecules in UHV as first demonstrated by Grill *et al.* via the previously discussed dehalogenation reaction [19] has inspired other research groups to investigate different reaction mechanisms leading to similar nanosized 2D COFs [18, 20, 21, 199]. This development is fueled by the ability of organic chemists to synthesise many different kinds of molecular precursors “a la carte”, with various geometries and functional end-groups or connectors [21]. In the past five years, six different

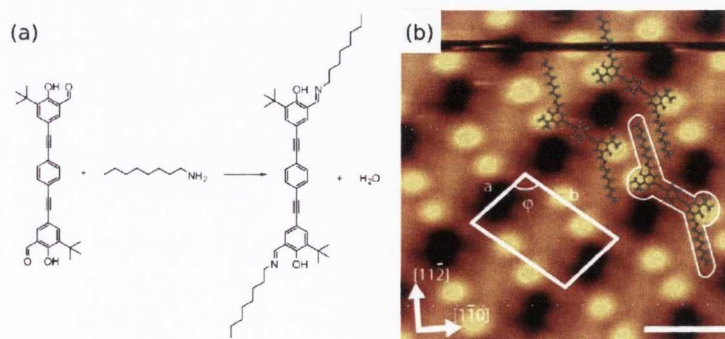


Figure 8.1 (a) Reaction scheme of the imidisation of bis(hydroxybenzaldehyde) and octylamine, (b) Self-assembled diimine reaction product formed *in situ* on Au(111) at RT (STM image taken at 1.9 V and 0.27 nA, bar size 2 nm). Adapted from Weigelt *et al.* [198].

¹only as a coverage indicator, insufficient resolution and intensity for further analysis

²see section 3.3.5

³see section 3.3.6

basic reaction mechanisms (other than dehalogenation) have been reported to result in the covalent interconnection of organic molecular precursors on several surfaces and will be outlined in this section.

As one of the first alternative reaction pathways to selective dehalogenation, Weigelt *et al.* observed the condensation reaction between an aldehyde and an amine on the Au(111) surface [198]. The reaction scheme is shown in Fig. 8.1a. Fig. 8.1b shows an STM image of the self-assembled imine reaction product, resulting merely from coadsorption of the two precursor molecules on Au(111) at room temperature. Additional XPS measurements and a comparison with STM images of the reaction product obtained from solution confirmed the covalent interconnection of the precursors. In traditional solution chemistry, the reaction involves the formation of several byproducts, while the reaction pathway appears to be much less complex on the Au(111) surface. It has therefore been suggested that the substrate reduces the reaction barrier significantly [20]. Furthermore, Weigelt *et al.* demonstrated the same imidisation reaction with a three-spoke aldehyde, resulting in a different geometry of the reaction product [201]. However, neither of those experiments resulted in extended periodic COFs. The co-deposition and subsequent polyimidisation of a porphyrin with amino end-groups and PTCDA⁴ recently investigated by Lee [202] did not yield networks of notable size either, due to competing reactions between the porphyrin precursors. Treier *et al.* studied other combinations of PTCDA with either linear or three-spoked amino-substituted molecules⁵, which resulted in covalently bonded wire-structures and occasional triangular pores, respectively [203].

The formation of porphyrin-based COFs via thermally induced, surface-assisted radical coupling of tetra(mesityl) porphyrins on Cu(110) was reported by In't Veld *et al.* [200]. The resulting networks are very similar to those observed by Grill *et al.* (see section 7.1), as can be seen in the STM image in Fig. 8.2. However, in this case the surface chemistry leading to molecular interconnection is based on the surface-catalysed dehydrogenation of the para-mesityl groups upon annealing of the sample, leading to CH_2^\bullet radicals which then homocouple and form ethylene bridges between the TPP units. This reaction is strongly dependent on the catalytic characteristics of the copper substrate and is not

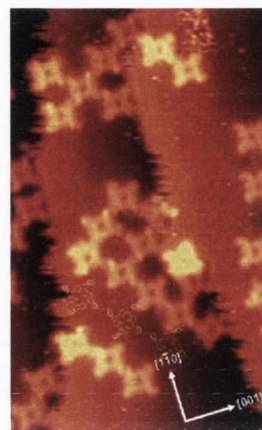


Figure 8.2 Filled state STM image of tetra(mesityl) porphyrin COFs, taken at -0.24 V and 0.26 nA, (12.6×20.6) nm. Additional graphic representation of trimer (not scaled to STM image). Taken from [200].

⁴3,4,9,10-perylene tetracarboxylic dianhydride

⁵4,4'-diamino-*p*-terphenyl (DATP) and 2,4,6-tris(4-aminophenyl)-1,3,5-triazine (TAPT)

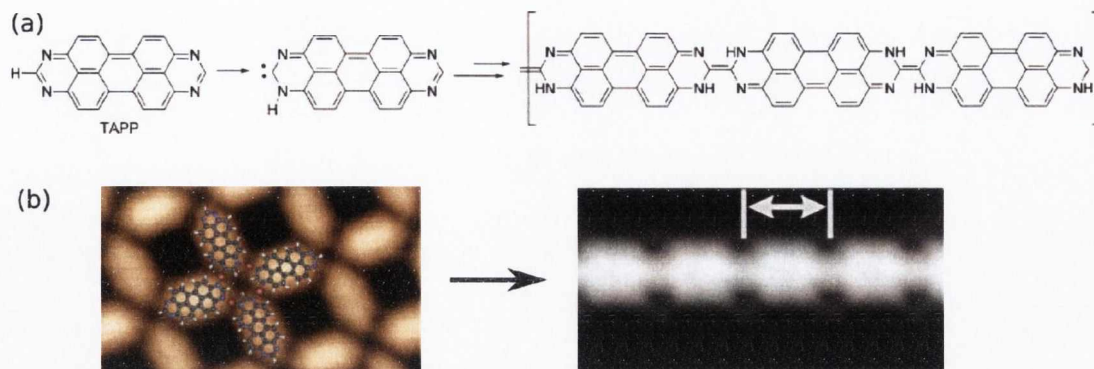


Figure 8.3 (a) Reaction scheme of the tautomerisation and polymerisation of TAPP, (b) STM images of the metal-coordinated porous network formed by TAPP on Cu(111) at 150°C (taken at 0.4 V and 0.02 nA, $5 \times 3 \text{ nm}^2$, red: copper atoms) and of the polymers formed after annealing at 250°C (taken at 0.1 V and 0.02 nA, distance between chain elements $1.23 \pm 0.12 \text{ nm}$). Adapted from Matena *et al.* [208].

expected to take place on the more inert Au(111) surface [20]. However, the previously discussed formation of graphene nanoribbons via both dehalogenation and subsequent cyclodehydrogenation reported by Cai *et al.* (see Fig. 7.4) has been demonstrated on the Au(111) surface, although annealing at relatively high temperatures around 400°C was required to initiate the reaction without the presence of a highly catalytic substrate. Other structures which have been synthesised via surface-assisted cyclodehydrogenation reactions include nanographenes [204] and even 3-dimensional structures like nanodomes and fullerenes [205–207].

Dehydrogenation has furthermore been observed among amino-substituted molecules. Weigelt *et al.* reported the reaction of octylamine into trioctylamine upon annealing of a self-assembled molecular monolayer on the Au(111) surface and suggested a dehydrogenation and a possible subsequent desorption of nitrogen complexes as the underlying reaction mechanism [209]. Lee *et al.* observed the same formation of covalent bonds between amino-substituted porphyrins on Au(111), Ag(111) and Cu(111) [202]. Recent DFT calculations suggest that the thermodynamically most favourable reaction product is a HN-NH bond between two molecular building blocks, with a possibility of some N=N or occasional C-C bonded side-products [210].

A third on-surface reaction pathway has been reported by Matena *et al.*, who demonstrated the formation of 1D oligomers from 1,3,8,20-tetraazaperopyrene (TAPP) on Cu(111) [208]. The precursor molecule was first evaporated onto the substrate surface held at 150°C, which resulted in a porous network coordinated by interactions between the nitrogen lone pairs of the adsorbed molecules and the copper atoms of the surface. After annealing at temperatures above 250°C, these networks evolved into covalently bonded TAPP chain-structures via the tautomerisation and subsequent polymerisation of the pre-

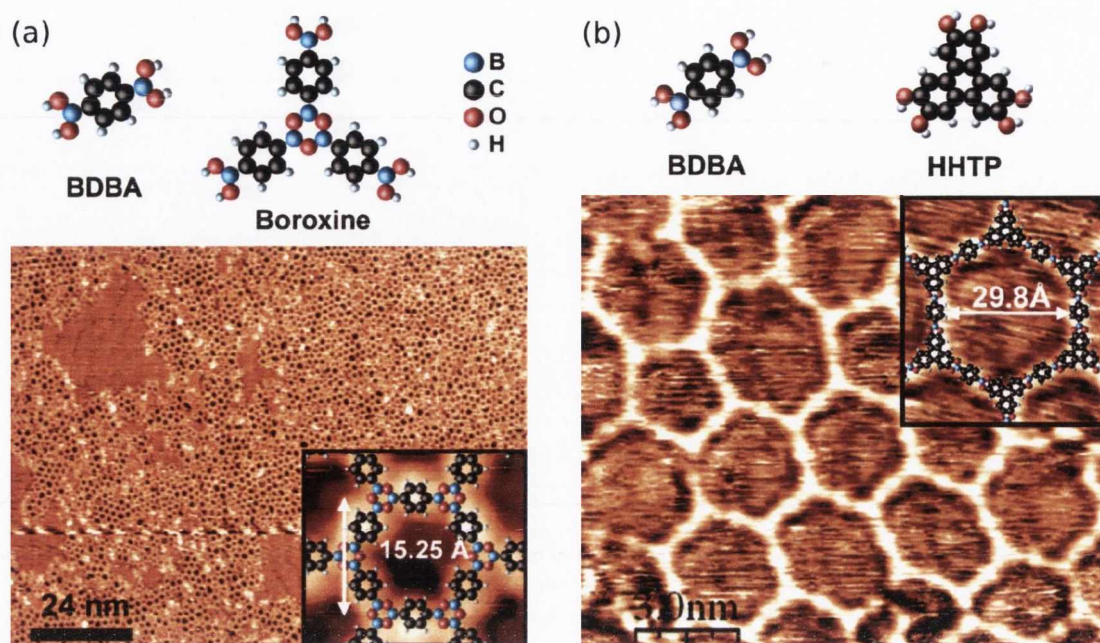


Figure 8.4 (a) COFs formed by BDBA upon deposition on Ag(111), top: molecular structures of precursor and boroxine reaction product, bottom: STM image ($120 \text{ nm} \times 90 \text{ nm}$) of BDBA-COF, taken at -2.1 V and 0.4 nA ; (b) COFs formed by BDBA and HHTP upon deposition on Ag(111), top: molecular structures, bottom: STM image of the COF, taken at -2.2 V and 1.7 nA . Adapted from Zwaneveld *et al.* [211].

cursors as shown in the reaction scheme in Fig. 8.3a. Fig. 8.3b shows the respective STM images. The thus formed wires have delocalised electrons and pave the way for high-conductance molecular wires that are impossible to synthesise by traditional solution chemistry.

Another reaction taking place at room temperature was described by Zwaneveld *et al.* and resulted in COFs extending over large surface areas [211]. The molecular precursor BDBA was evaporated on the Ag(111) surface and, upon adsorption, formed arrays of boroxine via intermolecular dehydration (loss of H_2O) as shown in Fig. 8.4a. These networks proved to be stable to temperatures of 750 K . In a follow-up study, the group investigated the influence of different substrates, of the flux and of the substrate temperature during deposition on the quality of the networks [196]. The least defected COFs were achieved on Ag(111) with a high flux during deposition. The substrate temperature was suggested to be tuned to a balance between enhanced diffusion and long residential time of the precursor molecules, which is different for every substrate. The study also emphasised that the defects in the networks are due to the irreversibility of the covalent bonds. In a further attempt to improve the BDBA COFs [212], Faury *et al.* recently followed a similar approach as Lafferentz *et al.* with their hierarchial growth of networks with two subsequent activation steps [186] (see section 7.1). They used *p*-bromo-benzenboronic acid

(BBBA) as precursor molecules, which first reacted via their boronic acid end-groups into boroxine trimers upon deposition, and were subsequently thermally activated by annealing of the sample to undergo Ullmann-type reactions on their bromine-substituted ends and form extended networks with fewer defects. The Au(111) surface was chosen as the more suitable substrate because the Ullmann-type reaction also happens at room temperature on Ag(111).

A second reaction presented by Zwaneveld *et al.* also uses BDBA precursors, but combined with 2,3,6,7,10,11-hexahydroxytriphenylene (HHTP) [211]. The boronic acid groups of BDBA and the diol groups of HHTP undergo an esterification reaction and form a dioxaborole heterocycle, as shown in Fig. 8.4b. This mechanism facilitated large pore-sizes and fewer defects than BDBA alone.

The most recently developed reaction mechanism results in the formation of extended sheets of polymeric Fe-phthalocyanine. Abel *et al.* used TCNB⁶ as the organic precursor, which underwent a metal-directed surface reaction when codeposited with Fe on both the Au(111) and Ag(111) surfaces [197], as shown in Fig. 8.5. The covalent nature of the bonds between the dicyano functional groups can be deduced from the small dimensions of the mesh pores (1.15 nm) and the square symmetry. The poly-FePc sheets are 10-30 nm large and come in three domain orientations on both Au(111) and Ag(111), reflecting the threefold symmetry of those surfaces. Remarkably, the formation of poly-FePc was also observed on a thin insulator film (NaCl) on Ag(111), showing that no metal surface is required as a catalyst for this reaction. Poly-FePc has a delocalised π -electron system and magnetic metal atoms spread periodically throughout the polymer lattice, which makes it an interesting system for the field of spintronics.

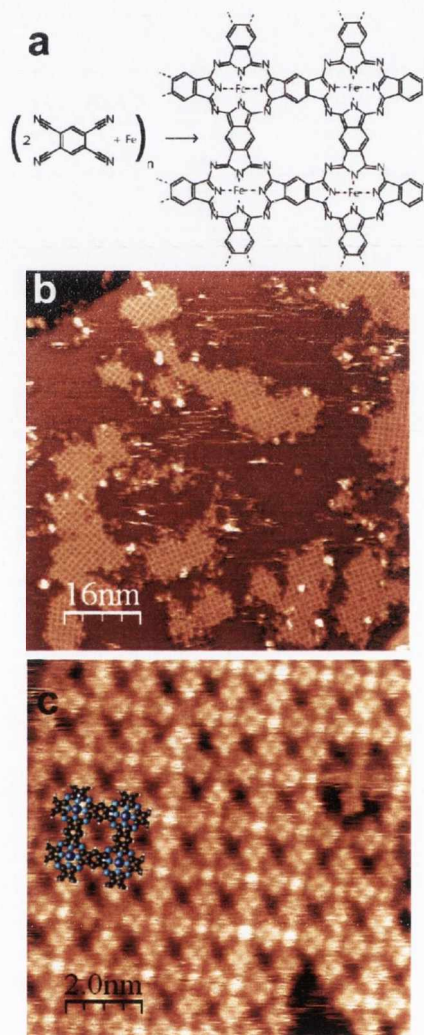


Figure 8.5 (a) Synthesis reaction scheme of poly-FePc; (b) and (c) STM images of poly-FePc formed on Ag(111). Taken from Abel *et al.* [197].

⁶see section 3.3.6

8.2 Dehydration of BDBA on Ge(001):Cl

The reaction of BDBA precursor molecules into boroxine (B_3O_3) rings with the elimination of water (see Fig. 8.4a) has been shown to occur at room temperature on various coinage metal surfaces [196], indicating a low reaction barrier. While thermal activation is most likely still required without the presence of a catalytic metal surface, comparatively low temperatures are expected to suffice. Furthermore, the elimination product H_2O is a closed compound and unlikely to attack a halogen passivation layer. The dehydrogenation of BDBA is therefore a promising reaction mechanism for the creation of 2D COFs on passivated Ge(001). Since the previous chapters have shown chlorine to be the most stable and suitable passivation agent and the time for experiments at IM2NP was restricted, only Ge(001):Cl has been used as a substrate for COF formation on a semiconductor surface.

The BDBA molecules were evaporated onto Ge(001):Cl at 105°C, for a duration which had previously been determined to result in a monolayer coverage on the coinage metal surfaces. Fig. 8.6a shows an STM image after the deposition, revealing only very few molecules, most likely adsorbed on defect sites. Some molecules (circled) appear or disappear while scanning the surface, suggesting that the interaction with the STM tip can be enough to overcome the bond between the molecules and the surface dangling bonds. Several further depositions did not change the molecular coverage and general appearance of the surface, which shows that the molecules are too small to remain adsorbed on the surface, similar to TBB (see section 7.3.3). Larger molecules with the same functional end-groups are available, but would require higher evaporation temperatures which

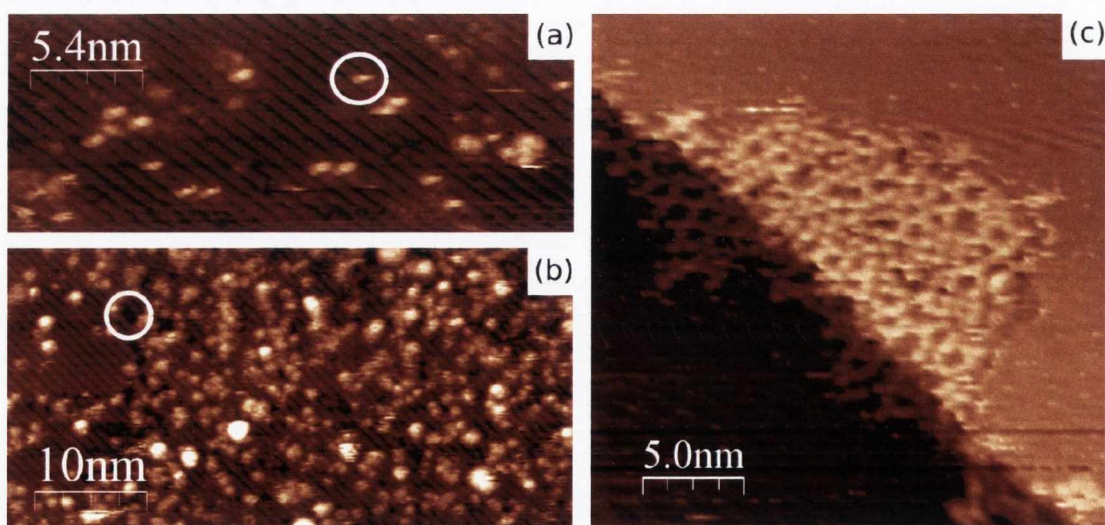


Figure 8.6 (a) Filled state STM image of BDBA on Ge(001):Cl, taken at -1.45 V and 0.25 nA; (b) filled state STM image of BDBA deposited on Ge(001):Cl held at 150°C, taken at -1.4 V and 0.3 nA; (c) empty state STM image of a COF formed by BDBA on Ag(100), taken at 1.9 V and 0.3 nA.

would result in polymerisation of the precursor molecules in the crucible. Therefore, on-surface reactions with low activation barriers require small precursor molecules, which consequently lack large enough conjugated π -systems to adsorb on passivated Ge(001).

A possible way to overcome this problem is the deposition of BDBA on the Ge(001):Cl surface held at an elevated temperature, causing the molecules to react with each other into larger compounds on impact on the surface. Fig. 8.6b shows an STM image after BDBA deposition at a substrate temperature of 150°C. The amount of adsorbed molecules is significantly higher than after deposition on the surface at room temperature. However, no indication for COF fragments can be found and the molecules appear disordered. Additionally, the underlying surface shows the onset of small etch pits (circled in Fig. 8.6b), which suggests that the increase in adsorbed molecules is connected with an increase in the defect density. The reason for this surprisingly low desorption temperature of the chlorine-passivation is difficult to determine since the resolution and intensity of the XPS system at IM2NP is insufficient to observe a change in the ratios between the carbon, boron and oxygen in the still relatively small coverage of BDBA.

Fig. 8.6c shows an STM image of a sub-monolayer coverage of BDBA on Ag(100)⁷, which has been taken as a reference experiment between depositions of BDBA on Ge(001):Cl. The image clearly shows the successful COF formation from BDBA on coinage metal surfaces at RT as reported by Zwaneveld, Ourdjini *et al.* [196,211]. The direct comparison between the behaviour of BDBA on a noble metal and on a passivated germanium surface exposes the importance of the substrate for the reaction mechanism. Since the dehydration of BDBA also occurs in solution without the presence of a catalyst, the substrate for the 2D COF formation only has to provide a degree of interaction which holds the molecules on the surface but enables them to be mobile enough to find reaction partners at the same time. While the coinage metal surfaces appear to be very suitable for this purpose, the passivated Ge(001) surface only sufficiently interacts with large, macrocyclic molecules to hold them on the surface and also displays unavoidable defects, which inhibit the mobility of the molecules more significantly than anticipated.

8.3 Formation of polymeric Mn-phthalocyanine

Another COF reaction mechanism with a low reaction barrier is the formation of polymeric metal-phthalocyanine by co-deposition of TCNB precursors and metal atoms (see Fig. 8.5). In this experiment, manganese (Mn) has been used instead of the iron previously employed for this reaction by Abel *et al.* [197]. As mentioned in section 8.1, this reaction has been shown to occur on an insulator film (NaCl/Ag(100)) and therefore does not require a metallic substrate. Additionally, the reaction does not create any byproducts

⁷This surface has only been used once for this work and is therefore not discussed in detail. For exemplary PES and STM studies of Ag(100) see references [213,214].

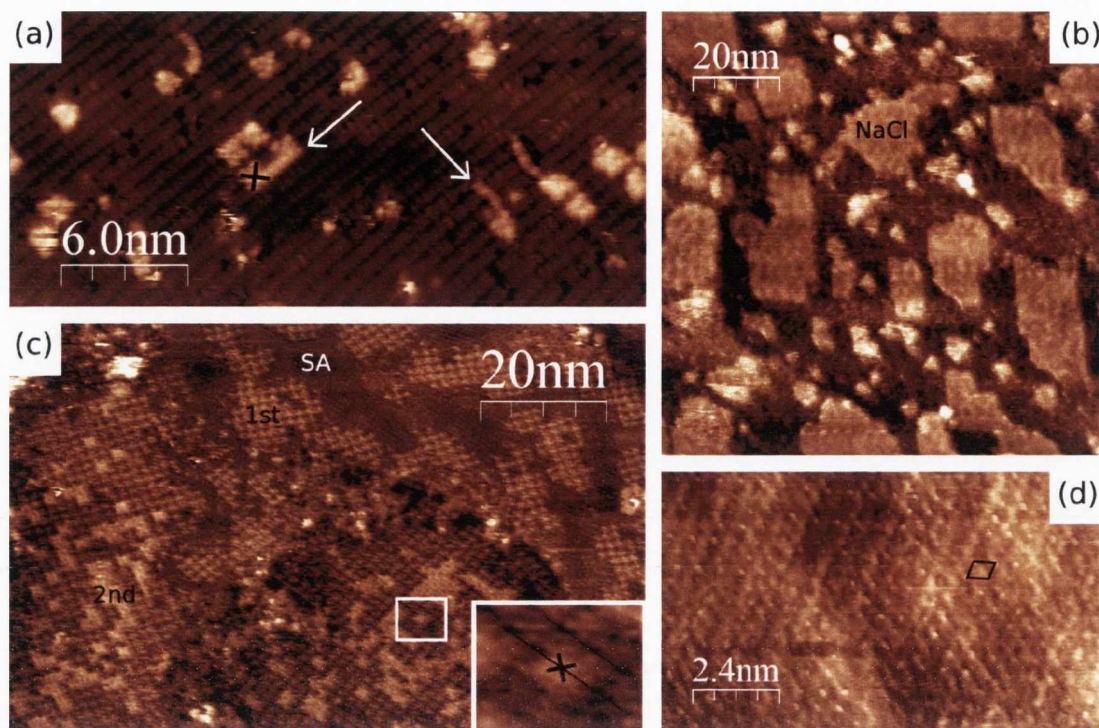


Figure 8.7 (a) Filled state STM image of TCNB and Mn codeposited on Ge(001):Cl at 100°C, taken at -1.5 V and 0.4 nA; (b) filled state STM image of 0.5 DL NaCl on Ge(001), taken at -2.0 V and 0.7 nA; (c) filled state STM image of >1 ML of poly-MnPc formed from TCNB and Mn on Au(111), taken at -1.7 V and 0.3 nA; (d) close-up STM image of an NaCl island grown on Ge(001), taken at -2.0 V and 0.7 nA.

like halogen radicals (Ullmann-type) or water (dehydrogenation). Both Ge(001):Cl and a NaCl film grown on Ge(001) have been used as substrates, as well as the alternative precursor molecule TCN-DBTTF⁸.

8.3.1 TCNB precursors

TCNB was first deposited on the Ge(001):Cl surface with a cell temperature of 105°C. As with BDBA, the STM images show no evidence of TCNB adsorbed on the surface (except on defects), due to its small size. The co-deposition of Mn from an e-beam evaporator with a flux of ~0.5 nA did not change this behaviour. However, after co-depositing both TCNB and Mn on the Ge(001):Cl surface held at ~100°C, occasional square features of phthalocyanine dimensions can be observed, as shown in Fig. 8.7a. Additionally, linear growth of adsorbates of the size of Mn atoms both across and along the dimer rows can be seen as indicated by the arrows, which could indicate that Mn adsorbs on the Ge(001):Cl surface much more readily than the TCNB molecules. This linear growth is reminiscent of the adsorption of styrene molecules on Si(001):H, which Tong *et al.* explained with

⁸see section 3.3.7

an adsorbate-induced dangling bond diffusion mechanism [215]. The small number of what appear to be single Pc features in the images indicates that the adsorption of either precursor molecules or Mn atoms or both is still dependent on the presence of defect sites. Once one of the components for on-surface Pc synthesis is absorbed on the surface, the elevated substrate temperature activates the reaction and a single Pc compound can be formed. No extended COF formation or even a Pc dimer has been observed. As with the previously discussed COF formation mechanisms on passivated Ge(001), the defects and the insufficient interaction with small precursor molecules can be identified as the main problems inhibiting network growth.

NaCl/Ge(001)

As on Ag(100), thin films of NaCl can be grown on Ge(001) when evaporated onto the surface cooled down to temperatures less than 200 K [216, 217], which was possible on the UHV system in IN2MP using liquid nitrogen. The resulting films do not have defect sites like the previously discussed surface passivation techniques and have been shown to be suitable substrates for poly-Pc formation [197]. Fig. 8.7b shows the Ge(001)/NaCl surface after the co-deposition of approximately 1 ML of TCNB molecules and of Mn atoms⁹. The size of the NaCl islands ranges from 10 to 30 nm, with an overall coverage of 0.5 DL (double layers) of NaCl dipoles. A close-up filled state STM image with atomic resolution in Fig. 8.7d shows a lattice of bright protrusions, which are associated with the Na⁺ ions [217]. The unit cell, as marked in black, is distorted from its previously reported square dimensions due to thermal drift, yet its average side length of 0.4 nm is in agreement with the value found by Glöckler *et al.*.

The STM images show no molecules or metal atoms on top of the NaCl islands, which did not change after additional evaporation steps. Additionally, the areas of clean Ge(001) surrounding the NaCl islands could not be resolved and were increasingly difficult to image with the STM. This indicates that both TCNB and Mn atoms adsorb on the clean and still very reactive areas of the surface and do not cover the inert NaCl films even at higher coverages, unlike what has been observed on Ag(100)/NaCl. It appears that despite the surface of the NaCl film appearing to be the same, the underlying substrate may have an influence on the adsorption behaviour of both organics and metal atoms. The origin of this effect has not been investigated further in this work.

Au(111)

As for the dehydration of BDBA, a reference experiment on the reaction mechanism leading to the formation of poly-MnPc has been conducted on a noble metal surface, in this case Au(111). Fig. 8.7c shows an STM image after the co-deposition of TCNB and Mn on

⁹Same deposition parameters as for the successful experiments on Ag(100)/NaCl as reported in [197].

Au(111) at RT. It shows some areas of self-assembled TCNB molecules (marked “SA”), areas with on-surface synthesised Pc molecules (marked “1st”), and some Pc molecules forming a second layer (marked “2nd”). The formation of a second layer of Pc molecules had not been observed before and is an additional confirmation that the reaction does not require a supporting metal surface. The centres of the second-layer Pc molecules always sit between two rows of first-layer Pc, as can be seen with the isolated second-layer molecule circled in Fig. 8.7c.

No poly-Pc network could be observed in the few STM images that were taken of this system. Abel *et al.* also observed the formation of single Pc instead of poly-Pc sheets on noble metal surfaces and attributed this to different ratios of the TCNB precursors and the metal atoms [197]. However, further experiments have recently shown that both phases coexist on most surfaces, therefore disproving their previous hypothesis of stoichiometry dependency [218]. The origin of the two different phases is still unknown and has not been investigated further in this work due to the restricted time for the experiments.

8.3.2 TCN-DBTTF precursors

To increase molecule-substrate interactions and prevent premature desorption of the precursors on chlorine-passivated Ge(001), a larger molecule with the same “outer” functionality as TCNB has been investigated as a precursor. The cyano groups of TCN-DBTTF are expected to undergo the metal-directed reaction into poly-Pc similar to TCNB, but with TTF bridges between the Pc units and therefore larger pores. As with TCNB, Mn atoms have been used for the experiments in this work. Since no previous work has been done on this molecule, it was first deposited on the Au(111) surface to investigate its behaviour.

Au(111)

TCN-DBTTF was evaporated at 290°C and codeposited with Mn on the Au(111) surface. Fig. 8.8a shows an STM image of the surface after deposition. No poly-MnPc networks were observed in the STM images, only two different patterns of self-assembled TCN-DBTTF molecules. Fig. 8.8b and c shows close-up STM images of the two patterns with possible packing structures. The pattern in Fig. 8.8b appears to be based on an interaction between the cyano end-groups and the central sulfur atoms of the molecules. The other configuration in Fig. 8.8c is more difficult to interpret. It shows rows of brighter and darker contrast, sometimes alternating as in the close-up and sometimes next to each other as can be seen on the top left in Fig. 8.8a. The darker rows also appear to be governed by the aforementioned cyano group-sulfur interaction, but in a different geometry than in Fig. 8.8b. The brighter rows have the dimensions of two TCN-DBTTF molecules directly next to each other, with the depression in the centre in the position of the fulvalene bridges.

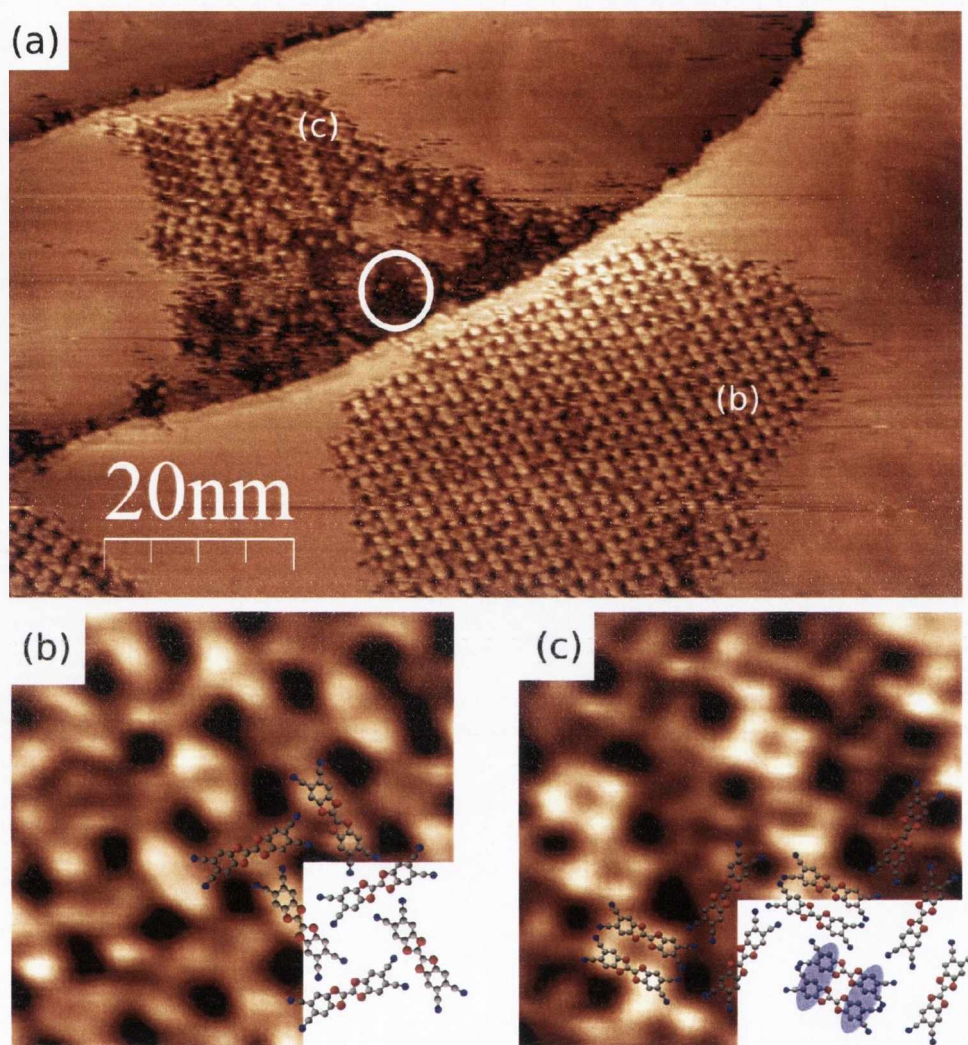


Figure 8.8 (a) Filled state STM image of TCN-DBTTF/Mn on Au(111), taken at -1.9 V and 0.3 nA; (b) and (c) close-up of respectively marked packing patterns in (a) with molecular structures.

It is also possible that the molecules are not adsorbed with their aromatic benzene rings parallel to the surface, but at an angle of 90° . This configuration would result in π - π interactions between the orbitals of two molecules as indicated in blue in the molecular structure, which could explain the contrast difference to the other configuration in Fig. 8.8c.

The only indication of the Mn atoms¹⁰ can be found close to the step-edge in Fig. 8.8a, as marked by the circle. Some areas of dark contrast show what looks like single atoms packed next to each other. This has not been observed for the TCNB precursors on this surface and could indicate that metal-coordination network and subsequent poly-Pc

¹⁰XPS data (not shown) indicates that Mn is present on the surface

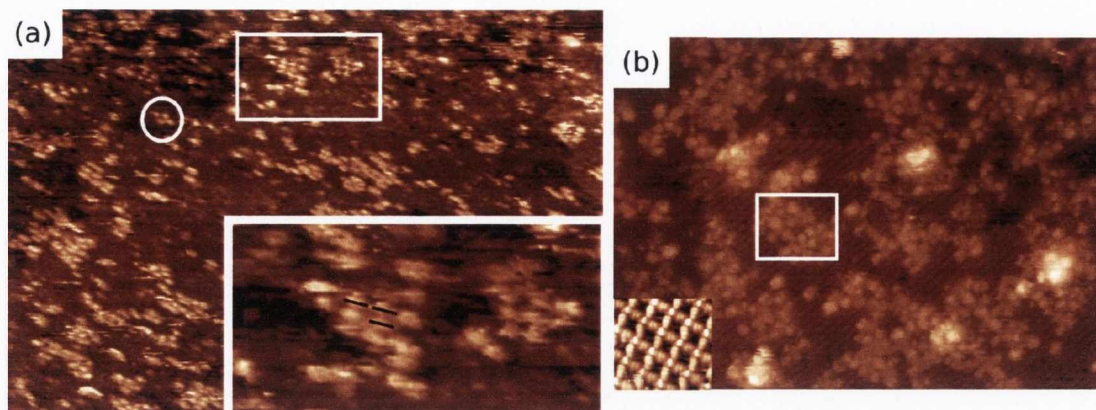


Figure 8.9 (a) Filled state STM image of TCN-DBTTF/Mn on Ge(001):Cl, taken at -1.9 V and 0.35 nA, (75×50) nm, with inset: close-up of marked area; (b) filled state STM image of TCN-DBTTF/Mn co-deposited on Ge(001):Cl held at 120°C and subsequently annealed at 160°C, taken at -1.7 V and 0.15 nA, (50×35)nm, with inset: comparable poly-Pc network (to scale) as observed on Au(111) by Abel *et al.* [218].

formation with TCN-DBTTF is not possible.

The restricted time frame did not allow for better resolved images which could possibly clarify the pattern configurations. No subsequent annealing steps or optimisation of the molecule-metal atom ratio in order to possibly obtain poly-Pc networks were performed either, but will be investigated in the future by Abel and co-workers [218].

Ge(001):Cl

After investigating the behaviour of TCN-DBTTF and Mn on Au(111), the molecules were deposited on the Ge(001):Cl surface, at first without Mn atoms. While the XPS data¹¹ shows the presence of molecules on the surface, no STM images could be obtained, suggesting that the molecules are very mobile on the surface. After the deposition of Mn atoms, the molecules appear to be less mobile and some STM images as shown in Fig. 8.9a could be taken. The molecules have assembled into islands, some of which appear like porous structures as shown in the close-up of the marked area in the inset of Fig. 8.9a. However, the dimensions of these islands do not agree with the TCN-DBTTF/Mn pore size of (2.0×2.0) nm [218], but are roughly (1.0×1.7) nm large. The length of a single TCN-DBTTF molecule is about 1.6 nm as indicated by the black lines in the close-up image, which suggests that the observed islands consist of merely self-assembled molecules. The position of the Mn atoms and their role in the molecule assemblies is unclear. The circle in Fig. 8.9a shows one instance of a Pc-like feature, which could indicate a metal-coordinated TCN-DBTTF assembly.

¹¹not shown

In another experiment, TCN-DBTTF and Mn were codeposited on the Ge(001):Cl surface held at 120°C and subsequently annealed to 160°C. An STM image of the resulting surface is shown in Fig. 8.9b. The molecules are comparatively well resolved, suggesting limited mobility. There are a few structures, as indicated by the white rectangle in Fig. 8.9b, with the dimensions of the metal-coordinated Pc networks that have very recently been found to form on Au(111) by Abel *et al.*¹² [218], as shown in the inset. However, no extended poly-Pc networks could be observed and the molecules appear in a mostly random assembly. As with all other investigated COF reaction mechanisms, it is reasonable to assume that the self-assembly and effective network formation of the molecules is restricted by defects in the surface-passivation. No experiments were performed on a NaCl film on Ge(001), since the time for the experiments at IM2NP was over and the required cooling of the sample during NaCl growth could not be performed in CRANN.

8.4 Summary

In addition to the dehalogenation reactions discussed in the previous chapter, two other reaction mechanisms were investigated for COF formation on a germanium surface. The dehydrogenation of BDBA precursors and the metal-directed formation of poly-Pc sheets from TCNB as well as TCN-DBTTF molecules and Mn atoms have been chosen mostly due to their low activation barrier and the lack of radical byproducts, in order to avoid elevated temperatures or pairing mechanisms which might cause partial desorption of the chlorine-passivation layer on Ge(001).

While the BDBA precursors were shown to form COFs directly upon adsorption at room temperature on the Ag(100) surface, they did not adsorb on the Ge(001):Cl surface except on defect sites. Their small size and lack of a large conjugated π -system restricts the interaction with the Ge(001):Cl surface. No larger molecules with the same functional groups as BDBA could be evaporated at temperatures low enough to avoid polymerisation in the crucible. It therefore remains unknown whether the dehydration reaction can occur without the presence of a catalysing metal surface. In any case, COF formation via this reaction is not possible on the Ge(001):Cl surface.

The TCNB precursor molecules for poly-MnPc formation showed the same non-adsorbent behaviour as BDBA, since their core only consists of a single benzene ring as well. However, when co-deposited with Mn at elevated sample temperatures, a few single features of Pc dimensions could be observed, suggesting that the metal atoms might be able to “trap” TCNB on the surface when provided with sufficient thermal energy. Yet those features remained isolated and no extended networks could be created. In order to avoid the limiting influence of the defects in the chlorine-passivation, the TCNB/Mn system was subsequently deposited onto thin NaCl islands grown on clean Ge(001). Independednt of

¹²unpublished

the coverage, no molecules or Mn atoms could be observed on the NaCl islands, while the surrounding areas of clean surface could not be resolved. This indicates preferred adsorption of both TCNB and Mn on the clean surface areas. To avoid this effect, the Ge(001) surface could be passivated after NaCl growth, but STM imaging of the insulating films was very time-consuming and difficult and no further experiments could be performed on this surface in the limited time at IM2NP.

TCN-DBTTF has the same end-groups as TCNB and is therefore expected to undergo the same reaction into poly-Pc sheets when co-deposited with metal atoms. However, a brief test-experiment with TCN-DBTTF/Mn on the Au(111) surface did not yield poly-Pc networks and only showed the molecules self-assembled in two different patterns as well as what appear to be separated islands of Mn atoms. Further experiments on this system by Abel *et al.* are in progress and have recently shown that the formation of poly-Pc networks is possible with this precursor. On Ge(001):Cl, some isolated features with the dimensions of metal-coordinated TCN-DBTTF assemblies could be observed, but without long range-order like on Au(111). It is reasonable to assume that this system also suffers from interactions between the molecules and the defects in the surface passivation, thereby prohibiting long-range order and extended COF formation.

Overall, it has been shown that neither the dehydration of BDBA nor the metal-directed poly-Pc formation were successful on the modified Ge(001) surfaces, either due to the insufficient degree of non-covalent interactions between the surface and the precursor molecules or due to defects which limit the mobility and long-range order of the adsorbates.

9 Conclusions

The original objective of this work was the *bottom-up* formation of covalently bonded nanostructures from organic molecular building blocks on a group IV semiconductor surface. The project was initially inspired by the first demonstration of an on-surface reaction of organic molecules into COFs via a dehalogenation reaction on Au(111) by Grill *et al.* in 2007 [19]. Transferring this concept to germanium(001) has highlighted several issues.

The first issue concerns the nature of the interactions between the molecular building blocks and the substrate. Chapter 5 of this work concentrates on the adsorption of $\text{H}_2\text{TBr}_4\text{PP}$, later used as a precursor molecule for COF formation, on clean Ge(001). Although no full adsorption geometry for the relatively complex porphyrin molecules could be determined, two main interaction mechanisms were identified. The PES shows evidence for charge transfer between the bromine substituents of the molecule and the underlying germanium surface atoms directly upon adsorption, as well as an interaction between the conjugated π -system of the macrocycle and the surface as it was previously observed for phthalocyanine molecules. The bromine-germanium interaction was also observed for $\text{H}_2\text{TBr}_4\text{PP}$ adsorbed on both Ge(111) and Ge(110).

The second issue concerns the local geometry as revealed by STM. Images of $\text{H}_2\text{TBr}_4\text{PP}$ on Ge(001) reveal two distinct adsorption geometries of the molecule in a coverage-independent 1:1 ratio. One of them appears to be strongly attached to the surface on one side and tilted away from the surface on the other, while the second type shows a conformational change to the saddle-shape which is frequently reported for strongly-interacting porphyrin molecules. The saddle conformation is also reflected in the valence band spectra for $\text{H}_2\text{TBr}_4\text{PP}$ on clean Ge(001), as a comparison with DFT calculated spectra for different geometries of the molecule shows. However, these calculations did not consider the specific interactions with the Ge(001) surface and therefore do not yield enough information to connect the STM images to the two interaction mechanisms observed in the PES data and to identify the exact adsorption geometry. A comparison between the adsorption geometries of the bromine-substituted TPP and the unsubstituted TPP shows significant differences, which demonstrates that the substituents influence the adsorption mechanism significantly.

Most importantly, none of the organic molecules investigated are mobile on the surface or show long-range order, independent on whether the molecule is bromine-substituted ($\text{H}_2\text{TBr}_4\text{PP}$ vs. H_2TPP) or has a large macrocycle ($\text{H}_2\text{TBr}_4\text{PP}$ vs. TBB). This suggests

that for all organic molecules the molecule-substrate interactions dominate over molecule-molecule interactions, which are essential for the desired intermolecular reactions and COF formation. It is therefore necessary to suppress the former interactions via passivation of the surface.

Atomic hydrogen is the most established passivation agent for Ge(001) in both UHV and wet-chemical processing, while halogens are almost exclusively used in the latter. Chapter 6 of this work discussed the passivation of Ge(001) with chlorine, bromine and iodine via deposition from respective electrochemical cells in UHV. Both the bromine- and chlorine- passivation of Ge(001) have been shown to be thermally more stable than the hydrogen-passivation and have a lower average defect density. Their desorption mechanism is comparatively complex and results in the formation of GeX_2 complexes and subsequent etching of the surface, which appears to follow different pathways (lines or pits) depending on the size of the halogen atom.

An STM investigation of the adsorption of single halogen atoms or very low coverages revealed several different adsorption configurations, in contrast to previous studies on Si(001) where the adsorption of halogens appears to be less complex than on Ge(001). Supporting DFT calculations for a single bromine atom adsorbed on Ge(001) show some agreement with the configuration found in the STM images. However, it is not the minimum energy configuration according to the calculations, which raises questions about the validity of the used code and whether halogen atoms appear as bright or dark contrast in the STM images. Work on these issues is still in progress.

Another issue became apparent when investigating the dehalogenation reaction as a pathway for COF formation on passivated Ge(001), as discussed in Chapter 7 of this work. Synchrotron PES data taken after annealing of $\text{H}_2\text{TBr}_4\text{PP}$ precursor molecules on Ge(001):H shows evidence for the successful activation, i.e. cleavage of the bromine-carbon bond, without the presence of a catalytic metal surface which is commonly considered essential for this reaction to take place. However, the bromine-dissociation appears to be associated with an unexpected partial loss of the hydrogen-passivation, which indicates a pairing mechanism leading to the formation of HBr and the resultant premature desorption of the passivation agent. In a subsequent STM study of this system, the $\text{H}_2\text{TBr}_4\text{PP}$ molecules were evaporated at a higher temperature and activated in the crucible. This resulted in a few chain-like structures on the surface, which could indicate intermolecular bonds, but more frequently there are single molecules which are most likely adsorbed on defect sites.

The most extensive and best resolved chain and pore structures were observed after activation of the previously self-assembled intact $\text{H}_2\text{TBr}_4\text{PP}$ molecules on chlorine-passivated Ge(001), confirming that the strong chlorine-germanium bonds make it the most suitable passivation agent for COF formation. However, the quality of the COFs is still very poor compared to the results achieved on the noble metal surfaces, indicating that the

unavoidable intrinsic defects in the passivation layer limit the mobility of the molecules significantly. Whether a similar pairing mechanism between the dissociated bromine-substituents and the passivation agent as suggested by the PES data on Ge(001):H occurs on the halogen-passivated surfaces, and if this is in fact an essential catalytic side-reaction, remains unclear due to the lack of well resolved synchrotron PES data.

Experiments with smaller precursor molecules revealed either increased clustering or premature desorption of the adsorbates as additional problems inhibiting COF formation on passivated Ge(001), suggesting that molecules with large conjugated π -systems are the better choice as precursors for COF formation on weakly-interacting substrates.

Two alternative reaction mechanisms with a lower reaction barrier than the dehalogenation and no radical byproducts on Ge(001):Cl were investigated in an attempt to avoid the previously identified issues. The BDBA molecules undergoing a dehydrogenation reaction on noble metal surfaces did not adsorb on passivated germanium due to their small size, and larger precursors with the same functional groups cannot be evaporated without polymerisation in the crucible. The metal atom-directed formation of poly-Pc sheets using TCNB precursors was restrained due to the same reason, while the larger TCN-DBTTF precursors only formed small metal-coordinated network-fragments, limited by defects on Ge(001):Cl.

All reaction mechanisms discussed in this thesis have been demonstrated to result in COF formation on Au(111), while only isolated instances of a few reacted molecules could be observed on Ge(001). This suggests that the properties which make the noble metal surfaces the perfect substrates for COF formation are, in addition to possible catalytic properties, the weak but sufficient surface attachment of organic adsorbates of any size and the simultaneous uniform lack of chemical bonding which enables the adsorbed molecules to be mobile enough to find reaction partners. These characteristics cannot be achieved using a clean group IV semiconductor surface as a substrate, since the molecule-surface interactions are too strong to allow diffusion of organic adsorbates. Equally, success on the passivated surface is limited by the fact that the interaction is too weak. A further complication is the presence of defects in the passivation, either intrinsic or induced by thermal activation of the molecules. For future work it is therefore suggested to grow the desired COFs on noble metal surfaces and subsequently use the wet-chemical methods that are already established for other 2D materials like graphene or MoS₂ [219, 220] for the transfer onto the technologically more relevant semiconductor surfaces.

Bibliography

- [1] Joachim, C., Gimzewski, J. K. & Aviram, A. Electronics using hybrid-molecular and mono-molecular devices. *Nature* **408**, 541 (2000).
- [2] Theobald, J. A., Oxtoby, N. S., Phillips, M. A., Champness, N. R. & Beton, P. H. Controlling molecular deposition and layer structure with supramolecular surface assemblies. *Nature* **424**, 1029 (2003).
- [3] Stepanow, S., Lin, N., Barth, J. V. & Kern, K. Surface-template assembly of two-dimensional metal-organic coordination networks. *Journal of Physical Chemistry* **110**, 23472 (2006).
- [4] MacLeod, J., Lipton-Duffin, J. & Rosei, F. Towards designing the form and function of 2D molecular systems. *SPIE Newsroom* (2009).
- [5] Barth, J. V., Costantini, G. & Kern, K. Engineering atomic and molecular nanostructures at surfaces. *Nature* **437**, 671 (2005).
- [6] Whitesides, G. M. & Grzybowski, B. Self-assembly at all scales. *Science* **295**, 2418 (2002).
- [7] Barth, J. V. Molecular architectonic on metal surfaces. *Annual Review of Physical Chemistry* **58**, 375 (2007).
- [8] De Feyter, S. & De Schryver, F. C. Two-dimensional supramolecular self-assembly probed by scanning tunneling microscopy. *Chemical Society Reviews* **32**, 139 (2003).
- [9] Stöhr, M. *et al.* Controlling molecular assembly in two dimensions: The concentration dependence of thermally induced 2D aggregation of molecules on a metal surface. *Angewandte Chemie International Edition* **44**, 7394–7398 (2005).
- [10] Keeling, D. L. *et al.* Assembly and processing of hydrogen bond induced supramolecular nanostructures. *Nano Letters* **3**, 9 (2003).
- [11] van Hameren, R. *et al.* Macroscopic hierarchical surface patterning of porphyrin trimers via self-assembly and dewetting. *Science* **314**, 1433 (2006).
- [12] Yokoyama, T., Yokoyama, S., Kamikado, T., Okuno, Y. & Mashiko, S. Selective assembly on a surface of supramolecular aggregates with controlled size and shape. *Nature* **413**, 619 (2001).
- [13] Rabe, J. P. & Buchholz, S. Commensurability and mobility in two-dimensional molecular patterns on graphite. *Science* **253**, 424 (1991).
- [14] Lin, N., Dmitriev, A., Weckesser, J., Barth, J. V. & Kern, K. Real-time single-molecule imaging of the formation and dynamics of coordination compounds. *Angewandte Chemie International Edition* **41**, 4779 (2002).
- [15] Barth, J. V. Fresh perspectives for surface coordination chemistry. *Surface Science* **603**, 1533 (2009).
- [16] Wang, Y. F. *et al.* Supramolecular patterns controlled by electron interference and direct intermolecular interactions. *Journal of the American Chemical Society* **131**, 10400 (2009).
- [17] Nitzan, A. & Ratner, M. A. Electron transport in molecular wire junctions. *Science* **300**, 1384 (2003).
- [18] Perepichka, D. F. & Rosei, F. Extending polymer conjugation into the second dimension. *Science* **323**, 216 (2009).

- [19] Grill, L. *et al.* Nano-architectures by covalent assembly of molecular building blocks. *Nature Nanotechnology* **2**, 687 (2007).
- [20] Gourdon, A. On-surface covalent coupling in ultrahigh vacuum. *Angewandte Chemie International Edition* **47**, 6950 (2008).
- [21] Mendez, J., Lopez, M. F. & Martin-Gago, J. A. On-surface synthesis of cyclic organic molecules. *Chemical Society Reviews* **40**, 4578 (2011).
- [22] Ahn, D. *et al.* High performance, waveguide integrated Ge photodetectors. *Optical Express* **15**, 3916 (2007).
- [23] Filler, M. A. & Bent, S. F. The surface as molecular reagent: organic chemistry at the semiconductor interface. *Progress in Surface Science* **73**, 1 (2003).
- [24] Loscutoff, P. W. & Bent, S. F. Reactivity of the germanium surface: Chemical passivation and functionalization. *Annual Review of Physical Chemistry* **57**, 467 (2006).
- [25] Oura, K., Lifshits, V., Saranin, A., Zotov, A. & Katayama, M. *Surface Science: An Introduction* (Berlin: Springer-Verlag, 2003).
- [26] Ley, L. & Cardona, M. *Photoemission in Solids II* (Springer-Verlag Berlin Heidelberg, 1979).
- [27] Holland, B. *An experimental investigation of metal phthalocyanine-germanium interfaces*. Dissertation, University of Dublin, Trinity College (2008).
- [28] Ibach, H. *Electron Spectroscopy for Surface Analysis* (Springer-Verlag Berlin Heidelberg, 1977).
- [29] Cardona, M. & Ley, L. *Photoemission in Solids I* (Springer-Verlag Berlin Heidelberg, 1978).
- [30] Hüfner, S. *Photoelectron Spectroscopy: Principles and Applications* (Berlin: Springer, 2003).
- [31] Henzler, M. & Göpel, W. *Oberflächenphysik des Festkörpers* (Teubner, 1994).
- [32] Doniach, S. & Sunjic, M. Many-electron singularity in X-ray photoemission and X-ray line spectra from metals. *Journal of Physics Part C Solid State Physics* **3**, 285 (1970).
- [33] Mahan, G. D. Collective excitations in X-ray spectra of metals. *Physical Review B* **11**, 4814 (1975).
- [34] Brisk, M. A. & Baker, D. A. Shake-up satellites in X-ray photoelectron spectroscopy. *Journal of Electron Spectroscopy and Related Phenomena* **7**, 197 (1975).
- [35] Shirley, D. A. High-resolution X-ray photoemission spectrum of the valence bands of gold. *Physical Review B* **5**, 4709 (1972).
- [36] Tougaard, S. Algorithm for analysis of low-energy-resolution REELS; determination of inelastic electron scattering cross-sections and applications in quantitative XPS. *Surface Science* **464**, 233 (2000).
- [37] Seah, M. P. & Dench, W. A. Quantitative electron spectroscopy of surfaces: A standard data base for electron inelastic mean free paths in solids. *Surface and Interface Analysis* **1**, 2 (1979).
- [38] Yeh, J. J. & Lindau, I. Atomic subshell photoionization cross sections and asymmetry parameters: $1 \leq z \leq 103$. *Atomic Data and Nuclear Data Tables* **32**, 1 (1985).
- [39] Moulder, J. F., Stickle, W. F., Sobol, P. E. & Bomben, K. D. *Handbook of X-Ray photoelectron spectroscopy* (Physical Electronics Inc., 1995).
- [40] Martensson, N. & Nilsson, A. On the origin of core-level binding energy shifts. *Journal of Electron Spectroscopy and Related Phenomena* **75**, 209 (1995).
- [41] Shirley, D. A. The effect of atomic and extra-atomic relaxation on atomic binding energies. *Chemical Physics Letters* **16**, 220 (1972).

- [42] Binnig, G., Rohrer, H., Gerber, C. & Weibel, E. Tunneling through a controllable vacuum gap. *Applied Physics Letters* **40**, 178 (1982).
- [43] Binnig, G., Rohrer, H., Gerber, C. & Weibel, E. Surface studies by scanning tunneling microscopy. *Physical Review Letters* **49**, 57 (1982).
- [44] Chen, C. J. *Introduction to Scanning Tunneling Microscopy* (Oxford University Press, 1983).
- [45] Bardeen, J. Tunneling from a many-particle point of view. *Physical Review Letters* **6**, 57 (1961).
- [46] Tersoff, J. & Hamann, D. R. Theory of scanning tunneling microscope. *Physical Review B* **31**, 805 (1985).
- [47] Tersoff, J. Method for the calculation of scanning tunneling microscope images and spectra. *Physical Review B* **40**, 11990 (1989).
- [48] Lang, N. D. Theory of single-atom imaging in the scanning tunneling microscope. *Physical Review Letters* **56**, 1164 (1986).
- [49] Stoll, E. Resolution of the scanning tunnel microscope. *Surface Science* **143**, L411 (1984).
- [50] Simmons, J. G. Generalized formula for the electric tunnel effect between similar electrodes separated by a thin insulating film. *Journal of Applied Physics* **34**, 1793 (1963).
- [51] Garcia, N., Ocal, C. & Flores, F. Model theory for scanning tunneling microscopy. *Physical Review Letters* **50**, 2002 (1983).
- [52] Feenstra, R. M. Band gap of the Ge(111)2×1, and Si(111)2×1 surfaces by scanning tunneling microscopy. *Physical Review B* **44**, 13791 (1991).
- [53] Feenstra, R. M., Stroscio, J. A. & Fein, A. P. Tunneling spectroscopy of the Si(111)2×1 surface. *Surface Science* **181**, 295 (1987).
- [54] Hohenberg, P. & Kohn, W. Inhomogeneous electron gas. *Physical Review* **136**, B864 (1964).
- [55] Kohn, W. & Sham, L. J. Self-consistent equations including exchange and correlation effects. *Physical Review* **140**, A1133 (1965).
- [56] Haller, E. E. Germanium: From its discovery to SiGe devices. *Materials Science In Semiconductor Processing* **9**, 408 (2006).
- [57] Cooper, A. S. Precise lattice constants of germanium, aluminum, gallium arsenide, uranium, sulphur, quartz and sapphire. *Acta Crystallographica* **15**, 578 (1962).
- [58] Rossmann, R. *et al.* The Ge(001) (2× 1) reconstruction: asymmetric dimers and multilayer relaxation observed by grazing incidence X-ray diffraction. *Surface Science* **279**, 199 (1992).
- [59] Conwell, E. M. Properties of silicon and germanium. *Proceedings of the Institute of Radio Engineers* **40**, 1327 (1952).
- [60] G. Masini and V. Cencelli and L. Colace and F. DeNotaristefani and G. Assanto. A germanium photodetector array for the near infrared monolithically integrated with silicon CMOS readout electronics. *Physica E: Low-dimensional Systems and Nanostructures* **16**, 614 (2003).
- [61] Duke, C. B. Semiconductor surface reconstruction: The structural chemistry of two-dimensional surface compounds. *Chemical Reviews* **96**, 1237 (1996).
- [62] Mönch, W. *Semiconductor Surfaces and Interfaces* (Surface Sciences, Springer-Verlag Berlin Heidelberg, 1995).
- [63] Konecny, R. & Doren, D. J. Adsorption of water on Si(100)-(2×1) A study with density functional theory. *Journal of Chemical Physics* **106**, 2426 (1997).
- [64] Kubby, J. A., Griffith, J. E., Becker, R. S. & Vickers, J. S. Tunneling microscopy of Ge(001). *Physical Review B* **36**, 6079 (1987).

- [65] Needels, M., Payne, M. C. & Joannopoulos, J. D. High-order reconstructions of the Ge(001) surface. *Physical Review B* **38**, 6543 (1988).
- [66] Ferrer, S., Torrelles, X., Etgens, V. H., van der Vegt, H. A. & Fajardo, P. Atomic Structure of the $c(4\times 2)$ Surface Reconstruction of Ge(001) as Determined by X-Ray Diffraction. *Physical Review Letters* **75**, 1771 (1995).
- [67] Yoshimoto, Y., Nakamura, Y., Kawai, H., Tsukada, M. & Nakayama, M. Ge(001) surface reconstruction studied using a first-principles calculation and a Monte Carlo simulation. *Physical Review B* **61**, 1965 (2000).
- [68] Radny, M. W., Shah, G. A., Smith, P. V., Schofield, S. R. & Curson, N. J. Electronic effects induced by single hydrogen atoms on the Ge(001) surface. *Journal of Chemical Physics* **128**, 244707 (2008).
- [69] Goldoni, A., Modesti, S., Dhanak, V., Sancrotti, M. & Santoni, A. Evidence for three surface components in the 3d core-level photoemission spectra of Ge(100)- (2×1) surface. *Physical Review B* **54**, 11340 (1996).
- [70] Göthelid, M., LeLay, G., Wigren, C., Björkqvist, M. & Karlsson, U. Iodine reaction and passivation of the Ge(111) surface. *Surface Science* **371**, 264 (1997).
- [71] Bent, S. F. Organic functionalization of group iv semiconductor surfaces: principles, examples, applications, and prospects. *Surface Science* **500**, 879 (2002).
- [72] Roche, J., Ryand, P. & Hughes, G. J. Core level photoemission studies of the sulphur terminated Ge(001) surface. *Applied Surface Science* **174**, 271 (2001).
- [73] Rivillon, S., Chabal, Y. J., Amy, F. & Kahn, A. Hydrogen passivation of germanium (100) surface using wet chemical preparation. *Applied Physics Letters* **87**, 253101 (2005).
- [74] Ardalan, P., Musgrave, C. B. & Bent, S. F. Formation of alkanethiolate self-assembled monolayers at halide-terminated Ge surfaces. *Langmuir* **25**, 2013 (2009).
- [75] Chabal, Y. High-resolution infrared spectroscopy of adsorbates on semiconductor surfaces: Hydrogen on Si(100) and Ge(100). *Surface Science* **168**, 594 (1986).
- [76] Lee, J. Y. *et al.* Atomic-scale structural evolution of Ge(100) surfaces etched by H and D. *Applied Physics Letters* **84**, 5028 (2004).
- [77] Boland, J. J. Manipulating chlorine atom bonding on the Si(100)- (2×1) surface with the STM. *Science* **262**, 1703 (1993).
- [78] Lee, J., Maeng, J., Kim, A., Cho, Y. & Kim, S. Kinetics of H_2 (D_2) desorption from a Ge(100)- $2\times 1:H$ (D) surface studied using scanning tunneling microscopy and temperature programmed desorption. *Journal of Chemical Physics* **128**, 1929 (2003).
- [79] Scappucci, G., Capellini, G., Lee, W. C. T. & Simmons, M. Y. Atomic-scale patterning of hydrogen terminated Ge(001) by scanning tunneling microscopy. *Nanotechnology* **20**, 495302 (2009).
- [80] Takayanagi, K., Tanishiro, Y., Takahashi, S. & Takahashi, M. Structure analysis of Si(111)- 7×7 reconstructed surface by transmission electron diffraction. *Surface Science* **164**, 367 (1985).
- [81] Feidenhans'l, R. *et al.* Surface structure and long-range order of the Ge(111)- $c(2\times 8)$ reconstruction. *Physical Review B* **38**, 9715 (1988).
- [82] Razado-Colambo, I., He, J., Zhang, H. M., Hansson, G. V. & Uhrberg, R. I. G. Electronic structure of Ge(111) $c(2\times 8)$: STM, angle-resolved photoemission, and theory. *Physical Review B* **79**, 205410 (2009).
- [83] Rich, D. H., Miller, T. & Chiang, T. C. Absolute determination of surface core-level emission for Ge(100)- (2×1) and Ge(111)- $c(2\times 8)$: Surface reconstruction and defects. *Physical Review Letters* **60**, 357 (1988).

- [84] Göthelid, M., Grehk, T. M., Hammar, M., Karlsson, U. O. & Flodström, S. A. Adatom and rest-atom contributions in Ge(111)c(2×8) and Ge(111)-Sn(7×7) core-level spectra. *Physical Review B* **48**, 2012 (1993).
- [85] Ichikawa, T. An ab initio study on the atomic geometry of reconstructed Ge(1 1 0)16×2 surface. *Surface Science* **544**, 58 (2003).
- [86] Stekolnikov, A. A., Furthmüller, J. & Bechstedt, F. Structural elements on reconstructed Si and Ge(110) surfaces. *Physical Review B* **70**, 045305 (2004).
- [87] Wöll, C., Chiang, S., Wilson, R. J. & Lippel, P. H. Determination of atom positions at stacking-fault dislocations on Au(111) by scanning tunneling microscopy. *Physical Review B* **39**, 7988 (1989).
- [88] Hove, M. V. *et al.* The surface reconstructions of the (100) crystal faces of iridium, platinum and gold: I. experimental observations and possible structural models. *Surface Science* **103**, 189 (1981).
- [89] Barth, J. V., Brune, H., Ertl, G. & Behm, R. J. Scanning tunneling microscopy observations on the reconstructed Au(111) surface: Atomic structure, long-range superstructure, rotational domains, and surface defects. *Physical Review B* **42**, 9307 (1990).
- [90] Gottfried, J. M., Flechtner, K., Kretschmann, A., Lukasczyk, T. & Steinrück, H.-P. Direct synthesis of a metalloporphyrin complex on a surface. *Journal of the American Chemical Society* **128**, 5644 (2006).
- [91] Yokoyama, T., Yokoyama, S., Kamikado, T. & Mashiko, S. Nonplanar adsorption and orientational ordering of porphyrin molecules on Au(111). *Journal of Chemical Physics* **115**, 3814 (2001).
- [92] Shelnutt, J. A. *et al.* Nonplanar porphyrins and their significance in proteins. *Chemical Society Review* **27**, 31 (1998).
- [93] Senge, M. O. Exercises in molecular gymnastics: bending, stretching and twisting porphyrins. *Chemical Communications* 243 (2006).
- [94] Cinacchi, G. & Prampolini, G. Estimate of benzene-triphenylene and triphenylene-triphenylene interactions: A topic relevant to columnar discotic liquid crystals. *Journal of Physical Chemistry C* **112**, 25 (2008).
- [95] Ritchie, G. & Vrbancich, J. Solution-state conformations of 1,3,5-triphenylbenzene, triphenyl-s-triazine and tri(2-pyridinyl)-s-triazine; A Kerr and Cotton-Mouton effect study. *Journal of Molecular Structure* **78**, 279 (1982).
- [96] Cailleau, H. *et al.* Double-well potentials and structural phase transitions in polyphenyls. *Faraday Discussions of the Chemical Society* **69**, 7 (1980).
- [97] Brédas, J. L., Thémans, B., Fripiat, J. G., André, J. M. & Chance, R. R. Highly conducting polyparaphenylene, polypyrrole, and polythiophene chains: An *ab initio* study of the geometry and electronic-structure modifications upon doping. *Physical Review B* **29**, 6761 (1984).
- [98] Wudl, F., Wobschall, D. & Hufnagel, E. J. Electrical conductivity by the bis(1,3-dithiole)-bis(1,3-dithiolium) system. *Journal of the American Chemical Society* **94**, 670 (1972).
- [99] Bendikov, M., Wudl, F. & Perepichka, D. F. Tetrathiafulvalenes, oligoacenes, and their buckminsterfullerene derivatives: The brick and mortar of organic electronics. *Chemical Reviews* **104**, 4891 (2004).
- [100] Norris, A. C. *Manipulating atoms using scanning probe microscopy*. Dissertation, University of Dublin, Trinity College (2009).
- [101] Spencer, N. D., Goddard, P. J., Davies, P. W., Kitson, M. & Lambert, R. M. A simple, controllable source for dosing molecular halogens in UHV. *Journal of Vacuum Science Technology A: Vacuum, Surfaces, and Films* **1**, 1554 (1983).

- [102] Bechtold, E. Adsorption of fluorine on Pt(111). *Applications of Surface Science* **7**, 231 (1981).
- [103] Li, Z. The SGM1-Scienta beamline at ASTRID (2009). URL <http://www.isa.au.dk/facilities/astrid/beamlines/sgm1/sgm1.asp>.
- [104] Li, Z. The SX700 beamline at ASTRID (2009). URL <http://www.isa.au.dk/facilities/astrid/beamlines/sx700/sx700.asp>.
- [105] Omicron. *EA125 hemispherical energy analyser* (2004). URL <http://www.omicron.de/en/products/ea-125-/instrument-concept>.
- [106] Hesse, R. Unifit for Windows - The Art of Peak Fit (2004). URL <http://www.uni-leipzig.de/unifit/>.
- [107] Hermann, K. & Pettersson, L. G. M. Stobe manual, stockholm, berlin (2005). URL <http://www.fhi-berlin.mpg.de/KHsoftware/StoBe/index.html>.
- [108] Perdew, J. P. & Yue, W. Accurate and simple density functional for the electronic exchange energy - generalized gradient approximation. *Physical Review B* **33**, 8800 (1986).
- [109] Becke, A. D. Density-functional exchange-energy approximation with correct asymptotic-behavior. *Physical Review A* **38**, 3098 (1988).
- [110] Omicron. *Variable temperature UHV SPM manual* (2005). URL <http://www.omicron.de/en/products/variable-temperature-spm>.
- [111] Ekvall, I., Wahlström, E., Claesson, D., Olin, H. & Olsson, E. Preparation and characterization of electrochemically etched W tips for STM. *Measurement Science and Technology* **10**, 11 (1999).
- [112] Yu, Z., Wang, C., Du, Y., Thevuthasan, S. & Lyubintsev, I. Reproducible tip fabrication and cleaning for UHV STM. *Ultramicroscopy* **108**, 873 (2008).
- [113] Zhang, R. & Ivey, D. Preparation of sharp polycrystalline tungsten tips for scanning tunneling microscopy imaging. *Journal of Vacuum Science and Technology* **14**, 1 (1996).
- [114] Horcas, I. *et al.* WSXM: A software for scanning probe microscopy and a tool for nanotechnology. *Review of Scientific Instruments* **78**, 013705 (2007).
- [115] Wolkow, R. A. Controlled molecular adsorption on silicon: Laying a foundation for molecular devices. *Annual Reviews in Physical Chemistry* **50**, 413 (1999).
- [116] Hamers, R., Tromp, R. & Demuth, J. Electronic and geometric structure of Si(111)-(7×7) and Si(001) surfaces. *Surface Science* **181**, 346 (1987).
- [117] Gill, G. & Willis, M. *Pericyclic reactions* (Chapman and Hall, London, 1974).
- [118] Carruthers, W. *Cycloaddition reactions in organic synthesis* (Pergamon Press, New York, 1990).
- [119] Wassermann, A. *Diels-Alder reactions: Organic background and physio-chemical aspect* (Elsevier, New York, 1965).
- [120] Woodward, R. & Hoffmann, R. *The conservation of orbital symmetry* (Academic Press, New York, 1970).
- [121] Hamers, R. J. *et al.* Cycloaddition chemistry of organic molecules with semiconductor surfaces. *Accounts of Chemical Research* **33**, 617 (2000).
- [122] Liu, H. & Hamers, R. J. Stereoselectivity in Molecule-Surface Reactions: Adsorption of Ethylene on the Silicon(001) Surface. *Journal of the American Chemical Society* **119**, 7593 (1997).
- [123] Lopinski, G. P., Moffatt, D. J., Wayner, D. D. M. & Wolkow, R. A. How Stereoselective Are Alkene Addition Reactions on Si(100)? *Journal of the American Chemical Society* **122**, 3548 (2000).
- [124] Hovis, J. S. *et al.* Cycloaddition chemistry at surfaces: Reaction of alkenes with the diamond(001)-2 × 1 surface. *Journal of the American Chemical Society* **122**, 732 (2000).

- [125] Konecny, R. & Doren, D. J. Theoretical prediction of a facile Diels-Alder reaction on the Si(100)-2×1 surface. *Journal of the American Chemical Society* **119**, 11098 (1997).
- [126] Teplyakov, A. V., Kong, M. J. & Bent, S. F. Vibrational Spectroscopic Studies of Diels-Alder Reactions with the Si(100)-2×1 Surface as a Dienophile. *Journal of the American Chemical Society* **119**, 11100 (1997).
- [127] Teplyakov, A. V., Lal, P., Noah, Y. A. & Bent, S. F. Evidence for a Retro-Diels-Alder Reaction on a Single Crystalline Surface: Butadienes on Ge(100). *Journal of the American Chemical Society* **120**, 7377 (1998).
- [128] Hovis, J. S., Liu, H. & Hamers, R. J. Cycloaddition Chemistry of 1,3-Dienes on the Silicon(001) Surface: Competition between [4 + 2] and [2 + 2] Reactions. *The Journal of Physical Chemistry B* **102**, 6873 (1998).
- [129] Kong, M. J. *et al.* Interaction of C6 cyclic hydrocarbons with a Si(100)-2×1 surface: Adsorption and hydrogenation reactions? *The Journal of Physical Chemistry B* **104**, 3000 (2000).
- [130] Teague, L. & Boland, J. STM study of multiple bonding configurations and mechanism of 1,3-cyclohexadiene attachment on Si(100)-2×1. *The Journal of Physical Chemistry B* **107**, 3820 (2003).
- [131] Fink, A., Menzel, D. & Widdra, W. Symmetry and Electronic Structure of Benzene Adsorbed on Single-Domain Ge(100)-(2×1) and Ge/Si(100)-(2×1). *The Journal of Physical Chemistry B* **105**, 3828 (2001).
- [132] Wang, G. T. *et al.* Reactions of Cyclic Aliphatic and Aromatic Amines on Ge(100)-2×1 and Si(100)-2×1. *The Journal of Physical Chemistry B* **107**, 4982 (2003).
- [133] Cabailh, G. *Synchrotron radiation studies of organic/inorganic semiconductor interfaces*. Dissertation, University of Dublin, Trinity College (2004).
- [134] Liu, L., Yu, J., Viernes, N. O. L., Moore, J. S. & Lyding, J. W. Adsorption of cobalt phthalocyanine on Si(100)2×1 and Si(100)-2×1:H surfaces studied by scanning tunneling microscopy and spectroscopy. *Surface Science* **516**, 118 (2002).
- [135] Kanai, M. *et al.* Scanning tunneling microscopy observation of copper-phthalocyanine molecules on Si(100) and Si(111) surfaces. *Surface Science* **329**, L619 (1995).
- [136] Otsuki, J. STM studies on porphyrins. *Coordination Chemistry Reviews* **254**, 2311 (2010).
- [137] Romaner, L., Nabok, D., Puschnig, P., Zojer, E. & Ambrosch-Draxl, C. Theoretical study of PTCDA adsorbed on the coinage metal surfaces, Ag(111), Au(111) and Cu(111). *New Journal of Physics* **11**, 053010 (2009).
- [138] Jung, T. A., Schlittler, R. R. & Gimzewski, J. K. Conformational identification of individual adsorbed molecules with the STM. *Nature* **386**, 696 (1997).
- [139] Auwärter, W. *et al.* Conformational adaptation and selective adatom capturing of tetrapyrrolyl-porphyrin molecules on a copper (111) surface. *Journal of the American Chemical Society* **129**, 11279 (2007).
- [140] Weber-Bargioni, A. *et al.* Visualizing the frontier orbitals of a conformationally adapted metalloporphyrin. *ChemPhysChem* **9**, 89 (2008).
- [141] Auwärter, W. *et al.* Visualizing the frontier orbitals of a conformationally adapted metalloporphyrin. *ChemPhysChem* **9**, 89 (2008).
- [142] Moresco, F. *et al.* Conformational changes of single molecules induced by scanning tunneling microscopy manipulation: A route to molecular switching. *Physical Review Letters* **86**, 672 (2001).
- [143] Qiu, X. H., Nazin, G. V. & Ho, W. Mechanisms of reversible conformational transitions in a single molecule. *Physical Review Letters* **93**, 196806 (2004).

- [144] Iancu, V., Deshpande, A. & Hla, S.-W. Manipulating Kondo Temperature via Single Molecule Switching. *Nano Letters* **6**, 820 (2006).
- [145] Niwa, Y., Kobayashi, H. & Tsuchiya, T. X-ray photoelectron spectroscopy of tetraphenylporphyrin and phthalocyanine. *Journal of Chemical Physics* **60**, 799 (1974).
- [146] McGuinness, C. Trinity College Dublin, private communication (2012).
- [147] Cudia, C. C. *et al.* Electronic structure and molecular orientation of a Zn-tetra-phenyl porphyrin multilayer on Si(1×1). *Surface Science* **600**, 4013 (2006).
- [148] Doyle, C. Dublin City University, private communication (2012).
- [149] Hill, I., Kahn, A., Cornil, J., dos Santos, D. & Brédas, J. Occupied and unoccupied electronic levels in organic π -conjugated molecules: comparison between experiment and theory. *Chemical Physics Letters* **317**, 444 (2000).
- [150] Hauschild, A. *et al.* Molecular distortions and chemical bonding of a large π -conjugated molecule on a metal surface. *Physical Review Letters* **94**, 036106 (2005).
- [151] Campuzano, J. C. *The Chemical Physics of Solid Surfaces and Heterogeneous Catalysis: Chemisorption Systems, Vol. 3A* (Elsevier, Amsterdam, 1990).
- [152] Krasnikov, S. *et al.* Formation of extended covalently bonded Ni porphyrin networks on the Au(111) surface. *Nano Research* **4**, 376 (2011).
- [153] Li, Q. *et al.* Adsorption, manipulation and self-assembling of TBrPP-Co molecules on a Ag/Si(111) surface by scanning tunnelling microscopy. *Nanotechnology* **19**, 465707 (2008).
- [154] Doyle, C. *et al.* Evidence for the formation of an intermediate complex in the direct metalation of tetra(4-bromophenyl)-porphyrin on the Cu(111) surface. *Chemical Communications* 12134 (2011).
- [155] Cottrell, T. L. *The Strengths of Chemical Bonds, 2nd edition* (Butterworths, London, 1958).
- [156] Ardalan, P. *et al.* Formation of an oxide-free Ge/TiO₂ interface by atomic layer deposition on brominated Ge. *Applied Physics Letters* **92**, 252902 (2008).
- [157] Sun, S., Sun, Y., Liu, Z., Lee, D.-I. & Pianetta, P. Roles of oxygen and water vapor in the oxidation of halogen terminated Ge(111) surfaces. *Applied Physics Letters* **89**, 231925 (2006).
- [158] Trucks, G. W., Raghavachari, K., Higashi, G. S. & Chabal, Y. J. Mechanism of hf etching of silicon surfaces: A theoretical understanding of hydrogen passivation. *Physical Review Letters* **65**, 504 (1990).
- [159] Deegan, T. & Hughes, G. An X-ray photoelectron spectroscopy study of the HF etching of native oxides on Ge(111) and Ge(100) surfaces. *Applied Surface Science* **123**, 66 (1998).
- [160] Kim, J., Saraswat, K. & Nishi, Y. *ECS Transcripts* **1**, 214 (2005).
- [161] Bodlaki, D., Yamamoto, H., Waldeck, D. H. & Borguet, E. Ambient stability of chemically passivated germanium interfaces. *Surface Science* **543**, 63 (2003).
- [162] Cao, S., Tang, J.-C., Wang, L., Zhu, P. & Shen, S. Multiple-scattering studies of the near edge X-ray absorption fine structure of the Cl-passivated Ge(1×1) surface. *Surface Science* **505**, 289 (2002).
- [163] Göthelid, M., Lay, G. L. & Karlsson, U. An ordered layer of molecular iodine on Ge(100)-2×1. *Surface Science* **556**, 203 (2004).
- [164] de Wijs, G. A., De Vita, A. & Selloni, A. First-principles study of chlorine adsorption and reactions on Si(100). *Physical Review B* **57**, 10021 (1998).
- [165] Chander, M., Goetsch, D. A., Aldao, C. M. & Weaver, J. H. Determination of dynamic parameters controlling atomic scale etching of Si(100)-(2×1) by chlorine. *Physical Review Letters* **74**, 2014 (1995).

- [166] Cohen, S. M., Hukka, T. I., Yang, Y. L. & D'Evelyn, M. P. Hydrogen-halogen chemistry on semiconductor surfaces. *Thin Solid Films* **225**, 155 (1993).
- [167] Okada, H. *et al.* First-principles molecular-dynamics calculations and STM observations of dissociative adsorption of Cl₂ and F₂ on Si(001) surface. *Surface Science* **515**, 287 (2002).
- [168] Mikolajczyk, P. & Stankiewicz, B. Bromine adsorption on Ge(001) surface: comparative study for coverages of 0.25, 0.5, 0.75 and 1 monolayer. *Central European Journal of Physics* **7**, 279 (2009).
- [169] Herrmann, C. F. & Boland, J. J. The role of repulsive interactions in molecular bromine adsorption and patterning of Si(100)-2×1. *Surface Science* **460**, 223 (2000).
- [170] Jackman, R., Price, R. & Foord, J. Semiconductor surface etching by halogens: Fundamental steps. *Applied Surface Science* **36**, 296 (1989).
- [171] Chander, M., Li, Y. Z., Patrin, J. C. & Weaver, J. H. Layer-by-layer etching of Si(100)-2×1 with Br₂: A scanning-tunneling-microscopy study. *Physical Review B* **47**, 13035 (1993).
- [172] Rioux, D., Stepniak, F., Pechman, R. J. & Weaver, J. H. Chemisorption and thermally activated etching of Si(100)-2×1 by iodine. *Physical Review B* **51**, 10981 (1995).
- [173] Ikeda, K., Imai, S. & Matsumura, M. Atomic layer etching of germanium. *Applied Surface Science* **112**, 87 (1997).
- [174] Simpson, W. & Yarmoff, J. Bonding geometries of F and Cl on Si(100)-2×1. *Surface Science* **359**, 135 (1996).
- [175] Thornton, G. *et al.* Bonding sites for Cl on Si(100)2 × 1 and Si(111)7 × 7. *Surface Science* **211/212**, 959 (1989).
- [176] Gao, Q., Cheng, C. C., Chen, P. J., Choyke, W. J. & J. T. Yates, J. Chlorine bonding sites and bonding configurations on Si(100)-(2 × 1). *The Journal of Chemical Physics* **98**, 8308 (1993).
- [177] Stankiewicz, B. Simulations of iodine adsorbed Ge(001) surface and its STM images. *Applied Surface Science* **254**, 4380 (2008).
- [178] Schnell, R. D., Himpfel, F. J., Bogen, A., Rieger, D. & Steinmann, W. Surface core-level shifts for clean and halogen-covered Ge(100) and Ge(111). *Physical Review B* **32**, 8052 (1985).
- [179] Radny, M. University of New South Wales, private communication (2012).
- [180] Chen, J.-M. *et al.* Adsorption and photon-stimulated desorption of CCl₄ on an Al(111) surface investigated with synchrotron radiation. *The Journal of Chemical Physics* **109**, 8027 (1998).
- [181] Jordan, K. & Shvets, I. V. Self-assembled Fe nanodots on Ge(001). *Applied Physics Letters* **88**, 193111 (2006).
- [182] Fujimoto, Y. *et al.* Theoretical Study on the Scanning Tunneling Microscopy Image of Cl-adsorbed Si(001). *Japanese Journal of Applied Physics* **42**, 5267 (2003).
- [183] Ullmann, F. & Bielecki, J. Ueber synthesen in der biphenylreihe. *Berichte der Deutschen Chemischen Gesellschaft* **34**, 2174 (1901).
- [184] Hassan, J., Sévignon, M., Gozzi, C., Schulz, E. & Lemaire, M. Aryl-aryl bond formation one century after the discovery of the Ullmann reaction. *Chemical Reviews* **102**, 1359 (2002).
- [185] McCarty, G. S. & Weiss, P. S. Formation and manipulation of protopolymer chains. *Journal of the American Chemical Society* **126**, 16772 (2004).
- [186] Lafferentz, L. *et al.* Controlling on-surface polymerization by hierarchical and substrate-directed growth. *Nature Chemistry* **4**, 215 (2012).
- [187] Cai, J. *et al.* Atomically precise bottom-up fabrication of graphene nanoribbons. *Nature* **466**, 470 (2010).

- [188] Gutzler, R. *et al.* Surface mediated synthesis of 2D covalent organic frameworks: 1,3,5-tris(4-bromophenyl)benzene on graphite(001), Cu(111), and Ag(110). *Chemical Communications* 4456 (2009).
- [189] Bieri, M. *et al.* Two-dimensional polymer formation on surfaces: Insight into the roles of precursor mobility and reactivity. *Journal of the American Chemical Society* **132**, 16669 (2010).
- [190] Kittelmann, M. *et al.* On-surface covalent linking of organic building blocks on a bulk insulator. *ACS Nano* **5**, 8420 (2011).
- [191] Hla, S.-W., Bartels, L., Meyer, G. & Rieder, K.-H. Inducing all steps of a chemical reaction with the scanning tunneling microscope tip: Towards single molecule engineering. *Phys. Rev. Lett.* **85**, 2777 (2000).
- [192] Beltran, L. M. C., Cui, C., Leung, D. H., Xu, J. & Hollander, F. J. 1,3,5-Tris(*p*-bromophenyl)-benzene. *Acta Crystallographica Section E* **58**, o782 (2002).
- [193] Zhou, X.-L., Solymosi, F., Blass, P., Cannon, K. & White, J. Interactions of methyl halides (Cl, Br and I) with Ag(111). *Surface Science* **219**, 294 (1989).
- [194] Lipton-Duffin, J. A., Ivashenko, O., Perepichka, D. F. & Rosei, F. Synthesis of polyphenylene molecular wires by surface-confined polymerization. *Small* **5**, 592 (2009).
- [195] Cafolla, A. A. Dublin City University, private communication (2008).
- [196] Ourdjini, O. *et al.* Substrate-mediated ordering and defect analysis of a surface covalent organic framework. *Physical Review B* **84**, 125421 (2011).
- [197] Abel, M., Clair, S., Ourdjini, O., Mossoyan, M. & Porte, L. Single layer of polymeric Fe-phthalocyanine: An organometallic sheet on metal and thin insulating film. *Journal of the American Chemical Society* **133**, 1203 (2011).
- [198] Weigelt, S. *et al.* Covalent Interlinking of an Aldehyde and an Amine on a Au(111) Surface in Ultrahigh Vacuum. *Angewandte Chemie International Edition* **46**, 9227 (2007).
- [199] Sakamoto, J., v. Heijst, J., Lukin, O. & Schlüter, A. D. Two-dimensional polymers: Just a dream of synthetic chemists? *Angewandte Chemie International Edition* **48**, 1030 (2009).
- [200] In't Veld, M., Iavicoli, P., Haq, S., Amabilino, D. B. & Raval, R. A two-dimensional porphyrin-based porous network featuring communicating cavities for the templated complexation of fullerenes. *Chemical Communications* 1536 (2008).
- [201] Weigelt, S. *et al.* Surface synthesis of 2D branched polymer nanostructures. *Angewandte Chemie International Edition* **47**, 4406 (2008).
- [202] Lee, H.-L. *Strategies for the Formation of Covalently Bonded Nano-Networks on Metal Surfaces through Amine Reactions*. Ph.D. thesis, Dublin City University (2012).
- [203] Treier, M., Fasel, R., Champness, N. R., Argent, S. & Richardson, N. V. Molecular imaging of polyimide formation. *Physical Chemistry Chemical Physics* **11**, 1209 (2009).
- [204] Treier, M. *et al.* Surface-assisted cyclodehydrogenation provides a synthetic route towards easily processable and chemically tailored nanographenes. *Nature Chemistry* **3**, 61 (2011).
- [205] Rim, K. *et al.* Forming aromatic hemispheres on transition-metal surfaces. *Angewandte Chemie International Edition* **46**, 7891 (2007).
- [206] Otero, G. *et al.* Fullerenes from aromatic precursors by surface-catalysed cyclodehydrogenation. *Nature* **454**, 865 (2008).
- [207] Amsharov, K. *et al.* Towards the isomer-specific synthesis of higher fullerenes and buckybowls by the surface-catalyzed cyclodehydrogenation of aromatic precursors. *Angewandte Chemie International Edition* **49**, 9392 (2010).

- [208] Matena, M., Riehm, T., Stöhr, M., Jung, T. & Gade, L. Transforming Surface Coordination Polymers into Covalent Surface Polymers: Linked Polycondensed Aromatics through Oligomerization of N-Heterocyclic Carbene Intermediates. *Angewandte Chemie* **120**, 2448 (2008).
- [209] Weigelt, S. *et al.* Formation of trioctylamine from octylamine on Au(111). *Journal of the American Chemical Society* **130**, 5388 (2008).
- [210] Lacaze-Dufaure, C. Centre Interuniversitaire de Recherche et d'Ingénierie des Matériaux, Toulouse; private communication (2012).
- [211] Zwaneveld, N. A. A. *et al.* Organized formation of 2D extended covalent organic frameworks at surfaces. *Journal of the American Chemical Society* **130**, 6678 (2008).
- [212] Faury, T. *et al.* Sequential linking to control growth of a surface covalent organic framework. *The Journal of Physical Chemistry C* **116**, 4819 (2012).
- [213] Neddermeyer, H. Photoemission-study of the surface electronic-structure of Ag(100). *Journal of Physics, F-Metal Physics* **12**, L241 (1982).
- [214] Costantini, G., Rusponi, S., Giudice, E., Boragno, C. & Valbusa, U. C-60 thin films on Ag(001): an STM study. *Carbon* **37**, 727 (1999). Symposium K on Carbon-Based Materials for Microelectronics of the European-Materials-Research-Society-Meeting, Strasbourg, France, Jun 16-19, 1998.
- [215] Tong, X., DiLabio, G. A. & Wolkow, R. A. A self-directed growth process for creating covalently bonded molecular assemblies on the H-Si(100)-3×1 surface. *Nano Letters* **4**, 979 (2004).
- [216] Fölsch, S., Barjenbruch, U. & Henzler, M. Atomically thin epitaxial films of NaCl on germanium. *Thin Solid Films* **172**, 123 (1989).
- [217] Glöckler, K., Sokolowski, M., Soukopp, A. & Umbach, E. Initial growth of insulating overlayers of NaCl on Ge(100) observed by scanning tunneling microscopy with atomic resolution. *Physical Review B* **54**, 7705 (1996).
- [218] Abel, M. & Clair, S. IM2NP, private communication (2012).
- [219] Mattevi, C., Kim, H. & Chhowalla, M. A review of chemical vapour deposition of graphene on copper. *Journal of Material Chemistry* **21**, 3324 (2011).
- [220] Coleman, J. N. *et al.* Two-dimensional nanosheets produced by liquid exfoliation of layered materials. *Science* **331**, 568 (2011).